



**HAL**  
open science

# Synthesis of zeolitic hybrid materials for ethanol-water separation and their characterization via advanced insitu IR spectroscopic techniques

Rita Zakhia Douaihy

► **To cite this version:**

Rita Zakhia Douaihy. Synthesis of zeolitic hybrid materials for ethanol-water separation and their characterization via advanced insitu IR spectroscopic techniques. Organic chemistry. Normandie Université, 2022. English. NNT : 2022NORMC223 . tel-04166573

**HAL Id: tel-04166573**

**<https://theses.hal.science/tel-04166573v1>**

Submitted on 20 Jul 2023

**HAL** is a multi-disciplinary open access archive for the deposit and dissemination of scientific research documents, whether they are published or not. The documents may come from teaching and research institutions in France or abroad, or from public or private research centers.

L'archive ouverte pluridisciplinaire **HAL**, est destinée au dépôt et à la diffusion de documents scientifiques de niveau recherche, publiés ou non, émanant des établissements d'enseignement et de recherche français ou étrangers, des laboratoires publics ou privés.



Normandie Université

## THÈSE

Pour obtenir le diplôme de doctorat

Spécialité CHIMIE

Préparée au sein de l'Université de Caen Normandie

### Synthesis of zeolitic hybrid materials for ethanol-water separation and their characterization via advanced insitu IR spectroscopic techniques

Présentée et soutenue par  
**RITA ZAKHIA DOUAIHY**

Thèse soutenue le 19/07/2022  
devant le jury composé de

M. CARLOS HENRIQUES	Professeur, Université de LISBONNE	Rapporteur du jury
M. ALI TRABOLSI	Professeur des universités, New York University of Abu Dhabi	Rapporteur du jury
M. PHILIPPE BAZIN	Ingénieur de recherche, Université de Caen Normandie	Membre du jury
MME SANDRINE BOURRELLY	Maître de conférences, Aix-Marseille Université	Membre du jury
M. ARNAUD TRAVERT	Professeur des universités, Université de Caen Normandie	Président du jury
M. ALEXANDRE VIMONT	Ingénieur de recherche au CNRS, Université de Caen Normandie	Directeur de thèse

Thèse dirigée par **ALEXANDRE VIMONT (Laboratoire catalyse et spectrochimie (Caen))**



UNIVERSITÉ  
CAEN  
NORMANDIE



Laboratoire  
Catalyse & Spectrochimie



This section is dedicated to all the people who participated in this long journey in one way or another.

First and foremost, I would like to thank my supervisors, Alexandre and Philippe, for allowing me to pursue my Ph.D. Thank you for your time and instruction, for your continuous support, for guiding me through my mistakes, and for helping me become a better scientist. I am grateful for the knowledge you have imparted to me and your confidence in me. Thank you both for everything; it has been a genuinely enjoyable journey.

Second, I would like to express my sincere gratitude to the jury members: Carlos Henriques, Ali Trabosli, Sandrine Bourrelly, and Arnaud Travert for reading this manuscript and providing helpful feedback.

Next, I would like to thank our main collaborator, Mohamad El-Roz, for the scientific discussions that contributed to this work. I sincerely appreciate the advice you have shared. Thank you for constantly pushing me to give the best in me. I want to thank also our collaborators Jean-François Chailan and Armand Fahs for the AFM measurements and Oleg Lebedev for the TEM images.

I convey special thanks to Valentin Valtchev and Louwanda Al Lakiss for sharing their knowledge on zeolites and helping me with the synthesis of zeolitic core-shell materials. To Houssein Nasrallah for his patience when working together in the organic synthesis.

Additionally, I would like to thank the LCS staff (technicians, engineers, and administrative staff...) for their helpful services, efforts, and expertise.

I want to thank all the people I have met at the LCS during these four years; you were so welcoming and helped me adapt quickly to a new place. Mariam, Elsy, Judy, Ibrahim, Ghinwa, Moussa, Edwin, Houeida, Florent, Pierre, Nicolas, Nuria, Igor, ... The list of amazing people that I have encountered during these four years is long, but to all of them: Thanks for lots of memories that I will never forget. You made my stay at LCS so much fun. A particular word of thanks to Hussein: thanks for your support and always being there no matter what.

I want to thank all of my friends in Caen (Serge, Lea, Anthony, Rima...) who helped make this stay so memorable. I consider myself fortunate to have met them and glad to call them friends. A special thanks to Marie for our special friendship and your support. To my friends abroad: Alaa, Eliane, Hamsa, Samar, Chantal, Meghrie, and Nayri, I am very thankful for having you on this whole journey. You were always encouraging me despite the distance between us.

Words fail to express my indebtedness and gratitude to my family:

A heartfelt thanks to Mom and Dad. Without your unfailing emotional support, unconditional trust, and timely encouragement, I would not have been where I am today. I am very grateful to my brother and sister for believing in me and supporting me unconditionally.

**All that I am or hope to be, I owe to you.**

Thank you all for making this possible, and I hope I make you all proud.



# Table of Contents

<b>GENERAL INTRODUCTION .....</b>	<b>9</b>
<b>References .....</b>	<b>16</b>
<b>CHAPTER ONE: LITERATURE REVIEW .....</b>	<b>19</b>
<b>1. Ethanol: Importance and Applications.....</b>	<b>21</b>
<b>2. Ethanol purification .....</b>	<b>22</b>
2.1. Chemical dehydration .....	23
2.2. Distillation processes.....	23
2.3. Pervaporation .....	23
2.4. Selective adsorption-based procedures .....	24
<b>3. Porous and hybrid materials for ethanol purification.....</b>	<b>25</b>
3.1. Porous materials: Zeolites .....	25
3.1.1. Generality.....	25
3.1.2. Porosity of the zeolites .....	26
3.1.3. Acid sites.....	27
3.1.4. Synthesis and post-treatment of zeolites .....	28
3.1.5. Applications of zeolites .....	30
3.2. Hybrid Materials.....	32
3.2.1. Core-shell materials .....	33
3.2.2. Mixed matrix membranes.....	37
<b>4. Scope of the work .....</b>	<b>43</b>
<b>References .....</b>	<b>45</b>
<b>CHAPTER TWO: EXPERIMENTAL PART.....</b>	<b>55</b>
<b>1. Materials: MFI zeolites .....</b>	<b>57</b>
<b>2. Methods .....</b>	<b>58</b>
2.1. Characterization techniques.....	58
2.1.1. Powder X-Ray Diffraction (PXRD) .....	58
2.1.2. Scanning Electron Microscopy (SEM) .....	59
2.1.3. Transmission Electron Microscopy (TEM) .....	59
2.1.4. Thermogravimetric Analysis (TGA).....	60
2.1.5. UV-Vis spectroscopy.....	60
2.1.6. Gas Physisorption.....	60
2.1.7. Inductively coupled plasma spectroscopy (ICP-MS) .....	62
2.2. FTIR Spectroscopy .....	62
2.2.1. In-situ FTIR .....	63
2.2.2. AGIR experiments.....	66
2.2.3. CARROUCELL experiments.....	68
<b>References.....</b>	<b>70</b>
<b>CHAPTER THREE: Quantitative IR study of ethanol/water coadsorption on MFI zeolites with different Si/Al ratios.....</b>	<b>73</b>
<b>Abstract.....</b>	<b>76</b>
<b>1. Introduction .....</b>	<b>77</b>

<b>2. Experimental section</b>	<b>78</b>
2.1. Materials	78
2.2. Characterization techniques:	78
2.3. In situ IR Spectroscopy:	79
2.4. Determination of the molar absorption coefficients of adsorbed ethanol and water:	80
2.5. Adsorption and coadsorption of ethanol and water using the CARROUCELL high-throughput IR cell:	80
<b>3. Results and discussion</b>	<b>81</b>
3.1. Structural and textural properties:	81
3.2. Accessibility of acid sites:	82
3.3. Determination of the molar absorption coefficients of adsorbed ethanol $\epsilon(\delta EtOH 1450\text{ cm}^{-1})$ and water and $\epsilon(\delta H_2O 1630\text{ cm}^{-1})$ :	84
3.4. Adsorption of Ethanol or Water on MFI-45:	85
3.4.1. Isotherm of Ethanol adsorption	85
3.4.2. Isotherm of Water adsorption	87
3.5. Adsorption of ethanol or water on MFI zeolites with different Si/Al ratios	89
3.6. Coadsorption of ethanol and water on MFI zeolites with different Si/Al ratios:	91
3.6.1. Validation of the $\epsilon(\delta EtOH 1450\text{ cm}^{-1})$ and $\epsilon(\delta H_2O 1630\text{ cm}^{-1})$ values for coadsorption experiments: comparison between AGIR and CARROUCELL setups:	91
3.6.2. Ethanol/water selectivity:	93
3.6.3. Influence of the Si/Al and the fraction of H <sub>2</sub> O in the gas phase on the relative amount of adsorbed EtOH ( <i>RC2H5OH</i> )	94
<b>4. Conclusion</b>	<b>97</b>
<b>Author Contributions</b>	<b>97</b>
<b>Acknowledgments</b>	<b>97</b>
<b>References</b>	<b>98</b>
<b>Supplementary Information</b>	<b>101</b>
<b>CHAPTER FOUR: Synthesis of silica-polymer core-shell hybrid materials with enhanced mechanical properties using a new bifunctional silane-based photoinitiator as coupling agent</b>	<b>107</b>
<b>General introduction</b>	<b>109</b>
<b>References</b>	<b>111</b>
<b>Abstract</b>	<b>116</b>
<b>1. Introduction</b>	<b>117</b>
<b>2. Materials and methods</b>	<b>118</b>
2.1. Materials	118
2.2. Methods	118
2.2.1. Synthesis of SPI-1	118
2.2.2. Grafting of SPI-1 on the surface of silica nanoparticles	119
2.2.3. Photopolymerization Process	119

2.2.4.	Film preparation .....	120
2.2.5.	Photopolymerization in solution .....	120
<b>2.3.</b>	<b>Characterization techniques.....</b>	<b>121</b>
<b>3.</b>	<b>Results and discussion.....</b>	<b>122</b>
<b>4.</b>	<b>Conclusion.....</b>	<b>131</b>
	<b>Acknowledgment.....</b>	<b>131</b>
	<b>Supplementary Information.....</b>	<b>131</b>
	<b>References.....</b>	<b>132</b>
	<b>Supplementary Information.....</b>	<b>134</b>
	<b>APPENDIX I.....</b>	<b>139</b>
<b>1.</b>	<b>Introduction.....</b>	<b>141</b>
<b>2.</b>	<b>Results and discussion.....</b>	<b>141</b>
<b>3.</b>	<b>Conclusion.....</b>	<b>146</b>
	<b>CHAPTER FIVE : New approach for preparing zeolite-polymer hybrid materials with hierarchical porosity: promising materials for separation and membrane's applications .....</b>	<b>149</b>
	<b>Abstract.....</b>	<b>152</b>
<b>1.</b>	<b>Introduction.....</b>	<b>153</b>
<b>2.</b>	<b>Experimental.....</b>	<b>154</b>
2.1.	Materials:.....	154
2.2.	Synthesis of 2,2-dimethyl-1-phenyl-5-(triethoxysilyl) pentane-1-one (SPI-1): 155	
2.3.	Grafting of SPI-1 on the surface of the MFI zeolites (SPI-1-MFI): .....	155
2.4.	Photopolymerization efficiency:.....	155
2.5.	Preparation of MFI@Polymer:.....	156
2.6.	Characterization techniques:.....	156
2.7.	Adsorption and coadsorption of ethanol and/or water:.....	157
<b>3.</b>	<b>Results and discussion.....</b>	<b>158</b>
3.1.	Characteristic of SPI-1-MFI samples: .....	158
3.2.	Efficiency of the grafted SPI-1-MFI in the photopolymerization of TMPA: ..	160
3.3.	Preparation and characterization of MFI@Polymer hybrid materials: .....	161
3.3.1.	Polymer loading in the MFI@Polymer hybrid material:.....	162
3.3.2.	Structural and textural properties:.....	163
3.3.3.	Morphological characterization .....	165
3.3.4.	Accessibility of the acid sites of MFI in MFI@Polymer .....	167
3.4.	Affinities of MFI and MFI@Polymer hybrid materials toward ethanol, water and ethanol/water mixture:.....	169
3.4.1.	Water and ethanol adsorption capacities of MFI and MFI@Polymer: .....	169
3.4.2.	Ethanol /water co-adsorption capacities of MFI and MFI@Polymer:.....	171
<b>4.</b>	<b>Conclusion.....</b>	<b>173</b>

<b>Associated content</b> .....	<b>174</b>
<b>Acknowledgment</b> .....	<b>174</b>
<b>References</b> .....	<b>175</b>
<b>Supporting Information</b> .....	<b>179</b>
<b>GENERAL CONCLUSION AND PERSPECTIVES</b> .....	<b>191</b>
1. <b>General conclusions</b> .....	<b>193</b>
2. <b>Perspectives</b> .....	<b>195</b>
<b>Résumé étendu en Français</b> .....	<b>199</b>
<b>References</b> .....	<b>206</b>





---

# GENERAL INTRODUCTION

---



In the last decade, environmental concerns have attracted the interest of experts worldwide due to their high importance and effect on human survival. The increase in the greenhouse gas levels, the depletion of oil supplies, and the dramatic increase in energy consumption have required the search for alternative sustainable resources for hydrocarbon-based fuels [1]. Biofuels, including bio alcohols and biogases, have been extensively produced among these clean and sustainable resources [2]. Bioethanol is considered one of the major constituents of these biofuels since it can be used to replace gasoline to a certain extent [3].

Bioethanol is characterized by its high-octane number, low cetane number, and combustion emits low NO<sub>x</sub> yields [4]. It is mainly obtained from the degradation and decomposition of the biomass [5]. Before its use as an additive or alternative to gasoline, a purification process is mandatory to remove undesired water traces. Conventional distillation processes were used for this aim [6]. However, the crucial part is to overcome the azeotrope barrier of the ethanol/water mixture [7]. Hence, alternate separation techniques were implemented, such as the separation on porous materials, hybrid porous materials, and membranes [8, 9]. For instance, zeolites offer high potential separation capacities since they are characterized by their high and tunable porosity, tunable hydrophilic/hydrophobic character, and important activity on their active acidic sites [10]. These properties are particularly enhanced when coupled with other materials to form core-shell hybrid particles or when used as fillers for mixed matrix membranes [11, 12]. The latter has been extensively synthesized and used to separate gaseous and liquid mixtures. Their importance results from combining the selective separation and adsorption characteristics of inorganic porous particles and polymeric matrices' mechanical and economic properties.

The synthesis of mixed matrix membranes has been prone to several problems, including the homogeneous dispersion of the inorganic filler in the polymeric matrix, the presence of strong interactions between the two constituents of the membrane, and notably, the accessibility to the pores of the inorganic compounds after their coverage [11]. Thus, overcoming these drawbacks to improve the activity of the membrane, particularly in the purification of ethanol from its aqueous mixture, is considered crucial for the dehydration of bioethanol.

Different techniques have extensively studied the separation or selective ethanol adsorption from a hydrous mixture on MMMs. To this end, coupled volumetric and gravimetric methods have been employed to study each component's adsorption/desorption isotherms from the mixture [13, 14]. Pulsed-field gradient (PFG)-nuclear magnetic resonance (NMR) was also used to study the diffusion of water, ethanol, and their mixture in polyacrylic acid (PAA) PAA-polysulfone and chitosan membranes [15, 16]. This technique allowed determining the preferential adsorptive sites towards ethanol and water present in these membranes. The experimental methods agreed with the theoretical studies, including grand canonical Monte Carlo and molecular dynamic simulations, conducted for the same purpose [17-19]. Nevertheless, infrared spectroscopy was only used to study the adsorption of either ethanol or water separately. The coadsorption of ethanol and water studied using IR spectroscopy was not discussed in the literature except for one study conducted in our laboratory on MOFs [20].

Consequently, this project was initiated to synthesize zeolitic core-shell hybrid materials via a promising procedure for enhancing the synthesis of mixed matrix membranes. After successfully synthesizing the desired hybrid materials, the second aim of this research work is to understand the mechanisms of adsorption and diffusion of ethanol and/or water adsorbed via developed spectroscopic techniques. The manuscript is written in the form of published/submitted articles and is divided into two parts. The first part discusses the unary and binary adsorptions of ethanol and water on parent zeolite materials. The second part focuses on the synthesis of hybrid materials for their application in the selective adsorption of ethanol and/or water.

While the **first chapter** summarizes the research work on porous materials for the purification of bioethanol and **the second chapter** quickly presents the experimental part of in this work, the **third chapter** is devoted to the spectroscopic study of ethanol and/or water adsorption on MFI zeolites. It is currently in preparation for submission. MFI zeolites were used since their active acidic sites show a dual affinity for ethanol and water. They were characterized using conventional characterization techniques such as PXRD, SEM, and Nitrogen sorption. Then, the strength of their acid sites and their quantification by adsorption of basic probe molecule (pyridine) was conducted via IR spectroscopy. Moreover, ethanol and

water's unary and binary adsorption systems were studied using spectroscopic techniques developed in the laboratory (AGIR and CARROUCELL setups). IR spectroscopy coupled with gravimetric analyses was used to determine the quantities of the adsorbed species, their nature, and the nature of the adsorption sites.

Interestingly, by correlating the acidic sites of MFI zeolites and the quantities of the adsorbed species, the number of each adsorbent per acid site has been determined and compared to the experimental and theoretical approaches in the literature. Finally, the effect of the Si/Al ratio was investigated in the coadsorption of ethanol and water. The selectivity of ethanol on MFI zeolites has been studied for some of them. Due to some limitations in measuring the characteristic vibrational bands of the adsorbed species, a new parameter (Ratio of adsorbed ethanol) has been introduced to study the effect of the Si/Al ratio during the adsorption of ethanol and water in the binary system. It was shown that the adsorption of ethanol on MFI zeolites is affected by the Si/Al ratio and the water content in the gas phase. For instance, ethanol is less adsorbed when the Al or water content is important. Hence, it has been concluded that the choice of the material for synthesizing membranes for ethanol purification is affected.

In the **fourth chapter**, the synthesis of hybrid materials is elucidated via the polymerization under UV-visible irradiation of an acrylate monomer on the surface of silica nanoparticles, previously grafted with a newly silane-based photoinitiator (SPI-1). The successful grafting of the silane-based photoinitiator on silica nanoparticles has been proved by UV-Visible and IR spectroscopies. The grafting mechanism has been studied by IR spectroscopy and occurs via strong covalent interactions between the ethoxy groups of the silane photoinitiator and the silanol groups of the silica nanoparticles. The quantity of the grafted material and its thermal stability were determined by thermogravimetric analyses. The efficiency of the grafted SPI-1 was then tested in the free radical polymerization of an acrylate monomer under UV-Visible irradiation. Homogeneous polymerization has occurred on the surface of the silica nanoparticles, resulting in their full coverage. The mechanical properties of the synthesized hybrid materials were studied using Atomic force microscopy, and their morphology was examined using electron microscopy. The synthesized hybrid materials were subjected to nitrogen sorption, and the results have shown that an additional mesoporosity attributed to the presence of the polymer was formed. The

distinguished properties of the hybrid materials were attributed to the core-shell-like structure at the microscale level, allowing their application to purify ethanol from its aqueous mixture. It has been shown that the adsorption capacity of the material increased towards ethanol while it decreased for water. Part of this work has been published in Materials Today Communications ([10.1016/j.mtcomm.2021.102248](https://doi.org/10.1016/j.mtcomm.2021.102248)).

Since MFI zeolites present a high affinity toward both ethanol and water, it is important to modify their surface to adjust their selective adsorption capacities. Moreover, since the previously discussed synthesis technique revealed promising results in altering the surface of silica nanoparticles, we apply this approach to synthesize zeolite-polymer-based core-shell materials in the **fifth chapter**.

So, the efficiency of the silane-based photoinitiator (SPI-1) under UV-Visible conditions is tested after grafting on the surface of MFI zeolites to form MFI@Polymer hybrid materials. First, the modified materials (SPI-1-MFI and MFI@Polymer) have been characterized by PXRD, UV-Visible, and IR spectroscopy to detect the vibrational characteristic bands of the SPI-1 structure and the polymer, TGA to determine the hydrocarbon loading, and electron microscopy (SEM and TEM) to examine their morphologies. Then the thermal stability of the SPI-1-MFI samples was investigated by thermal programmed desorption conducted on IR spectroscopy. Moreover, the accessibility of the pores of the zeolitic particles is studied after Nitrogen adsorption and basic probe molecules via IR spectroscopy. It was observed that the MFI pores are still accessible at ~ 90 % after grafting and polymerization, with an additional mesoporosity due to the polymer. The results indicate that this novel technique can be applied to synthesize new hierarchical hybrid materials and can be a potential synthesis route for mixed matrix membranes since the inorganic fillers remain accessible. Accordingly, one can say that a major drawback of the synthesis of MMMs has been outpaced. Finally, the synthesized hierarchical hybrid materials are tested in the selective separation and purification of ethanol from its aqueous mixture to assess the alteration of their hydrophobic/hydrophilic character. The hybrid materials revealed high ethanol adsorption capacity with a lower water capacity than the parent zeolite. This work is currently submitted for publication.

In conclusion, the combination of the novelty of the synthesis route with the overall results gives rise to the development of hierarchical hybrid materials, which are

promising candidates for synthesizing membranes for many applications, particularly for separating ethanol and water. Additionally, the overall findings obtained using IR spectroscopy offer opportunities to extend this study to other mixtures.

## References

1. Karl, T.R. and K.E. Trenberth, *Modern global climate change*. science, 2003. **302**(5651): p. 1719-1723.
2. Abdeshahian, P., et al., *Production of biofuel using biomass as a sustainable biological resource*. Biotechnology, 2010. **9**(3): p. 274-282.
3. Kumar, S., N. Singh, and R. Prasad, *Anhydrous ethanol: A renewable source of energy*. Renewable and Sustainable Energy Reviews, 2010. **14**(7): p. 1830-1844.
4. Balat, M., *Global bio-fuel processing and production trends*. Energy Exploration & Exploitation, 2007. **25**(3): p. 195-218.
5. Soccol, C.R., et al., *Lignocellulosic bioethanol: current status and future perspectives*, in *Biofuels: Alternative Feedstocks and Conversion Processes for the Production of Liquid and Gaseous Biofuels*. 2019, Elsevier. p. 331-354.
6. Vane, L.M., *Separation technologies for the recovery and dehydration of alcohols from fermentation broths*. Biofuels, Bioproducts and Biorefining, 2008. **2**(6): p. 553-588.
7. Siepmann, J.I., P. Bai, and M. Tsapatsis, *Zeolites for separation of ethanol and water*. 2018, Univ. of Minnesota, Minneapolis, MN (United States).
8. Davey, C.J., D. Leak, and D.A. Patterson, *Hybrid and mixed matrix membranes for separations from fermentations*. Membranes, 2016. **6**(1): p. 17.
9. Zhan, X., et al., *Pervaporation separation of ethanol/water mixtures with chlorosilane modified silicalite-1/PDMS hybrid membranes*. Chinese Journal of Polymer Science, 2010. **28**(4): p. 625-635.
10. Mintova, S., J.-P. Gilson, and V. Valtchev, *Advances in nanosized zeolites*. Nanoscale, 2013. **5**(15): p. 6693-6703.
11. Bastani, D., N. Esmaeili, and M. Asadollahi, *Polymeric mixed matrix membranes containing zeolites as a filler for gas separation applications: A review*. Journal of Industrial and Engineering Chemistry, 2013. **19**(2): p. 375-393.
12. Ghosh Chaudhuri, R. and S. Paria, *Core/shell nanoparticles: classes, properties, synthesis mechanisms, characterization, and applications*. Chemical reviews, 2012. **112**(4): p. 2373-2433.
13. Dreisbach, F., H.W. Lösch, and K. Nakai, *Adsorption measurement of water/ethanol mixtures on activated carbon fiber*. Chemical engineering & technology, 2001. **24**(10): p. 1001-1005.
14. Naono, H., et al., *Separation of water and ethanol by the adsorption technique: selective desorption of water from micropores of active carbon*. Journal of Colloid and Interface science, 1996. **182**(1): p. 230-238.
15. Volkov, V.I., et al., *Self-diffusion of water-ethanol mixture in chitosan membranes obtained by pulsed-field gradient nuclear magnetic resonance technique*. Journal of Membrane Science, 1998. **138**(2): p. 221-225.
16. Volkov, V.I., et al., *Self-diffusion of water-ethanol mixtures in polyacrylic acid-polysulfone composite membranes obtained by pulsed-field gradient nuclear magnetic resonance spectroscopy*. Journal of membrane science, 1995. **100**(3): p. 273-286.
17. Furukawa, S.-i., et al., *Molecular simulation study on adsorption and diffusion behavior of ethanol/water molecules in NaA zeolite crystal*. Journal of chemical engineering of Japan, 2004. **37**(1): p. 67-74.
18. Shi, Q., et al., *Efficient ethanol/water separation via functionalized nanoporous graphene membranes: insights from molecular dynamics study*. Journal of Materials Science, 2017. **52**(1): p. 173-184.
19. Mulder, M. and C. Smolders, *On the mechanism of separation of ethanol/water mixtures by pervaporation I. Calculations of concentration profiles*. Journal of membrane science, 1984. **17**(3): p. 289-307.
20. El-Roz, M., et al., *Pore Occupancy Changes Water/Ethanol Separation in a Metal-Organic Framework: Quantitative Map of Coadsorption by IR*. The Journal of Physical Chemistry C, 2015. **119**(39): p. 22570-22576.





# CHAPTER ONE

---

## LITERATURE REVIEW

---



## 1. Ethanol: Importance and Applications

Non-renewable fossil fuels are considered essential elements in our daily lives, such as coal, oil, and gases. The combustion of these fuels produces tons of gases, including carbon dioxide. The long atmospheric lifetime of this gas made it one of the main reasons for global warming [1, 2]. Additionally, due to the increase in the consumption of these resources, it is predicted that the reserve of fossil fuels might be depleted in the coming 100 years [3]. Therefore, efforts have been placed to find sustainable alternatives for hydrocarbon-based fuels. This need arises from preserving the environment and the concern about the long-term supply of hydrocarbon-based fuels [2, 4].

Among various alternatives, biofuels, such as bio alcohols, biogases, and biodiesel, have been used as sustainable gasoline and diesel fuel alternatives. Their contribution to the world's energy demand is about 10 % [5]. Biofuels are obtained from the degradation of organic matter without oxygen. This degradation produces a mixture of methanol, carbon dioxide, and other components (water) [6]. However, the obtained CO<sub>2</sub> is recycled when biofuels are consumed, reducing its contribution to the main cause of climate change [2]. The use of biofuels as renewable energy in vehicle engines also reduces the emission of carbon monoxide and unburned hydrocarbons [7]. These characteristics made biofuels great candidates for improving air quality and renewable energy.

Biofuels are divided into three generations: the first one derives from comestible mass, whereas the second one is from non-comestible mass, and the third generation results from carbon dioxide sequestration [8]. The latter leads to biodiesel production, considered a better alternative for petroleum-based fuels. This is due to its non-toxicity and biodegradable nature [9, 10]. However, the second generation is considered as modified primary fuels. They favor the production of charcoal, bio-oil, biogases, and particularly bioethanol and biobutanol [2, 11]. These bio-alcohols are being used as a partial replacement for gasoline [7]. The waste substrates and the agricultural residues are implemented to produce biofuels capable of reducing greenhouse gases (GHG), carbon dioxide, and polycyclic aromatic hydrocarbons emissions [12]. Besides the

various benefits offered by biofuels, several disadvantages and challenges can be present. For instance, the storage of organic wastes is managed by numerous laws and policies that delay the production of biofuels. The present technologies also offer costly procedures from storage to pretreatments and productions [13]. Hence, more research is being conducted in this field for better improvements.

One of the most important biofuels is bioethanol since it is being used to replace gasoline [2, 7]. Due to its high-octane number, low cetane number, and high heat of vaporization, it has been recognized as a potential alternative to petroleum fuels [14]. It is also known that the flame temperature for ethanol is lower than that for gasoline. Consequently, ethanol combustion will yield lower amounts of emitted  $\text{NO}_x$  compared to gasoline. Since the oxygen content in ethanol is very low compared to gasoline (35 wt% for ethanol), its combustion requires less air reduction; thus, carbon monoxide is considered a hazardous gas to children and seniors [7].

Bioethanol can be produced from different sources ranging from renewable food sources such as corn starch and sugarcanes to non-food renewable sources, including the organic fraction of municipal solid waste and lignocellulosic biomasses [15]. Several techniques are applied to synthesize bioethanol; yet, the main challenges remain in separating ethanol from its dilute aqueous mixture [16]. According to the literature, an azeotrope mixture of 89.4 mol % of ethanol and 10.6 mol % of water can be obtained [17]. The resulting vapor has the same composition as the initial mixture when partially boiling it. Hence, the best-obtained solution contains 89.4 mol % of ethanol [7, 18]. Therefore, it remains crucial and challenging to increase the purity of ethanol via an eco-friendly process which will be discussed in the upcoming section.

## 2. Ethanol purification

Several techniques were used to improve or increase the degree of purity of ethanol in the final vapor, such as chemical dehydration [19], different distillation processes [20, 21], pervaporation [22-24], adsorption processes [25, 26], and many others [27, 28].

## 2.1. Chemical dehydration

The traditional process to separate ethanol from its aqueous mixture is the chemical dehydration. This process is based on the chemical reaction of water with the main substance used: quicklime, calcium chloride, or potassium carbonate. Usually, the formed precipitates are insoluble in ethanol. Therefore, the precipitates settle to the bottom, and ethanol is on the top of the container. However, this aging process is used only on a laboratory scale, and in some cases, further expensive treatments are required to remove the precipitates [7, 29]. Thus, this technique has been replaced by the traditional distillation process.

## 2.2. Distillation processes

The distillation of ethanol-water mixture can be carried out using different processes such as vacuum distillation, extractive distillations with salts and solvents, continuous flash distillation, batch distillation, and fractional distillation, and steam distillation [7, 20, 30, 31]. However, these classic procedures required a large amount of energy because of the low concentrations of alcohol in the aqueous solutions [32]. The energy cost needed to conduct the distillation is much higher than the product itself [16]. For this aim, researchers shifted to a more economical alcohol recovery process, using less energy and giving higher yields of alcohol that can reach up to 98 % [7, 33].

## 2.3. Pervaporation

Pervaporation is a membrane process based on the difference in chemical potentials between both sides of the used membrane. It can be established through temperature [34], gas [35], or pressure [36] differences between both sides. The energy consumed in the separation process using thermopervaporation is reduced due to the decrease of the dimensions in the separation units. This decrease in the dimensions is accompanied by an increase in the condensation temperature of the permeate [34]. As for vacuum pervaporation, the vacuum's driving force is created on the membrane's permeate side [36]. Pervaporation membranes are divided into two main processes: hydrophilic and organophilic pervaporation. The first one is used to dehydrate concentrated organic compounds by permeating water across the

membrane. The latter is concerned with permeating dilute organic compounds in aqueous solutions across an organophilic membrane (**Figure 1**) [37]. Different membranes can be used in this separation process, such as poly (dimethylsiloxane), known as PDMS, ethylene propylene diene rubber (EPDR), styrene-butadiene rubber (SBR), and poly (methoxy siloxane) (PMS) [22, 23]. Additionally, these membranes can be modified by incorporating porous materials such as zeolites (ZSM-5, silicalite, etc.) to enhance their separative activities [38-42].

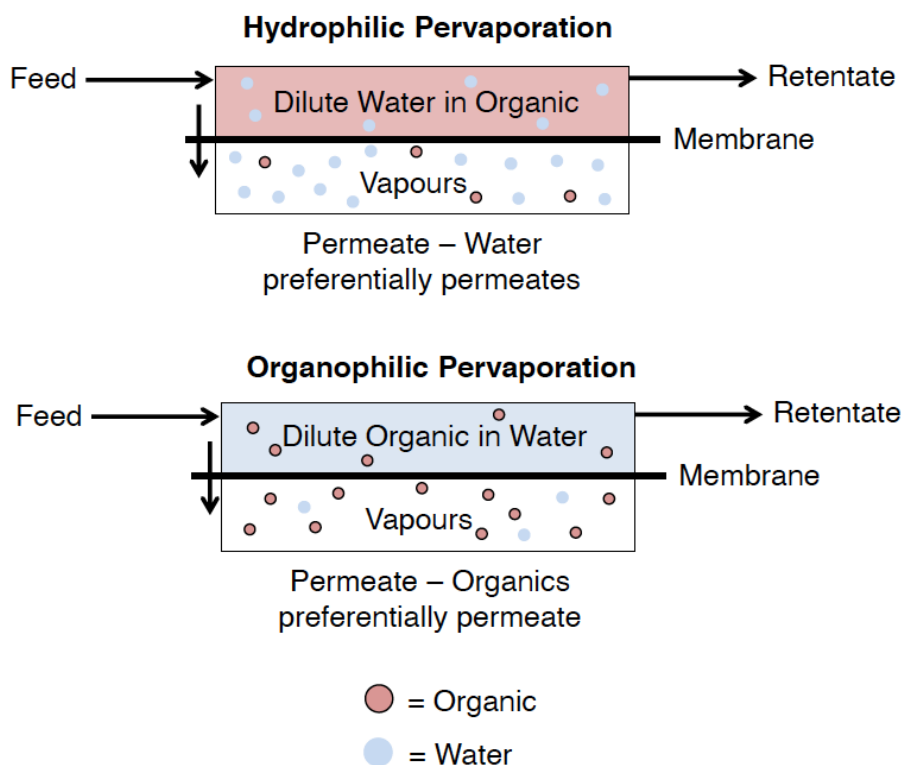


**Figure 1:** Schematic representations of organophilic and hydrophilic pervaporation processes. Reprinted with permission from ref [37]. Copyright 2016, Membranes.

#### 2.4. Selective adsorption-based procedures

Among the various separation processes, adsorptive separation emerges as one of the most efficient procedures for separation. This technique is generally based on a selective molecular sieve of one component and molecular adsorption in a mixture. The selectivity results from the difference in molecular size between the components of the mixture, for example, water and ethanol [7]. These molecular sieves are synthetic porous materials such as zeolites, activated carbon, carbon nanotubes, metal-organic frameworks, or plant-derived adsorbents, including cornmeal, straw, and sawdust [16, 29, 43-45]. Two mechanisms were exploited to

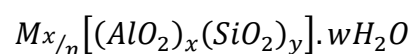
understand the adsorption process on porous materials. The first mechanism is rendered by the difference in the diffusion coefficients of each component through the pores constitutes, whereas the second mechanism is based on the preferential equilibrated uptake of one component over the other [32]. Nowadays, all studies are conducted to enhance the present adsorption techniques since they offer better efficiency and are less energy-consuming than other dehydration processes. Mainly, zeolites and modified zeolites are extensively used in adsorption/separation for different reasons that will be elucidated in the next section.

### 3. Porous and hybrid materials for ethanol purification

#### 3.1. Porous materials: Zeolites

##### 3.1.1. Generality

First described by the Swedish mineralogist Axel Fredrick Cronstedt in 1756, zeolites are crystalline porous solid materials with well-defined structures. The word 'zeolite' originates from the Greek words 'zein' and 'lithos,' meaning 'to boil' and 'stone'[46]. The three-dimensional structure of the zeolite is formed of primary and secondary building units. The primary building unit (PBU) is formed of the tetrahedral coordination of the  $[SiO_4]^{4-}$  and  $[AlO_4]^{5-}$  through the shared oxygen atoms [47]. The secondary building unit (SBU) is described as a lattice with identical building blocks of repeating units. In another way, SBUs are defined as the primary unit used to describe the zeolite structure [48-50] (**Figure 2**). The following formula usually expresses zeolites:



where  $M$  is the alkali metal or alkaline earth-metal cation of a valence  $n$ ,  $w$  is the amount of water per unit cell of the zeolite, while  $y$  and  $x$  represent the total number of  $[SiO_4]^{4-}$  and  $[AlO_4]^{5-}$  tetrahedral ion in the unit cell of the zeolite.

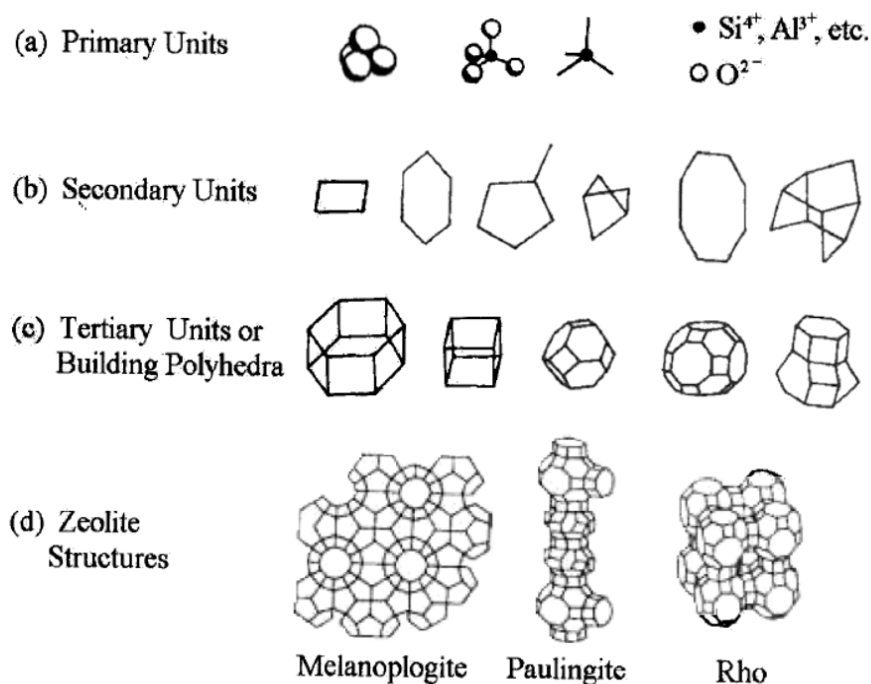


**Figure 2:** (a) Development of zeolite from the primary building unit, (b) to the secondary building unit, then to (c) the building polyhedra, and (d) the final structure. Reprinted with the permission of ref [48]. Copyright 2017, American Journal of Materials Science.

The ratio Si/Al ( $y/x$ ) can range from 1 in zeolite type A to infinity in Silicalite, known as an aluminum-free crystalline silica modified zeolite [51, 52]. The synthesis mixture allows determining the Si/Al ratio, and the more it is low (high aluminum content), the more hydrophilic the zeolite is. The presence of the  $[\text{AlO}_4]^{5-}$  tetrahedra in the zeolite structure give it a negative charge which is compensated by a positive counter ion present in the pores. These ions are exchangeable, thus providing an ion-exchange capacity to the zeolite [53].

### 3.1.2. Porosity of the zeolites

The porous structure of the zeolite is formed of cavities or channels present in the lattice. These cavities are interconnected with one another to form the pores of the zeolite. The pores have a diameter ranging between 3 to 10 Å, characteristic of each zeolite. Therefore, the pore diameter plays a significant role in allowing or prohibiting the entrance of the molecules into the system [51]. The channels can also be circular or elliptical, straight or zigzag, and tubular or containing periodic cavities.

The type of the pore opening is considered one of the main factors in determining the catalytic and the adsorptive processes of the zeolite [54]. We distinguish three different types: the 8-member ring pore, often denoted as the small

pore size zeolite with a diameter from 3 to 4.5 Å; the 10-member ring known as a medium pore size zeolite with a diameter ranging between 4.5 Å and 6 Å and the 12-member ring. The latter is known as the large pore-sized zeolite having a diameter between 6 Å and 8 Å [51]. Zeolites of 7, 9, and 11 member rings can be present in addition to some with openings limited by 14 member rings, 18 member rings, or more [55]. Due to their significant characteristics and properties, today, around 248 zeolite frameworks are present, according to the International Zeolite Association (IZA), both natural and synthetic. Each framework is represented by three capital letters derived from the source material: MFI, BEA, FER, etc. [56].

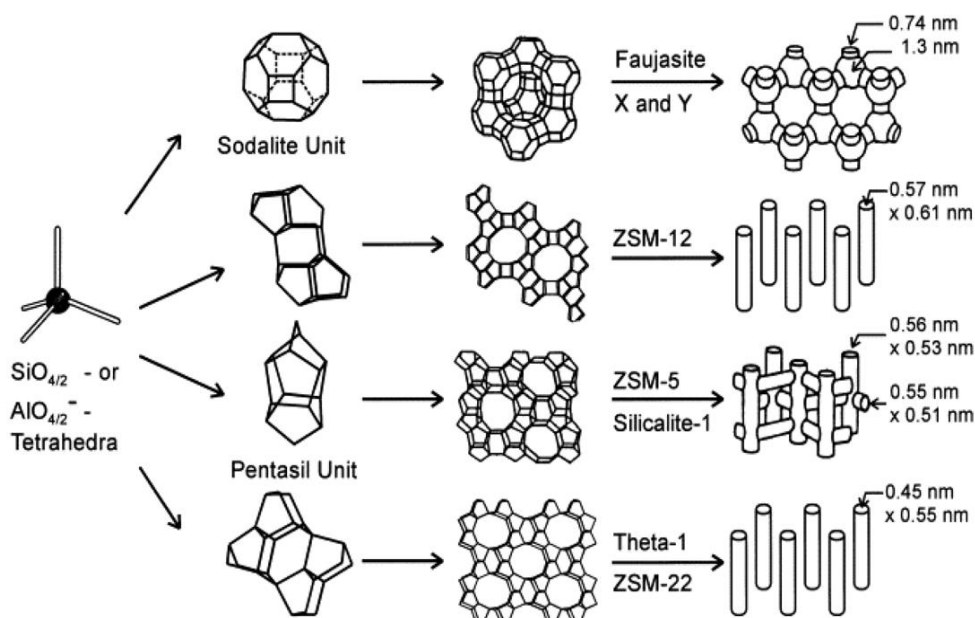


**Figure 3:** Structures of different zeolites with their micropore system and dimensions. Reprinted with the permission of ref [49]. Copyright 2000, Solid-state Ionics.

### 3.1.3. Acid sites

Besides their tunable porosity, zeolites are characterized by their acid sites allowing their use in catalytic reactions. The activity of the acid sites is measured by their accessibility, strength, and concentration. When Al replaces Si in the zeolite structure, a balancing cation is required to compensate for the negative charge. This compensating cation is usually replaced with protons to create a solid acid zeolite. Therefore, a bridged hydroxyl group is formed and can act as a proton donor (**Figure 4**). This site is a Bronsted acid site and is responsible for the catalytic activity in zeolites. Other Bronsted acid sites can be formed but have weaker activity than the BAS, such as Al-OH and Si-OH groups. The formation of a zeolite in the H-form is

generally conducted by ammonium exchange followed by a calcination step at high temperatures [57-60].

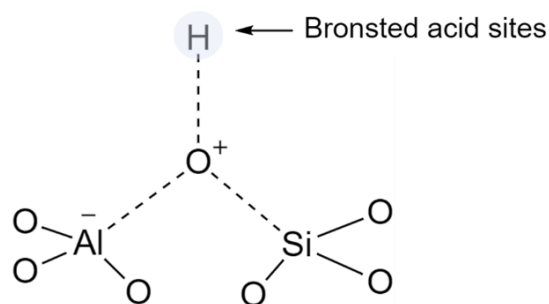


**Figure 4:** Schematic representation of the Bronsted acid site (BAS)

Besides Bronsted acid sites, zeolites are characterized by their Lewis sites (**Figure 5**) found in tri-coordinated Al sites, the extra-framework Al, and the charge compensating cations. These sites are obtained when the zeolitic acidic sites are dehydroxylated, and water is released. Aluminum is removed during the steaming process, although it might remain in the zeolite micropores or move to the external surface as extra framework cations. As a result of the dehydroxylation, the crystallinity of the zeolite is affected, and more defects are generated, thus additional Lewis sites.

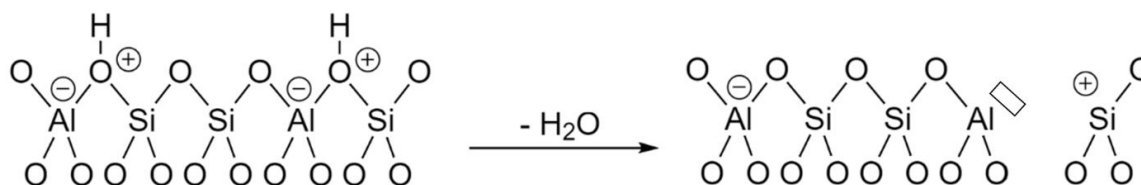


**Figure 5:** Schematic representation of the Lewis acid sites (dehydroxylation)

#### 3.1.4. Synthesis and post-treatment of zeolites

Natural zeolites are the products of indirect volcanic activities, whereas synthetic zeolites are obtained from natural raw materials (kaolin) or synthetic materials such as aluminates and silica [52]. The synthesis of zeolites in the laboratory is based on transforming the initial amorphous materials into a crystalline product [61]. These transformations principally occur in aqueous media under hydrothermal conditions in the presence of organic structure-directing agents and/or inorganic cations [62]. Although several studies were carried out to understand the connections between the starting materials and the final structure, the precise mechanism of the zeolite synthesis is still undetermined nowadays. Various parameters govern the

synthesis of zeolites: the composition of the hydrogel, the pH of the solution (between 9 and 18), the temperature, the crystallization time, and the organic structure-directing agents [63]. Each zeolite is characterized by a specific gel composition allowing, therefore, to determine the morphology of the crystals and the Si/Al ratio. The pH of the solution affects the Si/Al ratio. For instance, the increase of the alkalinity of the solution increases the pH and triggers the decrease in the Si/Al ratio. However, basic solutions are an essential keyword in the synthesis procedure. The presence of OH<sup>-</sup> ions is essential for the nucleation and the growth of the crystals and the major role they play in the depolymerization of the amorphous gel at the adequate velocity [64]. Additionally, high pH induces an increase in the nucleation and the growth of the crystals, a similar effect produced by high temperatures. Thus, increasing the temperature will increase the rate of nucleation and growth and simultaneously decrease crystallization time [64]. On the other hand, organic structure-directing agents were introduced later in synthesizing zeolites to obtain new structures [65, 66]. These structure-directing agents are based on quaternary ammonium cations and generate appropriate species for the crystals' nucleation and growth. Their role is basically to ensure a kinetically and thermodynamically stable synthesis and endorse the stability of the obtained zeolite [67].

After the synthesis, zeolites undergo post-synthetic treatments to adjust their characteristics. We have the calcination process, ion exchange, and dealumination among these treatments. The calcination process occurs at high temperatures (around 450 °C) to remove the remaining organic templates from the structure, thus making the zeolite's pore accessible for the adsorption of molecules. On the other hand, the ability to endure ion-exchange made zeolites great candidates for catalytic and adsorption reactions [68]. For example, the alkali cations obtained from the initial synthesis reactants can be exchanged by ammonium cations to remove NH<sub>3</sub> and NH<sub>4</sub><sup>+</sup> from residual water. Note that the ammonium cation (NH<sub>4</sub><sup>+</sup>) can be removed by thermal treatment to obtain the protonic form of the zeolite essential for some catalytic reactions. In rare cases, ion exchange can generate structure modification. For example, upon ion exchange with K<sup>+</sup>, Cs<sup>+</sup> flexible zeolites can exhibit volume expansion of around 18 %, thus allowing the adsorption of bigger molecules [69]. The dealumination process is mainly conducted to adjust the properties of the zeolite (acidity, strength, and density of the acid sites) and the creation of mesopores through

the structure crucial for some reactions [55]. Several efforts have been conducted in the past decade to obtain an environmentally friendly synthesis of zeolite, where zeolite seeds have replaced organic structure agents. These seeds are used to induce nucleation and crystallization of the amorphous gel in the absence of an organic template. Therefore, calcination at high temperatures is not required any more [70-72].

### 3.1.5. Applications of zeolites

Whether extracted naturally or synthesized in the laboratory in the presence or absence of organic templates, zeolites are known for their high chemical and thermal stabilities [73], tunable pore and cavity sizes, and vast and various framework topology [56]. The combination of these physical-chemical properties has allowed the application of zeolites in diverse areas such as separation [73], adsorption [74], catalysis [75], and recently in medicine and biotechnologies [76].

#### 3.1.5.1. Zeolites in catalysis

Among the various porous materials used for catalysis, zeolites have shown high importance in this field, especially in petroleum refining. This is due to the presence of different catalytic sites in their structure, which are essential for most catalytic reactions, and the ability to tailor the access to these sites [50]. Soon after their first synthesis, these materials, specially ZSM-5, zeolite Y, beta, and mordenite, have been extensively used in heterogeneous catalysis even under harsh conditions (temperature above 300 °C) [77]. As an example, the alkylation of benzene and ethylene was conducted primarily in the presence of a Lewis homogeneous catalysis such as  $\text{AlCl}_3$  supported on phosphoric acid or fluoric acid. When MCM-22 zeolites replaced these catalysts, the alkylation became more selective and the ratio of benzene-to-ethylene decreased from 5 to 3, thus reducing benzene recycling [78]. Additionally,  $\text{CO}_2$  cycloaddition into epoxides is a well-known reaction in pharmaceuticals and polymers industries. This reaction was carried out in the presence of different porous materials, including MFI zeolites and ZIF-8. Its yield is greater when MFI zeolites are present, with 86% compared to 44 % in the presence of ZIF-8 [79, 80]. The significant industrial interest remains in producing olefins from

methanol and the dramatic increase in the global demand for ethylene and propylene. Zeolites emerged as great candidates for methanol to olefin transformation to enhance this production. ZSM-5 has been significantly used; however, it has been found that it is not suitable for light olefins such as propylene and ethylene. Thus, it was replaced by another zeolite, the SAPO-34, a more suitable catalyst for making light olefins [81-84].

### 3.1.5.2. Zeolites in separation and adsorption

Besides their eminent catalytic activity, zeolites have been applied to the adsorption and separation of gases and liquids. Experimental and theoretical studies were conducted to understand the interactions between the zeolites and the adsorbent molecules. They have been extensively used in carbon dioxide [85-87], methane [88-91], and water [92-95] adsorptions. For example, Ohlin *et al.* conducted an ATR-FTIR study to study the adsorption isotherm of CO<sub>2</sub>, CH<sub>4</sub>, and H<sub>2</sub>O on ZSM-5 zeolites [88]. On the other hand, Mofarahi *et al.* analyzed CO<sub>2</sub>/CH<sub>4</sub> separation using zeolite 5A, where they found that this zeolite is highly selective for CO<sub>2</sub> [96]. The same group also studied pure and binary adsorption of oxygen/nitrogen, ethane/ethylene, and methane/nitrogen systems on zeolite 5A [96, 97]. LTA zeolites exhibited preferential adsorption of water owing to their small pore opening and the polar nature of the cage [16, 98, 99].

Furthermore, zeolites have proven to be efficient in adsorbing or separating alcohols from their aqueous mixtures [100-111]. For this, computational and experimental studies have been devoted to understanding the adsorption and the separation mechanisms of water/alcohol mixtures. It is reported that zeolites with high silica content, such as silicalite-1, are more hydrophobic than that with higher alumina content [16, 107]. Therefore, silica zeolites are well known for their selective adsorption of alcohol over water. According to Olson *et al.*, the correlation between hydrophobicity and the alumina is due to the increase in the number of hydrophobic bonds ( $\equiv\text{Si-O-Si}\equiv$ ) and a decrease in the number of the partially ionic, hydrophilic centers associated with the tetrahedrally coordinated aluminum [112]. In a recent study, Gómez-Álvarez *et al.* have attributed the selectivity of ethanol over water to the zigzag structure of the MFI zeolite compared to MEL zeolites, having a linear structure

[32]. The organophilic nature of the MFI zeolite was also confirmed by Zhang *et al.* In their comparative study on ethanol and water adsorptions between different MFI zeolites with different Si/Al ratios; they found that no matter what the Si/Al ratio is, MFI zeolites showed similar behavior upon ethanol adsorption. Nevertheless, this was not the case for water adsorption, where the hydrophobic silicalite-1 (F<sup>-</sup>), where OH<sup>-</sup> ions are substituted by the fluorine group, had the lowest water uptake compared to silicalite -1 (OH<sup>-</sup>), less hydrophobic, and ZSM-5, more hydrophilic. The water uptake at 35 °C on silicalite-1 (F<sup>-</sup>) is found to be 12.6 % , 10 % and 3 % of the capacity for silicalite -1 (OH<sup>-</sup>), ZSM- 5 (Si/Al = 140) and ZSM- 5 (Si/Al = 15) , respectively [103]. According to Gómez-Álvarez *et al.*, although silica zeolites are hydrophobic, the adsorption of alcohol is accompanied simultaneously by the coadsorption of water. This adsorption is generated by hydrogen bond formation [16, 32]. Nevertheless, the data reported in the literature concerning alcohol adsorption is not quietly consistent for the same zeolite. This is due to hydrophilic defects formed during the synthesis, including aluminum and silanol sites in the samples. In these cases, water co-adsorption is facilitated by enhancing hydrogen bonding via these defects [32]. Therefore, more experiments were conducted to avoid this co-adsorption by implementing zeolites in the vicinity of some polymers and thus forming membranes or by covering them with a shell disfavoring water co-adsorption. The coming section will discuss core-shell zeolites and membranes for alcohol/water separation, especially ethanol/water separation.

### 3.2. Hybrid Materials

Recent attention has been focused on synthesizing hybrid porous materials and their application in different fields instead of pure porous materials. Mixed matrix membranes or core-shell materials have been distinctively studied due to their prominent properties formed by the properties of both constituents separately and the properties obtained from new interactions. The upcoming section will conduct a dissertation about zeolitic hybrid materials, their importance, and their application in alcohol/water separation.

### 3.2.1. Core-shell materials

#### 3.2.1.1. Generality

Despite their significant properties and wide applications, the use of zeolites in the industry is limited to certain drawbacks, mainly in catalysis. Their small channels can alter their performance, and they are prone to promote side effect reactions and deactivation due to the formation of coke and the blockage of their pores. Hence, the improvement and the alteration of their properties have been required. This has been carried out in several ways, ranging from modifications during the synthesis procedures to introducing a new type of material known as hybrid materials or core-shells. Core-shells have been studied since the 1980s, although the idea of encapsulated materials was present back in the 1920s [113]. They are defined as an inner compartment, the core, fully coated by an external layer, the shell (**Figure 6**). The core-shell combination has emerged to improve the properties of each original building part taken individually or their physical mixture and is considered seeding for the synthesis of mixed matrix membranes [114].

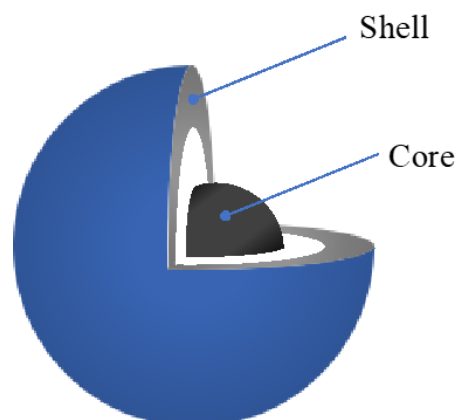


**Figure 6:** Schematic representation of the core-shell material

Different types and classes of core-shell materials can be synthesized depending on the shape and nature of the constituents. They can be spherical when the core is spherical and coated uniformly; multiple core-shell nanoparticles, when one outer layer is coating different small core particles together; and the moveable core-shell formed of a particle encapsulated within a uniformed hollow shell particle as represented in **Figure 7** [114].

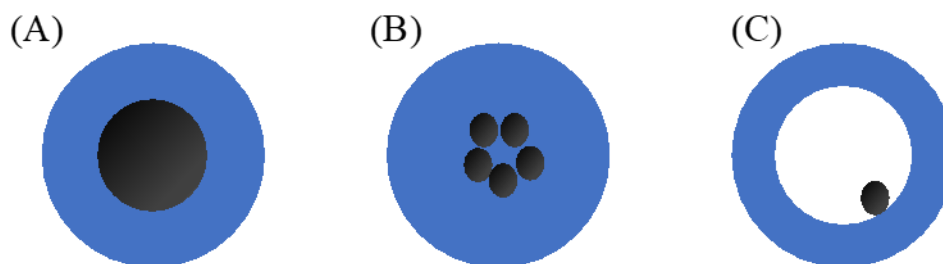


**Figure 7:** Schematic representation of different core-shell particles: (A) Spherical core-shell, (B) multiple cores coated by single shell material, and (C) moveable core within a hollow shell

Moreover, these materials were classed upon the nature of their components, such as inorganic/inorganic, organic/inorganic, and organic/inorganic core-shell particles. These classifications allowed the application of the obtained material according to the properties of their components. For example, inorganic/inorganic core-shell materials are used for their importance in improving the semiconductor behaviors, quantum dots, and biological labeling [115]. The organic layer coating the inorganic core in organic/inorganic core-shells is important to increase the optical stability of the core, enhance the biocompatibility for bio-applications and induce its stabilization in the suspension media [116]. At the same time, the role of the inorganic outer layer in organic/inorganic core-shells is crucial in increasing the strength of the overall material, resistance to oxidation, thermal and colloidal stabilities, and abrasion resistance [114]. Among all types of the building materials of core-shells, zeolitic core-shell materials constitute an important subfamily in the family of core-shell materials where at least one part is a zeolite. Particularly, the synthesis of zeolite core-shell materials has been studied throughout the years to improve the external shell coverage and avoid any damage to the functionalities of the core [113, 114, 117]. Bouizi *et al.* conducted a study on the factors affecting the formation of these composites where both the shell and the core are zeolites [118]. They found that the best combination is between zeolites with compatible frameworks and close crystallization conditions.

### 3.2.1.2. Synthesis of core-shell materials

Analogously to the synthesis of MMMs, the synthesis of core-shell has been prone to numerous limitations. During the synthesis steps, different factors have been considered, including the synthesis media, temperature, concentration of the reactants, and the concentration of the surface modifier of the core in some cases.

The synthesis procedures are divided into three categories: the top-down, the bottom-up, and the coupling of both approaches [114]. The first approach regroups the traditional methods such as UV, electron, or ion beam, machining, grinding, and polishing to cut, mill, and shape materials with a desired shape and order. On the other hand, the bottom-up approach exploits the chemical properties of the molecules to cause them to self-assemble into desired materials. The bottom-up approach uses chemical synthesis, chemical vapor deposition, and film deposition and growth. In the third approach, the top-down is reserved for synthesizing the core particles, and the bottom-up is used to synthesize the shell layer. In addition to these two approaches, two different pathways are used to generate these materials based on the availability of the core material. The core is synthesized separately and then incorporated into the system with proper surface modification, reducing thus the impurities on the surface of the core. The core can be synthesized *in situ* and then coated with the shell material.

### 3.2.1.3. Applications of core-shell materials

Due to their variety, core-shell materials have arisen to be good candidates for catalysis, adsorption, electronics, and biomedical applications [119-122]. They have been applied in adsorption and separation. For example, MIL-101@UiO-66 has significantly enhanced H<sub>2</sub> uptake compared to MIL-101 and UiO-66 separately [123]. The hydrophobic pore of the ZIF-8 shell was also used to control the entrance of the guest molecules into the hydrophilic mesoporous silica structure in a ZIF-8@silica core-shell [124].

Although numerous factors in the synthesis procedures have strongly affected the performance of zeolitic core-shell materials, they have been applied in different fields [125]. For instance, the presence of a shell was crucial for catalytic reactions. Indeed, the shell ensures the accessibility of reactant molecules to the active core and increases its durability. Additionally, it can introduce size selectivity toward different molecules, tunes the diffusion rate of the molecules, manipulates the orientation and configuration of the surface molecules, or enriches the reactants on the catalyst surfaces. The shell is also responsible for isolating the catalytically active core during reactions at high temperatures [122]. Zeolitic core-shell particles have been highly recommended in catalytic reactions. This is because they enhance the catalytic

activities and offer size and shape selectivity, a protective shell layer, and easy recovery from the solution [113]. In their study, Khaledi *et al.* investigated the synthesis of ZSM-5@MnO catalyst to convert methanol to light olefins. They found that the Mn-based shell increased the selectivity of nanoparticles towards olefin products and to methane and ethylene compared to the bare ZSM-5, MnO separately, or to their physical mixture [126]. According to Li *et al.*, SAPO-34@ZSM-5 core-shell particles have been attributed to a relatively high ethanol conversion at 400 °C. Moreover, compared to the parent SAPO-34, it exhibited better propylene selectivity. The selectivity has increased from 74% over ZSM-5 to 80% and 90% over SAPO-34@ZSM-5 and SAPO-34@silicate-1, respectively [127].

Additionally, non-zeolitic core-shells have been applied in catalysis. For example, Joo *et al.* studied the effect of temperature on Pt@mesoporous Silica core-shell, where they found that Pt@mSiO<sub>2</sub> is stable at 350 °C where the polyhedral Pt particles become less edged, whereas, at 550 °C, the core-shell structure is still maintained. However, at 750 °C, Pt-free hollow silica particles and some core-shell particles with larger Pt cores are observed. Some Pt diffused from the core of Pt@mSiO<sub>2</sub> particles to other Pt@mSiO<sub>2</sub> at this temperature [128]. These particles have been extensively used in the oxidation of CO and ethylene hydrogenation reactions [128].

Few reports have shown core-shell particles in mixture separation, such as water/ethanol mixtures. Kudasheva *et al.* synthesized polyimide-based mixed matrix membranes containing ZIF-8/silica core-shell spheres and used them to separate water/ethanol mixtures [129]. On the other hand, several studies were conducted on ethanol sensing using core-shell nanofibers. ZnO/SnO<sub>2</sub> core-shell nanofibers enhanced the ethanol sensing performance and shortened its response/recovery time [122, 130, 131]. Very recently, Miyamoto *et al.* studied the effect of coating a CHA zeolite with a purely siliceous CHA layer on the preferential adsorption of ethanol and butanol from an acetone-butanol-ethanol mixture. A negative effect of the hydrophobic layer was observed on the adsorption capacity of ethanol. Additionally, the diffusion of butanol was slower in the siliceous layer due to reducing the number of the surface adsorption sites [132].

### 3.2.2. Mixed matrix membranes

#### 3.2.2.1. Generality

Mixed matrix membranes are based on a solid-solid system of inorganic materials or particles inserted in a polymer matrix (**Figure 8**) [133]. These materials combine the properties of both separate compounds and the organic-inorganic interactions between the two components [134]. The idea of synthesizing these materials was initiated to overcome the expensive and challenging syntheses of zeolite molecular sieves characterized by their high diffusivity and selectivity compared to polymeric materials such as silica/polymers or metal oxide nanoparticles incorporated in the vicinity of the polymers [135, 136].

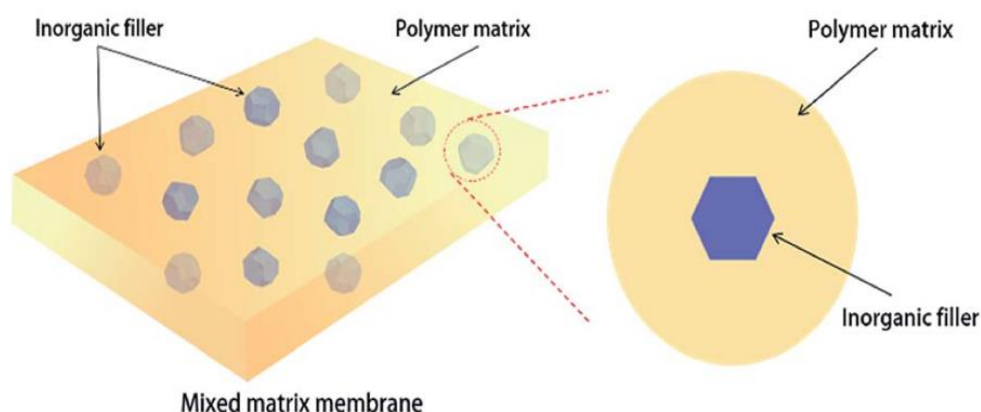


**Figure 8:** Schematic diagram of an ideal mixed matrix membrane. Reprinted with the permission of ref [133]. Copyright 2018, Journal of Materials Chemistry A.

The first zeolite mixed matrix membrane was reported in the 1970s when zeolite 5A was added into polydimethylsiloxane polymer. The obtained membrane was tested in the study on the time lag for CO<sub>2</sub> and CH<sub>4</sub> adsorptions [137]. Since then, zeolite mixed matrix membranes have been widely used in gas separation, such as CO<sub>2</sub>/CH<sub>4</sub> [138, 139], CO<sub>2</sub>/N<sub>2</sub>[139, 140], O<sub>2</sub>/N<sub>2</sub> [141], CO<sub>2</sub>/H<sub>2</sub> [142], and separation of mixtures such as water/ethanol [38, 143-145]. This is due to the molecular sieves' important high gas separation properties and the polymers' desirable mechanical and economic properties.

### 3.2.2.2. Synthesis of MMMs

Although they show important properties and a wide range of applications, the synthesis of mixed matrix membranes is still facing some challenges where the poor interactions between the molecular sieve and the polymer are causing defects in the final membrane [134]. Therefore, different studies were carried out to improve these interactions and thus avoid non-selective voids. The polymer is treated during the synthesis procedures either by annealing above its glass transition temperature or mixing it with a plasticizer. The purpose of these treatments is to maintain chain flexibility [146].

On the other hand, to induce the adhesion between the zeolite and the glass polymer, the external surface of the zeolite is modified by a silane coupling agent or surface-initiated polymerization with preformed particles [147]. Additionally, before starting the synthesis procedure, different factors should be considered. The main factors are the type of the polymeric membrane, the properties of the different zeolites used (pore size, pore volume, hydrophobicity...), and the zeolite-solvent-polymer interactions in the synthesis of MMMs. According to the literature, usually, glassy polymers are the most used in the industrial field rather than rubbery polymers [144]. This is due to their high rigidity, glass-like behavior, and low permeability but high selectivity. Moreover, the gas transport in the polymeric membranes can be affected by several polymer properties, including polarity, free volume content, defect, degree of crystallization, etc. For example, crystalline domains in the polymer make the gas transport more complicated. It is also preferred that zeolites with three-dimensional networks are used since they offer less restricted diffusion paths. As for the zeolite-solvent-polymer interactions, it is worthy to note that an ideal system would be where the polymer and the zeolite have high affinities for each other rather than having a high affinity to the solvent. The loaded zeolite can play a crucial role in enhancing or reducing the permeability of the gas through the polymer [148-152]. The enhancement can be accomplished by increasing the zeolite particle size, as indicated by Tantekin-Ersolmaz et al. Therefore, the area and number of zeolite-polymer interfaces increases, thus increasing the permeability [149]. Studies have also shown that an increase in the pore size leads to a better gas separation performance. Using large pore-size zeolites, the effect of pore blockage of zeolites by polymer chains attached

to their surfaces would be annulled [151]. Another main challenge in the synthesis of zeolite/polymer MMMs remains the determination of the same zeolite loading. So, it is crucial to determine that percentage since, at high zeolite loading, the zeolite crystals tend to agglomerate on the surface or precipitate during the preparation process. The first phenomenon can occur when the membranes are formed at high temperatures creating zones rich in zeolites and other defected [146]. This agglomeration is due to the differences in densities and physical properties between the zeolites and the polymer [153-155]. Therefore, pinholes are formed, creating nonselective defects in the matrix. These non-selective defects are the main reason why permeability increases at the expense of selectivity [155]. In their work, Zhao *et al.* showed that the high percentage of zeolite loading disobeys the upper bound relationship that states higher permeability leads to lower selectivity. However, the inverse was obtained when the loading of SAPO-34 zeolite increased above 23 wt% in the Pebax polymer. Accordingly, gas permeates through the nonselective voids with much smaller resistance than the zeolite pore in the zeolite layer. Furthermore, these nonselective voids are due to the agglomeration of the zeolites during the preparation process [155]. This was also proved by the work of Goldman *et al.*, where they defined three different transport mechanisms operating in the zeolite A/polymer membrane used to separate water/ethanol mixtures [144].

### 3.2.2.3. Applications of MMMs

Once overcoming these challenges, zeolite mixed matrix membranes are investigated in gas separations. The table below (**Table 1**) summarizes some of the results obtained for gas separation using mixed matrix membranes formed of zeolites and different polymers. For instance, Gong *et al.* showed in their work that CO<sub>2</sub> uptake was higher when LTA zeolites were loaded in the Matrimid matrix. The enhancement of CO<sub>2</sub> permeability was calculated and found to be around 120%. This huge improvement is accompanied by a small increase in CO<sub>2</sub>/CH<sub>4</sub> selectivity (ca 10%) compared to the pure polymer [138].

In contrast, Huang *et al.* synthesized a mixed matrix membrane of polyethersulfone and zeolite 4A, which was used to study the permeability and selectivity of different gas pairs, including CO<sub>2</sub>/H<sub>2</sub>, He/N<sub>2</sub>, H<sub>2</sub>/N<sub>2</sub>, He/CO<sub>2</sub>. Interestingly, the selectivity of this membrane towards these gases was increased compared to that

with pure PES dense films. However, the permeabilities for all gases decreased [142]. This decrease was explained by the small pore size of the zeolite 4A, hindering the diffusion of gaseous molecules. Another interesting study was carried out by Marand *et al.* where they were able to increase gas selectivity using MMMs and separation using size discrimination. This was done using zeolite L loaded in the polyimide matrix [156].

**Table 1:** Summary of some gas separations using different MMMs with various zeolites and polymer matrices.

References	Zeolite	Polymer	Gas mixture
Gong <i>et al.</i> [138]	LTA	Matrimid	CO <sub>2</sub> /CH <sub>4</sub>
Kulprathipanja <i>et al.</i> [157]	Silicalite	Cellulose acetate	O <sub>2</sub> /N <sub>2</sub>
Mahajan <i>et al.</i> [158]	Zeolite 4A	Poly(vinyl)acetate	O <sub>2</sub> /N <sub>2</sub>
Huang <i>et al.</i> [142]	Zeolite 4A	Polyethersulfone	CO <sub>2</sub> /H <sub>2</sub>
			He/N <sub>2</sub>
			H <sub>2</sub> /N <sub>2</sub>
Zhao <i>et al.</i> [155]	SAPO-34	Pebax	CO <sub>2</sub> /CH <sub>4</sub>
			CO <sub>2</sub> /N <sub>2</sub>

In addition to their high applicability in gas separation, mixed matrix membranes loaded with zeolites have been particularly used in water/alcohol separation. In 1995, Vankelecom *et al.* studied the influence of zeolites in PDMS membranes on the pervaporation of water/alcohol mixtures. It is well known that long and branched alcohols exhibit limited diffusion through the membrane. Thus, the same trend for ramified alcohols is observed by incorporating different zeolites (Silicalite-1 and ZSM-5) in the PDMS matrix: the alcohol with the longest chain sorbs the best (t-But, Butanol, propanol, ethanol). However, when Zeolite Y is loaded, more water is sorbed. This trend is explained by the hydrophilic nature of the latter zeolite. Additionally, incorporating any type of zeolite led to a reduced swelling membrane. Nevertheless, the more hydrophobic the zeolite is, the more the sorption capacity of alcohol is and with lower water sorption [143].

Based on these results, several studies were carried out to investigate more the behavior and the activity of zeolite/polymer MMMs in the pervaporation of water/alcohol mixtures. Particularly, MMMs membranes have been used for purifying ethanol using the pervaporation process for the last decade. A hydrophobic membrane

is used for ethanol purification, whereas, for ethanol dehydration, a hydrophilic membrane is used [159]. For example, Zhan *et al.* proved that HF etched ZSM-5 surface loading increased ethanol permeation and selectivity. This increase was also observed when the zeolite loading was increased from 10% to 30%. However, the excess zeolite loading resulted in a decrease in selectivity [39]. The same trend was observed when the thickness of a selective layer of the component was also decreased [40]. In another study, zeolites filled in PDMS membranes led to a great increase in ethanol permeability. These results also agreed with the ones obtained by various studies [23, 41, 160-162]. **Table 2** summarizes some of the zeolitic MMMs used for ethanol dehydration and purification with different zeolite structures, loading, and polymers. It is clear that in some cases, the separation factor ( $\alpha$ ) is reduced, whereas the flux is increased and vice-versa. Therefore, it is important to choose the polymer and the zeolite loading properly to obtain better performance.

**Table 2:** Examples of hydrophilic and hydrophobic pervaporation processes.

	Zeolite	Polymer	Neat Membrane performance		MMM performance		Temp (°C)	Ref
			total flux (g.m <sup>-2</sup> . h <sup>-1</sup> )	Separation factor ( $\alpha$ )	total flux (g.m <sup>-2</sup> . h <sup>-1</sup> )	Separation factor ( $\alpha$ )		
ethanol /water (90/10)	HZSM-5	Chitosan	54.18	158	231	153	80	[163]
ethanol /water (80/20)	Zeolite KA	PVA	140	40	164	40	50	[164]
ethanol /water (80/20)	Zeolite NaA	PVA	140	40	172	36.6	50	[164]
ethanol /water (80/20)	Zeolite CaA	PVA	140	40	194	22.3	50	[164]
ethanol /water (80/20)	Zeolite NaX	PVA	140	40	214	19.4	50	[164]
5 wt % ethanol	ZSM-5	PDMS	-	-	408	14	40	[165]
5 wt % ethanol	HF etched ZSM-5	PDMS	-	-	211	9.2	50	[40]
5 wt % ethanol	Silicalite	PDMS	24	7.6	50.7	16.5	22.5	[166]
5 wt % ethanol	Silicalite	PEBA	-	-	833	3.6	40	[167]
5 wt % ethanol	Silicalite	PIM-1	6520	3.61	5460	5.68	60	[168]

## 4. Scope of the work

Bioethanol is emerging to be a good alternative for gasoline to reduce the latter's impact on the environment and human survival. However, the purification process from the aqueous mixture remains very challenging and is the subject of extensive experimental studies. Among the different purification processes, the separation on porous materials and mixed matrix membranes has shown its efficiency on the overall purification yield and the economic energy and time consumption. Nevertheless, the synthesis of hybrid materials has been subjected to several challenges, previously elaborated in the chapter above.

Despite the considerable amount of research in the fields of hybrid material synthesis, other approaches are needed to develop the synthetic pathways of hybrid materials. Additionally, a detailed vibrational spectroscopic study is necessary to understand the mechanism of adsorption and separation of ethanol and water on porous materials since there is no such study using this technique. IR spectroscopy coupled with gravimetric analysis allows determining the quantity and the nature of the adsorbed species, particularly in the binary system, and the nature of the adsorption sites.

Our work aims to develop hybrid materials via a new promising approach for their potential application in the synthesis of mixed matrix membranes and to study their adsorption capacity for the selective separation of water and ethanol using IR spectroscopy.

Hence, the first task was to study quantitatively the adsorption of ethanol and/or water on zeolitic porous materials. For this, vibrational spectroscopic techniques developed in our laboratory were applied. The effect the Si/Al ratios of the zeolites and the effect of water content in the vapor phase on their adsorption capacity were further investigated to direct the choice for the synthesis of the separation membrane.

Furthermore, the synthesis of hybrid materials has been conducted via a new approach consisting of the formation of core-shell-like structures (silica and zeolite/polymer) via photopolymerization.

Ethanol and water adsorption capacities of the synthesized hybrid materials were studied and compared to that of the parent material after their full characterization.

Finally, the third objective was to test their efficiency in the selective separation of ethanol and water using IR spectroscopy.

## References

1. Karl, T.R. and K.E. Trenberth, *Modern global climate change*. science, 2003. **302**(5651): p. 1719-1723.
2. Cheng, J.J. and G.R. Timilsina, *Status and barriers of advanced biofuel technologies: a review*. Renewable Energy, 2011. **36**(12): p. 3541-3549.
3. Aftabuzzaman, M. and E. Mazloumi, *Achieving sustainable urban transport mobility in post peak oil era*. Transport Policy, 2011. **18**(5): p. 695-702.
4. Malhotra, R. and L. Das, *Biofuels as blending components for motor gasoline and diesel fuels*. 2003.
5. Maity, S.K., *Opportunities, recent trends and challenges of integrated biorefinery: Part I*. Renewable and Sustainable Energy Reviews, 2015. **43**: p. 1427-1445.
6. Abdeshahian, P., et al., *Production of biofuel using biomass as a sustainable biological resource*. Biotechnology, 2010. **9**(3): p. 274-282.
7. Kumar, S., N. Singh, and R. Prasad, *Anhydrous ethanol: A renewable source of energy*. Renewable and Sustainable Energy Reviews, 2010. **14**(7): p. 1830-1844.
8. Ghosh, A., et al., *Progress toward isolation of strains and genetically engineered strains of microalgae for production of biofuel and other value added chemicals: a review*. Energy Conversion and Management, 2016. **113**: p. 104-118.
9. Alam, F., S. Mobin, and H. Chowdhury, *Third generation biofuel from Algae*. Procedia Engineering, 2015. **105**: p. 763-768.
10. Van Gerpen, J., *Biodiesel processing and production*. Fuel processing technology, 2005. **86**(10): p. 1097-1107.
11. Naik, S.N., et al., *Production of first and second generation biofuels: a comprehensive review*. Renewable and sustainable energy reviews, 2010. **14**(2): p. 578-597.
12. Demirbas, A., *Progress and recent trends in biodiesel fuels*. Energy conversion and management, 2009. **50**(1): p. 14-34.
13. Nigam, P.S. and A. Singh, *Production of liquid biofuels from renewable resources*. Progress in energy and combustion science, 2011. **37**(1): p. 52-68.
14. Balat, M., *Global bio-fuel processing and production trends*. Energy Exploration & Exploitation, 2007. **25**(3): p. 195-218.
15. Soccol, C.R., et al., *Lignocellulosic bioethanol: current status and future perspectives*, in *Biofuels: Alternative feedstocks and conversion processes for the production of liquid and gaseous biofuels*. 2019, Elsevier. p. 331-354.
16. Siepmann, J.I., P. Bai, and M. Tsapatsis, *Zeolites for separation of ethanol and water*. 2018, Univ. of Minnesota, Minneapolis, MN (United States).
17. Treybal, R.E., *Mass transfer operations*. New York, 1980. **466**.
18. Kujawska, A., et al., *ABE fermentation products recovery methods—a review*. Renewable and Sustainable Energy Reviews, 2015. **48**: p. 648-661.
19. Vane, L.M., *Separation technologies for the recovery and dehydration of alcohols from fermentation broths*. Biofuels, Bioproducts and Biorefining, 2008. **2**(6): p. 553-588.
20. Ravagnani, M., et al., *Anhydrous ethanol production by extractive distillation: A solvent case study*. Process Safety and Environmental Protection, 2010. **88**(1): p. 67-73.
21. Messick, J.R., W.R. Ackley, and G.D. Moon Jr, *Anhydrous ethanol distillation method and apparatus*. 1983, Google Patents.
22. Liu, F., L. Liu, and X. Feng, *Separation of acetone–butanol–ethanol (ABE) from dilute aqueous solutions by pervaporation*. Separation and Purification Technology, 2005. **42**(3): p. 273-282.
23. Liu, X., et al., *Preparation and characterization of S ilicalite-1/PDMS surface sieving pervaporation membrane for separation of ethanol/water mixture*. Journal of Applied Polymer Science, 2015. **132**(34).
24. Rozicka, A., et al., *Apparent and intrinsic properties of commercial PDMS based membranes in pervaporative removal of acetone, butanol and ethanol from binary aqueous mixtures*. Journal of Membrane Science, 2014. **453**: p. 108-118.

25. Levario, T.J., et al., *Rapid adsorption of alcohol biofuels by high surface area mesoporous carbons*. *Microporous and Mesoporous Materials*, 2012. **148**(1): p. 107-114.
26. Adnadevic, B., et al., *Isoconversional Kinetic Analysis of Isothermal Selective Ethanol Adsorption on Zeolite Type NaZSM-5*. *Chemical Engineering & Technology: Industrial Chemistry-Plant Equipment-Process Engineering-Biotechnology*, 2007. **30**(9): p. 1228-1234.
27. Ezeji, T., N. Qureshi, and H. Blaschek, *Production of acetone, butanol and ethanol by Clostridium beijerinckii BA101 and in situ recovery by gas stripping*. *World Journal of Microbiology and Biotechnology*, 2003. **19**(6): p. 595-603.
28. Park, C.H., M.R. Okos, and P.C. Wankat, *Acetone-butanol-ethanol (ABE) fermentation and simultaneous separation in a trickle bed reactor*. *Biotechnology progress*, 1991. **7**(2): p. 185-194.
29. Ladisch, M.R., et al., *Commeal adsorber for dehydrating ethanol vapors*. *Industrial & Engineering Chemistry Process Design and Development*, 1984. **23**(3): p. 437-443.
30. Pacheco-Basulto, J.Á., et al., *Purification of bioethanol using extractive batch distillation: Simulation and experimental studies*. *Chemical Engineering and Processing: Process Intensification*, 2012. **61**: p. 30-35.
31. Zhu, Z., et al., *Extractive distillation for ethanol dehydration using imidazolium-based ionic liquids as solvents*. *Chemical Engineering and Processing-Process Intensification*, 2016. **109**: p. 190-198.
32. Gómez-Álvarez, P., et al., *Study of Short-Chain Alcohol and Alcohol–Water Adsorption in MEL and MFI Zeolites*. *Langmuir*, 2018. **34**(43): p. 12739-12750.
33. CLEMENT, R. and A. JONQUIERES, *Pervaporation*. *Techniques de l'ingénieur. Génie des procédés*, 2001. **3**(J2820): p. J2820. 1-J2820. 15.
34. Kujawska, A., et al., *Removal of volatile organic compounds from aqueous solutions applying thermally driven membrane processes. 1. Thermopervaporation*. *Chemical Engineering and Processing - Process Intensification*, 2015. **94**: p. 62-71.
35. Kujawski, W. and S.R. Krajewski, *Sweeping gas pervaporation with hollow-fiber ion-exchange membranes*. *Desalination*, 2004. **162**: p. 129-135.
36. Kujawski, W., *Application of pervaporation and vapor permeation in environmental protection*. *Polish Journal of Environmental Studies*, 2000. **9**(1): p. 13-26.
37. Davey, C.J., D. Leak, and D.A. Patterson, *Hybrid and mixed matrix membranes for separations from fermentations*. *Membranes*, 2016. **6**(1): p. 17.
38. Huang, Z., et al., *Multilayer poly (vinyl alcohol)–zeolite 4A composite membranes for ethanol dehydration by means of pervaporation*. *Separation and Purification Technology*, 2006. **51**(2): p. 126-136.
39. Zhan, X., et al., *Pervaporation separation of ethanol/water mixtures with chlorosilane modified silicalite-1/PDMS hybrid membranes*. *Chinese Journal of Polymer Science*, 2010. **28**(4): p. 625-635.
40. Zhan, X., et al., *Mixed matrix membranes with HF acid etched ZSM-5 for ethanol/water separation: preparation and pervaporation performance*. *Applied Surface Science*, 2012. **259**: p. 547-556.
41. Bowen, T.C., R.G. Meier, and L.M. Vane, *Stability of MFI zeolite-filled PDMS membranes during pervaporative ethanol recovery from aqueous mixtures containing acetic acid*. *Journal of membrane science*, 2007. **298**(1-2): p. 117-125.
42. Miller, J.R. and P. Simon, *The Chalkboard: Fundamentals of Electrochemical Capacitor Design and Operation*. *The Electrochemical society interface*, 2008. **17**(1): p. 31.
43. Anozie, A., et al., *Dehydration of ethanol-water mixture using activated carbons from sawdust and palm kernel shells*. *Separation Science and Technology*, 2010. **45**(10): p. 1482-1489.
44. Gee, J.A., et al., *Adsorption and diffusion of small alcohols in zeolitic imidazolate frameworks ZIF-8 and ZIF-90*. *The Journal of Physical Chemistry C*, 2013. **117**(6): p. 3169-3176.

45. Someya, T., et al., *Alcohol vapor sensors based on single-walled carbon nanotube field effect transistors*. Nano letters, 2003. **3**(7): p. 877-881.
46. Cronstedt, A., *Natural zeolite and minerals*. Svenska Vetenskaps Akademiens Handlingar Stockholm, 1756. **17**: p. 120.
47. Mintova, S., J.-P. Gilson, and V. Valtchev, *Advances in nanosized zeolites*. Nanoscale, 2013. **5**(15): p. 6693-6703.
48. Xu, R., et al., *Chemistry of zeolites and related porous materials: synthesis and structure*. 2009: John Wiley & Sons.
49. Moshoeshoe, M., M. Nadiye-Tabbiruka, and V. Obuseng, *A review of the chemistry, structure, properties and applications of zeolites*. Am. J. Mater. Sci, 2017. **7**(5): p. 196-221.
50. Weitkamp, J., *Zeolites and catalysis*. Solid state ionics, 2000. **131**(1-2): p. 175-188.
51. Mgbemere, H., I. Ekpe, and G. Lawal, *Zeolite synthesis, characterization and application areas: a review*. Int Res J Environ Sci, 2017. **6**(10): p. 45-49.
52. Auerbach, S.M., K.A. Carrado, and P.K. Dutta, *Handbook of zeolite science and technology*. 2003: CRC press.
53. Inglezakis, V.J., *The concept of "capacity" in zeolite ion-exchange systems*. Journal of Colloid and Interface Science, 2005. **281**(1): p. 68-79.
54. Martinez Sanchez, C. and J. Pérez Pariente, *Zeolites and ordered porous solids: fundamentals and applications*. 2011: Editorial Universitat Politècnica de València.
55. WRIGHT, P.A. and M. LOZINSKA, *Structural Chemistry and Properties of zeolites*. Zeolites and ordered porous solids, 2011: p. 1.
56. IZA. *International Zeolite Association*. 2019; Available from: <http://www.iza-structure.org>.
57. Gounder, R. and E. Iglesia, *Catalytic consequences of spatial constraints and acid site location for monomolecular alkane activation on zeolites*. Journal of the American Chemical Society, 2009. **131**(5): p. 1958-1971.
58. Valtchev, V., et al., *Tailored crystalline microporous materials by post-synthesis modification*. Chemical Society Reviews, 2013. **42**(1): p. 263-290.
59. Dwyer, J. and P. Jo'Malley, *Relation between Acidic and Catalytic Properties of Zeolites*, in *Studies in Surface Science and Catalysis*. 1988, Elsevier. p. 5-100.
60. Derouane, E., et al., *The acidity of zeolites: concepts, measurements and relation to catalysis: a review on experimental and theoretical methods for the study of zeolite acidity*. Catalysis Reviews, 2013. **55**(4): p. 454-515.
61. Barrer, R.M., *33. Synthesis of a zeolitic mineral with chabazite-like sorptive properties*. Journal of the Chemical Society (Resumed), 1948: p. 127-132.
62. MOLINER, M., *Basic principles of zeolite synthesis*. Zeolites and Ordered Porous Solids, 2011: p. 37.
63. Georgiev, D., et al. *Synthetic zeolites—Structure, classification, current trends in zeolite synthesis*. in *Economics and Society Development on the Base of Knowledge: International Scientific Conference*. 2009.
64. Ribeiro, F.R. and M. Guisnet, *Les zéolithes, un nanomonde au service de la catalyse: un nanomonde au service de la catalyse*. 2012: EDP Sciences.
65. Wadlinger, R.L., G.T. Kerr, and E.J. Rosinski, *Catalytic composition of a crystalline zeolite*. 1967, Google Patents.
66. Argauer, R.J. and G.R. Landolt, *Crystalline zeolite ZSM-5 and method of preparing the same*. 1972, Google Patents.
67. Cundy, C.S. and P.A. Cox, *The hydrothermal synthesis of zeolites: history and development from the earliest days to the present time*. Chemical reviews, 2003. **103**(3): p. 663-702.
68. Weller, M.T. and S.E. Dann, *Hydrothermal synthesis of zeolites*. Current Opinion in Solid State and Materials Science, 1998. **3**(2): p. 137-143.
69. Shin, J., et al., *PST-1: A Synthetic Small-Pore Zeolite that Selectively Adsorbs H<sub>2</sub>*. Angewandte Chemie International Edition, 2009. **48**(36): p. 6647-6649.

70. Awala, H., et al., *Template-free nanosized faujasite-type zeolites*. Nature materials, 2015. **14**(4): p. 447-451.
71. Wong, S.-F., et al., *KF zeolite nanocrystals synthesized from organic-template-free precursor mixture*. Microporous and Mesoporous Materials, 2017. **249**: p. 105-110.
72. Yu, Q., et al., *Inductive effect of various seeds on the organic template-free synthesis of zeolite ZSM-5*. CrystEngComm, 2013. **15**(38): p. 7680-7687.
73. Kosinov, N., et al., *Recent developments in zeolite membranes for gas separation*. Journal of Membrane Science, 2016. **499**: p. 65-79.
74. Jiang, N., et al., *High-silica zeolites for adsorption of organic micro-pollutants in water treatment: A review*. Water research, 2018. **144**: p. 145-161.
75. Guisnet, M. and J.-P. Gilson, *Zeolites for cleaner technologies*. Vol. 3. 2002: Imperial College Press London.
76. Bacakova, L., et al., *Applications of zeolites in biotechnology and medicine—a review*. Biomaterials science, 2018. **6**(5): p. 974-989.
77. Flanigen, E.M., J. Jansen, and H. van Bekkum, *Introduction to zeolite science and practice*. 1991: Elsevier.
78. Degnan Jr, T.F., C.M. Smith, and C.R. Venkat, *Alkylation of aromatics with ethylene and propylene: recent developments in commercial processes*. Applied catalysis A: general, 2001. **221**(1-2): p. 283-294.
79. Li, C.-G., et al., *Efficient cycloaddition of epoxides and carbon dioxide over novel organic-inorganic hybrid zeolite catalysts*. Chemical Communications, 2014. **50**(99): p. 15764-15767.
80. Miralda, C.M., et al., *Zeolitic imidazole framework-8 catalysts in the conversion of CO<sub>2</sub> to chloropropene carbonate*. ACS Catalysis, 2012. **2**(1): p. 180-183.
81. Yilmaz, B. and U. Müller, *Catalytic applications of zeolites in chemical industry*. Topics in Catalysis, 2009. **52**(6-7): p. 888-895.
82. Li, J., et al., *Comparative study of MTO conversion over SAPO-34, H-ZSM-5 and H-ZSM-22: Correlating catalytic performance and reaction mechanism to zeolite topology*. Catalysis today, 2011. **171**(1): p. 221-228.
83. Chen, D., K. Moljord, and A. Holmen, *A methanol to olefins review: Diffusion, coke formation and deactivation on SAPO type catalysts*. Microporous and mesoporous materials, 2012. **164**: p. 239-250.
84. Vermeiren, W. and J.-P. Gilson, *Impact of zeolites on the petroleum and petrochemical industry*. Topics in Catalysis, 2009. **52**(9): p. 1131-1161.
85. Su, F., et al., *Adsorption of CO<sub>2</sub> on amine-functionalized Y-type zeolites*. Energy & Fuels, 2010. **24**(2): p. 1441-1448.
86. Saha, D., et al., *Adsorption of CO<sub>2</sub>, CH<sub>4</sub>, N<sub>2</sub>O, and N<sub>2</sub> on MOF-5, MOF-177, and zeolite 5A*. Environmental science & technology, 2010. **44**(5): p. 1820-1826.
87. Won, W., S. Lee, and K.-S. Lee, *Modeling and parameter estimation for a fixed-bed adsorption process for CO<sub>2</sub> capture using zeolite 13X*. Separation and purification technology, 2012. **85**: p. 120-129.
88. Ohlin, L., et al., *Effect of Water on the Adsorption of Methane and Carbon Dioxide in Zeolite Na-ZSM-5 Studied Using in Situ ATR-FTIR Spectroscopy*. The Journal of Physical Chemistry C, 2016. **120**(51): p. 29144-29152.
89. Ohlin, L., et al., *Ternary adsorption of methane, water, and carbon dioxide in zeolite Na-ZSM-5 studied using in situ ATR-FTIR spectroscopy*. The Journal of Physical Chemistry C, 2017. **121**(27): p. 14703-14711.
90. Wang, P., et al., *Effective removal of methane using nano-sized zeolite 4A synthesized from kaolin*. Inorganic Chemistry Communications, 2020. **111**: p. 107639.
91. Seabra, R., et al., *Adsorption equilibrium and kinetics of carbon dioxide, methane and nitrogen on binderless zeolite 4A adsorbents*. Microporous and Mesoporous Materials, 2019. **277**: p. 105-114.
92. Jentys, A., et al., *Adsorption of water on ZSM 5 zeolites*. The Journal of Physical Chemistry, 1989. **93**(12): p. 4837-4843.

93. Hunger, B., et al., *Adsorption of water on zeolites of different types*. Journal of Thermal Analysis and Calorimetry, 1997. **49**(1): p. 553-565.
94. Ramachandran, C.E., et al., *Water adsorption in hydrophobic nanopores: Monte Carlo simulations of water in silicalite*. Microporous and mesoporous materials, 2006. **90**(1-3): p. 293-298.
95. Wang, S. and Y. Peng, *Natural zeolites as effective adsorbents in water and wastewater treatment*. Chemical Engineering Journal, 2010. **156**(1): p. 11-24.
96. Mofarahi, M. and F. Gholipour, *Gas adsorption separation of CO<sub>2</sub>/CH<sub>4</sub> system using zeolite 5A*. Microporous and Mesoporous Materials, 2014. **200**: p. 1-10.
97. Khoramzadeh, E., M. Mofarahi, and C.-H. Lee, *Equilibrium Adsorption Study of CO<sub>2</sub> and N<sub>2</sub> on Synthesized Zeolites 13X, 4A, 5A, and Beta*. Journal of Chemical & Engineering Data, 2019.
98. Fakin, T., et al. *Water adsorption study on the zeolite LTA granules*. in *Proceedings of the 5th Serbian-Croatian-Slovenian Symposium on Zeolites*. 2013.
99. Jaramillo, E. and M. Chandross, *Adsorption of small molecules in LTA zeolites. 1. NH<sub>3</sub>, CO<sub>2</sub>, and H<sub>2</sub>O in zeolite 4A*. The Journal of Physical Chemistry B, 2004. **108**(52): p. 20155-20159.
100. Xiong, R., S.I. Sandler, and D.G. Vlachos, *Molecular screening of alcohol and polyol adsorption onto MFI-type zeolites*. Langmuir, 2012. **28**(9): p. 4491-4499.
101. Xiong, R., S.I. Sandler, and D.G. Vlachos, *Alcohol adsorption onto silicalite from aqueous solution*. The Journal of Physical Chemistry C, 2011. **115**(38): p. 18659-18669.
102. Zhou, H., et al., *Colloidal defect-free silicalite-1 single crystals: preparation, structure characterization, adsorption, and separation properties for alcohol/water mixtures*. Langmuir, 2015. **31**(30): p. 8488-8494.
103. Zhang, K., et al., *Adsorption of water and ethanol in MFI-type zeolites*. Langmuir, 2012. **28**(23): p. 8664-8673.
104. DeJaco, R.F., et al., *Adsorptive separation of 1-butanol from aqueous solutions using MFI-and FER-type zeolite frameworks: a Monte Carlo study*. Langmuir, 2016. **32**(8): p. 2093-2101.
105. Krishna, R. and J.M. van Baten, *Hydrogen bonding effects in adsorption of water-alcohol mixtures in zeolites and the consequences for the characteristics of the Maxwell– Stefan diffusivities*. Langmuir, 2010. **26**(13): p. 10854-10867.
106. Pahari, S., et al., *Ethanol and Water Adsorption in Conventional and Hierarchical All-Silica MFI Zeolites*. ACS Physical Chemistry Au, 2021.
107. Trzpit, M., et al., *The effect of local defects on water adsorption in silicalite-1 zeolite: A joint experimental and molecular simulation study*. Langmuir, 2007. **23**(20): p. 10131-10139.
108. DeJaco, R.F., et al., *Vapor-and liquid-phase adsorption of alcohol and water in silicalite-1 synthesized in fluoride media*. AIChE Journal, 2020. **66**(4): p. e16868.
109. Castillo, J.M., et al., *Water adsorption in hydrophilic zeolites: experiment and simulation*. Physical Chemistry Chemical Physics, 2013. **15**(40): p. 17374-17382.
110. Ahmad, H.A., et al., *Nanosized Na-EMT and Li-EMT zeolites: selective sorption of water and methanol studied by a combined IR and TG approach*. Physical Chemistry Chemical Physics, 2016. **18**(44): p. 30585-30594.
111. Bowen, T.C. and L.M. Vane, *Ethanol, acetic acid, and water adsorption from binary and ternary liquid mixtures on high-silica zeolites*. Langmuir, 2006. **22**(8): p. 3721-3727.
112. Olson, D., W. Haag, and W. Borghard, *Use of water as a probe of zeolitic properties: interaction of water with HZSM-5*. Microporous and Mesoporous Materials, 2000. **35**: p. 435-446.
113. Masoumifard, N., R. Guillet-Nicolas, and F. Kleitz, *Synthesis of engineered zeolitic materials: from classical zeolites to hierarchical core-shell materials*. Advanced Materials, 2018. **30**(16): p. 1704439.

114. Ghosh Chaudhuri, R. and S. Paria, *Core/shell nanoparticles: classes, properties, synthesis mechanisms, characterization, and applications*. Chemical reviews, 2012. **112**(4): p. 2373-2433.
115. Jankiewicz, B., et al., *Silica–metal core–shell nanostructures*. Advances in colloid and interface science, 2012. **170**(1-2): p. 28-47.
116. Blackman, B., D. Battaglia, and X. Peng, *Bright and water-soluble near IR-emitting CdSe/CdTe/ZnSe type-II/type-I nanocrystals, tuning the efficiency and stability by growth*. Chemistry of Materials, 2008. **20**(15): p. 4847-4853.
117. Bouizi, Y., et al., *Core–shell zeolite microcomposites*. Advanced Functional Materials, 2005. **15**(12): p. 1955-1960.
118. Bouizi, Y., L. Rouleau, and V.P. Valtchev, *Factors controlling the formation of core–shell zeolite–zeolite composites*. Chemistry of materials, 2006. **18**(20): p. 4959-4966.
119. Elahi, M.F., et al., *Core-shell fibers for biomedical applications-a review*. J. Bioeng. Biomed. Sci, 2013. **3**(1): p. 1-14.
120. Schärtl, W., *Current directions in core–shell nanoparticle design*. Nanoscale, 2010. **2**(6): p. 829-843.
121. Zhong, C.-J. and M.M. Maye, *Core–shell assembled nanoparticles as catalysts*. Advanced Materials, 2001. **13**(19): p. 1507-1511.
122. Gawande, M.B., et al., *Core–shell nanoparticles: synthesis and applications in catalysis and electrocatalysis*. Chemical Society Reviews, 2015. **44**(21): p. 7540-7590.
123. Ren, J., et al., *Fabrication of core–shell MIL-101 (Cr)@ UiO-66 (Zr) nanocrystals for hydrogen storage*. international journal of hydrogen energy, 2014. **39**(27): p. 14912-14917.
124. Sorribas, S., et al., *Ordered mesoporous silica–(ZIF-8) core–shell spheres*. Chemical Communications, 2012. **48**(75): p. 9388-9390.
125. Bouizi, Y., *Micro-composites formés d'une couche continue de zéolithe recouvrant un coeur de zéolithe–Etude des processus de formation*. 2005.
126. Khaledi, K., M. Haghighi, and P. Sadeghpour, *On the catalytic properties and performance of core-shell ZSM-5@ MnO nanocatalyst used in conversion of methanol to light olefins*. Microporous and Mesoporous Materials, 2017. **246**: p. 51-61.
127. Li, X.R., Fateme ; K. Ludlow, Douglas; Rownaghi, Ali A. , *Synthesis of SAPO-34@ZSM-5 and SAPO-34@Silicalite-1 Core–Shell Zeolite Composites for Ethanol Dehydration*. 2018.
128. Joo, S.H., et al., *Thermally stable Pt/mesoporous silica core–shell nanocatalysts for high-temperature reactions*. Nature materials, 2009. **8**(2): p. 126-131.
129. Kudasheva, A., et al., *Pervaporation of water/ethanol mixtures through polyimide based mixed matrix membranes containing ZIF-8, ordered mesoporous silica and ZIF-8-silica core-shell spheres*. Journal of Chemical Technology & Biotechnology, 2015. **90**(4): p. 669-677.
130. Khoang, N.D., et al., *Design of SnO<sub>2</sub>/ZnO hierarchical nanostructures for enhanced ethanol gas-sensing performance*. Sensors and Actuators B: Chemical, 2012. **174**: p. 594-601.
131. Song, X. and L. Liu, *Characterization of electrospun ZnO–SnO<sub>2</sub> nanofibers for ethanol sensor*. Sensors and actuators A: Physical, 2009. **154**(1): p. 175-179.
132. Miyamoto, M., et al., *Effect of core-shell structuring of chabazite zeolite with a siliceous zeolite thin layer on the separation of acetone-butanol-ethanol vapor in humid vapor conditions*. Chemical Engineering Journal, 2019. **363**: p. 292-299.
133. Lin, R., et al., *Metal organic framework based mixed matrix membranes: an overview on filler/polymer interfaces*. Journal of Materials Chemistry A, 2018. **6**(2): p. 293-312.
134. Bastani, D., N. Esmaeili, and M. Asadollahi, *Polymeric mixed matrix membranes containing zeolites as a filler for gas separation applications: A review*. Journal of Industrial and Engineering Chemistry, 2013. **19**(2): p. 375-393.
135. Caro, J. and M. Noack, *Zeolite membranes–recent developments and progress*. Microporous and Mesoporous Materials, 2008. **115**(3): p. 215-233.

136. Xu, X., et al., *Synthesis, characterization and single gas permeation properties of NaA zeolite membrane*. Journal of Membrane Science, 2005. **249**(1-2): p. 51-64.
137. Paul, D.R. and D. Kemp. *The diffusion time lag in polymer membranes containing adsorptive fillers*. in *Journal of Polymer Science: Polymer Symposia*. 1973. Wiley Online Library.
138. Gong, H., S.S. Lee, and T.-H. Bae, *Mixed-matrix membranes containing inorganically surface-modified 5A zeolite for enhanced CO<sub>2</sub>/CH<sub>4</sub> separation*. Microporous and Mesoporous Materials, 2017. **237**: p. 82-89.
139. Karkhanechi, H., et al., *Fabrication of Homogenous Polymer-Zeolite Nanocomposites as Mixed-Matrix Membranes for Gas Separation*. Chemical engineering & technology, 2012. **35**(5): p. 885-892.
140. Wu, D., et al., *Scale-up of zeolite-Y/polyethersulfone substrate for composite membrane fabrication in CO<sub>2</sub> separation*. Journal of Membrane Science, 2018. **562**: p. 56-66.
141. Wang, H., B.A. Holmberg, and Y. Yan, *Homogeneous polymer-zeolite nanocomposite membranes by incorporating dispersible template-removed zeolite nanocrystals*. Journal of Materials Chemistry, 2002. **12**(12): p. 3640-3643.
142. Huang, Z., et al., *Enhanced gas separation properties by using nanostructured PES-Zeolite 4A mixed matrix membranes*. Journal of applied polymer science, 2006. **101**(6): p. 3800-3805.
143. Vankelecom, I.F., et al., *Influence of zeolites in PDMS membranes: pervaporation of water/alcohol mixtures*. The Journal of Physical Chemistry, 1995. **99**(35): p. 13193-13197.
144. Goldman, M., D. Fraenkel, and G. Levin, *A zeolite/polymer membrane for separation of ethanol-water azeotrope*. Journal of applied polymer science, 1989. **37**(7): p. 1791-1800.
145. Amnuaypanich, S., J. Patthana, and P. Phinyocheep, *Mixed matrix membranes prepared from natural rubber/poly (vinyl alcohol) semi-interpenetrating polymer network (NR/PVA semi-IPN) incorporating with zeolite 4A for the pervaporation dehydration of water-ethanol mixtures*. Chemical Engineering Science, 2009. **64**(23): p. 4908-4918.
146. Mahajan, R., et al., *Challenges in forming successful mixed matrix membranes with rigid polymeric materials*. Journal of Applied Polymer Science, 2002. **86**(4): p. 881-890.
147. Clarizia, G., et al., *Zeolite-based composite PEEK-WC membranes: gas transport and surface properties*. Microporous and Mesoporous Materials, 2008. **115**(1-2): p. 67-74.
148. Li, Y., et al., *The effects of polymer chain rigidification, zeolite pore size and pore blockage on polyethersulfone (PES)-zeolite A mixed matrix membranes*. Journal of Membrane Science, 2005. **260**(1-2): p. 45-55.
149. Tantekin-Ersolmaz, Ş.B., et al., *Effect of zeolite particle size on the performance of polymer-zeolite mixed matrix membranes*. Journal of Membrane Science, 2000. **175**(2): p. 285-288.
150. Nik, O.G., X.Y. Chen, and S. Kaliaguine, *Amine-functionalized zeolite FAU/EMT-polyimide mixed matrix membranes for CO<sub>2</sub>/CH<sub>4</sub> separation*. Journal of Membrane Science, 2011. **379**(1-2): p. 468-478.
151. Casado-Coterillo, C., et al., *Preparation and characterization of ITQ-29/polysulfone mixed-matrix membranes for gas separation: Effect of zeolite composition and crystal size*. Chemical engineering science, 2012. **73**: p. 116-122.
152. Kumbhar, S.M., et al., *ORMOCERs (organic-inorganic hybrid copolymers)-zeolite Beta (BEA) nanocomposite membranes for gas separation applications*. Journal of Membrane Science, 2010. **347**(1-2): p. 132-140.
153. Ismail, A., R. Rahim, and W. Rahman, *Characterization of polyethersulfone/Matrimid® 5218 miscible blend mixed matrix membranes for O<sub>2</sub>/N<sub>2</sub> gas separation*. Separation and Purification Technology, 2008. **63**(1): p. 200-206.

154. Chung, T.-S., et al., *Mixed matrix membranes (MMMs) comprising organic polymers with dispersed inorganic fillers for gas separation*. Progress in polymer science, 2007. **32**(4): p. 483-507.
155. Zhao, D., et al., *Poly (amide-6-b-ethylene oxide)/SAPO-34 mixed matrix membrane for CO<sub>2</sub> separation*. Journal of energy chemistry, 2014. **23**(2): p. 227-234.
156. Pechar, T.W., et al., *Fabrication and characterization of polyimide-zeolite L mixed matrix membranes for gas separations*. Journal of Membrane Science, 2006. **277**(1-2): p. 195-202.
157. Kulprathipanja, S., R.W. Neuzil, and N.N. Li, *Separation of fluids by means of mixed matrix membranes*. 1988, Google Patents.
158. Mahajan, R. and W.J. Koros, *Factors controlling successful formation of mixed-matrix gas separation materials*. Industrial & Engineering Chemistry Research, 2000. **39**(8): p. 2692-2696.
159. Castro-Muñoz, R., et al., *Mixed matrix membranes (MMMs) for ethanol purification through pervaporation: current state of the art*. Reviews in Chemical Engineering, 2019. **35**(5): p. 565-590.
160. Yadav, A., et al., *Nanocomposite silicalite-1/polydimethylsiloxane membranes for pervaporation of ethanol from dilute aqueous solutions*. Industrial & Engineering Chemistry Research, 2013. **52**(14): p. 5207-5212.
161. Dobrak, A., et al., *Performance of PDMS membranes in pervaporation: effect of silicalite fillers and comparison with SBS membranes*. Journal of colloid and interface science, 2010. **346**(1): p. 254-264.
162. Vane, L.M., V.V. Namboodiri, and R.G. Meier, *Factors affecting alcohol-water pervaporation performance of hydrophobic zeolite-silicone rubber mixed matrix membranes*. Journal of Membrane Science, 2010. **364**(1-2): p. 102-110.
163. Sun, H., et al., *Pervaporation dehydration of aqueous ethanol solution using H-ZSM-5 filled chitosan membranes*. Separation and purification technology, 2008. **58**(3): p. 429-436.
164. Gao, Z., Y. Yue, and W. Li, *Application of zeolite-filled pervaporation membrane*. Zeolites, 1996. **16**(1): p. 70-74.
165. Liu, G., et al., *Improved performance of PDMS/ceramic composite pervaporation membranes by ZSM-5 homogeneously dispersed in PDMS via a surface graft/coating approach*. Chemical Engineering Journal, 2011. **174**(2-3): p. 495-503.
166. Te Hennepe, H., et al., *Zeolite-filled silicone rubber membranes: Part 1. Membrane preparation and pervaporation results*. Journal of membrane science, 1987. **35**(1): p. 39-55.
167. Gu, J., et al., *Silicalite-Filled PEBA Membranes for recovering ethanol from aqueous solution by pervaporation*. Chemical Engineering & Technology: Industrial Chemistry-Plant Equipment-Process Engineering-Biotechnology, 2009. **32**(1): p. 155-160.
168. Mason, C.R., et al., *New organophilic mixed matrix membranes derived from a polymer of intrinsic microporosity and silicalite-1*. Polymer, 2013. **54**(9): p. 2222-2230.





# CHAPTER TWO

---

## EXPERIMENTAL PART

---



## 1. Materials: MFI zeolites

MFI structure (**Figure 1**) comprises two types of three-dimensional interconnected channels with a pore diameter of 5 Å and a medium pore of 0.54 x 0.56. Linear channels parallel to the *b* axis with circular openings and diameters of 5.4 and 5.6 Å are perpendicular to the sinusoidal channels present in the (*a,c*) plane. The latter channels are elliptical openings with 5.1 Å x 5.5 Å as dimensions [1, 2].

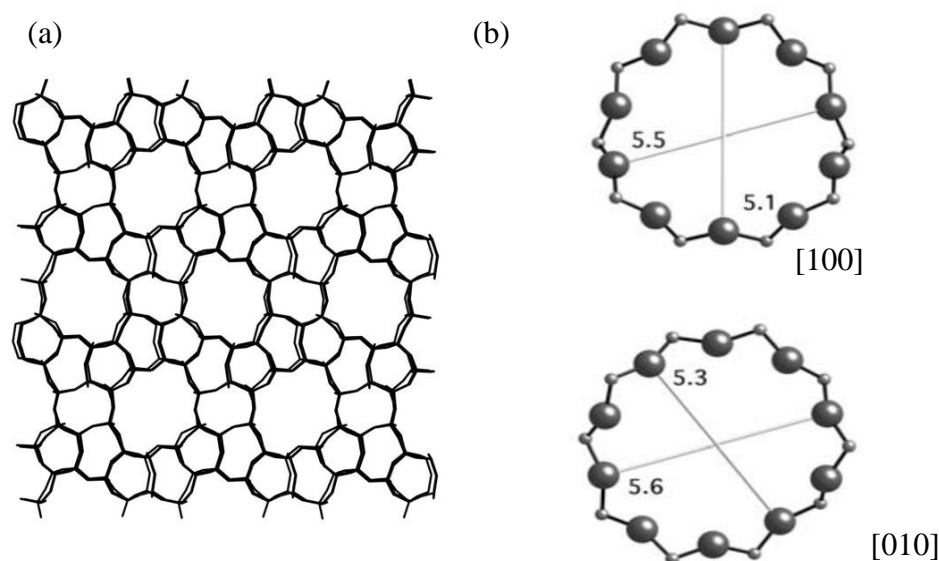


**Figure 1:** (a) MFI structure and the pore opening according to (b) the planes [100] and [010]. Reprinted with the permission of ref [2].

Different MFI zeolites have been synthesized with a vast Si/Al ratio range. The very well-known zeolites with MFI structure are ZSM-5 and silicalite-1. Whereas silicalite-1 is purely formed of silica, ZSM-5 is an aluminosilicate belonging to the pentasil family [3, 4]. This zeolite crystallizes in two different forms depending on the presence of the structure-directing agent (tetra propylammonium hydroxide). Before removing the organic template, the ZSM-5 structure is orthorhombic, with a *Pnma* space group with  $a = 2.01$  nm,  $b = 1.97$  nm, and  $c = 1.31$  nm as coordinates. However, upon calcination or removal of the organic template at high temperature and when the Si/Al ratio is greater than 80, the symmetry is monoclinic ( $P2_1/n$  as a space group), and the coordinates become  $a = 1.34$  nm,  $b = 2.01$  nm and  $c = 1.99$  nm with  $\beta = 90.47^\circ$  [1]. The general formula or the crystal-chemical data of ZSM-5 zeolite is the following:



with  $n < 27$  [1].

In this work, different MFI zeolites were used. They were previously synthesized and subjected to ion-exchange to obtain their protonic and calcined at high temperatures to remove the organic templates. Silicalite-1 was synthesized using the procedure in Lakiss *et al.*'s article [5], MFI-25 from Qin *et al.*'s work [6]. However, MFI-45 was a commercial sample provided from Sudchemie (similar material to that used in Lakiss *et al.*'s work [7]). MFI-75 and MFI-38 were synthesized by the procedure in ref [8]. MFI-15, MFI-11, and MFI-10, provided by IFP, were synthesized without a template in pre-synthesized germinal zeolites and in a basic medium.

## 2. Methods

### 2.1. Characterization techniques

After the synthesis, the obtained materials are fully characterized using different techniques, including Powder X-Ray Diffraction (PXRD), Scanning Electron Microscopy (SEM), Transmission Electron Microscopy (TEM), Thermogravimetric Analysis (TGA), UV-Vis spectroscopy, gas physisorption and inductively coupled plasma spectroscopy (ICP-MS).

#### 2.1.1. Powder X-Ray Diffraction (PXRD)

Using X-rays, this technique allows us to determine the crystal structure and the purity of the crystalline material. It is based on the diffraction of a monochromatic X-ray beam in contact with the sample at an angle ( $\theta$ ) upon interactions with the planes of atoms of the material. To determine the distance  $d_{hkl}$  between the different planes in the crystalline structure, Bragg's law is applied following the below equation:

$$n\lambda = 2d_{hkl} \sin(\theta)$$

with  $n$  a positive integer,  $\lambda$  the wavelength of the incident X-Ray beam and  $d_{hkl}$  the interplanar distance (**Figure 2**).

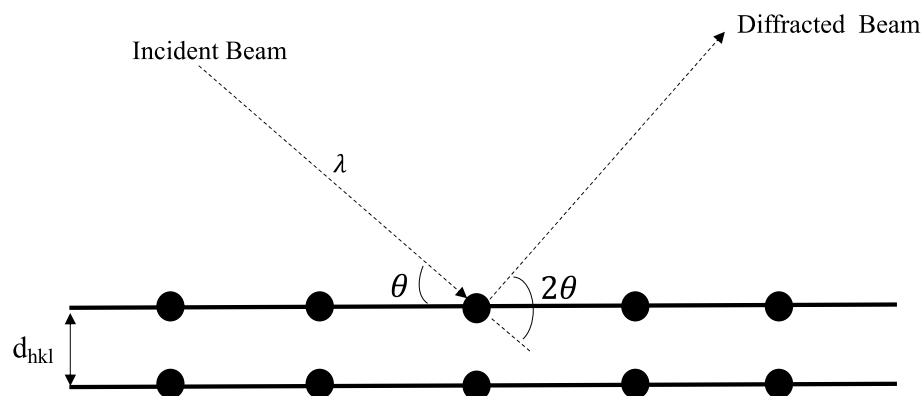


**Figure 2:** Representation of a 2D crystal lattice showing Bragg's diffraction

Ultimately, a PXRD pattern is obtained, known as the fingerprint of the structure. The pattern is used to determine the phase and the purity of the sample, its structure, the unit cell parameters, crystallinity, and size of the particles upon interpretation of the widths and the intensities of the peaks.

In the present work, PXRD patterns were recorded on a 'PANalytical X'pert Pro' diffractometer with  $\text{CuK}\alpha$  radiation ( $\lambda = 0.15443 \text{ nm}$ ). The measurements were carried out at  $2\theta$  between  $5^\circ$  and  $50^\circ$  with a step size of  $0.02^\circ$ .

### 2.1.2. Scanning Electron Microscopy (SEM)

Scanning Electron Microscopy (SEM) is used to determine the morphology and the size of the particles. An electron beam ejected from a filament interacts with the sample under vacuum and produces different signals detected on a cathode ray tube. Before SEM, the powder is mounted on a specimen holder using carbon double tape. After, the sample is coated with platinum using CRESSINGTON 108 auto evaporative coating machine. This coating is carried out to improve the electrical conductivity of the sample. SEM micrographs in this study were recorded using a TESCAN Mira field-emission scanning microscope at 30 kV.

### 2.1.3. Transmission Electron Microscopy (TEM)

This technique allows the acquisition of sample monographs at high magnification with high resolution using in-depth structural analysis. It gives additional data about the material porosity, atom arrangements, and structural defects. Unlike

SEM, TEM is based on the transmitted electrons passing through a condenser before hitting the thin layer of the sample. The sample was prepared by dispersing the powder in ethanol on a holey carbon film and coated with copper. The TEM micrographs in this work were recorded on a JEM200F cold FEG double aberration-corrected microscope equipped with a CENTURIO large-angle EDX detector.

#### 2.1.4. Thermogravimetric Analysis (TGA)

Thermogravimetric analysis is carried out to study the thermal stability of the sample and determine the loading of organic compounds. This technique measures the weight change as a function of the time or/temperature. In this work, the sample weight change is evaluated as a function of time and temperature using a SETSYS 1750 CS evolution instrument. Before conducting the study, around 10-15 mg of the powder was placed in an alumina crucible and loaded later into the analyzer chamber. The sample was heated from 30 °C to 800 °C with a heating ramp of 10 °C.min<sup>-1</sup> under a flow of air (40 mL.min<sup>-1</sup>).

#### 2.1.5. UV-Vis spectroscopy

This technique is used to determine the characteristic bands of the material upon absorbance of the UV-Visible light. In this work, UV-Vis measurements were performed with a Cary 4000 (Varian) spectrophotometer in the spectral range between 200 and 400 nm. The spectrophotometer is equipped with a Praying Mantis diffuse reflection accessory.

#### 2.1.6. Gas Physisorption

Generally, gas adsorption is used to study the physical adsorption and textural characterization of porous materials. It is based on the adsorption of inert gases such as nitrogen, argon, and CO<sub>2</sub> at cryogenic temperatures over a range of pressures. During the physisorption process, Van der Waals forces are the only involved forces since the interactions occur between the surface of the adsorbent and gas molecules. The process begins with the outgassing of the sample to remove physically adsorbed molecules. The degassing procedure is followed by a gradual increase of the partial pressure to finish with its decrease. The adsorption/desorption isotherms are

represented as the quantity of the adsorbed gas as a function of the relative pressure. Five types of adsorption/desorption isotherms specific to every type of porous material are characterized according to the Brunauer classification and represented in **Figure 3** [9].

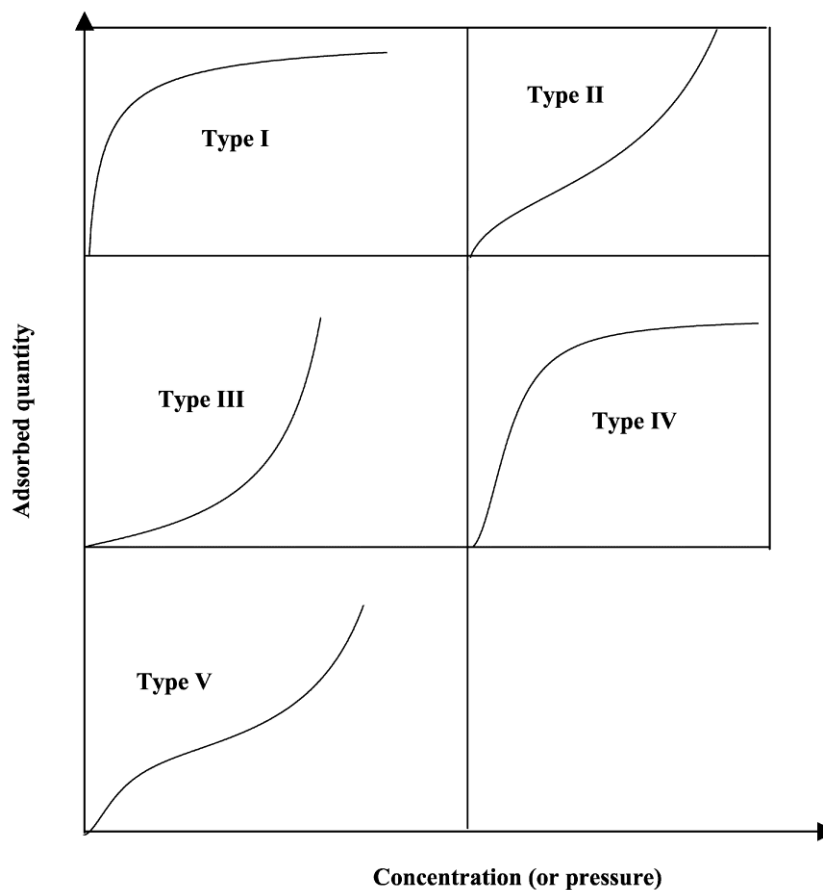


**Figure 3:** Adsorption isotherms according to Brunauer classification. Reprinted with permission from ref [9]. Copyright 2003 Journal of colloid and interface science.

Type (I) isotherm is characteristic of microporous materials like zeolites with pore width  $< 0.7$  nm and  $0.7-2$  nm. This isotherm is recognized as Langmuir adsorption isotherm. Type (II) and Type (III) occur on macro-porous materials where a multi-layer surface governs the adsorption. Isotherms of type (IV) are common for materials with a pore greater than the diameter of the adsorbed molecule. These isotherms are observed for mesoporous materials. Finally, type (V) isotherms represent typical layer-by-layer adsorption on non-porous materials. This type is comparable to type III at low pressures where weak interactions are present. Upon the adsorption/desorption processes, the surface area of the particles can be determined using the Brunauer-Emmet-Teller method and the size and volume of the pores.

In this study, nitrogen adsorption/desorption isotherms were measured using Micrometrics ASAP 2020 volumetric adsorption analyzer. Around 100 mg of the powder was degassed at 350 °C and 150 °C, depending on the sample, under vacuum overnight (for 12 hours) before measurement. The external surface area ( $S_{\text{ext}} / \text{m}^2\text{g}^{-1}$ ) and micropore volume ( $V_{\text{mic}} / \text{cm}^3\text{g}^{-1}$ ) were estimated by the t-plot method based on the Harkins-Jura equation using Silica-1000 ( $22.1 \text{ m}^2\text{g}^{-1}$  assumed) as a reference.

#### 2.1.7. Inductively coupled plasma spectroscopy (ICP-MS)

Elemental analyses are conducted by atomic emission using an inductively coupled plasma spectroscopy combined with mass spectrometry (ICP-MS). This analysis aims to determine the exact amount of every element in the sample. The quantitative determination is measured by the excitation of the element in the presence of argon and hot plasma. The excited sample emits wavelengths characteristic of each element in the visible or ultraviolet region. The intensity of the emitted light is proportional to the concentration of each element. The specific importance of this technique is its extensive use to determine the Si/Al ratio for zeolites. 50 mg of the powder was dissolved in a mixture of aqua regia ( $\text{HCl}+\text{HNO}_3$ ) and hydrofluoric acid (HF) at 90 °C. The HF was then neutralized using boric acid ( $\text{H}_3\text{BO}_4$ ). The mass spectrum of the diluted analyte solution was recorded after ionizing the solution with a high-energy Ar-plasma.

#### 2.2. FTIR Spectroscopy

FTIR spectroscopy is based on the Fourier transformation of a detected signal into a spectrum. The detected signal results from irradiating a sample with an infrared beam. Once the beam is emitted, it passes through two mirrors forming the interferometer, then into a sample compartment to reach a detector. Upon its irradiation, the material adsorbs the infrared radiation, which is of the same frequency as its natural vibration frequency. Thus, molecules will undergo vibrational transition from a low energy state to a higher energy state and vibrates with an increased amplitude. The vibrations of the molecule are visualized in two different modes: stretching and bending. Stretching vibration modes are characterized by the change of the bond length between the atoms, whereas bending vibration modes change the angle between two bonds [10]. Similarly to other spectroscopic techniques, FTIR

spectroscopy allows us to study the physicochemical properties of the material and provides information about its chemical composition. Remarkably, FTIR spectroscopy enables quantitative and qualitative analyses from spectral data. A quantitative analysis is possible by linking the spectral changes to the measured adsorbed quantities of an adsorbate. The qualitative analysis can be conducted by monitoring the minor changes in the spectrum of the material to understand its chemical or physical behavior. Several FTIR techniques were developed for these purposes, such as *in-situ* FTIR and *Operando* FTIR.

### 2.2.1. In-situ FTIR

*In-situ* FTIR spectroscopy allows us to measure the surface properties of the zeolite or any other catalyst. For zeolitic materials, these properties are condensed in the basicity, acidity of the zeolite, and diffusion and accessibility through their pores. These properties can be determined qualitatively and quantitatively by the adsorption of probe molecules such as pyridine, CO, CO<sub>2</sub>, alcohols, and many others. The probe molecules can interact with adsorption sites on the surface of the zeolite to determine the strength and density of the adsorption site.

The *in-situ* FTIR system used in this work is formed of three compartments represented in **Figure 4**: the IR cell, the evacuation system, and the spectrometer [11].

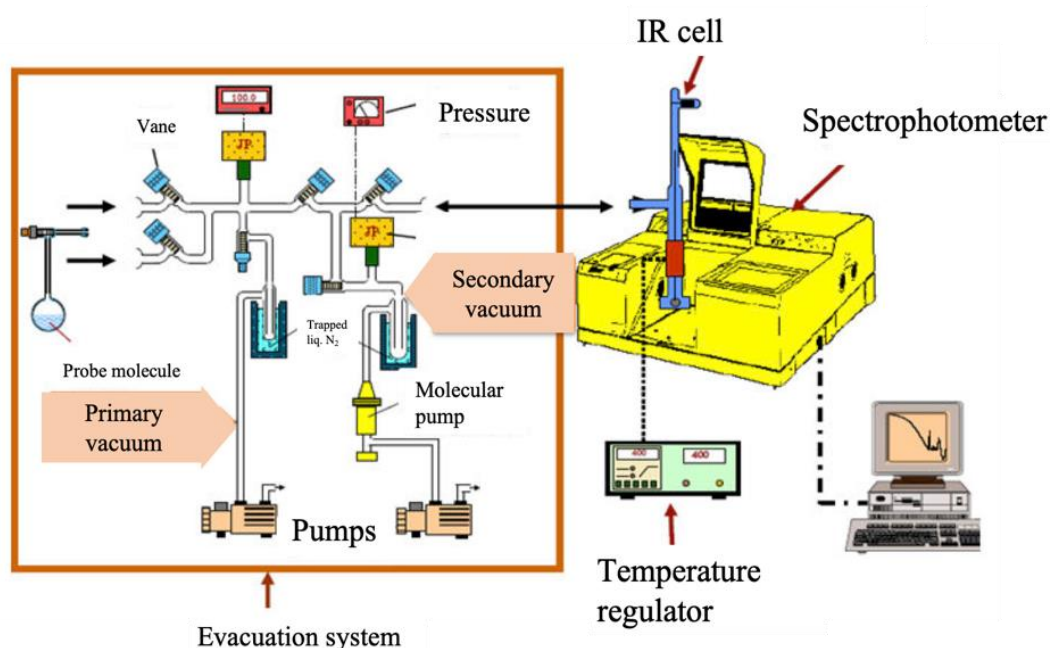


**Figure 4:** Scheme of the *in-situ* FTIR system.

The IR cell is designed to allow the *in-situ* activation of the sample. It is formed of two parts: the lower one with two KBr windows and the upper part made of Pyrex with the connections to the evacuation system and the connections for the entrance of a specific dose of the probe molecule. The sample is attached to a movable sample holder in quartz that passes through the cell. A magnet is placed on its top to assure its mobility. This movable feature allows us to place the sample at the same level as the oven equipped on the IR cell. This cell is connected to the evacuation system using a big vane to guarantee a fast evacuation. Next to this vane, two small others connected to the cell delimit a small known volume. This volume permits introducing a known amount of probe molecules (**Figure 5**).

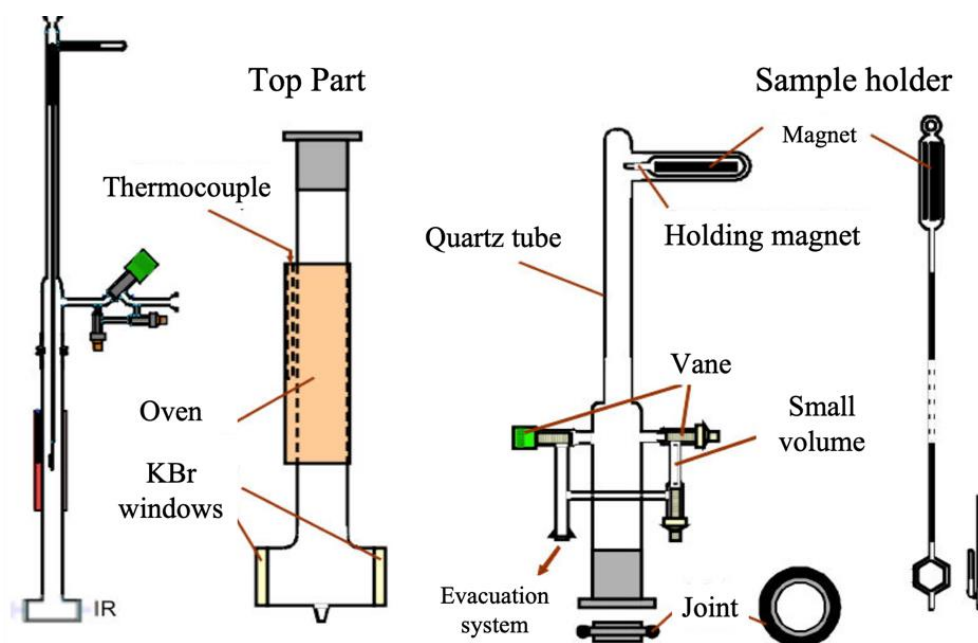


**Figure 5:** Scheme of the in-situ IR cell.

As for the evacuation system, it assures a vacuum in the IR cell below  $10^{-3}$  Pa. It also allows the introduction of probe molecules in the IR cell and their evacuation via its connection to a pump system. Two vacuum systems are established using two different pumps: the primary vacuum via a primary pump decreasing the pressure below 1 Pa and the secondary vacuum, established after decreasing the pressure to  $10^{-5}$  Pa. Spectra were recorded on a Nicolet 6700 IR spectrophotometer equipped with a DTGS detector and were collected in the region between 400 and  $5500\text{ cm}^{-1}$  by 128 scans with a resolution of  $4\text{ cm}^{-1}$ . Before recording the spectra, the powder was pressed in a self-supported disk ( $S = 2.0\text{ cm}^2$ ,  $m \sim 20\text{ mg}$ ) and subjected to *in-situ*

activation to remove the adsorbed water and other impurities. The activation of zeolites was conducted at 400 °C for 5 hours (0.8 °C.min<sup>-1</sup>); however, zeolitic core-shell materials were activated at 150 °C (2 °C.min<sup>-1</sup>) for 1 hour under vacuum (around 10<sup>-5</sup> Torr). After activation, the sample was cooled down to room temperature under vacuum, and its IR spectrum was recorded. This step was followed by introducing the probe molecule in small doses through the calibrated and calculated volume. In this study, different probe molecules were used (pyridine and collidine) to determine the pore accessibility and their acidity of the zeolites. Pyridine and collidine adsorption were conducted at 150 °C to optimize the diffusion of the probe molecules in the porosity. After establishing a pressure of 1 Torr at the equilibrium of each adsorbate, the cell was evacuated at 150 °C for pyridine, and at 100 °C for collidine to remove all physisorbed species. Thermal programmed desorption was also conducted after the evacuation of the pyridine at different increasing temperatures, from 150 °C to 350 °C.

A new automated cell, the PELICAEN cell, developed at the LCS was also used in this work (**Figure 6**). It is developed to control the temperature of the sample better and automate the main functions e.g. change of the sample position from the oven to the IR beam. The cell is formed of quartz, and the sample holder is designed with a platinum wire. The activation of the pellet is assured by a tubular furnace (ERALY France). A thermocouple is added inside the cell, near the sample to control its temperature under vacuum. An internal gauge is added to the standard IR cell to measure the internal pressure of the chamber. The PELICAEN cell is connected to vacuum system, and the probe molecules are added via a small calibrated volume, similar to the standard IR cell previously described.

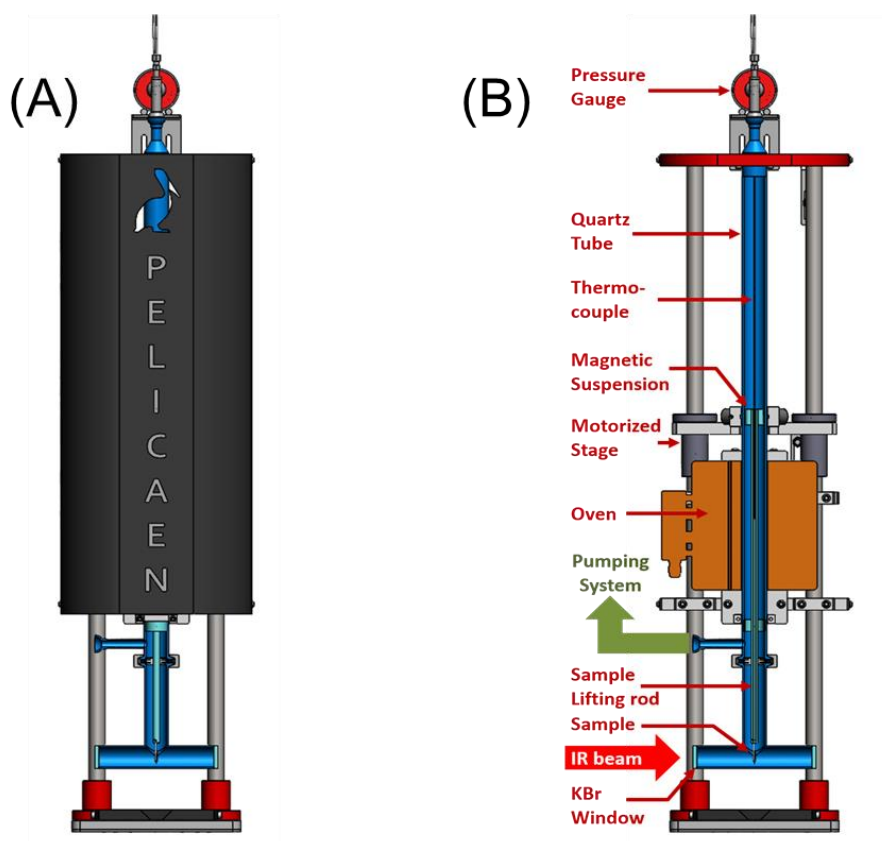


**Figure 6:** Schematic representation of the PELICAEN cell

### 2.2.2. AGIR experiments

AGIR is a technique developed in the laboratory by Bazin *et al.*, based on coupling thermogravimetry analysis with IR [12]. It allows us to quantitatively and qualitatively determine the adsorbed species on the catalyst's surface using TG and operando IR. Therefore, the mass of the adsorbed species and the IR spectra are recorded simultaneously in a gas flow system. The apparatus, presented in **Figure 7**, is formed of a SESTYS-B microbalance from SETARAM connected to an IR cell or operando reactor. The balance is continuously flushed with a gas flow to prevent its pollution. Its mobility is assured using a telescopic column to lift the sample holder upon its loading. The change in mass is recorded with an accuracy up to 0.1  $\mu\text{g}$ . As for the operando reactor, it is a stainless-steel cylinder holding in its center a self-supported wafer of 16 mm, and  $\sim 20$  mg (**Figure 7**). The sample is perpendicular to the IR beam, penetrating the reactor through KBr windows. The system is equipped with a thermocoax heating wire, allowing heating of the sample at a temperature up to 773 K. The overall structure is fed with a gas flow monitored by mass flow regulators.

The gas flow is analyzed on its exit using a Pfeiffer mass spectrometer (OMNISTAR GSD 301) to ensure the steady-state of the adsorbate in the gas phase.

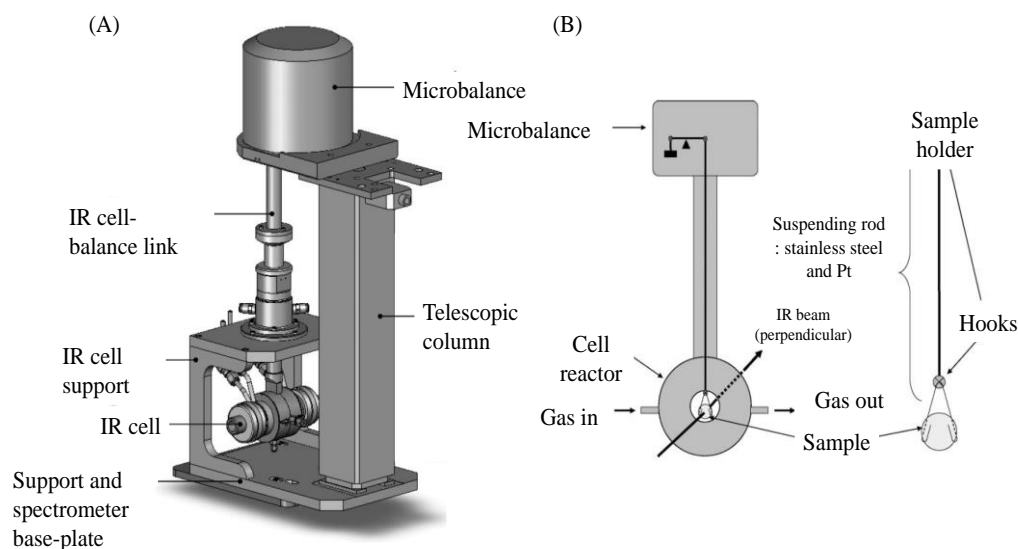


**Figure 7:** Schematic figures of (A) the AGIR system and (B) the sample holder in this setup. Reprinted with the permission of ref [12].

In this work, the AGIR setup was used to determine the molar absorbance coefficients  $\varepsilon$  of the adsorbed ethanol and water. It was applied to evaluate these adsorbates versus their partial pressures at room temperature. For this aim, self-supported wafers of zeolites ( $\sim 20$  mg,  $S = 2.0$  cm<sup>2</sup>) were prepared, mounted in the AGIR setup, and preheated at 400 °C for at least 5 hours under a mixed flow of oxygen and argon. The heating temperature is reached at a rate of 0.5 °C/min. After activation, the temperature is decreased to room temperature (25 °C) at a rate of 6 °C/min. Once reached, the setup was fed with the required adsorbate flow. Self-supported pellets of the core-shell hybrid materials were also prepared and mounted in the AGIR apparatus and activated at 150 °C (2 °C.min<sup>-1</sup>, 1 hour) prior to the adsorption of water or ethanol. The mass of the sample and the IR data were simultaneously recorded until reaching equilibrium. IR spectra (64 scans at a resolution of 4 cm<sup>-1</sup>) were collected using a Nicolet 6700 spectrometer outfitted with a liquid nitrogen cooled MCT detector (mercury, cadmium, and tellurium detector). Once the adsorption isotherm was completed, the spectra at the equilibrium of each concentration were subtracted from the gas phase spectrum of the added specie. This subtraction is followed by another one from the initial spectrum of every zeolite after activation before adding

any adsorbate. The areas of the specific bands were therefore measured. Simultaneously, the recorded mass changes were transformed into the quantities of the adsorbed species. Consequently, the law of Beer-Lambert, describing the relation between the absorbance and the concentration of the adsorbed species, can be easily applied to determine the molar absorption coefficients for ethanol and water adsorbed on the different zeolites used (equation below):

$$A = \varepsilon \cdot l \cdot c = \varepsilon \cdot l \cdot \frac{n}{V} = \varepsilon \cdot l \cdot \frac{n}{S \cdot l} = \varepsilon \cdot \frac{n}{S}$$

with  $A$  ( $\text{cm}^{-1}$ ) the area of the band at a certain wavenumber,  $\varepsilon$  is the molar absorption coefficient ( $\text{cm} \cdot \mu\text{mol}^{-1}$ ),  $c$  ( $\mu\text{mol} \cdot \text{L}^{-1}$ ) the concentration of the adsorbate,  $V$  ( $\text{cm}^3$ ) the volume of the wafer,  $l$  (cm) the optical pathway,  $S$  is the surface of the wafer ( $S = 2.0 \text{ cm}^2$ ), and  $n$  ( $\mu\text{mol}$ ) is the number of moles of the adsorbate.

### 2.2.3. CARROUCELL experiments

After determining the molar absorption coefficients  $\varepsilon$  of the adsorbed ethanol and water separately at room temperature, further IR experiments were carried out using the CARROUCELL system. This system is a sophisticated in situ cell where 12 samples can be mounted in a vacuum system (**Figure 8**) [13]. A remarkable advantage of this setup is that it facilitates running the experiments of more than one sample at once and facilitates the comparison between samples because they are all in the same environmental chamber (true identical conditions). The setup is connected to a Thermo iS50 FTIR spectrometer equipped with an MCT detector. A gas flow setup was added to the cell to assure the entrance of the gas mixtures introduced in the environmental chamber and to ensure the steady-state of the adsorbate in the gas phase. Analogously to the AGIR, the gas flow was analyzed at its exit by a mass spectrometer (Pfeiffer Omnistar GSD 301).

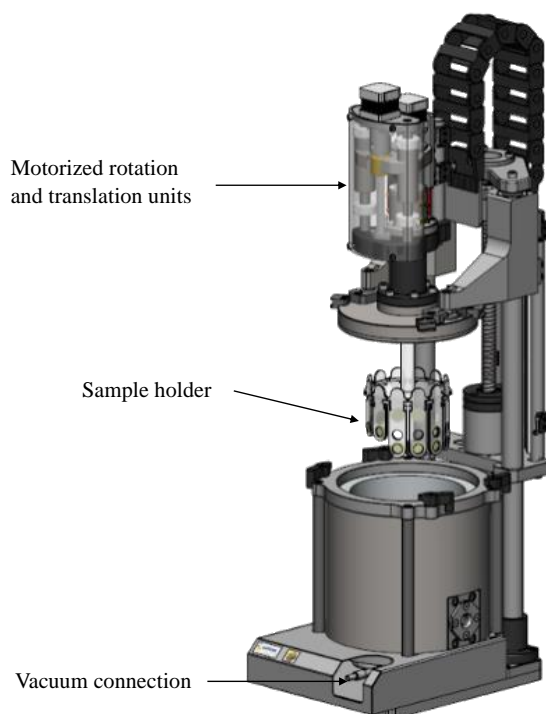


**Figure 8:** Schematic figure of the CARROUCELL setup. Reprinted with the permission of ref [13].

In the present study, 10 different zeolites with different structures and different Si/Al ratios were prepared in a self-supported pellet ( $m = 20\text{--}25\text{ mg}$ ,  $S = 2.0\text{ cm}^2$ ) and mounted in the CARROUCELL. The eleventh position is left vacant for recording the background, and a  $\text{BaSO}_4$  pellet is positioned at the level of the twelfth position to evaluate the exact temperature of the samples (shift of a temperature-sensitive band around  $1960\text{ cm}^{-1}$ ). IR spectra were collected (64 scans/ $4\text{ cm}^{-1}$  resolution) before activating the samples, at room temperature after their activation, and upon the introduction of the desired adsorbate concentration. The activation program was similar to that used during AGIR experiments: under a flow of a mixture of argon and oxygen (80/20), at a rate of  $0.5\text{ }^\circ\text{C}/\text{min}$ , the activation temperature ( $400\text{ }^\circ\text{C}$ ) was reached and maintained for at least 5 hours, and then decreased to room temperature at a rate of  $6\text{ }^\circ\text{C}/\text{min}$ . Later, a fixed flow of either water or ethanol was introduced, and when equilibrium was reached, various other gas flows were introduced to obtain two-dimensional cartography of ethanol/water (gas) vs. ethanol/water adsorbed on the different zeolites. The spectra taken at equilibrium were subtracted from the reference spectrum, the one after activation and before introducing any gas. Interestingly, using this technique, the gas phase was directly subtracted since it is possible to take its spectrum before recording the spectral data of the experiment.

## References

1. Baerlocher, C., L.B. McCusker, and D.H. Olson, *Atlas of zeolite framework types*. 2007: Elsevier.
2. IZA. *International Zeolite Association*. 2019; Available from: <http://www.iza-structure.org>.
3. Flanigen, E.M., et al., *Silicalite, a new hydrophobic crystalline silica molecular sieve*. *Nature*, 1978. **271**(5645): p. 512-516.
4. Argauer, R.J. and G.R. Landolt, *Crystalline zeolite ZSM-5 and method of preparing the same*. 1972, Google Patents.
5. Lakiss, L., et al., *Effect of stabilizing binder and dispersion media on spin-on zeolite thin films*. *Thin solid films*, 2010. **518**(8): p. 2241-2246.
6. Qin, Z., et al., *Comparative study of nano-ZSM-5 catalysts synthesized in OH<sup>-</sup> and F<sup>-</sup> media*. *Advanced Functional Materials*, 2014. **24**(2): p. 257-264.
7. Lakiss, L., et al., *On the remarkable resistance to coke formation of nanometer-sized and hierarchical MFI zeolites during ethanol to hydrocarbons transformation*. *Journal of Catalysis*, 2015. **328**: p. 165-172.
8. Jolly, S., et al., *Reaction mechanisms and kinetics in the n-hexane cracking over zeolites*. *Applied catalysis A: general*, 1997. **156**(1): p. 71-96.
9. Khalfaoui, M., et al., *New theoretical expressions for the five adsorption type isotherms classified by BET based on statistical physics treatment*. *Journal of colloid and interface science*, 2003. **263**(2): p. 350-356.
10. Griffiths, P.R. and J.A. De Haseth, *Fourier transform infrared spectrometry*. Vol. 171. 2007: John Wiley & Sons.
11. Le Guillouzer, C., *Etude spectroscopique de membranes à matrice mixte polymère/MOF pour la séparation CO<sub>2</sub>/N<sub>2</sub>*. 2017, Normandie.
12. Bazin, P., A. Alenda, and F. Thibault-Starzyk, *Interaction of water and ammonium in NaHY zeolite as detected by combined IR and gravimetric analysis (AGIR)*. *Dalton Transactions*, 2010. **39**(36): p. 8432-8436.
13. Zholobenko, V., et al., *Probing the acid sites of zeolites with pyridine: Quantitative AGIR measurements of the molar absorption coefficients*. *Journal of Catalysis*, 2020. **385**: p. 52-60.





## CHAPTER THREE

---

Quantitative IR study of ethanol/water  
coadsorption on MFI zeolites with different  
Si/Al ratios

---



## **Quantitative IR study of ethanol/water coadsorption on MFI zeolites with different Si/Al ratios**

Rita Zakhia Douaihy <sup>a</sup>, Louwanda Lakiss <sup>a</sup>, Mohamad EL-Roz<sup>a</sup>, Alexandre Vimont <sup>a,\*</sup>,  
Philippe Bazin <sup>a</sup>.

<sup>a</sup> Normandie Université, ENSICAEN, UNICAEN, CNRS, Laboratoire Catalyse et Spectrochimie, 14050 Caen, France

## Abstract

Advanced IR vibrational spectroscopic techniques, e.g., coupled gravimetric-IR surface analyzer (AGIR) and high-throughput in-situ IR cell (CARROUCELL), have been used for the quantitative studies of the adsorption and co-adsorption of ethanol and water on MFI zeolites with different Si/Al ratios. At low partial pressures, the unary water adsorption experiments suggest that the amount of adsorbed water results mainly from the preferential adsorption on Bronsted acid sites in tetrameric clusters. By contrast, adsorption of EtOH occurs on both silanol groups and Bronsted acid sites (BAS), while the effect of the Si/Al ratio is only observed at relatively low partial pressures. The molar absorption coefficients of adsorbed ethanol and water were determined and found to be independent of the Si/Al and are not affected during the coadsorption of ethanol and water. Their use allows to obtain the exact quantity of each adsorbate specie in the binary system. The effect of the Si/Al ratio on the ethanol adsorption capacity is also investigated and directs the choice of the separation membrane for ethanol purification.

## 1. Introduction

The recent energy and climate crisis have pushed researchers to find alternatives for fossil fuels [1]. Countries have shifted to environmentally friendly and more efficient biofuels to minimize the extraction of fossil fuels and greenhouse gases [2, 3]. Among the various biofuels and bio-alcohols, bioethanol has gained significant interest due to its presence in the liquid phase, its use as a partial replacement for gasoline, and its facile transportation [4-6]. It can be produced from different sources ranging from food renewable sources such as corn starch and sugarcane to non-food renewable sources, including the organic fraction of municipal solid waste and lignocellulosic biomasses [7, 8]. Several techniques are applied to synthesize bioethanol, yet the main challenge is separating ethanol from ethanol/water mixture [9]. Bioethanol should be anhydrous to be used as a replacement for gasoline [6, 10]. On an industrial scale, conventional distillation and separation processes are considered costly, energy, and time-consuming due to the necessity to overcome the azeotrope barrier [11]. Therefore, other separation methods (pervaporation [12], etc.) were elucidated to separate the ethanol-water mixture beyond the azeotropic mixture based on the adsorption on porous materials [10, 13]. Among them, zeolites are excellent candidates. They are used in catalysis, adsorption, and separation of gaseous mixtures and biotechnologies [14-16], due to their high tunable porosities, tunable characteristics, and high chemical and thermal stabilities [14, 17]. Adsorption of ethanol (EtOH) on zeolitic materials has been extensively studied using experimental or theoretical approaches [10, 18-27]. Silica zeolites with high silica contents present high selectivity for alcohols towards the water, contrary to zeolites with higher alumina content [21, 28]. Then, MFI zeolites have attracted attention due to the possibility of varying the aluminum content easily during the synthesis, allowing for tuning the hydrophobic/hydrophilic properties [29]. The organophilic nature of MFI zeolites was confirmed by Gómez-Álvarez *et al.* [30] and Zhang *et al.* [31]. They concluded that no matter the Si/Al ratio of the MFI zeolites, the same behavior towards ethanol was observed. This was not the case when adsorbing water, where water uptake decreased with the increase of the Si/Al ratio [32]. Experimental data relative to co-adsorption experiments (selectivity) are scarce [30]. Different techniques were implemented to study the adsorption and coadsorption of water and/or ethanol, such

as volumetric and gravimetric measurements and pulsed-field gradient (PFG)-nuclear magnetic resonance (NMR) [31, 33-35]. They necessitate long-time data acquisitions and quantifying each adsorbate during their coadsorption could be very challenging. Few studies reported the use of IR spectroscopy [36, 37]. In fact, IR spectroscopy can be used to determine the nature and the quantities of the adsorbed species when coupled with gravimetric analyses [13, 38].

The aim of this work is to study quantitatively the adsorption and co-adsorption of ethanol and water vapors on a series of MFI zeolites with various Si/Al ratios (from 10 to infinite (silicalite)) using (i) home-made coupled IR- gravimetry apparatus (namely AGIR) and a new multi-sample (10 samples) in situ cell (namely CARROUCELL). This latter allows us to obtain *in a reasonable time-acquisitions* some sets of quantitative co-adsorption data for large water and ethanol vapor phase concentrations ( $P/P_0=0.006-0.65$ ).

## 2. Experimental section

### 2.1. Materials

A series of MFI zeolites with different Si/Al ratios was used in this work. The MFI-X systematic notation was used to name the zeolitic materials with X for the Si/Al molar ratio. Silicalite-1 was provided by Lakiss *et al.* and synthesized according to the procedure in reference [39]. MFI-75 and MFI-38 were synthesized according to ref [40]; MFI-45 was a commercially synthesized zeolite by Clariant (formerly Süd Chemie), MFI-25 from Qin *et al.*'s work [41]. MFI-15, MFI-11, and MFI-10 were provided by IFP, synthesized without the template, in the presence of pre-synthesized germinal zeolites and in a basic medium, respectively.

### 2.2. Characterization techniques:

The PXRD patterns of the zeolites were recorded on a PANalytical X'Pert Pro diffractometer with an average Cu K $\alpha$  radiation ( $\lambda = 1.5418 \text{ \AA}$ ). The  $\theta$ - $2\theta$  scans were recorded in the range of  $2\theta$  between  $5^\circ$  and  $50^\circ$  and a step size of  $\sim 0.0167$ . The main characteristic peaks of the MFI structure are present on all the patterns without any additional peaks, confirming the purity of the samples.

The Si/Al ratio was determined from the elemental analysis using inductively coupled plasma spectroscopy coupled with mass spectrometry. The powder was dissolved in a mixture of aqua regia (HCl+HNO<sub>3</sub>) and hydrofluoric acid (HF) at 90 °C. HF was then neutralized using boric acid (H<sub>3</sub>BO<sub>4</sub>). The mass spectrum of the diluted analyte solution was recorded after ionizing the solution with a high-energy Ar-plasma.

Nitrogen sorption isotherms at 77 K have been recorded on Micrometrics ASAP 2020 volumetric adsorption analyzer after degassing the samples at 350 °C for 12 hours. The specific surface areas are determined from the BET equation. The total pore volumes and the external surface areas are calculated from the *t*-plot method.

The morphology of zeolite crystals was investigated using scanning electron microscopy (SEM). SEM images were recorded on a TESCAN Mira field-emission scanning microscope at 20 kV. Before recording the images, the powder was dispersed on carbon tape and coated with platinum.

### 2.3. In situ IR Spectroscopy:

Self-supported pellets of pressed powder of each zeolite (~20 mg, 10<sup>7</sup> Pa/cm<sup>2</sup>, S = 2.0 cm<sup>2</sup>) are mounted in an in-situ IR cell equipped with KBr windows connected to a Nicolet 6700 IR spectrophotometer. The spectrometer is equipped with a DTGS detector and an extended-KBr beam splitter. IR spectra were recorded in the region between 400 and 5500 cm<sup>-1</sup> with a resolution of 4 cm<sup>-1</sup> and 128 scans/spectrum [38]. The in-situ IR cell used in this work is the PELICAEN cell which is the latest version developed by the LCS laboratory to improve sample temperature control and automate the main functions (change of positions of the sample from the oven to the IR beam, acquisition of the IR spectra). The PELICAEN is mainly made of quartz. The sample holder is designed with a platinum wire. The heating system (up to 700 °C) is a tubular furnace from ERALY (France). A thermocouple is positioned inside the cell near the sample to perfectly control its temperature, particularly when placed under a vacuum (low thermal conductivity condition). An additional gauge is added to the IR cell to precisely measure the pressure inside the chamber. For the IR spectroscopic evaluation of the properties of porous materials, the addition of probe molecules can also be done gradually and quantitatively via a small calibrated volume (approximately 2.0 cm<sup>3</sup>) positioned at the front side of the cell. The PELICAEN cell is connected to the vacuum apparatus to treat the sample and introduce the gaseous phase when

necessary. In this work, zeolites were activated at 400 °C (heating rate 2 °C.min<sup>-1</sup>) under a vacuum (around 10<sup>-5</sup> Torr) for 5 hours.

#### 2.4. Determination of the molar absorption coefficients of adsorbed ethanol and water:

The AGIR technique allows to measure the gravimetric data and records the corresponding IR spectra simultaneously [13, 38, 42]. Therefore, the AGIR is very well suited to evaluate the molar absorption coefficients of the bands associated with the vibration modes of the adsorbed molecules. Note that these coefficients are essential for quantitative investigations. The setup is connected to a mass spectrometer to monitor the outlet flow of the adsorbates in the gas phase (Pfeiffer Omnistar GSD301). The experiments were conducted on a self-supported pellet of the pressed powder of the adsorbent (~20 mg, 10<sup>7</sup> Pa/cm<sup>2</sup>, S = 2.0 cm<sup>2</sup>), previously activated at 400 °C (heating rate 0.6 °C. min<sup>-1</sup>) under a gas flow (20 cm<sup>3</sup>.min<sup>-1</sup>) of a mixture of argon and oxygen (20 %). IR spectra were recorded using a Nicolet 6700 spectrometer outfitted with liquid nitrogen cooled MCT detector (mercury, cadmium, and tellurium detector) at a resolution of 4 cm<sup>-1</sup> in the spectral region between 600 cm<sup>-1</sup> and 6000 cm<sup>-1</sup>. The mass of the sample was recorded using a microbalance (accuracy= 0.1 µg), and the corresponding IR spectra were registered after the equilibrium state of H<sub>2</sub>O and EtOH concentration. The steady-state was determined by both the absence of change in mass and the intensity of the characteristic band of each adsorbate.

#### 2.5. Adsorption and coadsorption of ethanol and water using the CARROUCELL high-throughput IR cell:

To reduce the experimental time drastically due to the high number of samples and different partial pressure points of H<sub>2</sub>O and C<sub>2</sub>H<sub>5</sub>OH, the coadsorption measurements were carried out on the CARROUCELL apparatus [38]. This sophisticated IR apparatus developed in the laboratory allows us to do the same experimental conditions on twelve samples simultaneously (all samples are positioned in the same analysis chamber). The setup is formed of an *in-situ* IR cell, attached to a vacuum system, and adapted for 12 samples of self-supported pellets formed of a pressed powder (~20 mg, 10<sup>7</sup> Pa/cm<sup>2</sup>, S = 2.0 cm<sup>2</sup>). The background and the gas phase spectra are recorded between each sample and are automatically subtracted. In this work, CARROUCELL is adapted for experiments under gas flow, so

experimental conditions are similar to that of the AGIR setup. Upstream of the adsorption sequences, the zeolites are activated at 400 °C under an argon flow. At first, a water concentration was introduced to the cell at RT, followed by the adsorption of increasing ethanol concentrations after reaching equilibrium. The equilibrium after ethanol and water adsorption is determined between two consecutive IR spectra, where no change in the characteristic vibrational bands of the adsorbates is observed. The coadsorption experiments were conducted at 25 °C at different water concentrations, ranging between  $P/P_0 = 0.016$  and 0.64. As for the partial pressure of ethanol, it increases from 0.006 to 0.65.

### 3. Results and discussion

#### 3.1. Structural and textural properties:

The textural porosities of the zeolites are investigated using nitrogen adsorption/desorption and are summarized in **Table 1** after determining their Si/Al ratio and confirming their purity from the PXRD patterns (**Figure S1 (A)**). The  $N_2$  isotherms are represented in **Figure S1 (B)** and correspond to type I isotherms, characteristic of microporous zeolites [43]. The BET surface areas and the micropore volumes of the different zeolites vary in the same range. Zeolites are then characterized using IR spectroscopy, and the corresponding IR spectra are represented in the stretching OH spectral region of the between 3800 and 3500  $cm^{-1}$  (**Figure S2**). Two major peaks are observed : the first  $\nu_{OH}$  band at 3744  $cm^{-1}$  corresponds to the silanol groups located on the outer surface of the crystallite [44]. The second, situated at 3610  $cm^{-1}$  and absent in the IR spectrum of Silicalite-1 (**Figure S2**, spectrum (a)), is attributed to structural bridged Si(OH)Al, namely Bronsted acid sites (BAS) [45]. The absence of an additional vibrational band near 3665  $cm^{-1}$  indicates that no vibrations of the OH groups bound to the extra-framework Al species are present [46, 47].

Moreover, the morphology of the crystals is determined using scanning electron microscopy. SEM images (**Figure 1**) reveal aggregation of nanospheres of a size ranging between 30 to 100 nm for all zeolites. The SEM image of MFI-11 shows an agglomeration of nano-sheets of less than 100 nm.

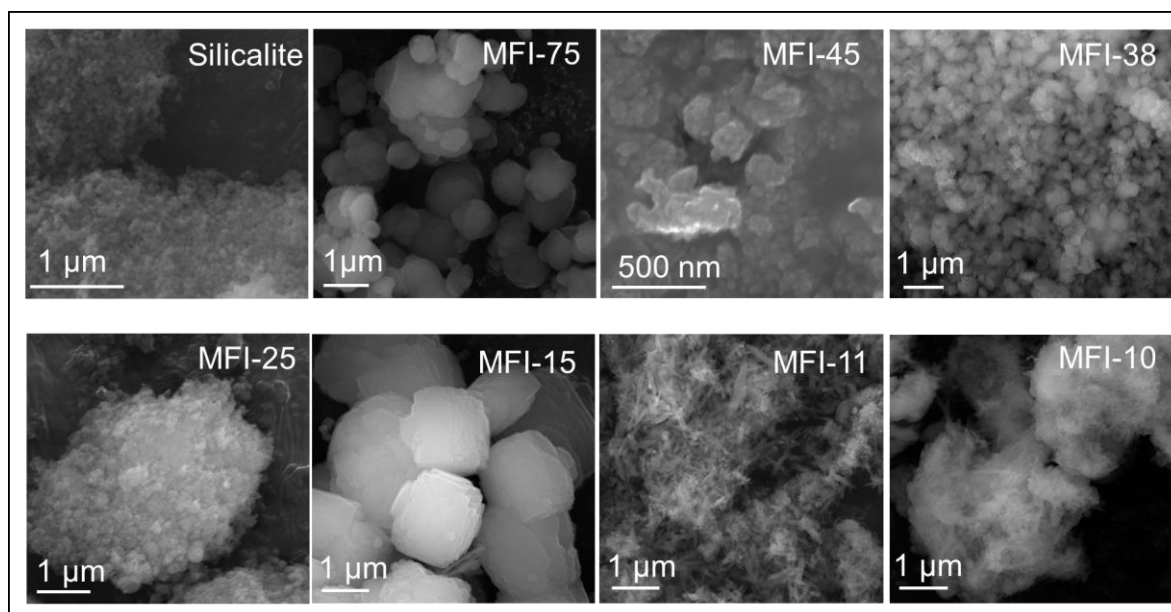


**Figure 1:** SEM images for the MFI zeolites with different Si/Al ratios.

**Table 1:** Si/Al ratio determined by elemental analysis and textural properties of different MFI zeolites tested by N<sub>2</sub> adsorption/desorption at 77 K.

	Silicalite	MFI-75	MFI-45	MFI-38	MFI-25	MFI-15	MFI-11	MFI-10
Si/Al ratio	∞	75	45	38	25	15	11	10
S <sub>BET</sub> <sup>a</sup> (m <sup>2</sup> /g)	502	421	452	423	475	413	444	401
External surface area <sup>b</sup> (m <sup>2</sup> /g)	138	76	77	89	123	29	57	42
Micropore volume <sup>c</sup> (cm <sup>3</sup> /g)	0.158	0.157	0.153	0.155	0.156	0.166	0.162	0.150

<sup>a</sup> BET surface area, <sup>b,c</sup> *t*-plot.

### 3.2. Accessibility of acid sites:

The concentrations of both Bronsted and Lewis acid sites have been determined from Pyridine adsorption for each zeolite. An excess of Pyridine sufficient to neutralize all acid sites was established in the IR cell at 150 °C (1 Torr at equilibrium pressure), followed by an evacuation (secondary vacuum) at the same temperature to remove the gaseous and physisorbed probe molecules. Finally, the corresponding spectra were recorded at RT to determine the number of acidic sites of each zeolite using the area of the 1547 cm<sup>-1</sup> band of pyridinium ions (Bronsted) and the 1455 cm<sup>-1</sup> band of Pyridine coordinatively bonded to Lewis sites by applying their respective

molar absorption coefficients. The subtraction spectra (before and after Pyridine adsorption) are represented in **Figure 2 (A)** in the spectral region between 1700 and 1400  $\text{cm}^{-1}$ . The quantities of adsorbed  $\text{PyH}^+$  and  $\text{PyL}$  formed on the acidic sites are summarized in **Table 2** using the calculated molar absorption coefficients for each type of MFI zeolite. The number of BAS is plotted as a function of the number of Al calculated per unit cell (**Figure 2 (B)**). The amount of Bronsted (BAS) and Lewis acid sites clearly increases proportionally with the number of the Al content per unit cell.

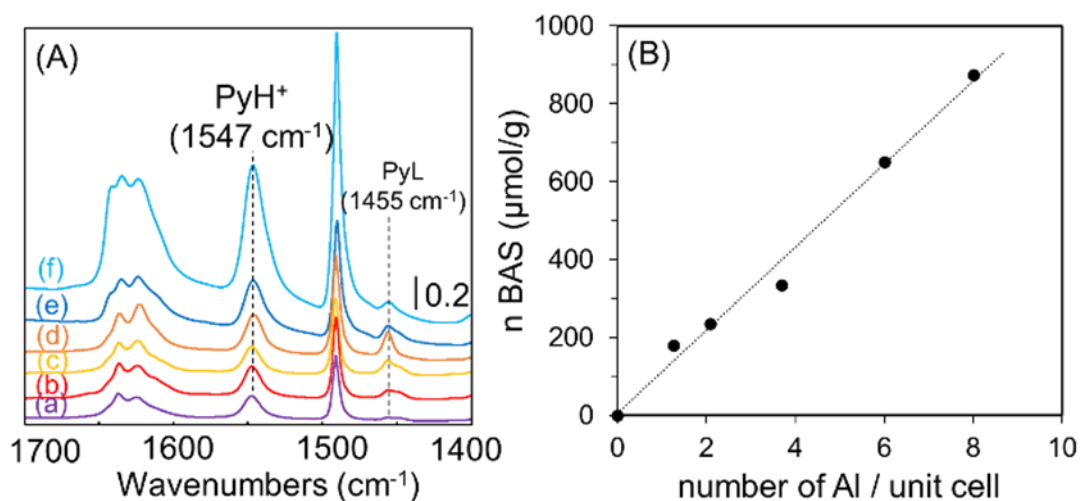


**Figure 2:** (A) Subtraction IR spectra before and after Pyridine adsorption for MFI-75 ((a), purple), MFI-45 ((b), red), MFI-38 ((c), yellow), MFI-25 ((d), orange), MFI-15 ((e), dark blue) and MFI-11 ((f), light blue). The spectra were collected at RT after Pyridine adsorption at 150 °C and normalized to the mass of the pellet (20 mg). (B) Evolution of the amount of Bronsted acid sites as a function of the Al content per unit cell.

**Table 2:** Accessibility of acid sites of different MFI zeolites tested by pyridine adsorption at 150 °C.

	MFI-75	MFI-45	MFI-38	MFI-25	MFI-15	MFI-11
Si/Al ratio <sup>a</sup>	75	45	38	25	15	11
Number of Al/ unit cell	1.3	2.1	2.5	3.7	6	8
n Lewis acid sites <sup>b</sup> ( $\mu\text{mol/g}$ )	12	44	61	75	126	34
n BAS ( $\mu\text{mol/g}$ )	179 <sup>c1</sup>	235 <sup>c1</sup>	195 <sup>c2</sup>	335 <sup>c1</sup>	650 <sup>c3</sup>	875 <sup>c4</sup>

<sup>a</sup> Calculated from ICP, <sup>b</sup>  $\epsilon_{1455} = 1.8 \text{ cm} \cdot \mu\text{mol}^{-1}$ . [38] <sup>c1</sup>  $\epsilon_{1547} = 1.13 \text{ cm} \cdot \mu\text{mol}^{-1}$ , <sup>c2</sup>  $\epsilon_{1547} = 1.24 \text{ cm} \cdot \mu\text{mol}^{-1}$ , <sup>c3</sup>  $\epsilon_{1547} = 1.57 \text{ cm} \cdot \mu\text{mol}^{-1}$ , <sup>c4</sup>  $\epsilon_{1547} = 1.87 \text{ cm} \cdot \mu\text{mol}^{-1}$ .

### 3.3. Determination of the molar absorption coefficients of adsorbed ethanol $\epsilon(\delta_{EtOH}^{1450\text{ cm}^{-1}})$ and water and $\epsilon(\delta_{H_2O}^{1630\text{ cm}^{-1}})$ :

Determining the molar absorption coefficients relative to the adsorbed water and alcohol is essential to convert the IR spectra into quantitative data. For this purpose, the adsorption of ethanol and water is investigated using IR spectroscopy and conducted on the AGIR setup for all MFI zeolites. The experiments were repeated two times to check the reproducibility.

Typical IR spectra recorded at room temperature of adsorbed ethanol and water are displayed in **Figure 3 (A)** for the MFI-45 sample. The main characteristic vibrational bands of adsorbed ethanol are situated at 3000-2800  $\text{cm}^{-1}$ , 1500-1350  $\text{cm}^{-1}$ , and 880  $\text{cm}^{-1}$  and are attributed to  $\nu_{CH}$ ,  $\delta_{CH}$  and  $\nu_s(CCO)$  modes, respectively. In the present study, only the band of ethanol at 1450  $\text{cm}^{-1}$  ( $\delta_{as_{CH_3}}$  mode) is considered: the  $\nu_{CH}$  bands of ethanol at 3000-2800  $\text{cm}^{-1}$  are intense, and the area is only measurable at low alcohol pressures, whereas the area of the band at 880  $\text{cm}^{-1}$  is difficult to assess precisely due to the strong fluctuations and perturbation of the baseline ("U" shape curve) by the structural bands of the zeolites.

In the case of  $\text{H}_2\text{O}$ , the main spectral bands observed at  $\sim 1630\text{ cm}^{-1}$  and  $\sim 5200\text{ cm}^{-1}$  are respectively assigned to the  $\delta_{H_2O}$  and  $(\delta + \nu)_{H_2O}$  vibration modes. Only the band at 1630  $\text{cm}^{-1}$  is considered since the signal-to-noise ratio at  $\sim 5200\text{ cm}^{-1}$  at low water pressure is too low for accurate integration of the band area.

The area of the characteristic band of ethanol ( $\delta_{EtOH}^{1450\text{ cm}^{-1}}$ ) (**Figure 3 (B)**) at 1450  $\text{cm}^{-1}$  and that of water ( $\delta_{H_2O}^{1630\text{ cm}^{-1}}$ ) situated at 1630  $\text{cm}^{-1}$  (**Figure 3 (C)**) are plotted as a function of the quantities of the adsorbed species determined by gravimetric measurements. For the overall zeolites, molar absorption coefficients ( $\epsilon$  ( $\text{cm} \cdot \mu\text{mol}^{-1}$ )) are thus determined as proportional to the slope of the plot (= double the slope) according to the Beer-Lambert law (**equation 1**):

$$A = \epsilon \cdot l \cdot c = \epsilon \cdot l \cdot \frac{n}{V} = \epsilon \cdot l \cdot \frac{n}{l \cdot S} = \epsilon \cdot \frac{n}{S} \quad (\text{equation 1})$$

with A ( $\text{cm}^{-1}$ ) the area of the band,  $\epsilon$  ( $\text{cm} \cdot \mu\text{mol}^{-1}$ ) the molar absorption coefficient, l (cm) the optical pathway, c ( $\mu\text{mol}$  per volume unity) the concentration of the adsorbate, V

( $\text{cm}^3$ ) the volume of the pellet,  $S$  ( $= 2.0 \text{ cm}^2$ ) the surface of the pellet and  $n$  ( $\mu\text{mol}$ ) the amount of the adsorbate.

From the slope of the straight line, an average value for the molar absorption coefficients  $\varepsilon_{\delta_{\text{EtOH}}}^{(1450 \text{ cm}^{-1})}$  and  $\varepsilon_{\delta_{\text{H}_2\text{O}}}^{(1630 \text{ cm}^{-1})}$  is calculated and found to be equal to  $0.14 \pm 0.01$  and  $1.29 \pm 0.06 \text{ cm} \cdot \mu\text{mol}^{-1}$ , respectively. These values are found to be independent of the Si/Al ratio of the MFI zeolites.

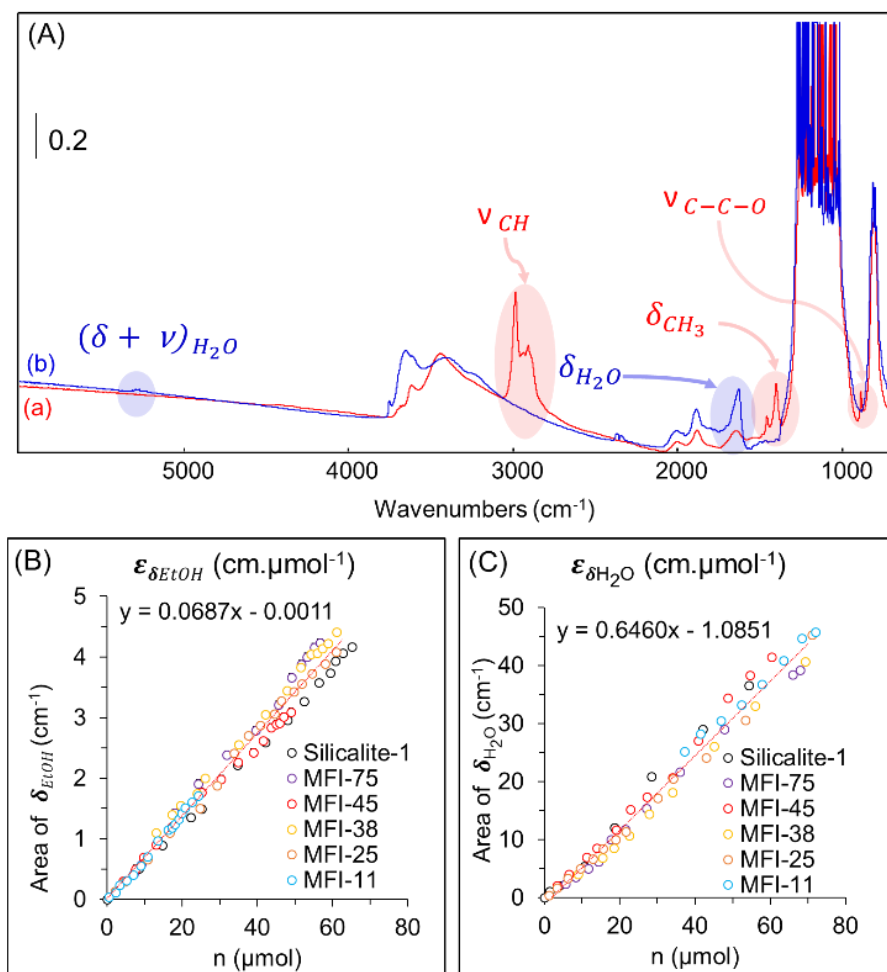


**Figure 3:** (A) IR spectra of MFI-45 with the characteristic bands after ethanol ((a)-red) and water ((b)-blue) adsorption at RT. Evolution of the area of the characteristic band of (B) ethanol ( $1450 \text{ cm}^{-1}$ ) and (C) water ( $1630 \text{ cm}^{-1}$ ) as a function of the quantities adsorbed on Silicalite-1 (black), MFI-75 (purple), MFI-45 (red), MFI-38 (yellow), MFI-25 (orange) and MFI-11 (light blue).

### 3.4. Adsorption of Ethanol or Water on MFI-45:

#### 3.4.1. Isotherm of Ethanol adsorption

Ethanol and water are adsorbed separately on MFI-45. MFI-45 was chosen as reference material to present in detail the spectroscopic study of water and ethanol adsorptions considering its intermediate Si/Al ratio (concomitant presence of Si-OH and BAS sites). The isotherms of ethanol adsorption with the corresponding IR spectra are represented in **Figure 4**; at low ethanol partial pressures ( $P/P_0 < 0.01$ ), ethanol is adsorbed to fill the porosity of the MFI zeolite (**Figure 4 (A)-curve (a)**). The corresponding IR spectra in the OH region are represented in **Figure 4 (B)** and reveal that the  $\nu_{OH}$  band at  $3610\text{ cm}^{-1}$ , characteristic of the BAS, disappears immediately after the first equilibrium pressure ( $P/P_0 = 0.0065$ ). This observation agrees with the results obtained by Alexopoulos et al. [27]. With the increase of the partial pressure, the quantity of adsorbed ethanol on MFI-45 increases to reach a maximum of around  $2500\text{ }\mu\text{mol/g}$  at  $P/P_0 = 0.65$ . As suggested by Gómez-Álvarez *et al.*, the zigzag channels of the MFI structure are responsible for the high adsorption capacity toward ethanol [30]. The ethanol adsorption on MFI-45 occurs in a monolayer adsorption model, previously described in the literature by a Langmuir model [31]. However, the concomitant decrease in the intensity of  $\nu_{OH}$  at  $3744\text{ cm}^{-1}$  assigned to external silanol groups at  $P/P_0 = 0.0065$  shows that ethanol adsorption takes place also on the outer surface of the zeolite structure. This agrees with the results stating that ethanol highly interacts with the silanol groups of the MFI zeolites in the membrane [48, 49].

To elucidate the role of BAS on the adsorption sites of ethanol on MFI zeolites, ethanol is adsorbed on MFI-45 previously treated with Lutidine, a basic probe molecule well-known to poison BAS of the zeolites, specifically [50, 51]. The spectra of MFI-45 before and after Lutidine adsorption (**Figure S3**) show that the characteristic band of the Bronsted acid sites at  $3610\text{ cm}^{-1}$  disappears after introducing Lutidine. In contrast, the bands of Lutidinium at  $1630$  and  $1650\text{ cm}^{-1}$  are well detected, showing the blockage of the BAS before ethanol adsorption. The gravimetric isotherms after ethanol adsorption in the presence of Lutidine and the corresponding IR spectra in the OH region are represented in (**Figure 4**) and compared to the gravimetric adsorption isotherms of the Lutidine free parent MFI zeolite. A slight decrease in the ethanol adsorbed quantity was observed (around 20 %) (**Figure 4 (A) – curve (b)**). After adsorbing ethanol, the characteristic vibrational band at  $3744\text{ cm}^{-1}$  is highly affected at very low ethanol partial pressures in the presence of Lutidine (**Figure 4 (C)**). Its

intensity decreases with the increase of the partial pressure. Based on these results, we can assume that the adsorption of ethanol takes place on the silanol groups since a slight decrease in the quantity of adsorbed ethanol is observed after blocking the BAS. In addition, the number of adsorbed ethanol molecules per Bronsted acid site could be determined from the subtraction between the gravimetric isotherms before and after adsorbing Lutidine. The difference suggests that two ethanol molecules are adsorbed on a BAS, agreeing with the data in the literature [27] (for example, for  $P/P_0=0.65$ , the difference in adsorbed EtOH is  $468 \mu\text{mol/g}$ , and the number of BAS is equal to  $235 \mu\text{mol/g}$ , i.e., an EtOH / BAS ratio equal to  $\sim 2$ ).

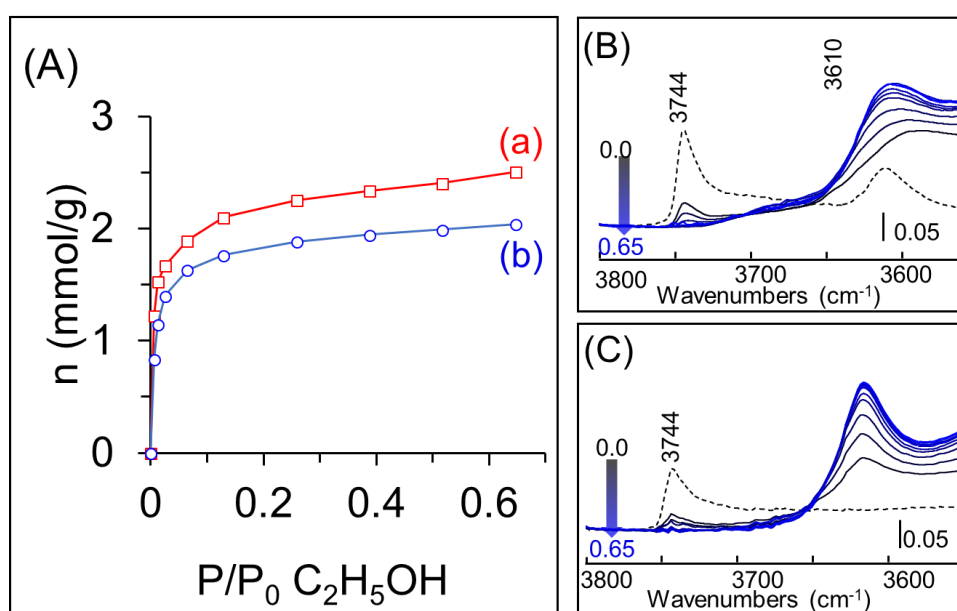


**Figure 4:** (A) Gravimetric adsorption isotherms after  $\text{C}_2\text{H}_5\text{OH}$  adsorption on MFI-45 at RT ((a)-red) without and ((b)-blue) with pre-adsorbed Lutidine. Evolution of the corresponding IR spectra at increasing partial pressures of  $\text{C}_2\text{H}_5\text{OH}$  in the spectral regions between the OH stretching region ( $3800\text{--}3550 \text{ cm}^{-1}$ ) (B) without and (C) with pre-adsorbed Lutidine. The dashed spectra correspond to the initial spectra after activation at RT and before adsorption. Spectra are normalized to 20 mg of zeolite.

### 3.4.2. Isotherm of Water adsorption

The isotherm of water adsorption is displayed in **Figure 5 (A)-curve (a)**, and the corresponding IR spectra are represented in **Figure 5 (B)**. The band of the BAS at  $3610 \text{ cm}^{-1}$  disappears at the first water uptake ( $P/P_0 = 0.01$ ), whereas the intensity of the SiOH groups at  $3744 \text{ cm}^{-1}$  is weakly affected and subsequently decreases significantly only for  $P/P_0$  up to 0.04. This suggests that water molecules interacts specifically with BAS at low partial pressure [52]. While the sensitivity of the  $\nu_{\text{OH}}$  band

of BAS upon water and ethanol adsorption is similar, this is not the case for the  $\nu_{OH}$  band of silanol, much more affected upon ethanol adsorption [27, 31, 53]. This can be explained considering the difference of affinity toward ethanol and water, e.g. the enthalpie of adsorption. The enthalpy of ethanol adsorption is higher than that of water and is characterized by two plateaus. Whereas that of water is characterized by a single plateau attributed to the clustering of water molecules [54]. Water molecules are first adsorbed on the Bronsted acid sites, and then strong interactions occur between the adsorbed water molecules and the second water molecules [55].

Water adsorption sites are further studied after adsorbing Lutidine. The gravimetric isotherm of water adsorption on MFI-45 with pre-adsorbed Lutidine and the corresponding IR spectra in the OH region are represented in **Figures 5 (A) and (C)**. By comparing the gravimetric isotherms, the quantity of adsorbed water on MFI-45 without Lutidine is more important than on MFI-45 filled with Lutidine. After adsorbing water, a minor decrease of the vibrational band at  $3744\text{ cm}^{-1}$  is observed at water partial pressure  $0 < P/P_0 < 0.16$ . At higher partial pressures, an important decrease in the intensity of the characteristic bands of the silanols is observed. These observations allow us to confirm the adsorption of water molecules on BAS and the weak interactions with the silanol groups [36, 56]. Moreover, the difference between the adsorption isotherms of water with and without Lutidine demonstrates that four water molecules are adsorbed on one BAS at low water partial pressure ( $P/P_0 \leq 0.02$ ). For example, for  $P/P_0=0.02$ , the difference in adsorbed water is  $931\text{ }\mu\text{mol/g}$ , and the number of BAS is equal to  $235\text{ }\mu\text{mol/g}$ , i.e., an  $\text{H}_2\text{O} / \text{BAS}$  ratio equal  $\sim 4$ ). Similar results were obtained by Olson et al. [32, 57] and Bolis et al. [56].

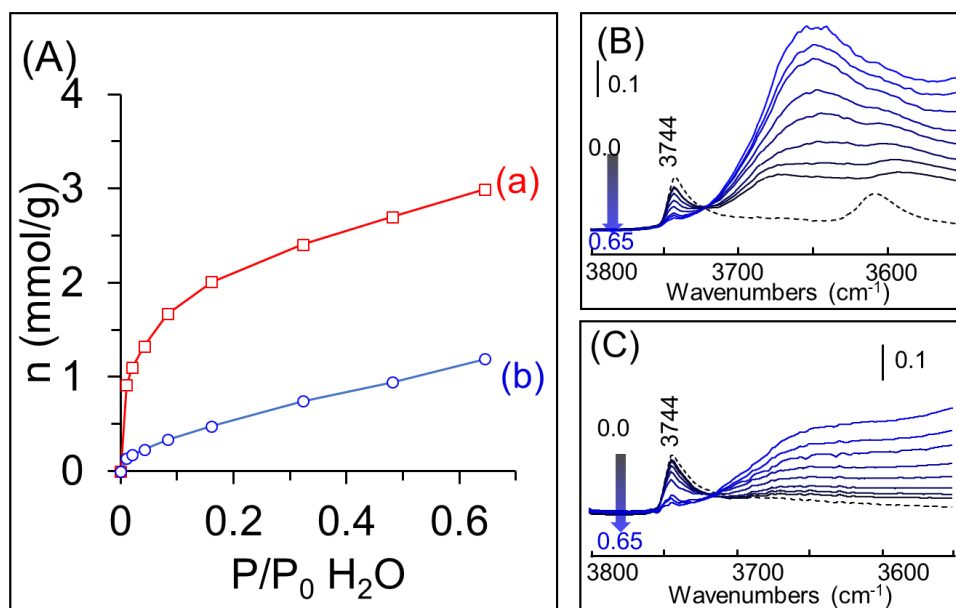


**Figure 5:** Gravimetric adsorption isotherms after H<sub>2</sub>O adsorption on MFI-45 at RT ((a)-red) without and ((b)-blue) with pre-adsorbed Lutidine (A). Evolution of the corresponding IR spectra at increasing partial pressures of H<sub>2</sub>O in the spectral regions between OH stretching region (3800-3550 cm<sup>-1</sup>) (B) without and (C) with pre-adsorbed Lutidine. The dashed spectra correspond to the initial spectra after activation at RT and before H<sub>2</sub>O adsorption. Spectra are normalized to 20 mg of zeolite.

### 3.5. Adsorption of ethanol or water on MFI zeolites with different Si/Al ratios

The adsorption of ethanol and water is further investigated on MFI with different Si/Al ratios. The gravimetric isotherms of ethanol and water are determined from the AGIR setup and are represented in **Figure 6**. The corresponding IR spectra at fixed partial pressures are represented in **Figure S4**. The quantity of adsorbed ethanol increases until reaching an equilibrium at  $P/P_0 = 0.3$ . At  $P/P_0 > 0.3$ , the quantity of adsorbed ethanol increases slightly to reach a maximum ranging between 2400 and 3100  $\mu\text{mol/g}$ . Ethanol adsorption isotherms follow a similar adsorption type regardless of the Si/Al ratio. A Langmuir-like model can be observed, where the organophilic character of MFI zeolites is responsible for the monolayer adsorption of ethanol. These results agree with the previous results described in the literature [31]. The effect of the Si/Al ratio is mainly observed at low ethanol partial pressures ( $P/P_0 < 0.01$ ) (**Figure 6 (C)**), where zeolites with low Si/Al ratio adsorb the highest amount ethanol amount.

A different trend is observed after water adsorption (**Figures 6 (B) and (D)**). First, all zeolites exhibit a Freundlich-like isotherm upon water adsorption, where different layers of adsorbed water are formed [55]. On silicalite-1 and MFI zeolites with

relatively high Si/Al ratios, the quantity of adsorbed water varies in the same range between 2700 and 3300  $\mu\text{mol/g}$ . However, at a lower Si/Al ratio, for MFI-25 and MFI-11, a significant increase in water adsorption capacity is observed. The adsorbed water quantity at  $P/P_0 = 0.64$  reaches 6100  $\mu\text{mol/g}$ . These differences are attributed to the change of the hydrophobic character of zeolite due to the presence of Al in the framework [31, 32]. The presence of Al is responsible for creating Bronsted acid sites in the framework (**Table 2**), considered as the adsorption sites for water. As a result, the hydrophobic character of the zeolite decreases, increasing, thus the adsorption capacity of water. This adsorption model is also confirmed by the linear correlation between the number of BAS determined by Pyridine adsorption and the quantity of adsorbed water at very low partial pressures ( $P/P_0 = 0.0065$ ) (**Figure S5**).

Additionally, the linear correlation between the quantities of these adsorbed species and the number of Bronsted acid sites determined by pyridine adsorption allows us to determine the number of adsorbed molecules per acid site for each adsorbate at each partial pressure. Two molecules of ethanol are adsorbed on the Bronsted acid sites at full coverage to form dimeric species (high partial pressures). In contrast, a bigger cluster is formed on the Bronsted acid sites upon adsorbing water. The slope of the linear correlation indicates that four water molecules are adsorbed at high partial pressure. These results are consistent with the previously demonstrated results on MFI-45 after adsorption of Lutidine.

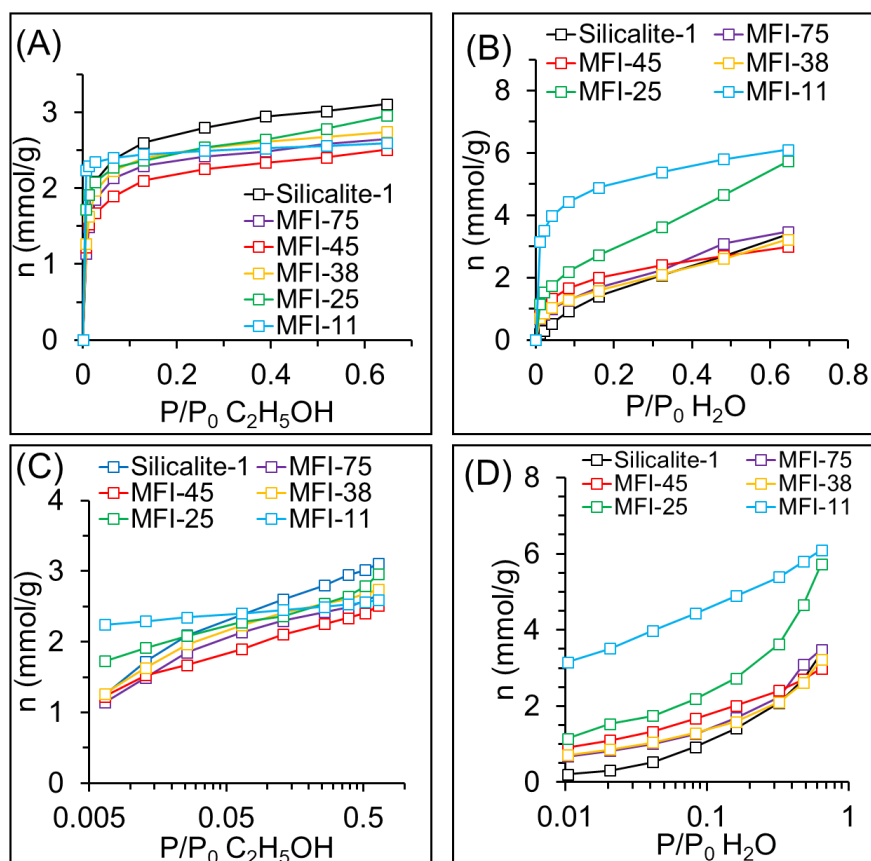


**Figure 6:** Adsorption isotherms of (A) ethanol and (B) water on Silicalite-1 (black), MFI-75 (purple), MFI-45 (red), MFI-38 (yellow), MFI-25 (green), and MFI-11 (light blue). Semi-log plot of the adsorption isotherms of (C) ethanol and (D) water.

### 3.6. Coadsorption of ethanol and water on MFI zeolites with different Si/Al ratios:

#### 3.6.1. Validation of the $\epsilon_{\delta_{EtOH}}^{(1450\text{ cm}^{-1})}$ and $\epsilon_{\delta_{H_2O}}^{(1630\text{ cm}^{-1})}$ values for coadsorption experiments: comparison between AGIR and CARROUCELL setups:

The coadsorption of ethanol and water on the MFI zeolites with different Si/Al ratios was conducted on the CARROUCELL setup, previously described in the experimental section. A single experiment was conducted first on the AGIR setup on MFI-45 to confirm that the molar absorption coefficients determined during pure ethanol and water adsorptions do not change during their coadsorption. Water is initially adsorbed on the zeolite, and when the equilibrium is reached, the gas flow is enriched with an increasing concentration of ethanol. IR spectra of MFI-45 recorded on the CARROUCELL for different  $P/P_0$  of  $C_2H_5OH$ , and at a fixed  $H_2O$  concentration ( $P/P_0 = 0.32$ ) are reported (**Figure 7(B)**). Initially, in the absence of EtOH, only the peak at  $\sim 1630\text{ cm}^{-1}$  characteristic of adsorbed water is present. Subsequently, the step-by-step increase in the partial pressure  $P/P_0$  of  $C_2H_5OH$  leads to a decrease in

the intensity of the  $\delta_{H_2O}$  band and to the concomitant increase of the characteristic bands of the adsorbed alcohol, in particular, the one positioned at  $1450\text{ cm}^{-1}$ . The molar absorption coefficients previously determined from the AGIR setup are used to determine the quantities of each adsorbed specie from the IR spectra recorded on the CARROUCELL. Finally, the calculated total quantity of ethanol+water adsorbed on the zeolite via the CARROUCELL is compared to the mass uptake recorded with the microbalance of the AGIR setup (**Figure 7(A)**). The results show that the quantities of adsorbed ethanol and water are similar, as illustrated by the linear correlation obtained between the total adsorbed quantities determined by the AGIR tool and the CARROUCELL via the molar absorption coefficients, respectively (inset **Figure 7(A)**). Thus, we conclude that the molar absorption coefficient of each adsorbate is not significantly affected by the presence of the second specie. Consequently, the CARROUCELL set-up can be used to drastically reduce the experimental time while rigorously reproducing the same conditions (temperature and pressure) since the experiment is carried out simultaneously for all the samples positioned in the same environmental environment chamber.

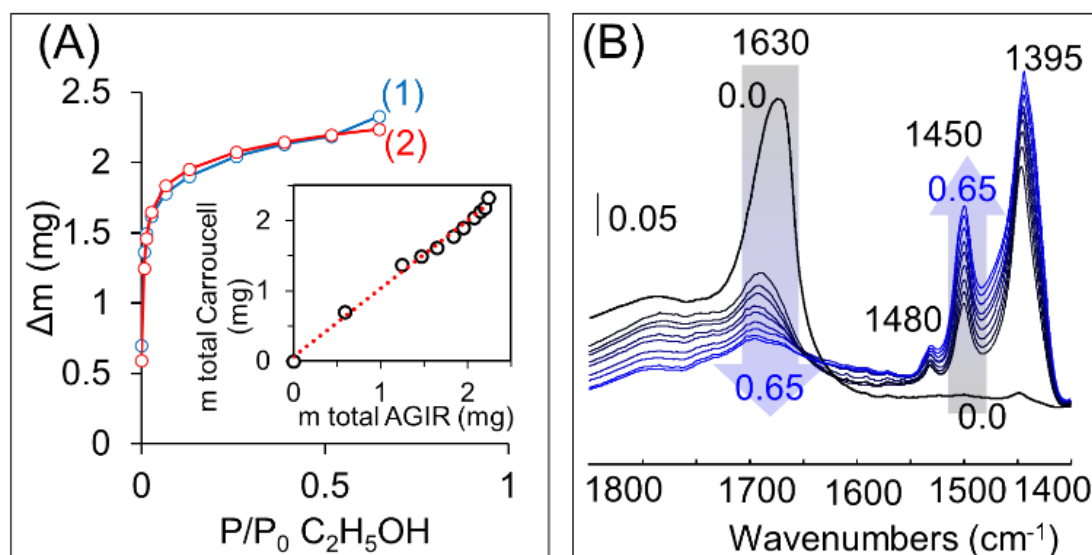


**Figure 7:** (A) Mass variation ( $\Delta m$ , mg) as a function of increasing  $P/P_0$  of  $C_2H_5OH$  determined using the CARROUCELL ((1), blue) and using AGIR ((2), red). (B) Evolution of IR spectra of MFI-45 recorded on the CARROUCELL for increasing  $P/P_0$  of  $C_2H_5OH$  and a fixed  $H_2O$  concentration ( $P/P_0 = 0.32$ ). The spectra correspond to the subtracted spectrum between the spectra after activation recorded at RT and the successive spectra recorded at RT at equilibrium after  $C_2H_5OH/H_2O$  adsorption. Inset of (A): Linear correlation between the total mass calculated from the CARROUCELL and the AGIR.

### 3.6.2. Ethanol/water selectivity:

The selectivity of ethanol over water is strongly related to the hydrophobic/hydrophilic properties of MFI zeolites and then to the Si/Al ratio [30]. Such selectivity ( $S_{C_2H_5OH, H_2O}$ ) is defined according to the following equation:

$$S_{C_2H_5OH, H_2O} = \frac{x_{C_2H_5OH}/y_{C_2H_5OH}}{x_{H_2O}/y_{H_2O}} \quad \text{(equation 2)}$$

With  $x$  and  $y$ , the molar fractions of a component in the adsorbed and vapor phases, respectively.

The selectivity factor has been determined for increasing ethanol partial pressures ( $P/P_0 = 0.006-0.52$ ) at water vapor partial pressure  $P/P_0 = 0.16$ . It is noted that some of the selectivity values are not reported due to uncertainties in the calculated values for the previously studied MFI zeolites.  $S_{C_2H_5OH, H_2O}$  values are reported in **Figure 8** for Silicalite-1, MFI-45, MFI-25, and MFI-11 for  $P/P_0 H_2O = 0.16$ , with an increasing  $P/P_0$  of ethanol. It is observed that the ethanol selectivity decreases with the increase of  $P/P_0 C_2H_5OH$  for all the zeolites and is always greater than 1 for Silicalite-1, MFI-45, and MFI-25, suggesting selective ethanol adsorption even at low  $P/P_0$  of  $C_2H_5OH$  for the highest silica material. However, the  $S_{C_2H_5OH, H_2O}$  is lower than 1 for MFI-11 at high ethanol partial pressures indicating preferential water adsorption. Comparing the selectivity between the four samples at a given ethanol partial pressure (for example, at  $P/P_0 = 0.26$ ) shows that the ethanol sorption selectivity decreases with the Si/Al ratio. Yet, it decreases drastically when comparing Silicalite-1 (**Figure 8 curve (a)**) and MFI-11 (**Figure 8 curve (d)**). Hence, MFI-11, the highest Al content zeolite, is highly selective for adsorbing water over ethanol. It is concluded that the lower the Si/Al ratio, the higher the zeolite hydrophilicity is, and then water is strongly adsorbed in the zeolite and is not easily replaced by ethanol. The effect of the Si/Al ratio on the selectivity of ethanol over water is in agreement with the results reported in the literature [31, 58], extending this conclusion to larger Si/Al range and at different partial pressures.

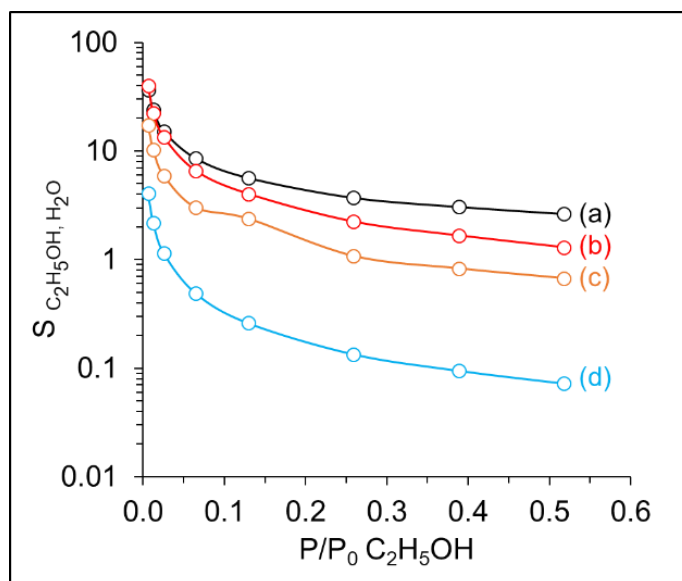


**Figure 8:** Selectivity of C<sub>2</sub>H<sub>5</sub>OH determined on Silicalite-1 ((a)-black), MFI-45 ((b)-red), MFI-25 ((c)-orange) and MFI-11 ((d)-light blue) at fixed P/P<sub>0</sub> = H<sub>2</sub>O (0.16) and increasing P/P<sub>0</sub> C<sub>2</sub>H<sub>5</sub>OH.

### 3.6.3. Influence of the Si/Al and the fraction of H<sub>2</sub>O in the gas phase on the relative amount of adsorbed EtOH ( $R_{C_2H_5OH}$ )

The area of the vibrational band of water at 1630 cm<sup>-1</sup> cannot always be measured precisely for all zeolites for small amounts of adsorbed H<sub>2</sub>O due to the distortion of the baseline in this range (distortion mainly resulting from the shift of the underlying combination and overtone bands of  $\nu_{Si-O}$  structural vibrations). This is why we have chosen to introduce a new factor independent of the measurement of the quantity of coadsorbed water in order to compare the ethanol adsorption capacities of the overall zeolites with and without water. Hence, the selective adsorption of ethanol is interpreted after introducing a new variable, the ratio of adsorbed ethanol ( $R_{C_2H_5OH}$ ). It is determined as the ratio between the quantity of coadsorbed ethanol ( $(Q_{C_2H_5OH})_{P/P_0, C_2H_5OH}^{P/P_0, H_2O}$ ) at a given water and ethanol partial pressures in the presence of water and the quantity of adsorbed EtOH at the same ethanol partial pressure in the absence of water ( $(Q_{C_2H_5OH})_{P/P_0, C_2H_5OH}^0$ ):

$$(R_{C_2H_5OH})_{P/P_0, C_2H_5OH} = \frac{(Q_{C_2H_5OH})_{P/P_0, C_2H_5OH}^{P/P_0, H_2O}}{(Q_{C_2H_5OH})_{P/P_0, C_2H_5OH}^0} \times 100 \quad \text{(equation 3)}$$

The ratio of adsorbed ethanol ( $R_{C_2H_5OH}$ ) is plotted as a function of the number of Al atoms per unit cell for different ethanol partial pressures at four different water

partial pressures (**Figure 9** and **Figure S6**). For a fixed water vapor concentration, for example,  $P/P_0 = 0.16$ , the ratio of adsorbed ethanol decreases with the increase of the number of Al per unit cell, regardless of the ethanol partial pressure. At low ethanol partial pressure ( $P/P_0 = 0.006$ ) (**Figure 9 (A)**), the ratio of adsorbed ethanol decreases with the increase of the number of Al for fixed water content. A dramatic difference between the ratios of adsorbed ethanol is observed when the initial water content increases at low ethanol concentrations for a fixed number of Al/unit cell. Nevertheless, this trend is not observed when ethanol concentration is close to saturation ( $P/P_0 = 0.52$ ), although the ratio of adsorbed  $C_2H_5OH$  keeps decreasing with the increase of the number of Al per unit cell (**Figure 9 (B)**). This demonstrates the clear effect of water on ethanol adsorption at low pressures and not at high pressures.

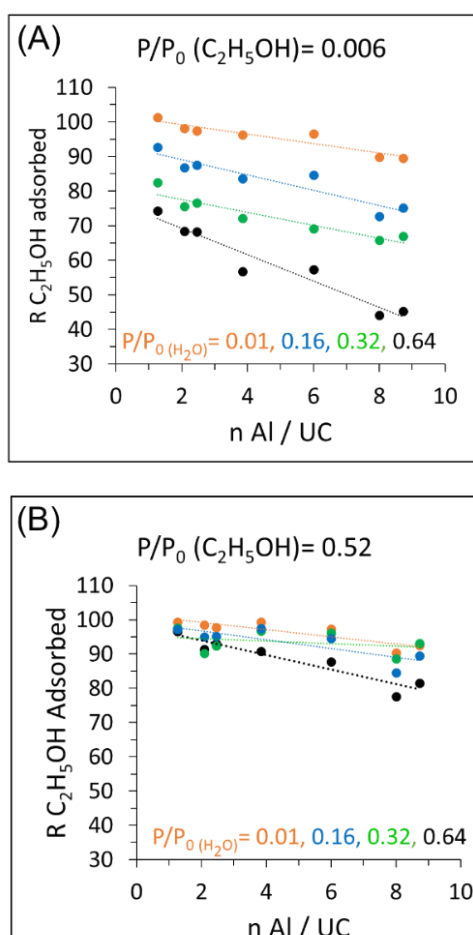


**Figure 9:** Ratio of adsorbed  $C_2H_5OH$  vs the number of Al per unit cell for  $P/P_0 C_2H_5OH = 0.006$  (A) and  $0.52$  (B) after adsorption of different water partial pressures ( $P/P_0 H_2O = 0.01$  (orange),  $P/P_0 H_2O = 0.16$  (blue),  $P/P_0 H_2O = 0.32$  (green) and  $P/P_0 H_2O = 0.64$  (black)) for different MFI zeolites.

Finally, the ratio of adsorbed  $C_2H_5OH$  during the coadsorption of ethanol and water at different ethanol and water partial pressures for all previously studied MFI zeolites is summarized in **Figure 10**. For this, and for each zeolite, a polynomial curve fitting (order 3) has been determined grouping all experimental data ( $R_{C_2H_5OH}$  vs % mol  $H_2O$  (in gas phase)) in order to reduce the effect of differences in experimental data. The effects of both the Si/Al and the water content in the gas phase are clearly observed on ethanol adsorption. The adsorption of ethanol is less affected by water at low water content. With the increase of the water content in the gas phase, ethanol is less adsorbed, regardless of the Si/Al ratio. Moreover, ethanol is highly adsorbed on high Si/Al ratio zeolites. These results are in good agreement with other studies claiming that the selectivity of ethanol increases with the increase of the Si/Al and the total flux [31, 59]. Therefore, the Si/Al ratio and the water content directly impact the ethanol sorption properties and govern the choice of the mixed membranes to separate bioethanol from its aqueous mixture.

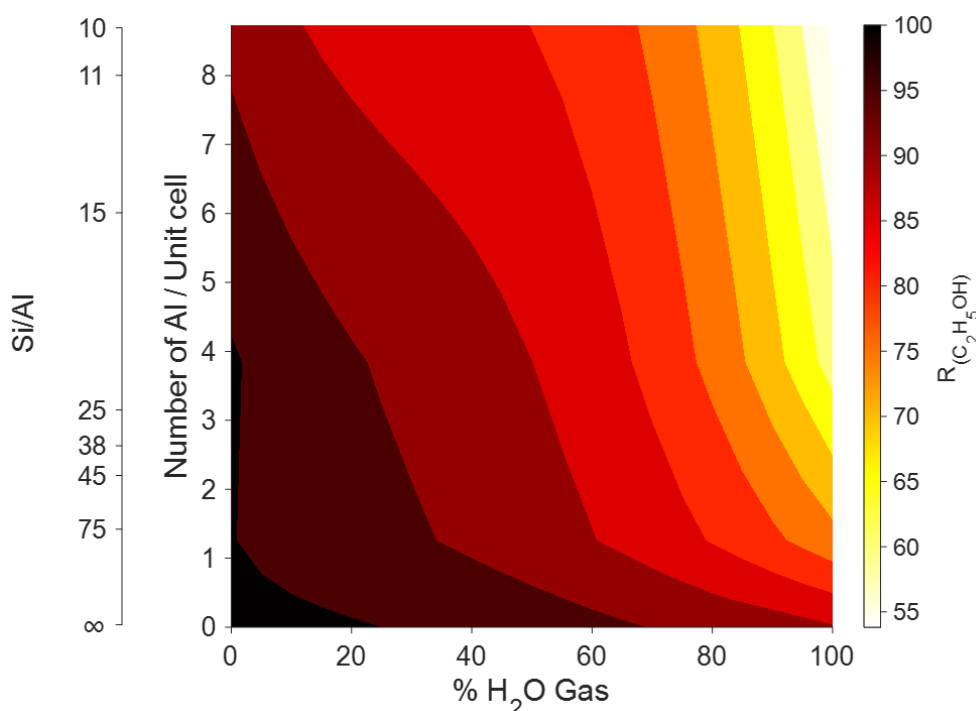


**Figure 10:** Ratio of adsorbed  $C_2H_5OH$  as a function of the number of Al / Unit cell, the Si/Al ratio, and the percentage of  $H_2O$  in the gas phase. Note that the adsorption of pure ethanol at 0%  $H_2O$  is not included in the figure to avoid mathematical problems in fitting the graph.

## 4. Conclusion

The use of advanced vibrational spectroscopic tools allows obtaining quantitative data on ethanol and water adsorption and coadsorption on MFI zeolites with different Si/Al ratios. This quantitative spectroscopic approach leads to the determination of the molar absorption coefficients of adsorbed ethanol and water. They are equal to  $0.14 \pm 0.01$  and  $1.29 \pm 0.06 \text{ cm} \cdot \mu\text{mol}^{-1}$ , respectively and are independent of the Si/Al ratio whether adsorbed or coadsorbed.

Gravimetric-IR coupled experiments reveal that water adsorbs specifically on BAS at low partial pressures, whereas ethanol adsorbs on both silanol and BAS sites. The number of adsorbed molecules per Bronsted acid site is estimated to be four water molecules and two ethanol molecules per site.

The Si/Al ratio effect was further studied and significantly affected ethanol adsorption isotherms only at low partial pressures. However, a significant effect on the amount of adsorbed water is evidenced at extended water partial pressure, illustrating its role on the hydrophobic character of the material.

The use of molar absorption coefficient of adsorbed water and ethanol allows to obtain an important data set relative to the concentration of ethanol and water from the binary adsorption measurements, using the developed multi-sample in-situ IR cell (CARROUCELL). Finally, water molar fraction in the gas phase plays a significant role in ethanol adsorption, leading to lower adsorption capacity at high water content. Furthermore, a higher Si/Al ratio leads to higher ethanol adsorption capacity in the presence of water. This work offers valuable insight into studying other mixtures' adsorption mechanisms using IR spectroscopy.

## Author Contributions

The manuscript was written with the contributions of all authors. All authors have approved the final version of the manuscript.

## Acknowledgments

Authors acknowledge the Normandy region for the doctoral funding of R.Zakhia Douaihy.

## References

1. Cheng, J.J. and G.R. Timilsina, *Status and barriers of advanced biofuel technologies: a review*. *Renewable Energy*, 2011. **36**(12): p. 3541-3549.
2. Gude, V.G. and E. Martinez-Guerra, *Green chemistry with process intensification for sustainable biodiesel production*. *Environmental chemistry letters*, 2018. **16**(2): p. 327-341.
3. Malhotra, R. and L. Das, *Biofuels as blending components for motor gasoline and diesel fuels*. 2003.
4. Jambo, S.A., et al., *A review on third generation bioethanol feedstock*. *Renewable and sustainable energy reviews*, 2016. **65**: p. 756-769.
5. Chauhan, S.K., S. Gangopadhyay, and N. Singh, *Environmental aspects of biofuels in road transportation*. *Environmental Chemistry Letters*, 2009. **7**(4): p. 289-299.
6. Karimi, S., et al., *Processes and separation technologies for the production of fuel-grade bioethanol: a review*. *Environmental Chemistry Letters*, 2021: p. 1-18.
7. Soccol, C.R., et al., *Lignocellulosic bioethanol: current status and future perspectives*, in *Biofuels: Alternative feedstocks and conversion processes for the production of liquid and gaseous biofuels*. 2019, Elsevier. p. 331-354.
8. Kumar, A.S., et al., *Recent Developments of Bioethanol Production*. *Bioenergy Research: Evaluating Strategies for Commercialization and Sustainability*, 2021: p. 175-208.
9. Tse, T.J., D.J. Wiens, and M.J. Reaney, *Production of bioethanol—A review of factors affecting ethanol yield*. *Fermentation*, 2021. **7**(4): p. 268.
10. Karimi, S., M.T. Yaraki, and R.R. Karri, *A comprehensive review of the adsorption mechanisms and factors influencing the adsorption process from the perspective of bioethanol dehydration*. *Renewable and Sustainable Energy Reviews*, 2019. **107**: p. 535-553.
11. Kumar, S., N. Singh, and R. Prasad, *Anhydrous ethanol: A renewable source of energy*. *Renewable and Sustainable Energy Reviews*, 2010. **14**(7): p. 1830-1844.
12. Liu, X., et al., *Preparation and characterization of S ilicalite-1/PDMS surface sieving pervaporation membrane for separation of ethanol/water mixture*. *Journal of Applied Polymer Science*, 2015. **132**(34).
13. El-Roz, M., et al., *Pore occupancy changes water/ethanol separation in MOF-Quantitative map of coadsorption by IR*. *Journal of Physical Chemistry C*, 2015. **119**(39): p. 22570-22576.
14. Mintova, S., J.-P. Gilson, and V. Valtchev, *Advances in nanosized zeolites*. *Nanoscale*, 2013. **5**(15): p. 6693-6703.
15. Kosinov, N., et al., *Recent developments in zeolite membranes for gas separation*. *Journal of Membrane Science*, 2016. **499**: p. 65-79.
16. Bacakova, L., et al., *Applications of zeolites in biotechnology and medicine—a review*. *Biomaterials science*, 2018. **6**(5): p. 974-989.
17. Moshoeshoe, M., M.S. Nadiye-Tabbiruka, and V. Obuseng, *A review of the chemistry, structure, properties and applications of zeolites*. *Am. J. Mater. Sci*, 2017. **7**(5): p. 196-221.
18. Delgado, J.A., et al., *Separation of ethanol–water liquid mixtures by adsorption on silicalite*. *Chemical Engineering Journal*, 2012. **180**: p. 137-144.
19. Laksmono, J., et al. *Kinetic studies of adsorption in the bioethanol dehydration using polyvinyl alcohol, zeolite and activated carbon as adsorbent*. in *AIP Conference Proceedings*. 2017. AIP Publishing LLC.
20. Simo, M., et al., *Adsorption/desorption of water and ethanol on 3A zeolite in near-adiabatic fixed bed*. *Industrial & Engineering Chemistry Research*, 2009. **48**(20): p. 9247-9260.

21. Siepmann, J.I., P. Bai, and M. Tsapatsis, *Zeolites for separation of ethanol and water*. 2018, Univ. of Minnesota, Minneapolis, MN (United States).
22. Zhou, H., et al., *Colloidal defect-free silicalite-1 single crystals: preparation, structure characterization, adsorption, and separation properties for alcohol/water mixtures*. *Langmuir*, 2015. **31**(30): p. 8488-8494.
23. DeJaco, R.F., et al., *Adsorptive separation of 1-butanol from aqueous solutions using MFI-and FER-type zeolite frameworks: a Monte Carlo study*. *Langmuir*, 2016. **32**(8): p. 2093-2101.
24. Zhang, K., et al., *Diffusion of water and ethanol in silicalite crystals synthesized in fluoride media*. *Microporous and mesoporous materials*, 2013. **170**: p. 259-265.
25. Furukawa, S.-i., et al., *Molecular simulation study on adsorption and diffusion behavior of ethanol/water molecules in NaA zeolite crystal*. *Journal of chemical engineering of Japan*, 2004. **37**(1): p. 67-74.
26. Shi, Q., et al., *Efficient ethanol/water separation via functionalized nanoporous graphene membranes: insights from molecular dynamics study*. *Journal of Materials Science*, 2017. **52**(1): p. 173-184.
27. Alexopoulos, K., et al., *Anharmonicity and confinement in zeolites: structure, spectroscopy, and adsorption free energy of ethanol in H-ZSM-5*. *The Journal of Physical Chemistry C*, 2016. **120**(13): p. 7172-7182.
28. Bastani, D., N. Esmaeili, and M. Asadollahi, *Polymeric mixed matrix membranes containing zeolites as a filler for gas separation applications: A review*. *Journal of Industrial and Engineering Chemistry*, 2013. **19**(2): p. 375-393.
29. Pérez Pariente, J. and M. Martínez Sánchez, *Zeolites and ordered porous solids: fundamentals and applications*. 2011.
30. Gomez-Alvarez, P., et al., *Study of short-chain alcohol and alcohol-water adsorption in MEL and MFI zeolites*. *Langmuir*, 2018. **34**(43): p. 12739-12750.
31. Zhang, K., et al., *Adsorption of water and ethanol in MFI-type zeolites*. *Langmuir*, 2012. **28**(23): p. 8664-8673.
32. Olson, D., W. Haag, and W. Borghard, *Use of water as a probe of zeolitic properties: interaction of water with HZSM-5*. *Microporous and Mesoporous Materials*, 2000. **35**: p. 435-446.
33. Volkov, V.I., et al., *Self-diffusion of water-ethanol mixture in chitosan membranes obtained by pulsed-field gradient nuclear magnetic resonance technique*. *Journal of Membrane Science*, 1998. **138**(2): p. 221-225.
34. Volkov, V.I., et al., *Self-diffusion of water-ethanol mixtures in polyacrylic acid-polysulfone composite membranes obtained by pulsed-field gradient nuclear magnetic resonance spectroscopy*. *Journal of membrane science*, 1995. **100**(3): p. 273-286.
35. Dreisbach, F., H.W. Lösch, and K. Nakai, *Adsorption measurement of water/ethanol mixtures on activated carbon fiber*. *Chemical engineering & technology*, 2001. **24**(10): p. 1001-1005.
36. Vjunov, A., et al., *Tracking the chemical transformations at the Brønsted acid site upon water-induced deprotonation in a zeolite pore*. *Chemistry of Materials*, 2017. **29**(21): p. 9030-9042.
37. Zecchina, A., et al., *IR spectroscopy of neutral and ionic hydrogen-bonded complexes formed upon interaction of CH<sub>3</sub>OH, C<sub>2</sub>H<sub>5</sub>OH, (CH<sub>3</sub>)<sub>2</sub>O, (C<sub>2</sub>H<sub>5</sub>)<sub>2</sub>O and C<sub>4</sub>H<sub>8</sub>O with HY, H-ZSM-5 and H-mordenite: comparison with analogous adducts formed on the H-Nafion superacidic membrane*. *Journal of the Chemical Society, Faraday Transactions*, 1996. **92**(23): p. 4863-4875.
38. Zholobenko, V., et al., *Probing the acid sites of zeolites with pyridine: Quantitative AGIR measurements of the molar absorption coefficients*. *Journal of Catalysis*, 2020. **385**: p. 52-60.
39. Lakiss, L., et al., *Effect of stabilizing binder and dispersion media on spin-on zeolite thin films*. *Thin solid films*, 2010. **518**(8): p. 2241-2246.

40. Jolly, S., et al., *Reaction mechanisms and kinetics in the n-hexane cracking over zeolites*. Applied catalysis A: general, 1997. **156**(1): p. 71-96.
41. Qin, Z., et al., *Comparative study of nano-ZSM-5 catalysts synthesized in OH<sup>-</sup> and F<sup>-</sup> media*. Advanced Functional Materials, 2014. **24**(2): p. 257-264.
42. Bazin, P., A. Alenda, and F. Thibault-Starzyk, *Interaction of water and ammonium in NaHY zeolite as detected by combined IR and gravimetric analysis (AGIR)*. Dalton Transactions, 2010. **39**(36): p. 8432-8436.
43. Thommes, M., et al., *Physisorption of gases, with special reference to the evaluation of surface area and pore size distribution (IUPAC Technical Report)*. Pure and applied chemistry, 2015. **87**(9-10): p. 1051-1069.
44. Thibault-Starzyk, F., A. Vimont, and J.-P. Gilson, *2D-COS IR study of coking in xylene isomerisation on H-MFI zeolite*. Catalysis today, 2001. **70**(1-3): p. 227-241.
45. Peng, P., et al., *Unraveling the diffusion properties of zeolite-based multicomponent catalyst by combined gravimetric analysis and IR spectroscopy (AGIR)*. ACS Catalysis, 2020. **10**(12): p. 6822-6830.
46. Khabtou, S., T. Chevreau, and J. Lavalley, *Quantitative infrared study of the distinct acidic hydroxyl groups contained in modified Y zeolites*. Microporous Materials, 1994. **3**(1-2): p. 133-148.
47. Fritz, P.O. and J.H. Lunsford, *The effect of sodium poisoning on dealuminated Y-type zeolites*. Journal of Catalysis, 1989. **118**(1): p. 85-98.
48. Wu, Z., et al., *Enhanced stability of MFI zeolite membranes for separation of ethanol/water by eliminating surface Si-OH groups*. ACS applied materials & interfaces, 2018. **10**(4): p. 3175-3180.
49. Selvaraj, M. and F. Banat, *Ethanol-Water Separation Using Membrane Technology*, in *Biorefinery*. 2019, Springer. p. 211-232.
50. Thibault-Starzyk, F., et al., *Quantification of enhanced acid site accessibility in hierarchical zeolites—the accessibility index*. Journal of Catalysis, 2009. **264**(1): p. 11-14.
51. Jacobs, P.A. and C. Heylen, *Active sites in zeolites: III. Selective poisoning of Bronsted sites on synthetic Y zeolites*. Journal of Catalysis, 1974. **34**(2): p. 267-274.
52. Parker, L.M., D.M. Bibby, and G.R. Burns, *An infrared study of H<sub>2</sub>O and D<sub>2</sub>O on HZSM-5 and DZSM-5*. Zeolites, 1993. **13**(2): p. 107-112.
53. Piccini, G., M. Alessio, and J. Sauer, *Ab initio study of methanol and ethanol adsorption on Brønsted sites in zeolite H-MFI*. Physical Chemistry Chemical Physics, 2018. **20**(30): p. 19964-19970.
54. Wu, D., et al., *Energy landscape of water and ethanol on silica surfaces*. The Journal of Physical Chemistry C, 2015. **119**(27): p. 15428-15433.
55. Jentys, A., et al., *Adsorption of water on ZSM 5 zeolites*. The Journal of Physical Chemistry, 1989. **93**(12): p. 4837-4843.
56. Bolis, V., C. Busco, and P. Ugliengo, *Thermodynamic study of water adsorption in high-silica zeolites*. The Journal of Physical Chemistry B, 2006. **110**(30): p. 14849-14859.
57. Olson, D., et al., *Evidence for dimeric and tetrameric water clusters in HZSM-5. Zeolites*, 1997. **18**(5-6): p. 347-349.
58. Ueno, K., et al., *Effect of Si/Al ratio and amount of deposited MFI-type seed crystals on the separation performance of silicalite-1 membranes for ethanol/water mixtures in the presence of succinic acid*. Microporous and Mesoporous Materials, 2018. **267**: p. 1-8.
59. Zhan, X., et al., *Pervaporation of ethanol/water mixtures with high flux by zeolite-filled PDMS/PVDF composite membranes*. Chinese Journal of polymer science, 2009. **27**(06): p. 771-780.

## **Quantitative IR study of ethanol/water coadsorption on MFI zeolites with different Si/Al ratios**

Rita Zakhia Douaihy <sup>a</sup>, Louwanda Lakiss <sup>a</sup>, Mohamad EL-Roz<sup>a</sup> , Alexandre Vimont <sup>a,\*</sup>,  
Philippe Bazin <sup>a</sup>.

<sup>a</sup> Normandie Université, ENSICAEN, UNICAEN, CNRS, Laboratoire Catalyse et Spectrochimie, 14050  
Caen, France

### Supplementary Information

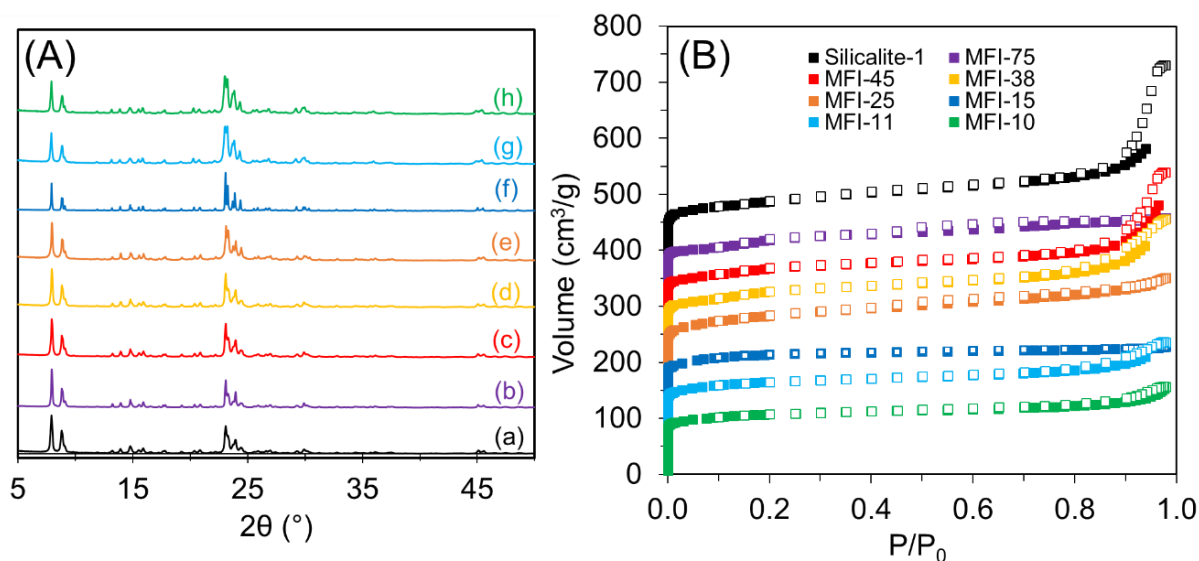


**Figure S1:** (A) PXRD patterns and (B)  $N_2$  adsorption/desorption isotherms at 77 K of Silicalite-1 (black, (a)), MFI-75 (purple, (b)), MFI-45 (red, (c)), MFI-38 (yellow, (d)), MFI-25 (orange, (e)), MFI-15 (dark blue, (f)), MFI-11 (light blue (g)) and MFI-10 (green, (h)). The adsorption/desorption isotherms are offset vertically for comparison.

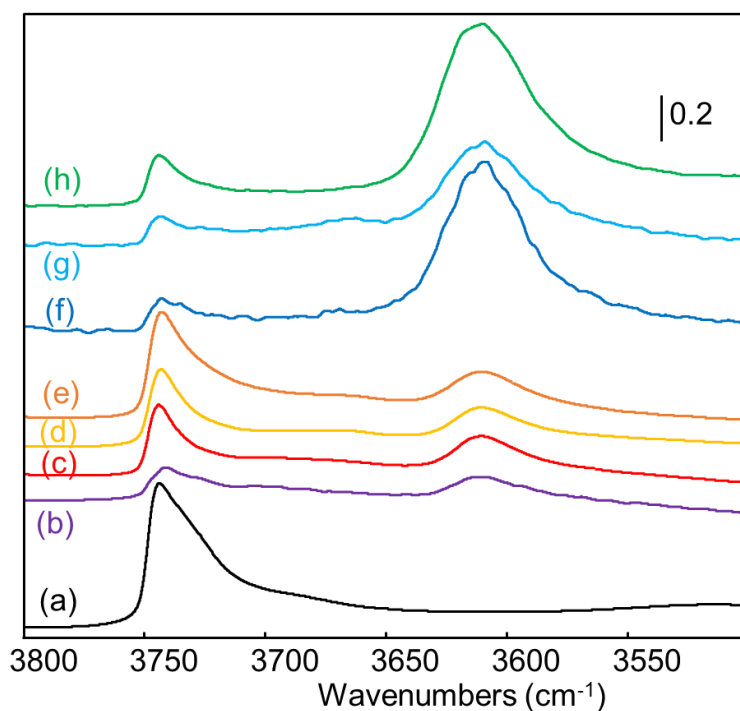


**Figure S2:** FTIR spectra in the OH region between 3800 and 3500  $cm^{-1}$  for Silicalite-1 (black, (a)), MFI-75 (purple, (b)), MFI-45 (red, (c)), MFI-38 (yellow, (d)), MFI-25 (orange, (e)), MFI-15 (dark blue, (f)), MFI-11 (light blue (g)) and MFI-10 (green, (h)). The spectra were recorded at RT and normalized to the mass of the pellet (20 mg)

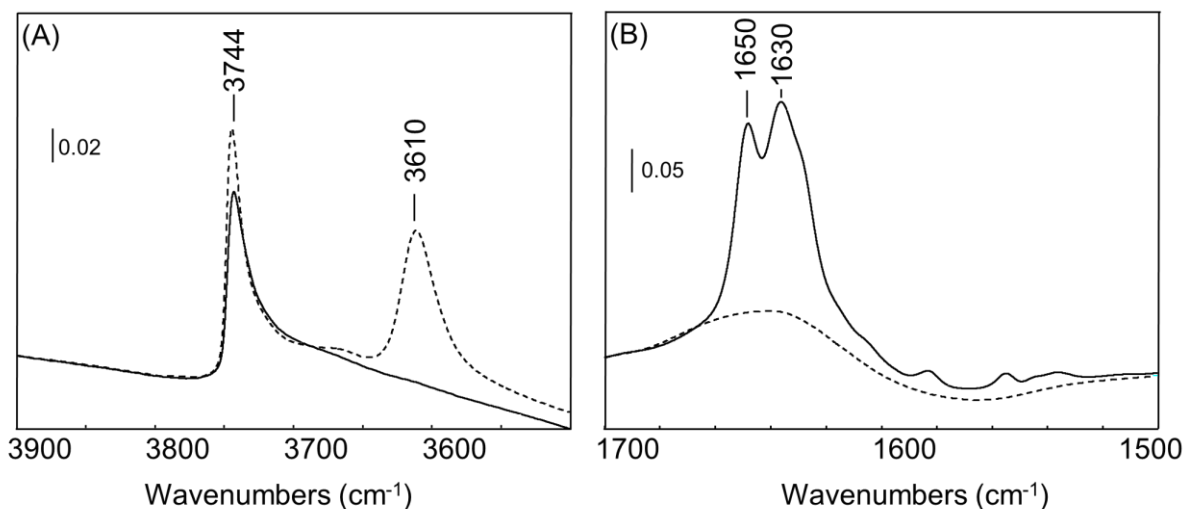


**Figure S3:** FTIR spectra in the OH region between 3800 and 3500 cm<sup>-1</sup> (A) and in the region between 1700 and 1500 cm<sup>-1</sup> (B) for MFI-45 before (dashed line) and after (solid line) adsorption of Lutidine.

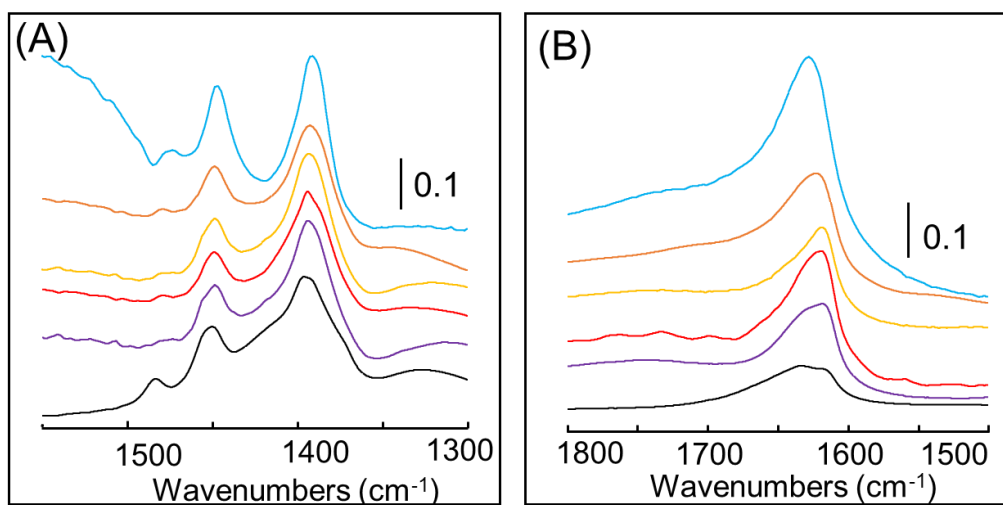


**Figure S4:** Evolution of the IR spectra (subtracted spectra) of different zeolites after adsorption of (A) ethanol ( $P/P_0 = 0.129$ ) and (B) water ( $P/P_0 = 0.16$ ) on Silicalite-1 (black), MFI-75 (purple), MFI-45 (red), MFI-38 (yellow), MFI-25 green, and MFI-11 (light blue). The spectra are normalized to the mass of the pellet (20 mg).

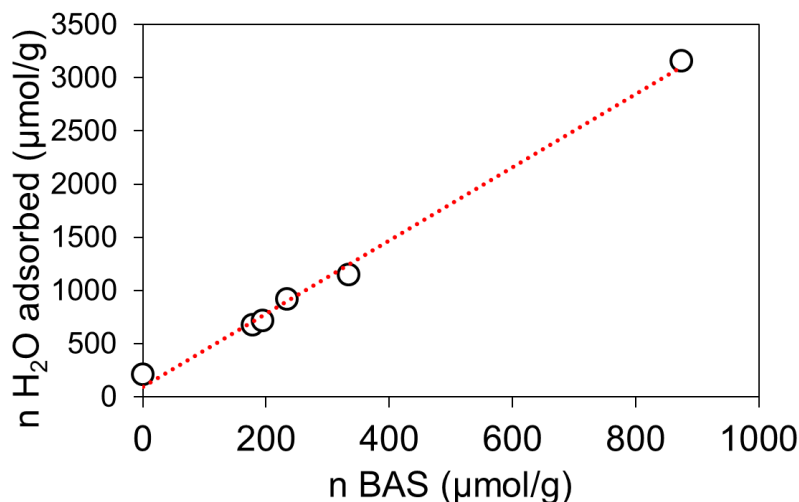


**Figure S5:** Linear correlation between Bronsted acid sites calculated after Pyridine adsorption and the quantity of adsorbed water at water partial pressure  $P/P_0 = 0.0065$ , for MFI zeolites with different Si/Al ratios.

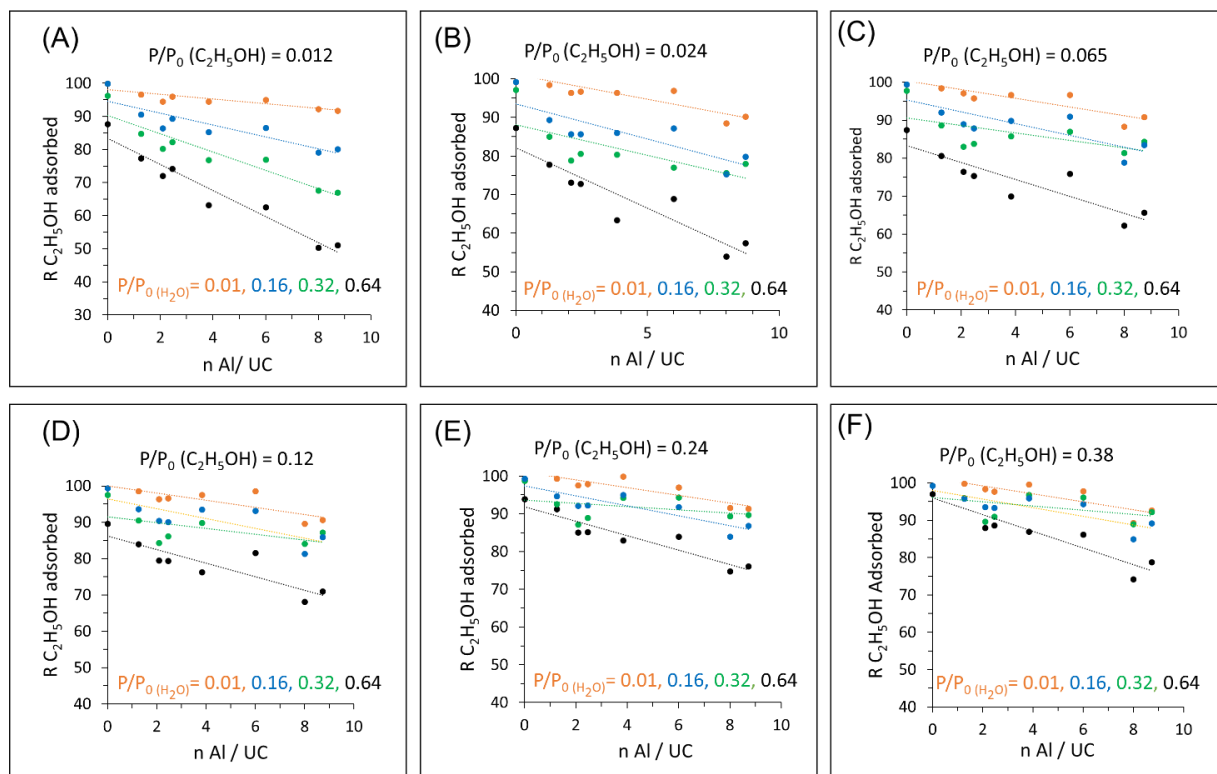


**Figure S6:** Ratio of adsorbed  $C_2H_5OH$  vs the number of Al per unit cell for  $P/P_0 C_2H_5OH = 0.012$  (A), 0.024 (B), 0.065 (C), 0.12 (D), 0.24 (E) and 0.38 (F) after adsorption of different water partial pressures ( $P/P_0 H_2O = 0.01$  (orange),  $P/P_0 H_2O = 0.16$  (blue),  $P/P_0 H_2O = 0.32$  (green) and  $P/P_0 H_2O = 0.64$  (black)) for different MFI zeolites.





# CHAPTER FOUR

---

Synthesis of silica-polymer core-shell hybrid materials with enhanced mechanical properties using a new bifunctional silane-based photoinitiator as coupling agent

---



## General introduction

The synthesis of core-shell materials has been extensively studied to improve the synthesis steps and ameliorate the homogeneity of the final hybrid material [1]. Particularly, hybrid inorganic-organic UV-curable materials have emerged to be good candidates for different daily life applications (cosmetics, clothing, carpentry, polish and paintings, glue, holography, dentistry, packaging, contact lenses, security glass, etc) [2-4]. In fact, polymerization reactions are chemical reactions that transform a liquid mixture (formed of monomers or oligomers) into a solid material (polymer) in few seconds. These transformations occur due to a certain activation energy that can be acquired either thermally or upon irradiation. Thermally induced polymerization reactions are characterized by their relatively slow reaction, high cost, high energy consumption and the presence of solvents, releasing significant amount of volatile organic compounds (VOCs) [5]. However, the photo-induced chemical reactions are considered fast reactions, environmentally friendly and less energy consuming [6]. These reactions occur at room temperature in the absence of solvent, reducing thus the emission of VOCs [7, 8]. During the photochemical induced polymerization, a light source (UV-Visible) transforms a photosensitive solution into a solid film, designed for different applications [2]. The photosensitive solution is usually formed of a monomer and the inorganic reactant. When none of the reactants can adsorb the photochemically active light, the presence of a photoinitiating system is mandatory [9, 10].

Besides its role in initiating the polymerization after absorbing the light, the photoinitiating system, grafted on the surface of the inorganic material, can be used as a coupling agent to prevent the agglomeration of the core nanoparticles, and limit the formation of clusters to assure a homogenous dispersion in the polymeric matrix. It also allows to control the thickness, the density and the functionality of the formed polymer [11, 12]. Depending on the nature of the formed initiating species, three different types of photopolymerization reactions can occur: radical, cationic or anionic [13]. Particularly, in radical photopolymerization, radicals are generated in the solution by two different mechanisms based on the type of the used photoinitiator [14, 15]. Type I photoinitiators (aromatic ketones) undergo a type Norrish I cleavage at the  $\alpha$  bond of the excited carbonyl [16]. Type II photoinitiators (benzophenone, tertiary

amines) form excited molecules upon light absorption, that abstract or initiate a fast electron transfer from creating thus an H-donor radical. The latter molecule is responsible for initiating the polymerization reaction [17]. Due to the back-electron transfer, the biomolecular process and the solvent cage effect in aqueous solutions type II systems are less efficient than the type I systems [18].

Among the different commercial photoinitiators DMPA, Irgacure 2959, and TPO are used [19, 20]. Upon UV irradiation and when grafted on the surface of the inorganic material, these photoinitiators generate benzoyl radicals on the surface and ketyl radicals released in the solution. However, benzoyl radicals are less efficient than ketyl radicals [21, 22]. Therefore, it was important to develop a new photoinitiator that generates ketyl radicals on the surface and releases benzoyl radicals in the solution.

For this, El-Roz et al. developed a new silane-based-photoinitiator efficient in polymerizing an acrylate monomer [23, 24]. In the upcoming section, the synthesis of the photoinitiator, its grafting on silica nanoparticles and zeolites, and its efficiency in the free-radical polymerization of trimethylolpropane triacrylate (TMPTA) monomer, and the characterization of the synthesized hybrid materials will be discussed. Finally, the hybrid materials are tested in the preferential adsorption and separation of water and/or ethanol. The mechanistic studies of adsorption, separation, and diffusion are studied using IR spectroscopy.

## References

1. Ghosh Chaudhuri, R. and S. Paria, *Core/shell nanoparticles: classes, properties, synthesis mechanisms, characterization, and applications*. Chemical reviews, 2012. **112**(4): p. 2373-2433.
2. Mendes-Felipe, C., et al., *State-of-the-art and future challenges of UV curable polymer-based smart materials for printing technologies*. Advanced Materials Technologies, 2019. **4**(3): p. 1800618.
3. Zheng, Z., et al., *Visible light-induced 3D bioprinting technologies and corresponding bioink materials for tissue engineering: A review*. Engineering, 2021. **7**(7): p. 966-978.
4. Zhao, L., et al., *Recent advances in functional 3D printing of foods: A review of functions of ingredients and internal structures*. Critical Reviews in Food Science and Nutrition, 2021. **61**(21): p. 3489-3503.
5. Yagci, Y., S. Jockusch, and N.J. Turro, *Photoinitiated polymerization: advances, challenges, and opportunities*. Macromolecules, 2010. **43**(15): p. 6245-6260.
6. Ibrahim-Ouali, M. and F. Dumur, *Recent advances on chalcone-based photoinitiators of polymerization*. European Polymer Journal, 2021. **158**: p. 110688.
7. Layani, M., X. Wang, and S. Magdassi, *Novel materials for 3D printing by photopolymerization*. Advanced Materials, 2018. **30**(41): p. 1706344.
8. Dietlin, C., et al., *Photopolymerization upon LEDs: New photoinitiating systems and strategies*. Polymer Chemistry, 2015. **6**(21): p. 3895-3912.
9. Fouassier, J.P., et al., *Photoinitiators for free radical polymerization reactions*. Photochemistry and photophysics of polymer materials, 2010: p. 351-419.
10. Decker, C., *The use of UV irradiation in polymerization*. Polymer International, 1998. **45**(2): p. 133-141.
11. Kahraman, M.V., et al., *Synthesis of a novel bifunctional photoinitiator: hybrid coatings on polycarbonate*. Macromolecular Chemistry and Physics, 2007. **208**(14): p. 1572-1581.
12. Kahraman, M.V., et al., *The novel use of organo alkoxy silane for the synthesis of organic-inorganic hybrid coatings*. Journal of non-crystalline solids, 2006. **352**(21-22): p. 2143-2151.
13. Tasdelen, M.A., J. Lalevée, and Y. Yagci, *Photoinduced free radical promoted cationic polymerization 40 years after its discovery*. Polymer Chemistry, 2020. **11**(6): p. 1111-1121.
14. Fouassier, J.-P., *Photoinitiation, photopolymerization, and photocuring: fundamentals and applications*. 1995: Hanser.
15. Koehler, M. and J. Ohngemach, *Coreactive photoinitiators for surface polymerization*. 1990, ACS Publications.
16. El-Roz, M., et al., *Mechanistic investigation of the silane, germane, and stannane behavior when incorporated in type I and type II photoinitiators of polymerization in aerated media*. Macromolecules, 2009. **42**(22): p. 8725-8732.
17. Davidson, R.S., A.A. Dias, and D. Illsley, *A new series of type II (benzophenone) polymeric photoinitiators*. Journal of Photochemistry and Photobiology A: Chemistry, 1995. **89**(1): p. 75-87.
18. Ullrich, G., et al., *Phenylglycine derivatives as coinitiators for the radical photopolymerization of acidic aqueous formulations*. Journal of Polymer Science Part A: Polymer Chemistry, 2006. **44**(1): p. 115-125.
19. Bagheri, A. and J. Jin, *Photopolymerization in 3D printing*. ACS Applied Polymer Materials, 2019. **1**(4): p. 593-611.
20. Zhang, J. and P. Xiao, *3D printing of photopolymers*. Polymer Chemistry, 2018. **9**(13): p. 1530-1540.
21. Colley, C.S., et al., *Probing the reactivity of photoinitiators for free radical polymerization: time-resolved infrared spectroscopic study of benzoyl radicals*. Journal of the American Chemical Society, 2002. **124**(50): p. 14952-14958.

22. Jockusch, S. and N.J. Turro, *Radical addition rate constants to acrylates and oxygen:  $\alpha$ -hydroxy and  $\alpha$ -amino radicals produced by photolysis of photoinitiators*. Journal of the American Chemical Society, 1999. **121**(16): p. 3921-3925.
23. EL ROZ, M.L., Sami ; TELEGEIEV, Igor *New photoinitiator based on bifunctional silane*. CNRS innovation, 2017.
24. El Roz, M., S. Lakhdar, and I. Telegeiev, *Novel photoinitiators made from bifunctional silane*, in *U.S. Patent Application*. 2021. p. 16/764805.





## **Synthesis of silica-polymer core-shell hybrid materials with enhanced mechanical properties using a new bifunctional silane-based photoinitiator as coupling agent**

Rita Zakhia Douaihy <sup>a,1</sup>, Igor Telegeiev <sup>a,1</sup>, Hussein Nasrallah <sup>a</sup>, Oleg Lebedev <sup>b</sup>, Philippe Bazin <sup>a</sup>, Alexandre Vimont <sup>a</sup>, Jean-François Chailan <sup>c</sup>, Armand Fahs <sup>c</sup>, Mohamad EL-Roz<sup>a,\*</sup>

<sup>a</sup> Normandie Université, ENSICAEN, UNICAEN, CNRS, Laboratoire Catalyse et Spectrochimie, 14050 Caen, France

<sup>b</sup> Normandie Université, ENSICAEN, UNICAEN, CNRS, Laboratoire CRISMAT, 14050 Caen, France

<sup>c</sup> Université de Toulon, Laboratoire MAPIEM, 83041 Toulon Cedex 9, France

<sup>1</sup> Equal contribution

\* Corresponding author

**Article published in Materials Today Communication**

<https://doi.org/10.1016/j.mtcomm.2021.102248>

## Abstract

Here, we report the use of new bifunctional silane-based type-1 photoinitiator (SPI-1) as a coupling agent for photopolymer filler and silica grafting. The SPI-1 is grafted on the surface of silica nanoparticles via interactions between the ethoxy group of the silane and the silanol groups of the silica surface. The grafted particles are then dispersed or embedded in/with acrylate polymer by a direct photopolymerization process. The materials were characterized using different techniques including UV-visible spectroscopy, FTIR, TGA, and TEM. Their mechanical properties and the surface morphology were also investigated using AFM and DMA analyses. A significant change and enhancement of the mechanical properties of the newly synthesized materials were observed with respect to that of the unmodified silica. The analysis of the morphology at the microscale level reveals interesting information on the origin of this enhancement and on the dispersion of the filler in the polymer matrix.

## 1. Introduction

Hybrid materials have received extensive interest and gained their effectiveness due to their excellent characteristics and their dramatic improvements in the material properties. Particularly, hybrid inorganic-organic UV-curable materials have emerged to be good candidates in different application fields such as in microelectronics, photolithography for micro and macro 3D printing, plastics, adhesives and coatings [1-9]. The rapid, inexpensive and environmentally friendly synthesis of these materials is based on the treatment of a photosensitive substance, the so-called photoinitiator, using light radiation to promote the polymerization of the organic layer [10-12]. Moreover, during the free radical photopolymerization, photoinitiators absorb the appropriate wavelength, generate primary radical species by  $\alpha$ -cleavage (type I) or H-abstraction (type II) depending on their type, and initiate therefore the polymerization [13-16]. However, various inert or active oxides (e.g. silica,  $\text{TiO}_2$ , etc.) are used as filler (core) to attend the desired properties of the hybrid products. When none of the reactants is capable of absorbing the photochemically active light, the grafting of an active photoinitiator on the surface of the support becomes crucial [17]. In fact, modifying the surface of the core reactant has been widely used in thermal polymerization (e.g. rubber vulcanization) since it prevents the agglomeration of the core nanoparticles, inhibits clusters formation, assures thus a homogeneous dispersion and simultaneously controls the thickness, the density and the functionality of the formed polymer [18-20].

Silica nanoparticles are commonly used as fillers for hybrid inorganic-organic UV-curable materials [7, 21, 22]. Their importance is due to the fact that they are optically inert, low toxic, highly abundant, thermally and chemically stable and permeable to template molecules. Their surface is highly rich in silanol groups, so they are extremely hydrophilic and are not adequate for a homogeneous dispersion in the polymer matrix [23]. Grafting core active photoinitiators on the silica surface allows their good dispersion and assures their stability by increasing their hydrophobicity. Therefore, strong covalent chemical interactions are generated between them and the polymer matrix, respectively [24].

Herein, a newly synthesized silane-based bifunctional type I photoinitiator coupling agent (SPI-1) [25, 26] is tested in the free-radical photopolymerization on the surface of silica nanoparticles. Particularly, SPI-1 is grafted on the surface of silica nanoparticles via interactions between the silane and the silanol groups on the silica surface. Then, highly active ketyl radicals are generated on the silica surface by direct fragmentation under UV irradiation. The efficiency of these grafted radicals is investigated in the photopolymerization of trimethylolpropane triacrylate (TMPTA). The hybrid materials are characterized using UV-visible and FTIR spectroscopies. The mechanical properties of the films are also exploited using AFM and DMA analyses. The reported results are compared with that obtained by using the parent polymer film. Finally, a photopolymerization in solution is tested to elucidate the mechanical properties and to examine the morphological aspects of the synthesized material.

## 2. Materials and methods

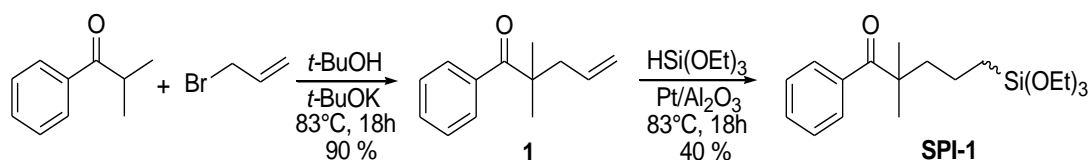
### 2.1. Materials

The chemicals, purchased from Aldrich, were used without any further purification: Isobutyrophenone (IBP, 97 %), Allyl bromide (99 %), Potassium t-butoxide (99.99 %), Decane ( $\geq 99$  %), Diethyl ether (99 %), Magnesium sulfate (99.99 %), Triethoxysilane (95 %) and Trimethylolpropanetriacrylate (TMPTA) (technical grade). Ultrasil 7000 GR (Evonik-Degussa), with a surface area of 175 m<sup>2</sup>/g and a primary particle size of around 14 nm, was used as silica filler.

### 2.2. Methods

#### 2.2.1. Synthesis of SPI-1

The synthesis of 2,2-dimethyl-1-phenyl-5-(triethoxysilyl) pentane-1-one (SPI-1) is conducted in a two-step reaction (**Scheme. 1**) as described below.



**Scheme. 1:** Schematic representation of the two-step reaction of the synthesis of SPI-1. NMR data of the precursor (**1**) and SPI-1 products are available in supplementary information (Figure S1-S2).

To a solution of isobutyrophenone (10 g, 67 mmol) and *t*-BuOK (15, 128 mmol) in 40 mL of *t*-BuOH, 11 mL of allylbromide (128 mmol) were added dropwise. The overall mixture was stirred for 18 hours at 83 °C and then poured into water and extracted with Et<sub>2</sub>O. The combined organic extracts were dried over Na<sub>2</sub>SO<sub>4</sub> and the solvent was removed at reduced pressure.

Later, a solution of triethoxysilane (685 uL, 3.7 mmol) and precursor **1** (1 g, 5.3 mmol) was stirred with 1.5 g of Pt/Al<sub>2</sub>O<sub>3</sub> 5 wt % at 83 °C without adding any solvent in a Schlenk tube. The reaction was conducted under N<sub>2</sub> for 18 hours. Following that, the mixture was filtered and washed with absolute EtOH<sub>abs</sub> through activated charcoal. The final product was collected after concentration and dried by rotary evaporation.

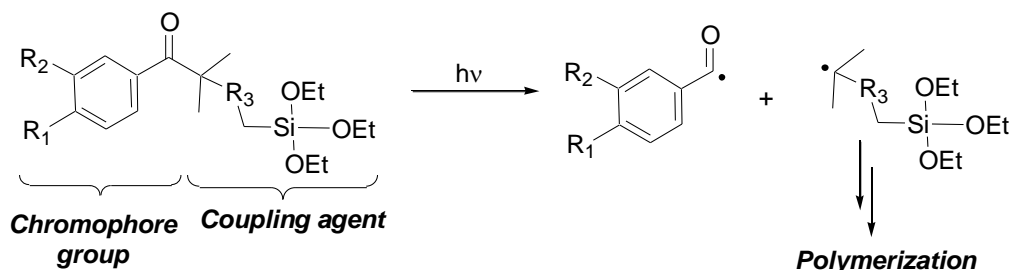
### 2.2.2. Grafting of SPI-1 on the surface of silica nanoparticles

1 g of silica nanoparticles was first dried at 150 °C and then dispersed in 20 mL of decane at 120 °C under vigorous stirring for 10 minutes. Later, 100 mg of the previously synthesized SPI-1 was added. The overall mixture was stirred for 30 minutes. The powder was obtained by centrifugation and re-dispersed in water/ethanol solvent (v/v) to remove the excess of the ungrafted SPI-1 and the solvent. Before characterization, the white precipitate was dried at 50 °C for 12 hours and stored in the dark.

### 2.2.3. Photopolymerization Process

The siloxane functions of the synthesized initiator can promote an efficient grafting of the molecule on the silica surface and the photosensitive group (benzoyl function) promotes the generation of free radicals by direct fragmentation under UV-irradiation (**Scheme. 2**). The UV light used to initiate the photopolymerization was generated by

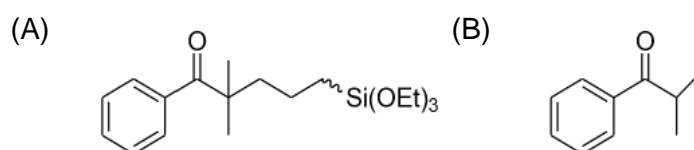
a polychromatic Xe–Hg lamp (LC8-01A spotlight, Hamamatsu, L10852, 200 W,  $I_0 \approx 100 \text{ mW.cm}^{-2}$ ) and was directed through a flexible fiberoptic. The prepared samples are take-free and the conversion degree is between 75 and 80 % for all the samples.



**Scheme. 2:** Schematic representation of the mechanism of the free radical generation under UV irradiation.

#### 2.2.4. Film preparation

Prior to AFM and DMA analyses, three different films were prepared for comparison: 1) pure polymer film; 2) polymer film containing 10 wt.% of ungrafted silica (silica@polymer) and prepared by adding 1 wt% of external photoinitiator (IBP, **Scheme. 3(B)**); and 3) polymer film prepared by the dispersion of 10 wt% grafted silica (SPI-1/silica) without adding the external photoinitiator, designated as SPI-1/silica@polymer film. The films were synthesized using a Teflon spacer of a width of 5 mm and a diameter of 50 mm. Ungrafted and grafted silica nanoparticles were dispersed with the external photoinitiator and the monomer. Few drops of the mixture were spread on polypropylene films and subjected to UV irradiation.



**Scheme. 3:** Schematic representation of (A) SPI-1 and (B) Isobutyrylphenone (IBP).

#### 2.2.5. Photopolymerization in solution

2 mL of acetonitrile (AcN) mixed with few drops of the monomer trimethylolpropane triacrylate (TMPTA) was added to a transparent vial containing 100 mg of SPI-1/Silica. Being one of the mostly used monomer, this trifunctional monomer can lead to a 3D

polymer matrix as a model in this specific polymerization. The mixture was stirred and bubbled with argon for degassing. The photopolymerization was then carried out under polychromatic irradiation and soft stirring at room temperature for 120 seconds. After polymerization, the excess solvent was removed using centrifugation and the precipitate was washed several times with AcN/H<sub>2</sub>O solution (1/1, v/v). The obtained precipitate was dried at 70 °C for more than 12 hours prior to characterization.

### 2.3. Characterization techniques

Diffuse reflectance UV-Vis (DR UV-Vis) measurements of the obtained powder (SPI-1/silica) were performed in the spectral range 200 – 900 nm with a Cary 4000 spectrophotometer (Varian), equipped with Praying Mantis Diffuse Reflection Accessory.

The thermogravimetric analysis was conducted on a SETSYS instrument (SETARAM) analyzer (25–800 °C, a heating rate of 5 °C.min<sup>-1</sup> under 40 mL.min<sup>-1</sup> flow of air) to determine water and hydrocarbon contents in the grafted sample.

FTIR spectroscopy was performed on a ~ 20 mg of the powder pressed (~ 10<sup>7</sup> Pa) into self-supported pellets (2 cm<sup>2</sup> area) and placed in an IR cell equipped with KBr windows. IR spectra were recorded in the region between 400 and 5500 cm<sup>-1</sup> at a resolution of 4 cm<sup>-1</sup> and for 128 scans, using a Nicolet 6700 IR spectrometer equipped with a DTGS detector and an extended-KBr beam splitter.

The AFM measurements were carried out on a Multimode 8 microscope (Bruker) using the PeakForce Quantitative Nanomechanics Mapping mode (PF-QNM). The scans were recorded on three different regions on the films and the maps were collected with 256 x 256 pixels at a scan rate of 1 Hz. The radius of the tip was estimated during the calibration step, was evaluated by the relative method on a polystyrene test sample, and was found to be equal to ~ 50 nm. Silicon probes were selected upon the recommendation of the AFM microscope producer, and the nominal spring constant of the cantilever was 40 N.m<sup>-1</sup> (RTESPA-300). As for the DMA analyses, the experiments were performed on a TA Instrument DMA 2980 in a single

cantilever mode. The dimensions of the sample were about 18 mm x 10 mm x 1 mm (length x width x thickness). A sinusoidal load, automatically adjusted to achieve a displacement of 10  $\mu\text{m}$  at the frequency of 1 Hz, was applied to remain in the viscoelastic range. The storage modulus was recorded from the ambient temperature to 150  $^{\circ}\text{C}$  with a heating rate of 3  $^{\circ}\text{C}\cdot\text{min}^{-1}$ .

The microstructure of the sample was examined using a transmission electron microscopy HAADF-STEM (High-angle annular dark field). TEM micrographs along with the elemental maps were recorded on JEM200F cold FEG double aberration corrected microscope equipped with CENTURIO large-angle EDX detector. Before that, the powder was dispersed in ethanol on a holey carbon film and coated with copper. Low-intensity beam conditions were applied during the measurements to minimize the degradation of the material under the electron beam

### 3. Results and discussion

After grafting on the silica surface, the characteristic bands of the grafted SPI-1 are examined using diffuse reflectance DR UV-visible and transmission FTIR spectroscopies. The DR UV-visible spectrum for the SPI-1/Silica in **Figure 1(A)** shows the presence of new bands centered at 315 and 276 nm. These bands are attributed to the  $n - \pi^*$  (315 nm) and  $\pi - \pi^*$  (230-300 nm) electronic transitions of the benzoyl groups of the SPI-1, respectively. Additionally, the FTIR spectrum of the grafted silica sample in **Figure 1(B)** displays new characteristic bands on the grafted silica pellets (summarized in **Table S1** in the SI), thus confirming the presence of SPI-1 on the silica surface.

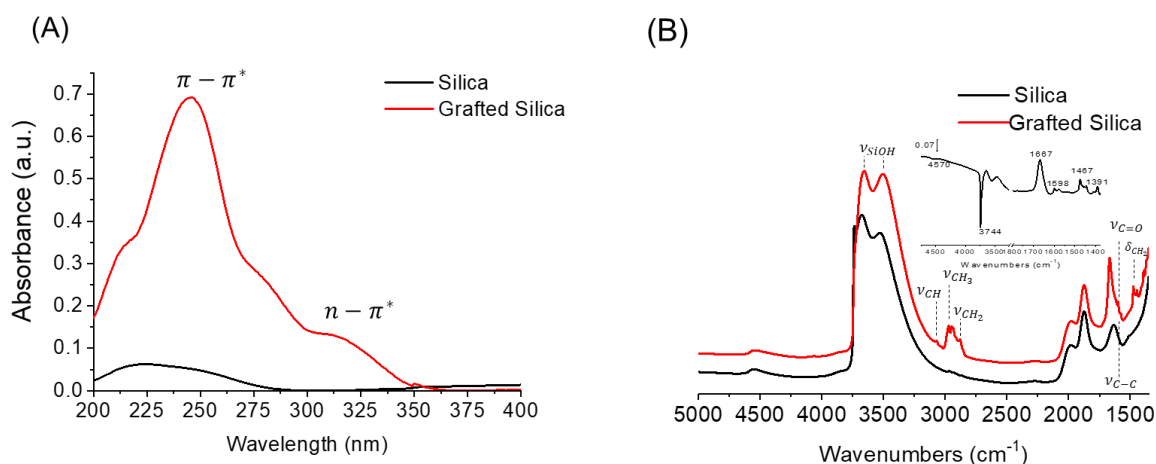


**Figure 1:** (A) Diffuse reflectance UV-visible spectra and (B) FTIR spectra of pure silica nanoparticles and grafted silica with SPI-1. The inset in (B) corresponds to the subtraction result of the FTIR spectra of the grafted silica with SPI-1 from that of the parent silica. FTIR spectra are recorded at RT under vacuum after activation at 150 °C.

Thermogravimetric analysis (TGA) and in-situ FTIR with thermal programmed desorption (TPD) are carried out to determine qualitatively and quantitatively the nature of the interactions between the SPI-1 and the silica surface. The TGA curve of the grafted silica powder is compared to that of the pure silica powder (**Figure 2(A)**). In both cases a first weight loss observed below 100 °C is attributed to the release of water and the desorption resulting from the condensation of the vicinal silanol groups ( $2 \text{ SiOH} \rightarrow \text{SiOSi} + \text{H}_2\text{O}$ ). As for the grafted silica sample, an additional weight loss is observed at relatively high temperature. It cannot be assigned to the condensation of supplementary silanol groups since the vicinal silanol content is similar in both samples (vicinal silanols are not active for grafting). It is then attributed to the thermal degradation of the grafted SPI-1 hydrocarbon. The derivative weight loss versus the temperature reveals three main peaks for SPI-1/Silica samples at 192 °C, 350 °C and 465 °C (**Figure 2(B)**). The peak centered at 192 °C is assigned to the physisorbed SPI-1 and represents less than 20% of the total SPI-1. The peaks at 350 °C and 465 °C are due to the degradation and the total oxidation of the strongly adsorbed SPI-1 species, respectively. Based on these results and considering the similar contents of water and silanol in the parent and in the grafted sample, the SPI-1 loading in this latter is estimated to  $1.7 \pm 0.5 \text{ wt } \%$ .

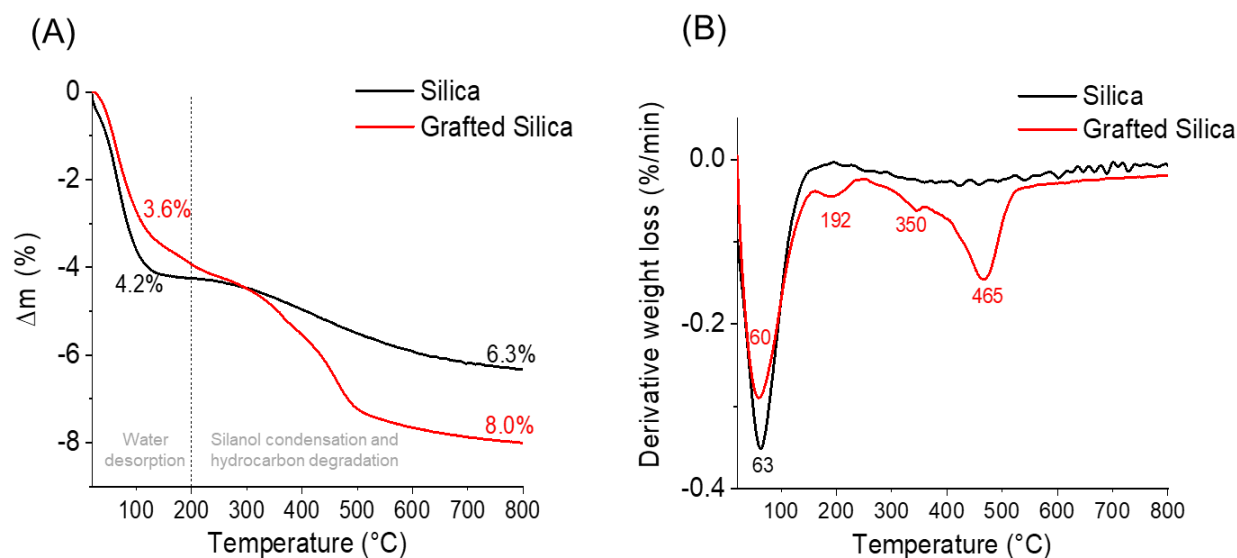


**Figure 2:** Thermogravimetric analysis of the pure silica before grafting with SPI-1 (black) and of the grafted silica with SPI-1 (red). (A) corresponds to the weight loss (%) and (B) corresponds to the derivative weight loss (%/min).

The grafting mechanism between the silane groups and the surface of the silica is generally explained by considering two types of surface interactions [27]: i) physisorption of the silane on the silica via hydrogen bond between the alkoxy function and isolated and terminal silanols, ii) chemisorption via the formation of a covalent bond by condensation of alkoxy function and silanol group forming a Si-O-Si bond and releasing alcohol molecules. The FTIR spectrum of SPI-1/silica recorded at a temperature up to 200 °C under secondary vacuum (**Figure 3(A)**) shows that the decrease in the intensities of the characteristic vibration bands at  $1390\text{ cm}^{-1}$  is weak ( $\sim 12\%$ ) (**Figure 3(B)**), confirming the low amount of physisorbed species and the high thermal stability of the remaining species. According to the literature [28], the high thermal stability of SPI-1 is typical of the covalent attachment of the silanes to the silica surface via the condensation of the alkoxy group with the silanol. Additionally, the comparison of the spectra of silica and SPI-1/silica recorded after evacuation at 200 °C reveal an irreversible decrease in the intensity of the  $\nu(OH)$  band of the isolated silanol functions at  $3744\text{ cm}^{-1}$  (of around 50 %) in the case of SPI-1/silica, showing the grafting of SPI-1 via the condensation of the alkoxy group with the isolated silanol.

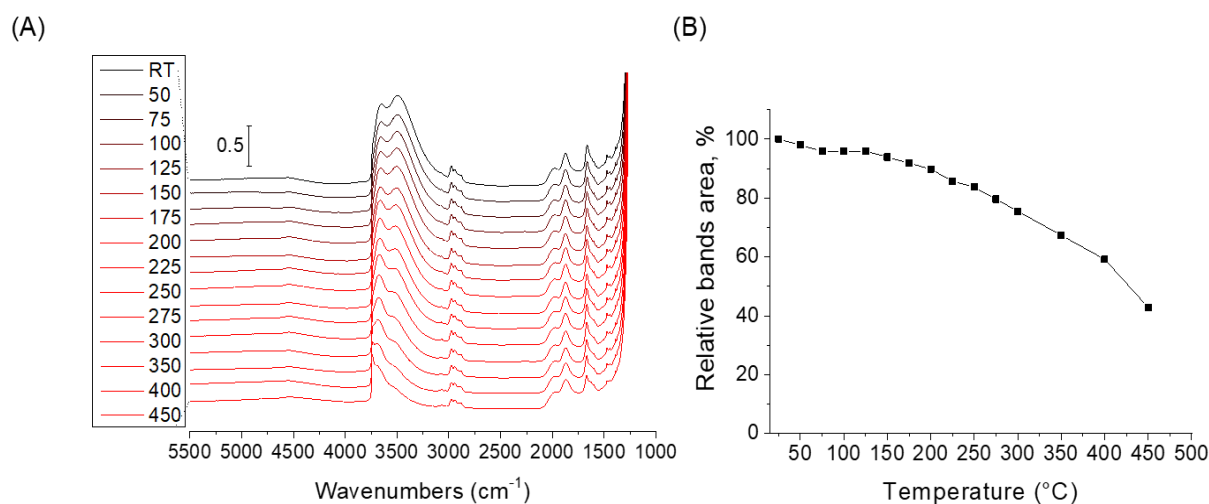


**Figure 3:** (A) Evolution of the FTIR spectra of the grafted silica with SPI-1 as a function of temperature under vacuum ( $P= 10^{-6}$ ) and (B) evolution of the intensity of the vibration band at  $1390\text{ cm}^{-1}$  attributed to the C-H bending of the SPI-1 structure.

After confirming the covalent interactions and the thermal stability of SPI-1 on the surface of the silica particles, a free radical photopolymerization is conducted, whereby radical initiators are created on the surface upon UV irradiation and therefore triggering the polymerization. A kinetic study is performed first to monitor the rate of photopolymerization and measure the conversion of the monomer using *in-situ* FTIR. For this, few drops of trimethylolpropane triacrylate (TMPTA) are added on a SPI-1/Silica self-supported pellet (diameter of the pellet =  $2\text{ cm}^2$  and thickness =  $65\text{ }\mu\text{m}$ ) without adding any external photoinitiator. The sample is placed in the *in-situ* FTIR cell, equipped with KBr windows and then subjected to polychromatic UV light and IR beam under controlled atmosphere (Ar), simultaneously. The evolution of the FTIR spectra along with the conversion yield are represented in **Figure 4**. The conversion is measured by the evolution of the characteristic stretching band of the C=C (at  $1635\text{ cm}^{-1}$ ) of the monomer, and is calculated according to the following equation:

$$\text{Conversion (\%)} = (A_0 - A_t)/A_0 * 100$$

where  $A_0$  and  $A_t$  correspond to the band area at  $t = 0$  and  $t = t$  of the photopolymerization, respectively.

The results reveal a high yield conversion  $\sim 75\%$  after 300 s of irradiation confirming that the SPI-1 is still highly photoactive after its grafting on the surface of

the silica. No polymerization observed when using pure silica without external photoinitiator under similar conditions. This result demonstrates the effectiveness of the grafted SPI-1.

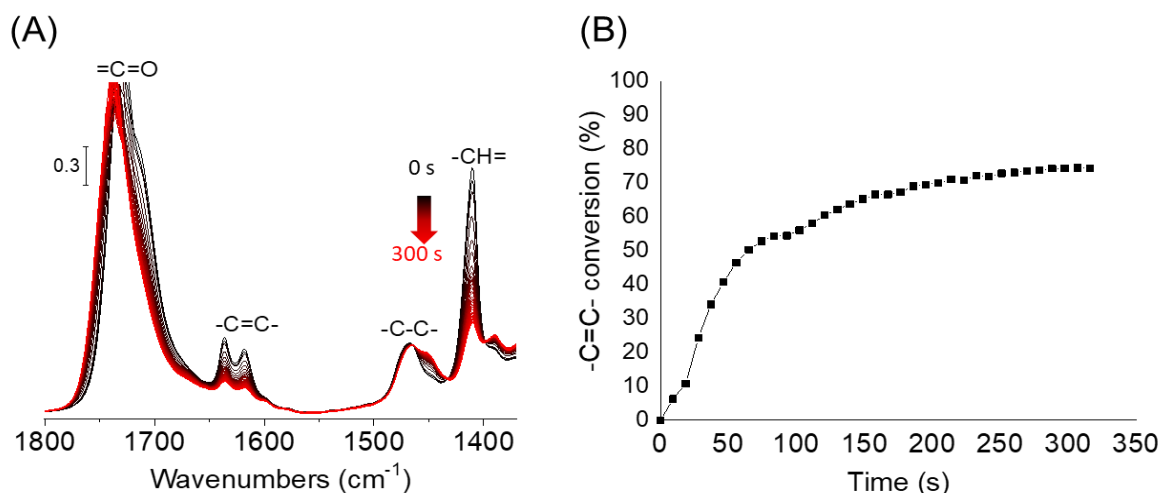


**Figure 4:** (A) Evolution of the FTIR spectra of SPI-1/silica pellet with 10 wt% of TMPTA during photopolymerization. (B) Kinetic behavior of the photopolymerization of the TMPTA.

Upon the successful synthesis of these hybrid materials via photopolymerization, their mechanical properties are examined using atomic force microscopy (AFM) and dynamic mechanical analysis (DMA). The topographic maps represented in **Figure 5** reveal smooth surfaces with nanometric roughness for the three films (**Figure 5(A)**). The surface elastic modulus is calculated using DMT model in contact mechanics [29] and is found to be two to three times higher in SPI-1/silica@polymer film ( $2.1 \pm 0.2$  GPa) than that in silica@polymer film and pure polymer (**Figure 5(B) and 5(C)**). Nanodomains (50 nm) with high elastic modulus are also observed on the SPI-1/silica@polymer film. No differences are detected in the surface elastic modulus ( $1.3 \pm 0.1$  GPa) between the films of the pure polymer and the silica@polymer with a heterogeneous dispersion of silica agglomerates in this latter. This rise is attributed to the homogenous and high dispersion of the grafted silica particles whereas ungrafted particles are heterogeneously dispersed or agglomerated in the bulk of the polymer film.

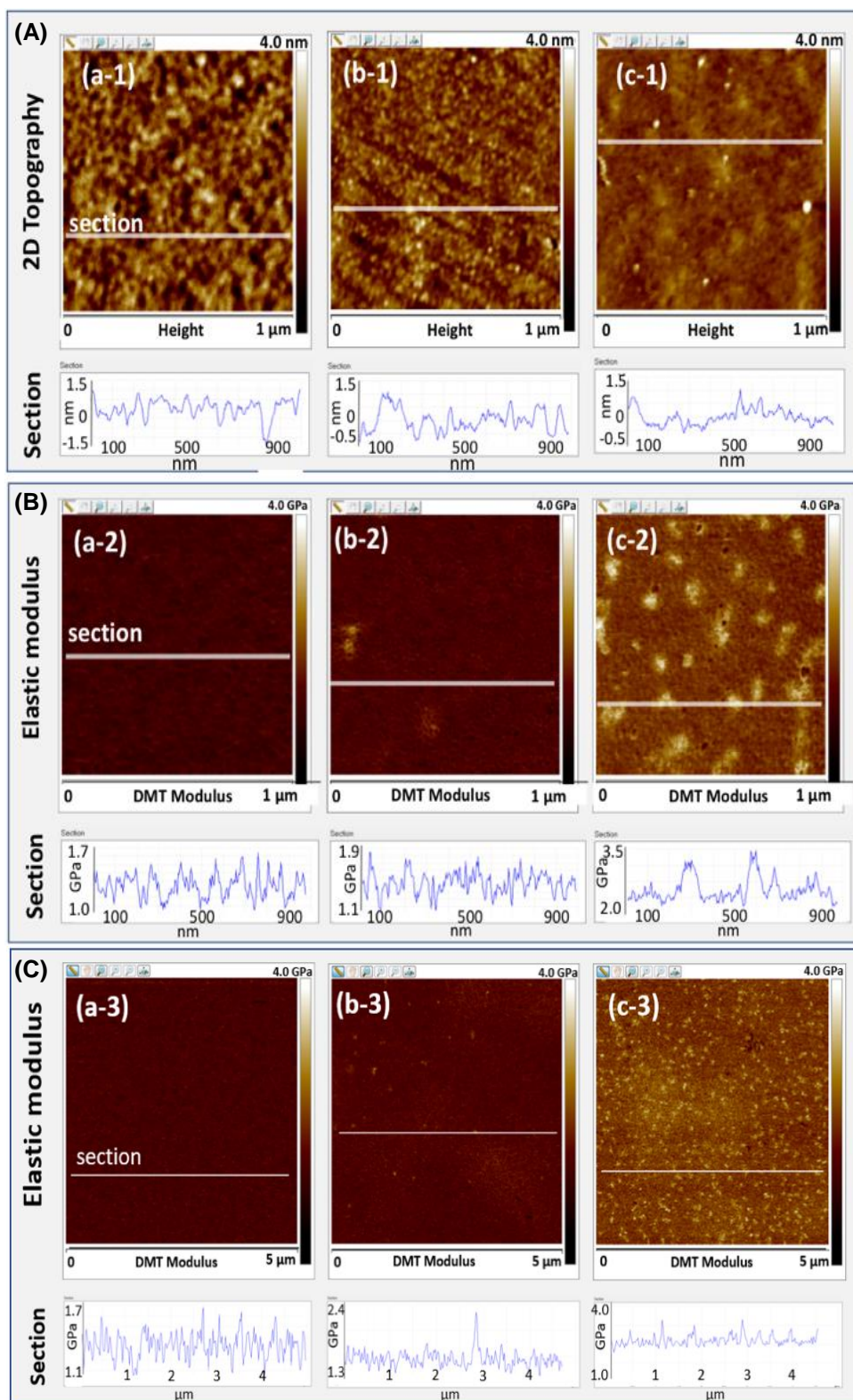


**Figure 5:** (A) AFM topographic images at 1  $\mu\text{m}$  scale (z scale 4 nm) and (B-C) mechanical maps at two different scales 1  $\mu\text{m}$  and 5  $\mu\text{m}$  respectively (z scale 4 GPa) of (a) pure polymer, (b) silica@polymer and (c) SPI-1/silica@polymer films. The white lines on the images correspond to the analysis range of the section's measurements illustrated at the bottom of each image.

The notable increase of the elastic modulus of the SPI-1/silica@polymer film is further investigated by the dynamic mechanical analysis since AFM is limited to report the properties of the surface. In fact, the DMA analysis scrutinizes the overall properties of the material. The elastic modulus ( $E'$ ) of the pure polymer calculated from AFM and DMA are similar (about 1.3 GPa). Nevertheless, after adding ungrafted silica particles to the polymer film, a slight increase of the modulus ( $E'$ ) is observed. An important increase of  $E'$  is calculated from the dynamic mechanical analysis for the SPI-1/silica@polymer film. This surge, obtained also from AFM experiments, indicates that the enhancement of the mechanical properties is not only detected on the surface but in the vicinity of the polymer matrix. The evolution of the elastic modulus as a function of temperature is also exploited for the three films (**Figure 6**). Its decrease is observed with the increase of the temperature for all the samples. This is due to the polymer softening upon heating. In accordance with AFM and DMA experiments, SPI-1/silica@polymer film has the highest modulus at different temperatures relative to pure polymer and ungrafted silica/polymer films. The pure polymer and the SPI-1/silica@polymer films behave similarly with the increase of temperature: a decrease of the storage modulus for both films is registered with the increase of the temperature. However, two remarkable decreases of the storage modulus of the silica@polymer film at 95 °C and 110 °C are distinguished. These shifts are probably due to the cracks of the film under the oscillation force indicating the presence of weak interfacial regions between the polymer matrix and the filler particle which promotes the propagation of cracks. The absence of these cracks in the SPI-1/silica@polymer film is consistent with the enhancement of the interfacial interactions between silica nanoparticles and the surrounding polymer matrix. The highest elastic modulus is obtained when the content of SPI-1/Silica reaches 7.5 % (**Figure S3**).

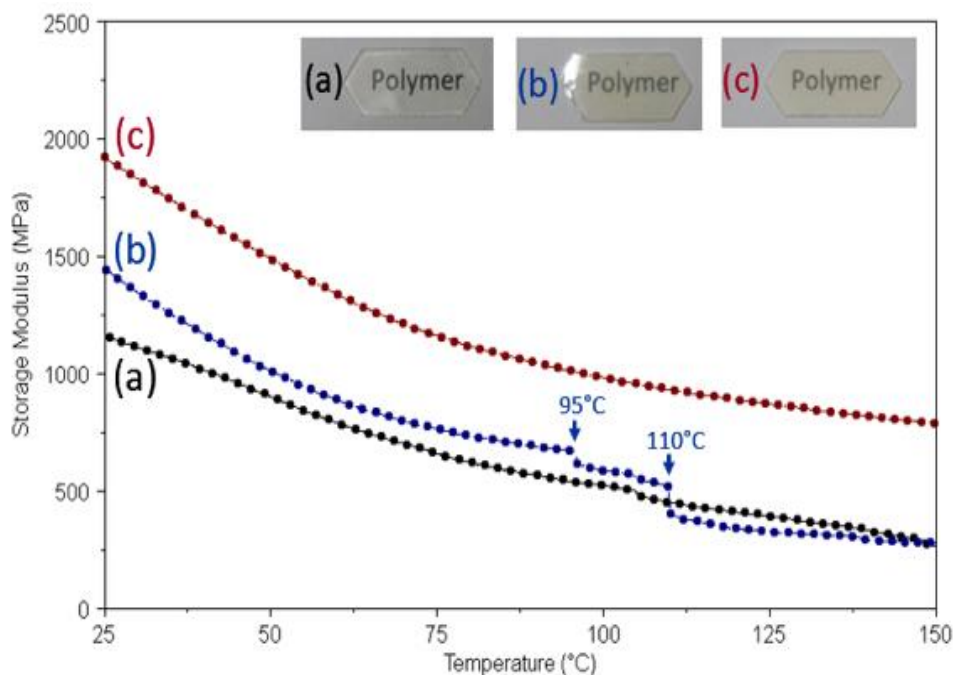


**Figure 6:** Evolution of the storage modulus studied by DMA of (a) the pure polymer film, (b) ungrafted silica/polymer and (c) SPI-1/silica@polymer film. Silica content = 10 wt.%. Sinusoidal strain of 10  $\mu\text{m}$  max at a frequency of 1 Hz, heating rate 3  $^{\circ}\text{C}\cdot\text{min}^{-1}$ .

To elucidate the origin of the prominent mechanical properties reported above, photopolymerization is studied in solution where the monomer is diluted in a solvent, to capture isolated particles. SPI-1/silica powder is dispersed in a solution of acetonitrile and then the photopolymerization is carried out under controlled atmosphere (Ar) and vigorous stirring in the presence of the monomer (TMPTA). The SPI-1/silica: monomer ratio is estimated by thermogravimetric analyses (TGA) and determined to be highest at 1:5 (**Figure S4**). Accordingly, a ratio of 1:5 wt./wt. of silica/monomer is adapted. The collected powder is subjected to TEM-EDX analysis to examine its morphology. The TEM micrographs in **Figure 7(A-B)** reveal a total coverage of silica particles by a shell layer of polymer. A close-up image on a single particle of  $\text{SiO}_2$ . **Figure 7(C)** shows the presence of a core-shell composite where silica particle is totally covered by an external shell layer of polymer. Furthermore, the EDX elemental maps in **Figure 7(D)** represent the distribution of silicon, oxygen and carbon through which a consistent distribution of Si and O is observed where silica nanoparticles are present. A remarkable dispersion of carbon is noticed on the surface of silica nanoparticles, confirming thus the presence of a polymer shell layer on the surface of the silica nanoparticles.

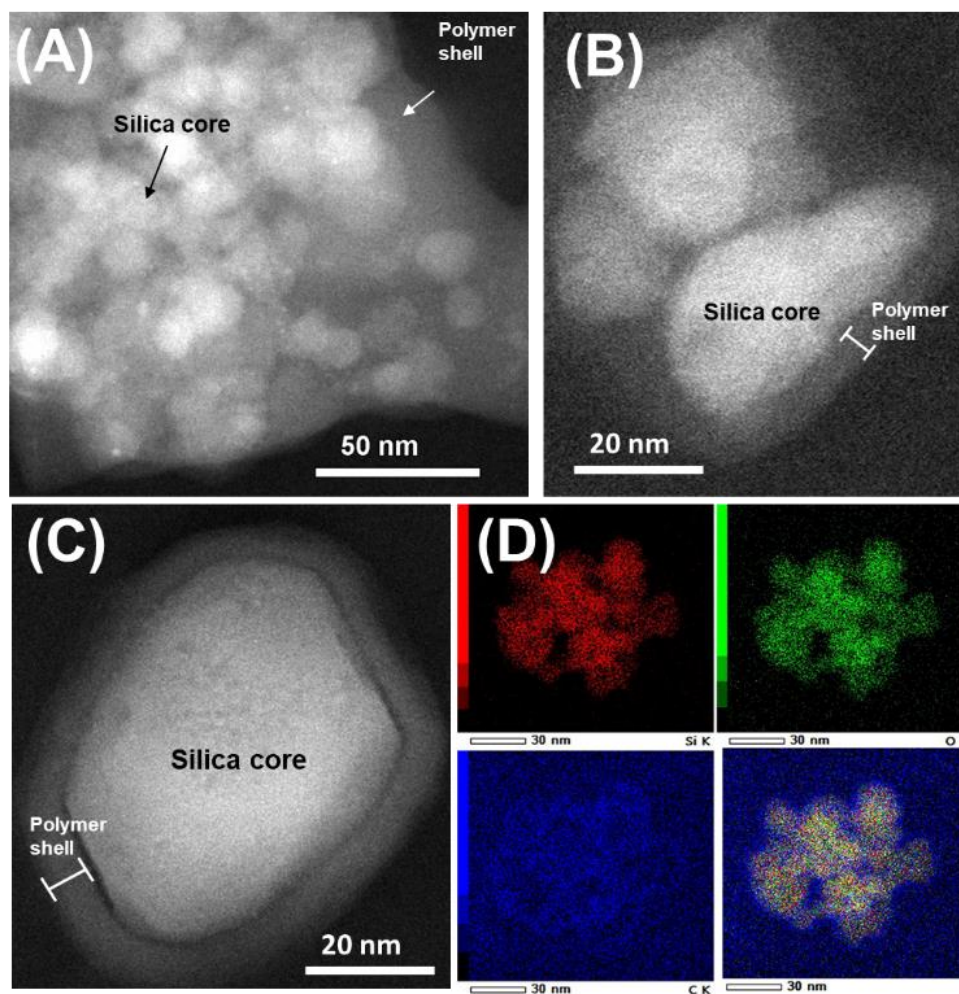


**Figure 7.**(A-B-C) HAADF-STEM images and (D) EDX elemental mapping of SPI-1/Silica after photopolymerization of TMPTA in the presence of AcN. Si (red), O (green) and C (blue).

The core-shell like structure at the microscale level explains the mechanical behavior at the macroscale level of the polymer film containing SPI-1/Silica filler. The high dispersion of the SPI-1 on the silica surface as well as the covalent bond created between the silica surface and the polymer generate a highly stable hybrid network of ultra-dispersed silica particles with the polymer matrix.

## 4. Conclusion

In conclusion, the efficiency of a newly synthesized silane-based photoinitiator (SPI-1) as a coupling agent for preparing hybrid SPI-1/silica@polymer materials via photopolymerization of trimethylolpropane triacrylate has been tested. Interestingly, the analysis of the mechanical properties of the hybrid materials shows a significant increase of the surface elastic modulus compared to that of the silica/polymer materials prepared using ungrafted silica as reference. The examination of the morphology of the SPI-1/silica@polymer single particles by HAADF-STEM indicates their core-shell structure resulting from a homogeneous polymerization at the silica surface. This behavior explains the increase of the elastic modulus by creating strong covalent bonds between the polymer and the silica surface through the grafting of the SPI-1 on this latter. The new procedure can be applied for preparing different core-shell materials for various applications, such as membranes, chromatographic columns, etc.

## Acknowledgment

Authors acknowledge the Normandy region and European union for the financial support (Carnot project 3DZeoPol).

## Supplementary Information

<sup>1</sup>H NMR and FTIR data of the products synthesized in this work. Evolution of the elastic modulus versus the SPI-1/silica contents. Evolution of the polymer content versus SPI-1/silica@TMPTA ratio used for the photopolymerization of TMPTA in presence of SPI-1/silica suspension in acetonitrile.

## References

1. Corrales, T., et al., *Free radical macrophotoinitiators: an overview on recent advances*. Journal of Photochemistry and Photobiology A: Chemistry, 2003. **159**(2): p. 103-114.
2. Bag, D.S. and K.B. Rao, *Synthesis of UV-curable difunctional silane monomer based on 3-methacryloxy propyl trimethoxysilane (3-MPTS) and its UV-curing characteristics and thermal stability*. Journal of applied polymer science, 2010. **115**(4): p. 2352-2358.
3. Zhou, S., et al., *Preparation, structure and properties of organic-inorganic nanocomposite coatings*. 2009, ACS Publications.
4. Cooperstein, I., M. Layani, and S. Magdassi, *3D printing of porous structures by UV-curable O/W emulsion for fabrication of conductive objects*. Journal of Materials Chemistry C, 2015. **3**(9): p. 2040-2044.
5. Vaezi, M., H. Seitz, and S. Yang, *A review on 3D micro-additive manufacturing technologies*. The International Journal of Advanced Manufacturing Technology, 2013. **67**(5-8): p. 1721-1754.
6. Sangermano, M., et al., *UV-Cured Acrylic Conductive Inks for Microelectronic Devices*. Macromolecular materials and engineering, 2013. **298**(6): p. 607-611.
7. Chang, C.-C., et al., *Preparation of polymer/silica hybrid hard coatings with enhanced hydrophobicity on plastic substrates*. Journal of non-crystalline solids, 2012. **358**(1): p. 72-76.
8. Zhang, L., et al., *Core-shell nanospheres to achieve ultralow friction polymer nanocomposites with superior mechanical properties*. Nanoscale, 2019. **11**(17): p. 8237-8246.
9. Guo, D., et al., *Elastic properties of polystyrene nanospheres evaluated with atomic force microscopy: size effect and error analysis*. Langmuir, 2014. **30**(24): p. 7206-7212.
10. Zhou, J., et al., *Progress in the development of polymeric and multifunctional photoinitiators*. Progress in Polymer Science, 2019. **99**: p. 101165.
11. El-Roz, M., J. Lalevee, and J. Fouassier, *A search for new radical sources in photoinitiating systems*. Current Trends in Polymer Science, 2011. **15**: p. 1-13.
12. El-Roz, M., et al., *Radical and cationic photopolymerization: New pyrylium and thiopyrylium salt-based photoinitiating systems*. Journal of Polymer Science Part A: Polymer Chemistry, 2008. **46**(22): p. 7369-7375.
13. Li, X., et al., *Synthesis of organic and inorganic hybrid nanoparticles as multifunctional photoinitiator and its application in UV-curable epoxy acrylate-based coating systems*. Progress in Organic Coatings, 2020. **141**: p. 105565.
14. Sahin, M., et al., *Photoactive silica nanoparticles: Influence of surface functionalization on migration and kinetics of radical-induced photopolymerization reactions*. European Polymer Journal, 2018. **98**: p. 430-438.
15. Schwalm, R., *UV coatings: basics, recent developments and new applications*. 2006: Elsevier.
16. El-Roz, M., et al., *Mechanistic investigation of the silane, germane, and stannane behavior when incorporated in type I and type II photoinitiators of polymerization in aerated media*. Macromolecules, 2009. **42**(22): p. 8725-8732.
17. Deng, J., et al., *Developments and new applications of UV-induced surface graft polymerizations*. Progress in polymer science, 2009. **34**(2): p. 156-193.
18. Zhao, B. and W.J. Brittain, *Synthesis of polystyrene brushes on silicate substrates via carbocationic polymerization from self-assembled monolayers*. Macromolecules, 2000. **33**(2): p. 342-348.
19. Dworjanyan, P.A., et al., *Novel additives for accelerating radiation grafting and curing reactions*. Radiation Physics and Chemistry, 1993. **42**(1-3): p. 31-40.
20. Chen, R., S. Zhu, and S. Maclaughlin, *Grafting acrylic polymers from flat nickel and copper surfaces by surface-initiated atom transfer radical polymerization*. Langmuir, 2008. **24**(13): p. 6889-6896.

21. Xu, G.C., et al., *Synthesis and characterization of silica nanocomposite in situ photopolymerization*. Journal of applied polymer science, 2003. **90**(3): p. 837-840.
22. Bauer, F., et al., *UV curing and matting of acrylate coatings reinforced by nano-silica and micro-corundum particles*. Progress in Organic Coatings, 2007. **60**(2): p. 121-126.
23. Wu, J., et al., *A comparative study of grafting steps on the preparation and properties of modified nanosilica for UV-curable coatings*. Journal of Coatings Technology and Research, 2014. **11**(5): p. 717-725.
24. Ranjbar, Z. and S. Rastegar, *The influence of surface chemistry of nano-silica on microstructure, optical and mechanical properties of the nano-silica containing clear-coats*. Progress in Organic Coatings, 2009. **65**(1): p. 125-130.
25. EL ROZ, M.L., Sami ; TELEGEIEV, Igor *New photoinitiator based on bifunctional silane*. CNRS innovation, 2017.
26. El Roz, M., S. Lakhdar, and I. Telegeiev, *Novel photoinitiators made from bifunctional silane*. 2021, Google Patents.
27. El-Roz, M., et al., *Silica-silane reaction: Deciphering the silica-silane reaction mechanism for the development of a new generation of low rolling resistance tires*. Tire technology international, 2016. **2016**(43): p. 93-94.
28. El-Roz, M., F. Thibault-Starzyk, and A. Blume, *Infrared study of the silica/silane reaction. Part II*. KGK Kautschuk, Gummi, Kunststoffe, 2014. **67**(5): p. 53-57.
29. Derjaguin, B.V., V.M. Muller, and Y.P. Toporov, *Effect of contact deformations on the adhesion of particles*. Journal of Colloid and interface science, 1975. **53**(2): p. 314-326.

## **Synthesis of silica-polymer core-shell hybrid materials with enhanced mechanical properties using a new bifunctional silane-based photoinitiator as coupling agent**

Rita Zakhia Douaihy <sup>a,1</sup>, Igor Telegeiev <sup>a,1</sup>, Hussein Nasrallah <sup>a</sup>, Oleg Lebedev <sup>b</sup>, Philippe Bazin <sup>a</sup>, Alexandre Vimont <sup>a</sup>, Jean-François Chailan <sup>c</sup>, Armand Fahs <sup>c</sup>, Mohamad EL-Roz<sup>a,\*</sup>

a Normandie Université, ENSICAEN, UNICAEN, CNRS, Laboratoire Catalyse et Spectrochimie, 14050 Caen, France

b Normandie Université, ENSICAEN, UNICAEN, CNRS, Laboratoire CRISMAT, 14050 Caen, France

c Université de Toulon, Laboratoire MAPIEM, 83041 Toulon Cedex 9, France  
1 Equal contribution

\* Corresponding author

### Supplementary Information

$^1\text{H}$  NMR (400 MHz,  $\text{CDCl}_3$ )  $\delta$  (ppm) 7.64 (d, 2H,  $J = 7.9$  Hz), 7.45 (t, 1H,  $J = 7.4$  Hz), 7.39 (t, 2H,  $J = 7.4$  Hz), 5.68-5.76 (m, 1H), 4.99-5.05 (m, 2H), 2.48 (d, 2H,  $J = 7.5$ ), 1.32 (s, 6H).

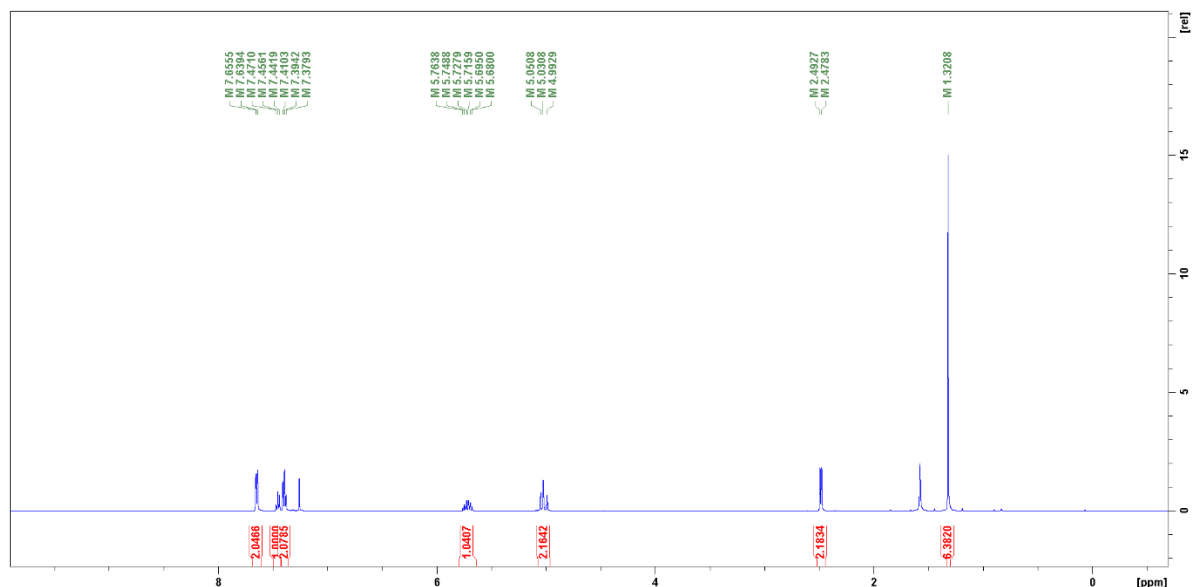


Figure S1:  $^1\text{H}$  NMR Spectrum of precursor 1

$^1\text{H}$  NMR (400 MHz,  $\text{CDCl}_3$ )  $\delta$  (ppm) 7.65 (d, 2H,  $J = 7.8$  Hz), 7.44 (t, 1H,  $J = 7.2$  Hz), 7.38 (t, 2H,  $J = 7.2$  Hz), 3.75 (q, 6H,  $J = 7.0$  Hz), 1.77-1.80 (m, 2H), 1.32-1.38 (m, 2H), 1.29 (s, 6H), 1.18 (t, 9H,  $J = 7.32$  Hz), 0.56 (t, 2H,  $J = 8.1$  Hz).

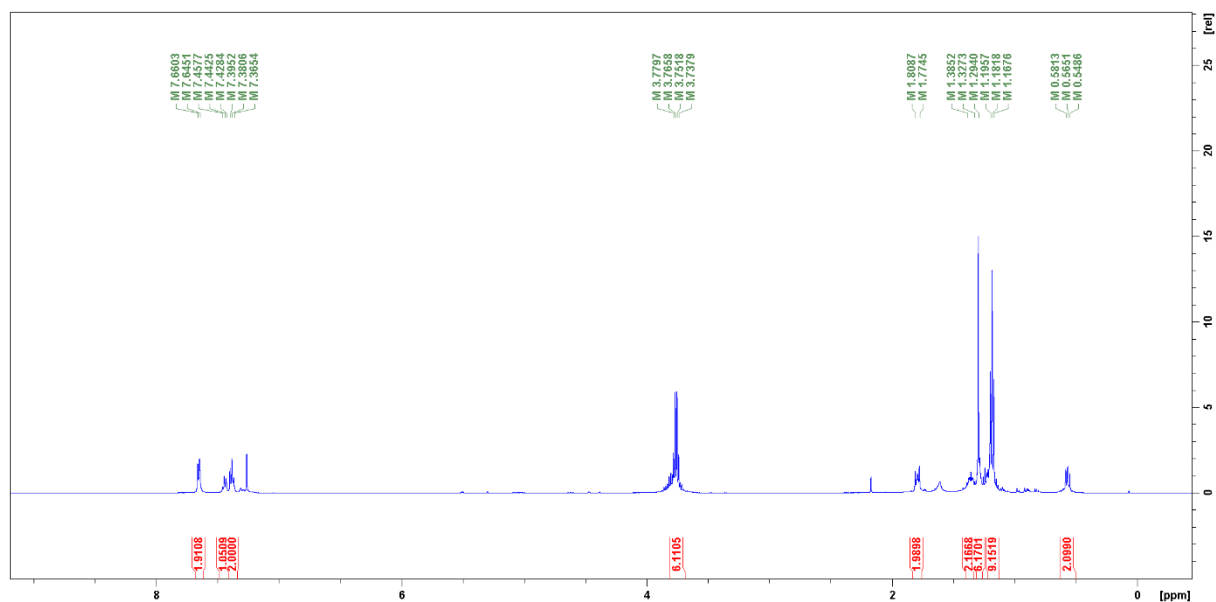
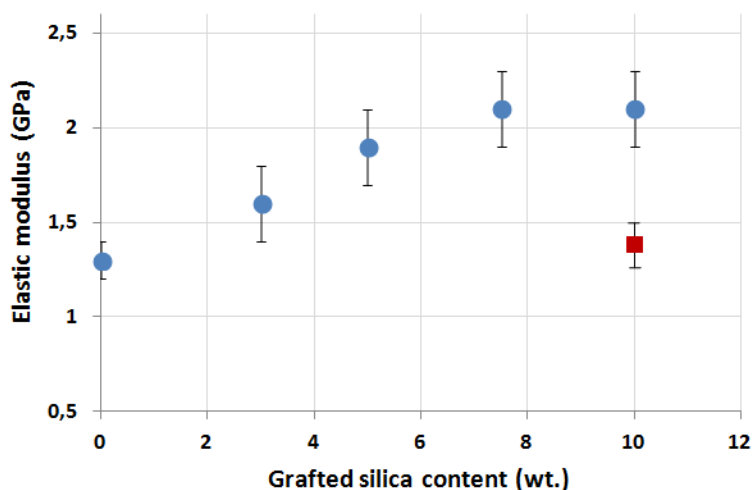


Figure S2:  $^1\text{H}$  NMR Spectrum of SPI-1

**Table S1:** The FTIR characteristic bands of the grafted SPI-1 and their assignments ( $\nu$  – stretch;  $\delta$  – deformation; bend – bending; asym – asymmetric; sym – symmetric)

Band position	Band assignment
3068	$\nu$ (CH)aromatics
2971	$\nu$ ( $CH_3$ ) <i>asym</i>
2941	$\nu$ ( $CH_2$ ) <i>asym</i>
2880	$\nu$ ( $CH_2$ ) <i>sym</i>
1667	$\nu$ (= O) <i>conjugated with phenyl group</i>
1600	$\nu$ (C – C)aromatics
1475	$\delta$ ( $CH_2$ )
1445	$\delta$ ( $CH_2$ )
1391	(CH) <i>bend</i> , $\nu$ ( $CH_3$ ), $\delta$ ( $CH_3$ ) <i>sym</i>



**Figure S3:** Calculated elastic modulus  $E'$  (GPa) as a function of the grafted silica content (wt %) in the polymer matrix from dynamic mechanical analyses. The square corresponds to the value of the ungrafted silica (10 wt%) in polymer.

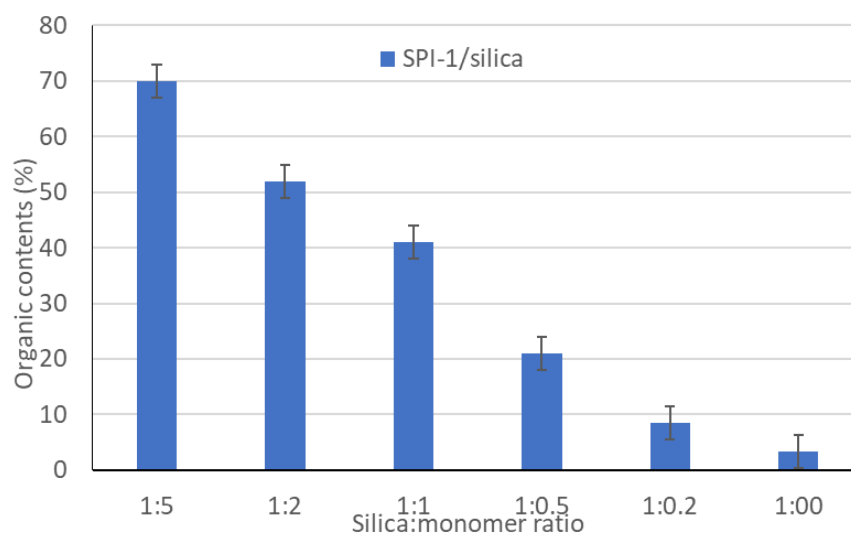


**Figure S4:** Organic contents (estimated by TGA) in silica samples grafted with SPI-I after 5 minutes of photopolymerization of TMPTA in the presence of AcN. The hydrocarbon content in 1:00 silica/monomer ratio samples corresponds to the amount of the grafted molecules before photopolymerization.



---

# APPENDIX I

---



## 1. Introduction

After modifying the mechanical properties of the silica nanoparticles and confirming the core-shell like structure at the macroscopic level by photopolymerization in solution, further experiments were conducted on SPI-1/Silica@polymer particles to determine the exact polymer loading by thermogravimetric analyses and study the textural properties of the hybrid materials by nitrogen adsorption. The materials are afterward used to study the adsorption of ethanol and water by IR spectroscopy.

## 2. Results and discussion

First, thermogravimetric analyses were conducted on SPI-1/Silica@Polymer and compared to that of the grafted silica (**Figure A1**) to determine the quantity of the organic layer on the surface of the silica nanoparticles after polymerization. Similarly to the TG curve of the grafted silica (SPI-1/Silica ((a)-black)) the TG curve of the SPI-1/Silica@Polymer (**Figure A1 ((b)-red)**) reveals a first weight loss (around 4%) below 200 °C, attributed to the water desorption. Above 200 °C, a second weight loss is observed and ascribed to the degradation of the polymer and the remaining SPI-1 structure starting around 400 °C and 505 °C. The calculated total weight loss is around 60 %. Therefore, the quantity of the hydrocarbon loading can be determined to be around  $56 \pm 4 \%$ .

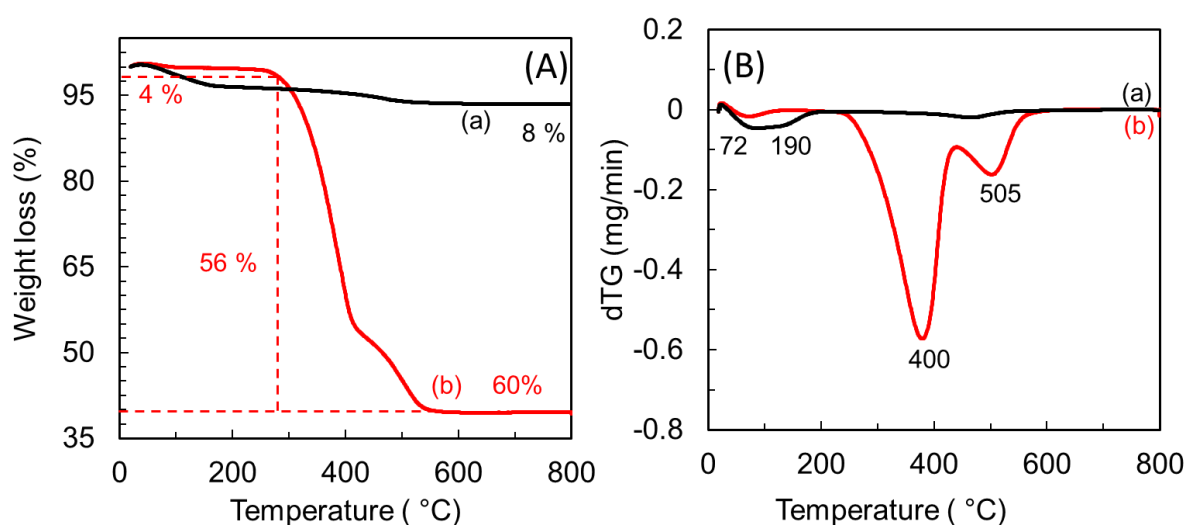


**Figure A1:** Thermogravimetric analysis of the grafted silica with SPI-1 ((a)-black) and SPI-1/Silica@Polymer ((b)-red). (A) corresponds to the weight loss (%) and (B) corresponds to the derivative weight loss (%/min).

After determining the exact hydrocarbon loading, the porosity of pure silica and SPI-1/Silica@Polymer was examined using Nitrogen adsorption at 77 K, after degassing at 150 °C. The textural porosities of both samples are summarized in **Table A1** and the N<sub>2</sub> adsorption/desorption isotherms are represented in **Figure A2**. The porosity in the parent sample is attributed to the textural porosity created between silica nanoparticles. After adding the external polymer layer, a decrease in the BET surface area, the external surface area, the total volume, and the micropore volume are observed. Interestingly, at  $P/P_0 = 0.4-0.5$  during the desorption, a H4-type hysteresis loop is observed for SPI-1/Silica@Polymer (**Figure A2 (b)**). This loop is created upon polymerization on the surface of silica nanoparticles, and suggests that the polymerization process is responsible for generating a supplementary mesoporosity. Therefore, the accessibility to the intermolecular voids is assured by smaller necks, characteristic of core-shell materials.

**Table A1:** Textural properties of Silica and SPI-1/Silica@Polymer texted by N<sub>2</sub> adsorption/desorption at 77 K

	Silica	SPI-1/Silica@Polymer
$S_{\text{BET}}^a$ (m <sup>2</sup> /g)	175	82
External surface area <sup>b</sup> (m <sup>2</sup> /g)	175	72
Total Volume (cm <sup>3</sup> /g)	0.64	0.21
Micropore volume <sup>c</sup> (cm <sup>3</sup> /g)	0.011	0.005

<sup>a</sup> BET surface area, <sup>b,c</sup> *t*-plot.

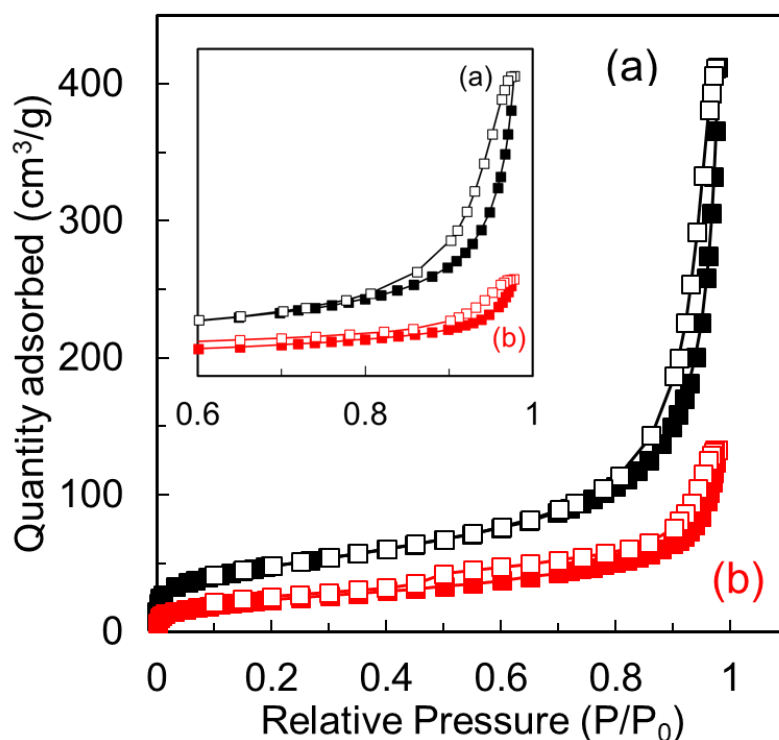


**Figure A2:** N<sub>2</sub> adsorption/desorption isotherms of Silica ((a)-black) and SPI-1/Silica@Polymer ((b)-red) at 77 K. The inset corresponds to zooming on the region of P/P<sub>0</sub> between 0.6 and 1.

After studying the porosity of the samples, the adsorption capacity of the hybrid materials is tested for ethanol and water adsorptions at RT, using the AGIR setup. The evolution of the characteristic bands of ethanol  $\nu_{C-C-O}$  and  $\delta_{CH_3}$  at 880 cm<sup>-1</sup> and 1450 cm<sup>-1</sup>, respectively and that for water at 1630 and 5200 cm<sup>-1</sup> attributed to  $\delta_{H_2O}$  and  $((\delta + \nu)_{H_2O})$ , respectively, was monitored using IR spectroscopy. In our case, due to the presence of a characteristic bands of the polymer at 1475 cm<sup>-1</sup> ( $\delta_{(C-H)}$ ) and 1600 cm<sup>-1</sup> ( $\nu_{C=C}$ ), only the bands at 880 cm<sup>-1</sup> and 5200 cm<sup>-1</sup> were studied (**Figure A3 and A4**). The molar absorption coefficient ( $\epsilon$  (cm.μmol<sup>-1</sup>)) for the characteristic bands of ethanol and that of water are therefore determined upon measuring the corresponding areas and quantifying the adsorbed species (**Figure A5**). A difference between the values of the adsorption coefficients of the two materials is observed for ethanol and water. These differences can be attributed to the presence of different configurations for the adsorption of ethanol and water after adding the polymer layer. Indeed, the shifts of the vibrational characteristic bands observed for SPI-1/Silica@Polymer ( $\Delta\nu = 5$  cm<sup>-1</sup> for  $\nu_{C-C-O}$  and  $\Delta\nu = 30$  cm<sup>-1</sup> for  $((\delta + \nu)_{H_2O})$ ) can explain the different adsorption configurations.

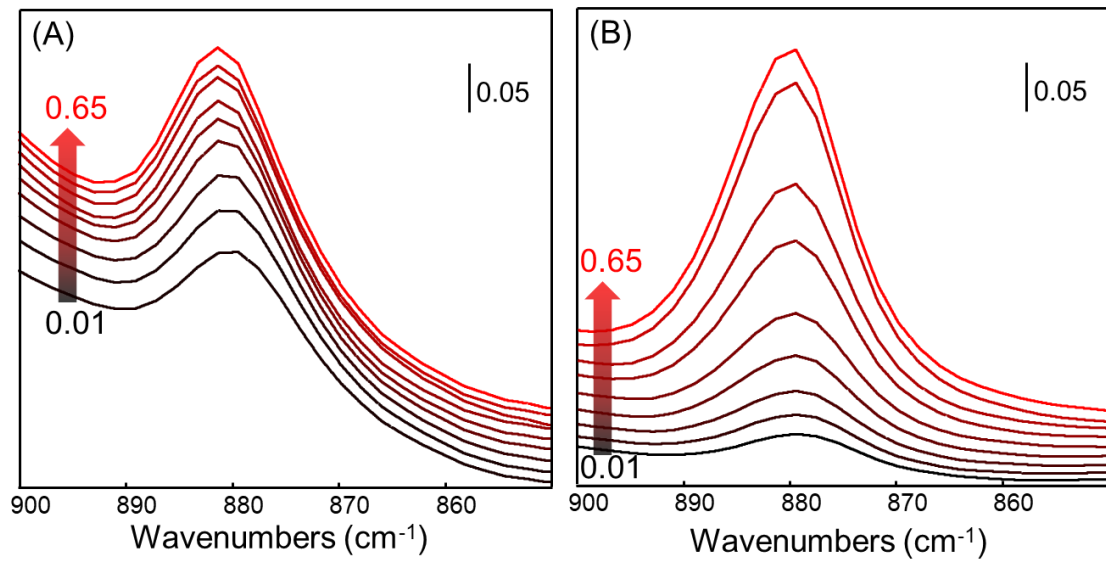


**Figure A3:** Evolution of the IR spectra after ethanol adsorption on (A) Silica, (B) SPI-1/Silica@Polymer (Subtracted spectra). Spectra are normalized to 20 mg of pressed powder.

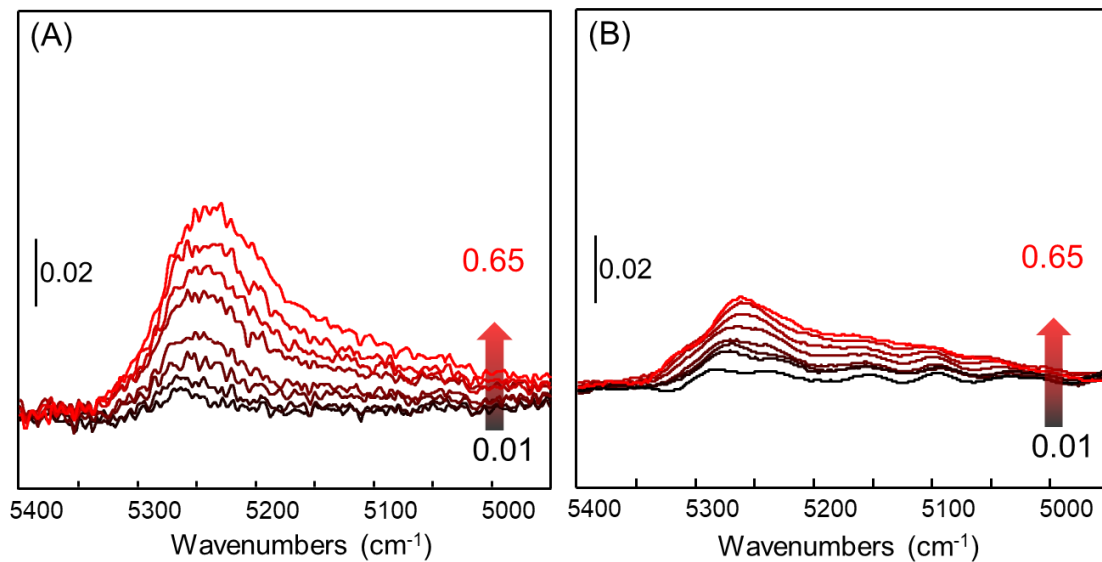


**Figure A4:** Evolution of the IR spectra after water adsorption on (A) Silica, (B) SPI-1/Silica@Polymer (Subtracted spectra). Spectra are normalized to 20 mg of pressed powder.

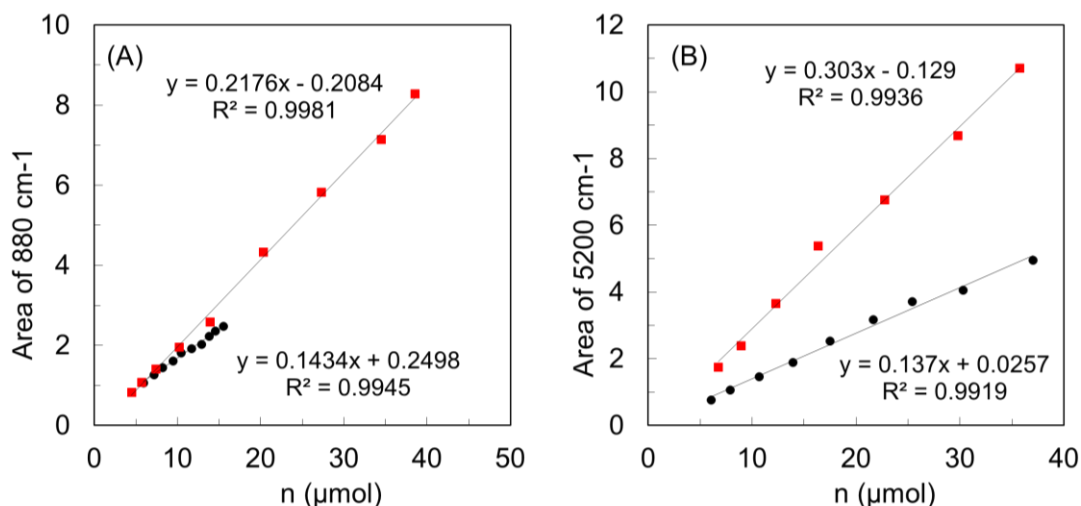


**Figure A5:** Evolution of the area of the characteristic bands of (A) ethanol ( $880\text{ cm}^{-1}$ ) and (B) water ( $5200\text{ cm}^{-1}$ ) as a function of the quantities adsorbed for Silica (black) and SPI-1/Silica@Polymer (red). The molar absorption coefficients are proportional to the slope of the area vs  $n$  (= double the slope) for the characteristic bands.

The gravimetric adsorption isotherms are represented in **Figure A6** after ethanol (**Figure A6(A)**) and water (**Figure A6(B)**) adsorption on silica and SPI-1/Silica@Polymer. Upon ethanol adsorption at low partial pressures, the textural porosity previously determined by nitrogen adsorption is partially filled with ethanol. However, at high partial pressures ( $P/P_0 > 0.3$ ), ethanol is highly adsorbed on the mesoporous polymer layer. The mesoporosity created upon adding the polymer is responsible for this high adsorption capacity. On the other hand, after water adsorption the adsorption capacity of silica is modified. The quantity adsorbed on the hybrid material is lower than that adsorbed on the parent sample. In fact, the presence of the polymeric shell layer disfavors the adsorption of water, making the material more hydrophobic. By comparing the adsorption isotherms of ethanol and water, silica nanoparticles have good capacity to adsorb both adsorbates. However, the capacity of the synthesized hybrid material to adsorb ethanol is higher than that to water. The probable weak interaction between the polymer and water molecules assures the relatively low water adsorption and is therefore accounted for the shift observed in the water vibration band. Therefore, these materials can be tested the separation of ethanol from its aqueous mixture.

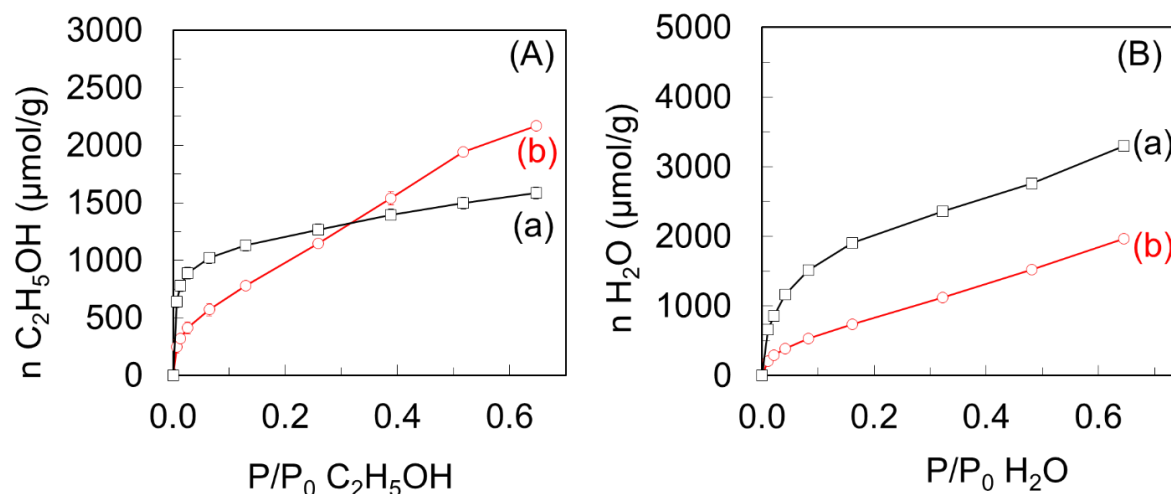


**Figure A6:** (A) Ethanol and (B) water gravimetric adsorption isotherms on Silica ((a)- black) and SPI-1/Silica@Polymer ((b)- red). The adsorptions were conducted at RT.

### 3. Conclusion

In conclusion, after determining the hydrocarbon loading, the textural properties of synthesized materials are tested by nitrogen adsorption. The formation of a hierarchical material via the photopolymerization of TMPTA monomer on the surface of silica nanoparticles is validated. The adsorption of ethanol and water using IR spectroscopy is studied. The adsorption capacity of the hybrid materials towards ethanol increases while that towards water decreases, making the material more hydrophobic. These prominent results suggest the use of this approach in the synthesis of different hierarchical materials, such as zeolites and their applications for the dehydration of ethanol.





# CHAPTER FIVE

---

New approach for preparing zeolite-polymer hybrid materials with hierarchical porosity: promising materials for separation and membrane's applications

---



# New approach for preparing zeolite-polymer hybrid materials with hierarchical porosity: promising materials for separation and membrane's applications

*Rita Zakhia Douaihy<sup>a</sup>, Houssein Nasrallah<sup>a</sup>, Oleg Lebedev<sup>b</sup>, Jaafar El Fallah<sup>a</sup>, Rémy Guillet-Nicolas<sup>a</sup>, Alexandre Vimont<sup>a</sup>, Philippe Bazin<sup>a,\*</sup>, Mohamad El-Roz<sup>a,\*</sup>*

<sup>a</sup> Normandie Université, ENSICAEN, UNICAEN, CNRS, Laboratoire Catalyse et Spectrochimie, 14050 Caen, France

<sup>b</sup> Normandie Université, ENSICAEN, UNICAEN, CNRS, Laboratoire CRISMAT, 14050 Caen, France

\* Corresponding authors: mohamad.elroz@ensicaen.fr; philippe.bazin@ensicaen.fr

KEYWORDS: hybrid materials, zeolites, polymer, core-shell, dehydration

## Abstract

Here, we report a new approach for preparing zeolite-polymer core-shell like materials with hierarchical porosity via photopolymerization of trifunctional acrylic monomer (TMPTA) under UV-visible irradiation, using bifunctional Silane-based Photoinitiator (SPI-1) as coupling agent. The free radicals, generated on the surface of zeolites, initiate the polymerization of the diluted monomers and therefore create an external and mesoporous polymer shell layer. The efficiency of the photopolymerization process and the textural properties of synthesized materials are investigated using different techniques including PXRD, TGA, UV-Vis, FTIR, SEM and TEM. The accessibility to the pores of the zeolite core are investigated by N<sub>2</sub> physisorption at 77 K and other probe molecules using IR spectroscopy. Interestingly, the results demonstrate a good covering of the zeolite surfaces by polymers shell. The new approach is highly repetitive and reproducible and the accessibility to the zeolite's micropores is preserved with around 90 %, which is not reported previously. The newly synthesized hybrid materials show modified adsorption/separation capacities compared to the parent material toward water and ethanol adsorptions and during the dehydration of ethanol, demonstrating a new and easy way for preparing zeolite/polymer hybrid materials for various applications.

## 1. Introduction

In the last decades, mixed matrix membranes (MMMs) emerged to be excellent alternatives for polymeric and inorganic membranes [1, 2]. This is due to their outstanding performance that exceeds Robeson's upper bound for gas separation [3, 4]. Their importance arises from the combination of the selective separative and adsorptive characteristics of the inorganic porous fillers and the mechanical and economical properties of the polymer matrices [5]. Different porous materials including zeolites [6-8], silica nanoparticles [9], MOFs [10-12], COFs [13, 14], and others [15-17] were dispersed in the polymer matrix for gas separation [18-21], permeation and water/alcohol purification [7, 12, 22-24]. Despite the diverse applications of MMMs, the heterogeneous dispersion of the inorganic filler, the accessibility to its pores, and the undesirable defect between the organic matrix and the inorganic particles in addition to the non-homogeneous coverage are the common limitations emanating during their synthesis [1, 25]. To overcome these limitations, the polymer is treated either by its annealing above its glass transition temperature or by mixing it with a plasticizer to maintain its chain flexibility [22, 26]. The inorganic filler can be thermally treated, or modified by coating with integral chain linkers and silane-based coupling agents. This assures better dispersion and promotes the adhesion of the filler particles to the polymer matrix [22, 27, 28]. Moreover, the synthesis procedures reported in the literature could be classified in the following three main approaches [29]: a) the polymer is added to a homogeneous suspension of inorganic particles, b) a predetermined quantity of inorganic particle is added to a homogeneous suspension of the polymer, or c) separate homogeneous suspensions of polymer and inorganic particles are mixed together. Nevertheless, the limitations previously mentioned were not completely surpassed via these approaches. Therefore, extensive work has been imputed to improve the synthesis of MMMs via new approaches such as radical or cationic photopolymerization-based processes in the presence of a photoinitiator [30, 31].

Recently, a new approach has been validated by our group, where a MMM was synthesized by photopolymerization of an acrylate monomer on the surface of previously grafted silica nanoparticles with a silane-based photo-initiator [32-34]. Throughout this rapid and easy technique, and upon generation of free radicals on the surface of well-dispersed silica nanoparticles, a homogenous external layer of polymer

is formed. The strong covalent bond between the silica particles and the polymer matrix resulted in a mixed membrane with enhanced mechanical properties. This synthesis procedure could be further conducted on other fillers such as zeolites. To the best of our knowledge, few works on the photopolymerization of monomers with zeolites as seedings for MMMs have been reported [35, 36]. However, some limitations have been encountered such as the effect of the Si/Al ratio on the efficiency of the polymerization and the homogeneous distribution of the polymer around the zeolite particles without affecting the accessibility to the zeolite micropores.

Thus, to surpass these limitations, we report here a new approach for the synthesis of MFI-zeolite@polymer core-shell like structure, considered as a seeding for zeolite mixed matrix membrane. MFI nanoparticles are grafted with a previously synthesized silane-based photoinitiator (SPI-1) by interactions between the silane groups of the zeolite and the ethoxy groups of the coupling agent. The grafted MFI nanoparticles are then tested in the free radical polymerization of diluted trimethylolpropane triacrylate (TMPTA). The obtained hybrid materials are then collected, purified and characterized using UV-Vis and IR spectroscopies and thermogravimetric analyses. Their morphologies are examined using SEM and TEM. The accessibility of the micropores in the zeolite-polymer hybrid materials are investigated using N<sub>2</sub> sorption and adsorption of probe molecules. Finally, the newly synthesized and the parent materials are tested in the preferential adsorption of ethanol, water, and water/ethanol mixture, a highly desirable process for bio-ethanol dehydration. The preferential adsorption is considered as an efficient and energy saving approach for purification of this mixture, since ethanol is always collected in an aqueous mixture and cannot be used directly as a biofuel or additive to gasoline.

## 2. Experimental

### 2.1. Materials:

Industrial H-MFI zeolites provided by Clariant (formerly Süd Chemie, Si/Al= 45) were used in this work without any further treatment. Isobutyrophenone (IBP, 97 %), Allyl bromide (99 %), Potassium t-butoxide (99.99 %), tert-butanol (≥ 99.5 %), Diethyl ether (99 %), Sodium sulfate (99.99 %), Triethoxysilane (95 %), Dodecane (≥ 99%), Pt/Al<sub>2</sub>O<sub>3</sub> (5 wt%) and Trimethylolpropanetriacrylate (TMPTA) (technical grade) purchased from

Aldrich, and Acetonitrile (AcN, 99 %) purchased from Alfa Aesar, were used without any further purification.

## 2.2. Synthesis of 2,2-dimethyl-1-phenyl-5-(triethoxysilyl) pentane-1-one (SPI-1):

The synthesis of SPI-1 is detailed in the supporting information (**Scheme S1** and **Figure S1**) and in reference 32.

## 2.3. Grafting of SPI-1 on the surface of the MFI zeolites (SPI-1-MFI):

1 g of MFI zeolites was dried at 150 °C and then dispersed in 10 mL of dodecane with 0.1 g of the previously synthesized SPI-1 under vigorous stirring for 20 minutes at 120 °C. The powder was collected by centrifugation and washed with acetonitrile (2 times) and several times with water and ethanol to remove the excess of the ungrafted SPI-1 and the solvent. The final precipitate is dried using a freeze-dryer before characterization. This procedure was repeated at least three times to check the repetition of the process and the reproducibility of the results.

## 2.4. Photopolymerization efficiency:

The capacity and the efficiency of the grafted SPI-1 on zeolite were investigated using IR spectroscopy by following the kinetic of the C=C bond conversion of the TMPTA monomer.

The conversion yield is calculated according to **equation 1**:

$$\text{Conversion (\%)} = (A_0 - A_t) / A_0 * 100 \quad (\text{equation 1})$$

where  $A_0$  and  $A_t$  correspond to the band area of the characteristic C=C stretching band of TMPTA at 1635  $\text{cm}^{-1}$  at  $t = 0$  and  $t =$  time of the photopolymerization, respectively.

The photopolymerizable samples were prepared by mixing the 1 wt.% of SPI-1 (used as reference) or the grafted SPI-1MFI (1.8 and 3.6 wt.%) with TMPTA monomer. Few drops of each mixture were spread on polypropylene films separated by a Teflon spacer (width = 100  $\mu\text{m}$  and diameter = 2  $\text{cm}^2$ ), and subjected to monochromatic (LED 365 nm, Irradiance (306.4  $\text{mW}/\text{cm}^2$ )) and polychromatic UV irradiations (Xe-Hg lamp (LC8-01A spotlight, Hamamatsu, L10852, 200 W,  $I_0 \approx 150 \text{ mW} \cdot \text{cm}^{-2}$ )).

## 2.5. Preparation of MFI@Polymer:

40 mg of the previously grafted MFI zeolites were dispersed in 20 mL of acetonitrile (AcN) via sonication. 80 mg of the TMPTA monomer were added to the solution in a transparent reactor. The overall mixture was bubbled with argon under stirring for at least 15 minutes and then subjected to polychromatic irradiation for 15 minutes using a polychromatic Xe–Hg lamp (LC8-01A spotlight, Hamamatsu, L10852, 200 W,  $I_0 \approx 150 \text{ mW.cm}^{-2}$ ). The bubbling and the stirring were maintained throughout the irradiation. After polymerization, the white precipitate was collected by centrifugation. Then, the excess of the monomer and the solvent were removed by washing with acetonitrile and water, respectively. The solid is then freeze-dried before characterization. The procedure was repeated at least three times to check the repetition of the process and the reproducibility of the results.

## 2.6. Characterization techniques:

The thermogravimetric analysis was recorded on a SETSYS analyzer (SETARAM) between 25 °C and 800 °C with a heating rate of 10 °C.min<sup>-1</sup> under a flow of air (40 mL.min<sup>-1</sup>).

UV-Vis measurements were performed with a Cary 4000 (Varian) spectrophotometer in the spectral range between 200 and 400 nm. The spectrophotometer is equipped with a Praying Mantis diffuse reflection accessory. PXRD patterns are recorded on a PANalytical X'Pert Pro diffractometer with an average Cu K $\alpha$  radiation ( $\lambda = 1.5418 \text{ \AA}$ ). The  $\theta$ -2 $\theta$  scans are recorded in the range of 2 $\theta$  between 5° and 50° and a step size  $\sim 0.0167$ .

Nitrogen sorption isotherms at 77K were recorded using a Micrometrics ASAP 2020 volumetric adsorption analyzer. Before the measurements, the samples were degassed under vacuum at 150 °C, 180 °C or 200 °C for 12 hours. The specific surface areas are determined from the BET equation following the procedure recommended by Rouquerol et al. for microporous sorbents [37]. The total pore volumes and the external surface areas are calculated from the  $t$ -plot method. Cumulative pore volume plots discussed in the SI were calculated via the VersaWin software 1.01 (Quantatec)

using the adsorption branches of the isotherms and by applying the NLDFT kernel of (metastable) adsorption isotherms, considering an oxidic surface.

The morphologies of the parent and the modified samples were examined using electron microscopy. The SEM images were recorded using a TESCAN Mira field-emission scanning microscope at 20 kV. The TEM micrographs were recorded on a JEM200F cold FEG double aberration-corrected microscope equipped with a CENTURIO large-angle EDX detector. For SEM, the powder was dispersed on a thin layer of tin, fixed on carbon tape and the MFI powder was coated with platinum. Before TEM, the powder was dispersed in ethanol on a holey carbon film and coated with copper.

The pore accessibility and their acidity are investigated by in-situ IR experiments of pyridine and collidine adsorption on a ~20 mg self-supported pellets of the pressed powder ( $10^7$  Pa/cm<sup>2</sup>,  $S = 2.0$  cm<sup>2</sup>). The spectra were recorded using an *in-situ* IR cell equipped with KBr windows connected to a Nicolet 6700 IR spectrophotometer, equipped with a DTGS detector and an extended-KBr beam splitter in the region between 400 and 5500 cm<sup>-1</sup> (resolution 4 cm<sup>-1</sup>, 128 scans) [38]. Before adsorption, MFI zeolites (MFI), MFI with grafted SPI-1 (SPI-1-MFI), and MFI with polymer (MFI@Polymer) were pretreated from room temperature to 150 °C (heating rate 2 °C.min<sup>-1</sup>) under vacuum (around 10<sup>-5</sup> Torr) for 1 hour in the IR cell connected to the vacuum apparatus. Pyridine and collidine adsorption were conducted at 150 °C. After establishing a pressure of 1 Torr at the equilibrium of each adsorbate, the cell was evacuated at 150 °C for pyridine, and at 100 °C for collidine to remove all physisorbed species.

## 2.7. Adsorption and coadsorption of ethanol and/or water:

The adsorption of water and ethanol, as well as their coadsorption at different relative pressures on MFI and MFI@Polymer, were performed using the AGIR technique [39, 40]. It couples the gravimetric analysis with IR spectroscopy to determine simultaneously the quantity of the adsorbed water and/or ethanol. The experiments were carried out on self-supported pellets (~ 20 mg,  $S = 2.0$  cm<sup>2</sup>) and the samples were activated at 150 °C under a gas mixture of argon and oxygen (20 %) at

20 cm<sup>3</sup>.min<sup>-1</sup>. The IR spectra were collected (64 scans at a resolution of 4 cm<sup>-1</sup>, in the spectral region between 600 cm<sup>-1</sup> and 6000 cm<sup>-1</sup>) using a Nicolet 6700 spectrometer outfitted with liquid nitrogen cooled MCT detector (mercury, cadmium, and tellurium detector). The mass of the sample and the corresponding spectra were recorded after reaching the equilibrium for each H<sub>2</sub>O, EtOH, or H<sub>2</sub>O/EtOH concentration. The stability at the equilibrium was detected by the absence of a change in the sample mass and in the intensity of the characteristic bands of ethanol (at 880 cm<sup>-1</sup>) and/or water (at 5275 cm<sup>-1</sup>). Additionally, the outlet flow was monitored by a mass spectrophotometer (Pfeiffer Omnistar GSD301) to ensure the steady state of H<sub>2</sub>O and EtOH in the gas phase. It should be noted that the control and stabilization of water at relatively high partial pressure was difficult due its condensation in the setup (the temperature of the saturator is close to the room temperature under our condition). Therefore, the water isotherms were performed up to  $P/P_0 = 0.3$ .

### 3. Results and discussion

#### 3.1. Characteristic of SPI-1-MFI samples:

The thermal grafting procedure of SPI-1 on the surface of MFI zeolites is reported in the experimental part. After grafting the SPI-1 on the surface of the MFI zeolites (SPI-1-MFI), the samples have been washed several times in water/ethanol mixture in order to remove the excess of SPI-1. The obtained samples were dried and characterized by UV-Vis and *in-situ* transmission IR spectroscopies and compared to the MFI parent (**Figure 1**). The UV-Vis spectrum of the grafted zeolite (spectrum (b) in **Figure 1(A)**) displays new bands situated between 225 and 300 nm and at 325 nm, not observed for the parent zeolite (spectrum (a)). These bands are attributed to the  $\pi - \pi^*$  (225- 300 nm) and  $n - \pi^*$ (325 nm) electronic transitions of the benzoyl groups of the SPI-1 structure, confirming that the photochemical properties of the SPI-1 are preserved after the thermal grafting [41].

The reported IR spectrum in **Figure 1(B)** of the SPI-1-MFI (spectrum (b)) displays the main characteristic bands of SPI-1:  $\nu_{(\text{CH}) \text{ aromatics}}$  at 3064 cm<sup>-1</sup>,  $\nu_{(\text{CH})}$  in the 3040-2700 cm<sup>-1</sup>,  $\nu_{(\text{CO})}$  at 1667 cm<sup>-1</sup>,  $\nu_{(\text{CC})}$  between 1580 and 1600 cm<sup>-1</sup> and 1500-1350 cm<sup>-1</sup> range assigned to the C=C stretching and CH deformation modes, respectively

[42]. The IR spectrum of MFI zeolite (**Figure 1(B)** spectrum (a)) displays  $\nu_{(\text{OH})}$  bands at 3743 and 3610  $\text{cm}^{-1}$  attributed to silanol located on the outer crystallite surface and to structural bridged SiO(H)Al group respectively. The band at 3743  $\text{cm}^{-1}$  totally disappears after grafting whereas the intensity of the bridged structural OH group (3610  $\text{cm}^{-1}$ ) is hardly affected. This shows that the interactions between the zeolite and the SPI-1 are located on the outer surface of the crystallite [43, 44], without affecting significantly the bridging OH groups. The decrease of the relative intensity of the bands  $-\text{CH}_3$  at 2971  $\text{cm}^{-1}$  and 1391  $\text{cm}^{-1}$  respectively in the subtraction spectrum of SPI-1-MFI and MFI (**Figure S2**), validates also the grafting procedure through the ethoxy groups of the SPI structure.

The SPI-1-MFI samples are subjected to thermogravimetric analyses (TGA) to determine the quantity of the grafted SPI-1 and to examine its thermal stability. The TG curves and their corresponding dTG curves (**Figure 1(C) and (D)**) reveal a first weight loss below 200 °C (at around 73 °C) for the two samples, which is attributed to the desorption of molecular water and/or weakly physisorbed SPI-1. The second weight loss in the SPI-1-MFI sample starting 180 °C to 800 °C with two peaks at 224 °C and 519 °C corresponds to the thermal degradation of the SPI-1 hydrocarbon. In order to distinguish between the physisorbed and chemisorbed amount of SPI-1, the thermal stability of the SPI-1-MFI structure is further investigated by thermal programmed desorption analysis (TPD) under vacuum ( $10^{-6}$  torr) using FTIR spectroscopy. The evolution of the characteristic vibrational bands of the SPI attributed to the  $\nu_{(\text{CH})}$  of the aromatics at different temperatures is reported in **Figure 1(E-F)**. Water is desorbed below 200 °C. Below this temperature the intensity of IR band attributed to the of benzoyl groups of the SPI structure is not affected. However, its intensity decreases between 150°C and 180 °C, indicating the decomposition of the SPI structure. Above 180 °C, the total degradation of the SPI structure is observed with the dramatic decrease in the intensity of  $\nu_{(\text{CH}) \text{ aromatics}}$  in the of the benzoyl group and the  $\nu_{(\text{CH})}$  in the spectral region between 3040 and 2700  $\text{cm}^{-1}$ . The results show a high thermal stability up to 180 °C with a low amount of physisorbed species (around 10 % of the total SPI quantity). Therefore, the total weight loss (around 9 wt.%) observed for the SPI-1-MFI sample is due to the loss of water (around  $3 \pm 1$  wt. %),

physisorbed SPI-1 (0,6 wt%) and of the chemisorbed SPI-1, which is estimated to be around  $5.4 \pm 1$  wt.%.

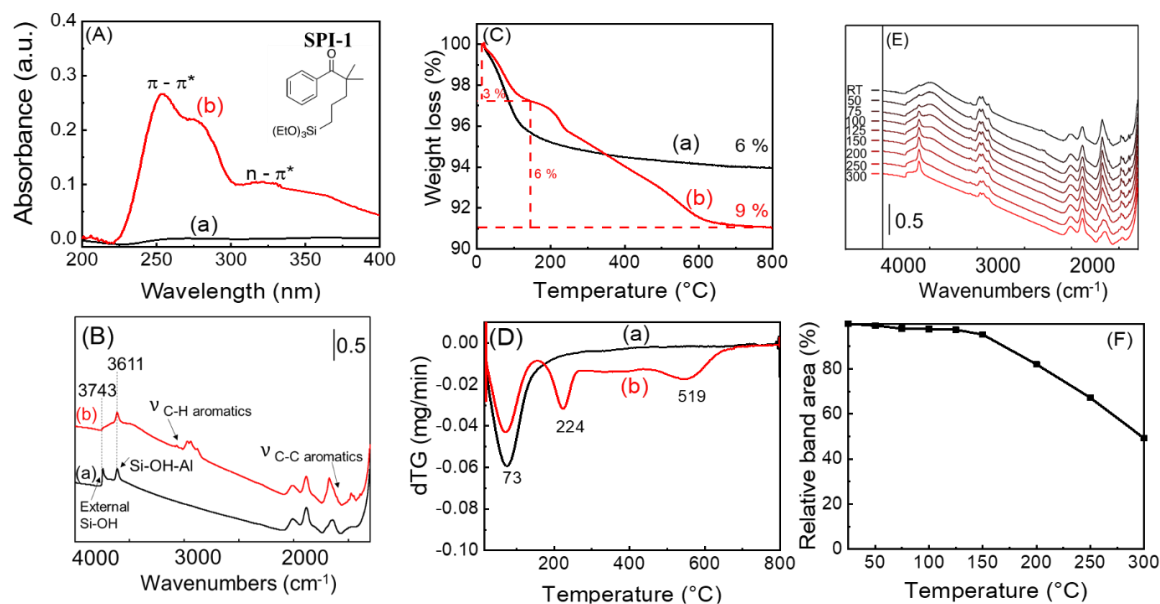


**Figure 1:** (A) UV-Vis and (B) FTIR spectra, (C) Thermogravimetric curves and (D) dTG of MFI ((a)-black) and SPI-1-MFI ((b)-red). (E) Evolution of the IR spectra of SPI-1-MFI after activation under vacuum at different temperatures. (F) Evolution of the intensity of the vibration band at  $3064 \text{ cm}^{-1}$  attributed to the  $\nu(\text{CH})$  of the benzoyl group. The samples are activated at  $150 \text{ }^{\circ}\text{C}$  before recording the IR spectra at RT in order to remove the residual solvent. Inset (A): chemical structure of SPI-1.

### 3.2. Efficiency of the grafted SPI-1-MFI in the photopolymerization of TMPTA:

A photopolymerization kinetic study is performed thereafter to test the efficiency of the grafted SPI-1 on the MFI surface in the TMPTA photopolymerization under polychromatic and monochromatic ( $365 \text{ nm}$ ) irradiations conditions (**Figure 2(A)** and **Figure 2(B)**, respectively). The evolution of the C=C of the TMPTA monomer is studied for SPI-1 (1wt%, **curve (a)**) and for 20 wt. % SPI-1-MFI (**curve (b)**). Freestanding polymer films are obtained for both samples under polychromatic UV irradiations.

Under polychromatic UV irradiation (**Figure 2(A)**), a decrease of around 20% in the conversion yield is observed when SPI-1 is grafted, which can be attributed to the shading effect of the inorganic filler on the absorbance of the SPI-1. On the other hand, under monochromatic irradiation (**Figure 2(B)**), the conversion yield of the SPI dispersed in the monomer (curve (a)) (around 30 %) is lower than that obtained under polychromatic irradiation (around 55 %) attributed to a low absorption of SPI at 365

nm. This explains the choice of the polychromatic irradiation in further experiments. Similar behavior is observed for 20 and 30 wt.% SPI-1-MFI under monochromatic and polychromatic irradiations: a decrease in the C=C conversion yield compared to the pure SPI and an induction time of 20 seconds are observed under 365 nm. This might be explained by the fact that the quantity of the quenchers (dissolved oxygen, radical-radical recombination, release of the adsorbed molecules in the zeolite pores (e.g. water and/or oxygen, etc.) is greater than that of the active radicals in such irradiation conditions. As a conclusion, despite the impact of the zeolite on efficiency of the grafted SPI-1, this later still shows a high photopolymerization capacity under polychromatic irradiation, and the optimal filler:monomer ratio was found to be around 1:2.

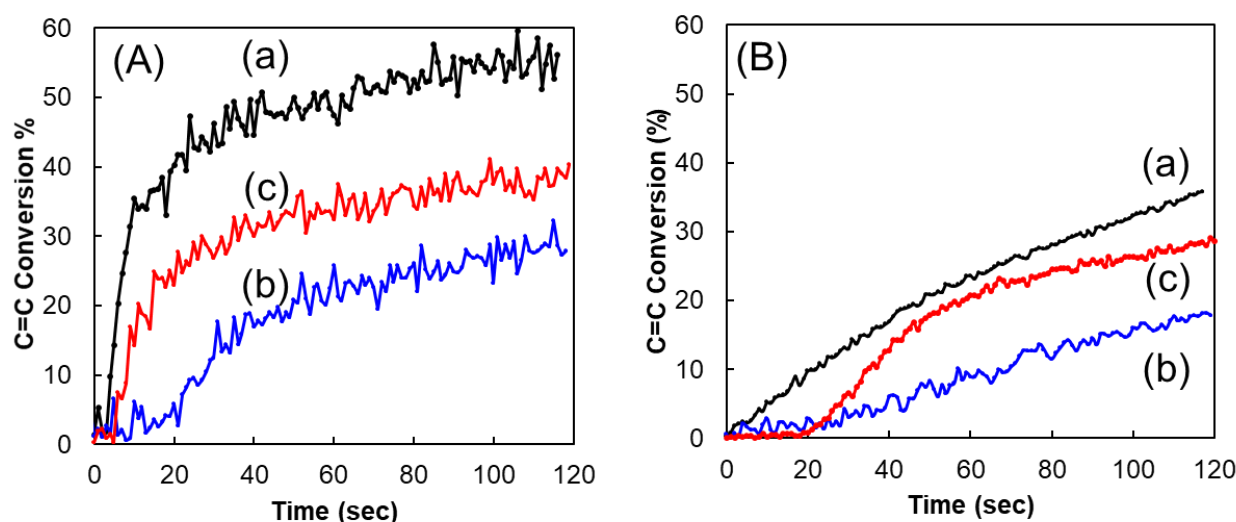


**Figure 2:** Photopolymerization of trimethylolpropane triacrylate (TMPTA) under (A) polychromatic UV (Hg-Xe lamp) and (B) 365 nm (LED) irradiation using (a) 1 wt.% of SPI-1, (b) 20 wt.% of SPI-1-MFI and (c) 30 wt.% of SPI-1-MFI (correspond to 1.2 and 1.8 wt.% of SPI-1 equivalent, respectively). Photopolymerization condition: photopolymerization realized in laminated (air-free) condition (100  $\mu$ m of thickness).

### 3.3. Preparation and characterization of MFI@Polymer hybrid materials:

Based on the previous results, the preparation of the MFI@Polymer was performed by dispersing SPI-1-MFI in TMPTA/AcN solution under Ar atmosphere and polychromatic irradiation (**Figure 3(A)**). More details on the preparation of the hybrid materials can be found in the experimental part. The powder was then collected by centrifugation in order to remove the excess of monomer/polymer dissolved in the solvent and the washed several times with water/ethanol. The dry MFI@Polymer

powder is then subjected to different characterization techniques including TGA, UV-Vis, and IR spectroscopy. The experiment was repeated several times and the error was estimated at around 10 %.

### 3.3.1. Polymer loading in the MFI@Polymer hybrid material:

The sample is subjected to IR spectroscopy to investigate the formation of the polymer. The IR spectrum in **Figure 3(B)** of the MFI@Polymer (spectrum (b)) shows the characteristic bands of the CH<sub>2</sub>- and CH<sub>3</sub>- groups of the polymer in the spectral region between 3040-2700 cm<sup>-1</sup> and 1350-1480 cm<sup>-1</sup> corresponding to the  $\nu_{(C-H)}$  and  $\delta_{(C-H)}$  respectively, the  $\nu_{(C-C)}$  of the alkene groups between 1650 cm<sup>-1</sup> and 1540 cm<sup>-1</sup> as well as the  $\nu_{(C=O)}$  at 1736 cm<sup>-1</sup>. However, the relative intensity of the  $\nu_{C=C}$  band at 1650 cm<sup>-1</sup> is very low confirming the high articulation of the polymers and the low content of terminal and unpolymerized function. It is interesting to mention that the benzoyl radicals formed from the homolytic cleavage of the SPI-1 structure under irradiation and released in the solution can also initiate the photopolymerization process leading to the formation of the zeolite-free polymers (despite its lower activity in respect to the grafted alkyl radical). However, the IR spectrum of MFI@Polymer demonstrate a total disappearance of any aromatic CH band characteristic of the benzoyl group of SPI-1. Therefore, the polymer originated from the benzoyl radical (free-zeolite polymers) are not significant or is removed during the purification process for various reason (highly dissolved in the ACN solvent, low amount, low weight, etc.). As 90% of SPI-1 is chemically grafted on the zeolite surface, we can assume that the amount of the zeolite-free polymers is negligible.

The TG curves of the grafted SPI-1-MFI and the prepared sample (MFI@Polymer), as well as the corresponding dTG curves, are represented in **Figure 3(B) and (C)**. Similarly, to the TG curve of SPI-1-MFI (**Figure 3 (B) curve (a)**), the TG curve of MFI@Polymer (**Figure 3(B) curve (b)**) reveals a first weight loss (around 4 wt.%) below 200 °C, attributed to the water/solvent desorption. Above 200 °C, the chemical and physical degradations of the polymer structure start as well as the degradation of the remaining anchoring group of the SPI-1. These degradations are determined at the two-weight losses observed at 412 °C and 519 °C. The total weight loss is calculated around 44 wt.%. The quantity of the hydrocarbon loading in the

MFI@Polymer sample is then determined to be around  $40 \pm 4\text{wt.}\%$  (error estimated on three independent experiments). This result reveals a high polymer loading if we consider the low mass density of the hydrocarbon in respect to the filler (2 to 3 times lower than that of MFI).

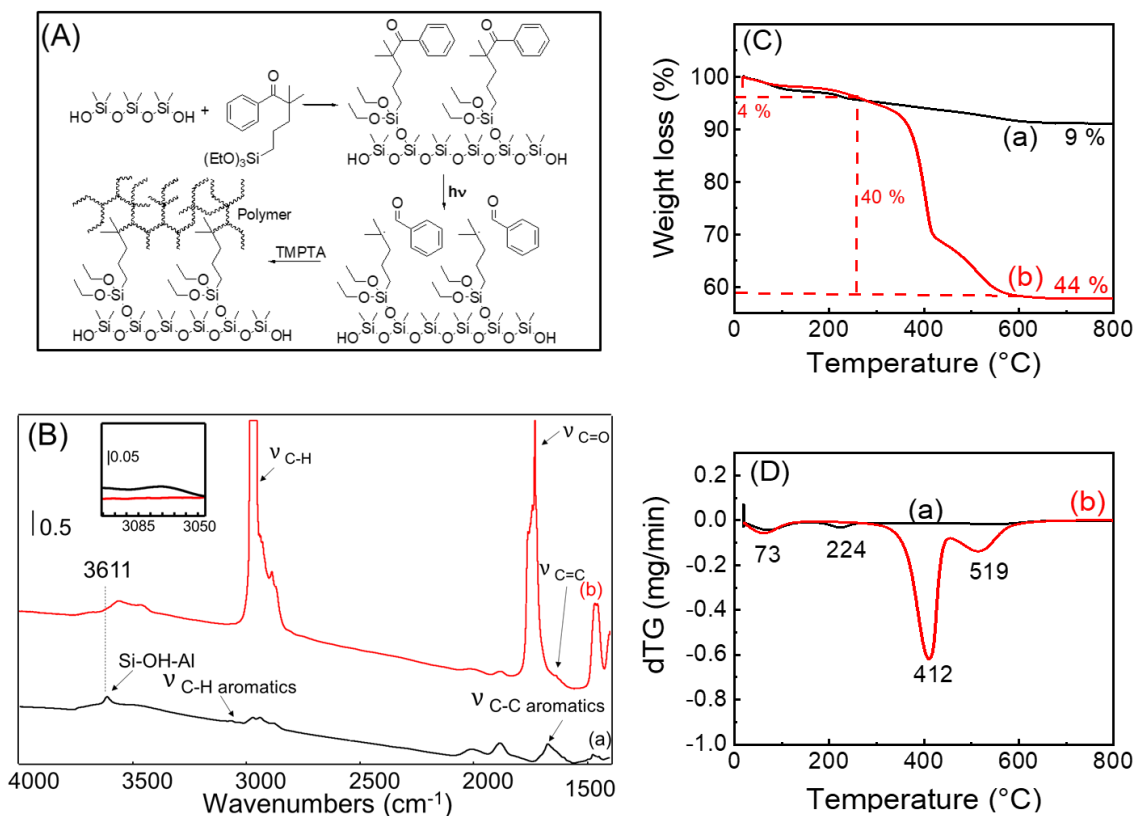


**Figure 3:** (A) Scheme of photopolymerization, (B) FTIR spectra, (C) thermogravimetric curves, and (D) dTG of SPI-1-MFI ((a)- black) and MFI@Polymer ((b)-red). The samples are activated at  $150\text{ }^{\circ}\text{C}$  before recording the IR spectra at RT. Inset of B: zoom on the characteristic vibration bands of the CH of the aromatics.

### 3.3.2. Structural and textural properties:

After confirming the grafting and the polymerization processes, the crystal structure of the zeolite is examined using powder X-ray diffraction analysis. The PXRD patterns in **Figure 4(A)** indicate the preservation of the zeolite crystallinity after both grafting and photopolymerization processes.

Moreover, the porosity of synthesized hybrid materials is investigated using  $\text{N}_2$  sorption at 77 K. The choice of the degassing temperature was made after a study conducted on MFI@Polymer at three different degassing temperatures:  $150\text{ }^{\circ}\text{C}$ ,  $180\text{ }^{\circ}\text{C}$ , and  $200\text{ }^{\circ}\text{C}$ . The  $\text{N}_2$  adsorption/desorption isotherms are represented in **Figure S3**

and **Table S1**. They show a significant decrease of the micropore volumes with the increase of the temperature. This decrease could be explained by the physical change of the polymer with the increase of the temperature of activation, which is probably due to a restructuring of the polymers around the zeolite particles (after cooling down at RT) and blocking partially the accessibility to the pores. Therefore, in all the coming experiments the activation temperature, when needed, is set at 150 °C. The N<sub>2</sub> isotherms at 77 K of MFI, SPI-1-MFI, MFI@Polymer and Polymer are represented in **Figure 4(B)** and the corresponding NLDFT cumulative pore volumes are shown in **Figure S4**. The micropore volumes, the surface areas deduced from BET analysis, and the t-plot method are summarized in **Table 1**. The measurements were conducted several times to ensure the reproducibility of the obtained results.

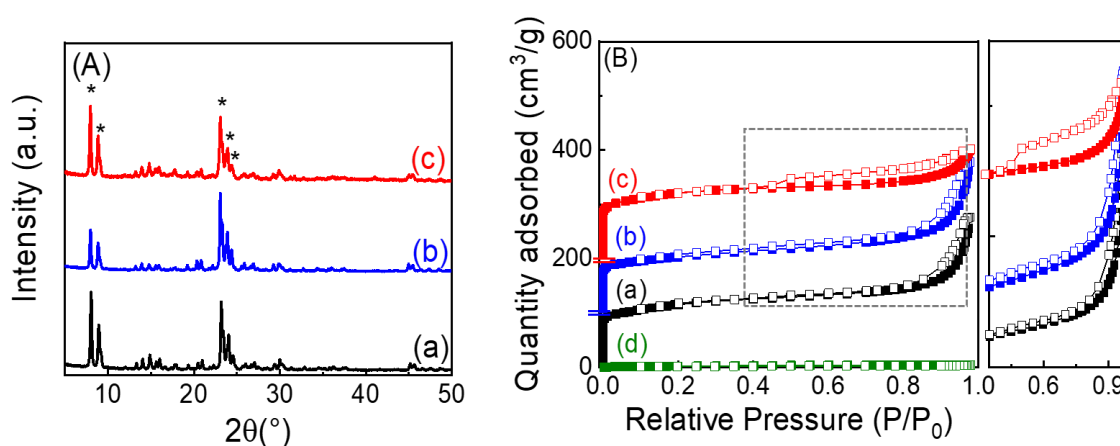


**Figure 4:** (A) PXRD patterns and (B) N<sub>2</sub> adsorption/desorption isotherms at 77 K of MFI ((a)- black), SPI-1-MFI ((b)- blue), MFI@Polymer ((c)- red)) and Polymer ((d)-green). The inset of (B) corresponds to zooming on the region of  $P/P_0$  between 0.4 and 1. The adsorption/desorption isotherms of SPI-1-MFI ((b)) and MFI@Polymer ((c)) are offset vertically for clarification of 100 and 200  $\text{cm}^3/\text{g}$ , respectively.

It is worthwhile noticing that the SPI grafting and then the polymerization processes did not affect significantly the micropore volume of the MFI zeolites since more than 90 % of the micropore volume is preserved for MFI@Polymer material. This confirms that the polymerization of the trifunctional monomers occurs on the outer surface of the crystallite without affecting the accessibility of N<sub>2</sub> towards the zeolite micropores. By contrast, the external surface area significantly increases after polymerization suggesting that the polymerization process generates a supplementary mesoporosity confirmed by the presence of a H4-type hysteresis loop [45]. Of particular interest, for the MFI@Polymer, a sharp closure of the hysteresis loop is observed at  $P/P_0 = 0.4-0.5$  during the desorption. This behavior is directly related with

the so-called cavitation phenomena indicating that a substantial fraction of the pores only have access to the outer surface via opening/necks being smaller than  $\sim 5$  nm, being very characteristic of core-shell materials[46] made from a mesoporous polymeric structure on the MFI zeolite,. Additionally, the comparison between the NLDFT cumulative pore volumes of the MFI and MFI@Polymer (**Figure S4**) reveals no difference in the volume distribution between the two samples at small pore width (below 10 nm), confirming that the polymer grafting happens only on the external surface of the zeolites. The absence of the microporosity in the pure polymer confirms also that the microporosity in the hybrid material is solely coming from the core zeolites and is still accessible after the polymerization process. Considering the hydrocarbon content in SPI-1-MFI and MFI@Polymer, we can assume that the microporosity of the zeolite is highly preserved after both grafting and photopolymerization processes. The (non-significant) decreases of the porosity in both cases can be assigned to the covering/poisoning of the external acid sites or to a partial blockage of the porosity (lower than 20%). Further investigation of the samples' acidity will be presented later in this paper.

**Table 1:** Textural properties of MFI, SPI-1-MFI, MFI@Polymer, and Polymer tested by  $N_2$  adsorption/desorption at 77 K.

	MFI	SPI-1-MFI	MFI@Polymer	Polymer
$S_{\text{BET}}^a$ ( $\text{m}^2/\text{g}$ )	413	378 * (355)	402 ** (241)	0
External surface area $^b$ ( $\text{m}^2/\text{g}$ )	83	101 * (95)	232 ** (139)	9
Total Volume ( $\text{cm}^3/\text{g}$ )	0.420	0.415 * (0.390)	0.312 ** (0.187)	< 0.01
Micropore volume $^c$ ( $\text{cm}^3/\text{g}$ )	0.145	0.120 * (0.113)	0.133 ** (0.08)	0

<sup>a</sup> BET surface area, <sup>b,c</sup>  $t$ -plot. The represented values between parentheses are the raw values, without normalization to the mass of zeolite. Values with \* and that with \*\* are normalized to the same mass of zeolite (94 %) and (60 %) respectively, based on the TG results.

### 3.3.3. Morphological characterization

The morphology of the MFI zeolites and the MFI@Polymer samples is then examined using scanning electron microscopy (SEM) and transmission electron microscopy (TEM) (**Figure 5**). The images in **Figure 5((A) and (C))** show that the pure

zeolite sample is formed of agglomerated nanospheres of around 30-50 nm. After the photopolymerization process, these nanocrystals are covered by an opaque layer of the polymer (**Figure 5(B)** and **(D)**).

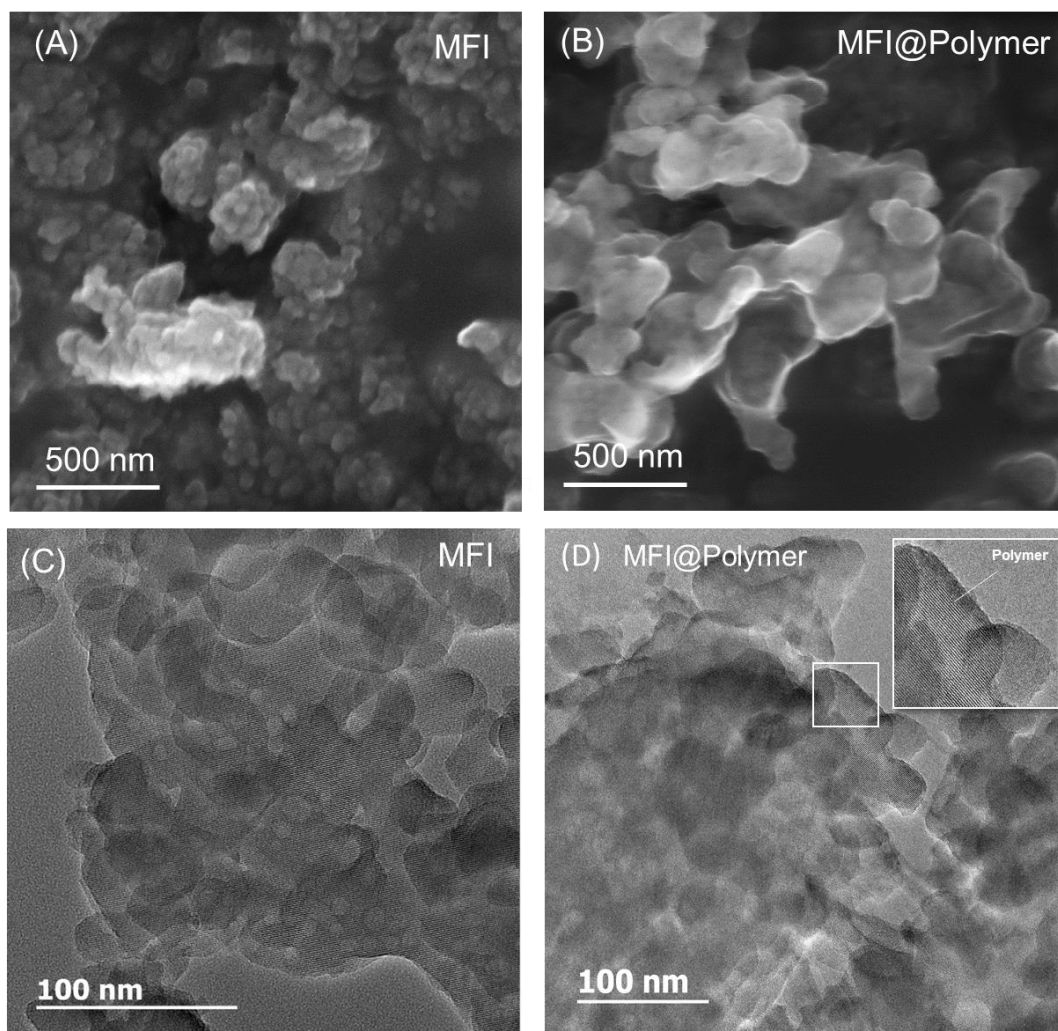


**Figure 5:** SEM images (A and B) and TEM images (C and D) of MFI ((A) and (C)) and MFI@Polymer ((B) and (D)). The inset of (D) corresponds to a zooming on the polymer layer at the edge of the zeolites

The TEM micrographs (**Figure 5 (D)**) confirm this coverage where darker regions are observed at the edge of the crystalline network of the MFI zeolite particles. A multiple core-shell like-structure can be observed, where MFI zeolites are covered by an external shell layer of polymer. This structure can be clearly noticed using elemental analysis EDX coupled to both SEM and TEM. The micrographs in **Figure 6** (and **Figures S5-S8** in SI) show the distribution of Si, O, and C atoms. The latter one is highly condensed on the edge of the particles whereas Si and O are homogeneously

distributed. The results confirm a selective and homogeneous distribution of the polymers around the zeolites particles and did not reveal the presence of any isolated polymer particles, in agreement with the previous results, where Si/Al and/or zeolite lattice structure are always observed.

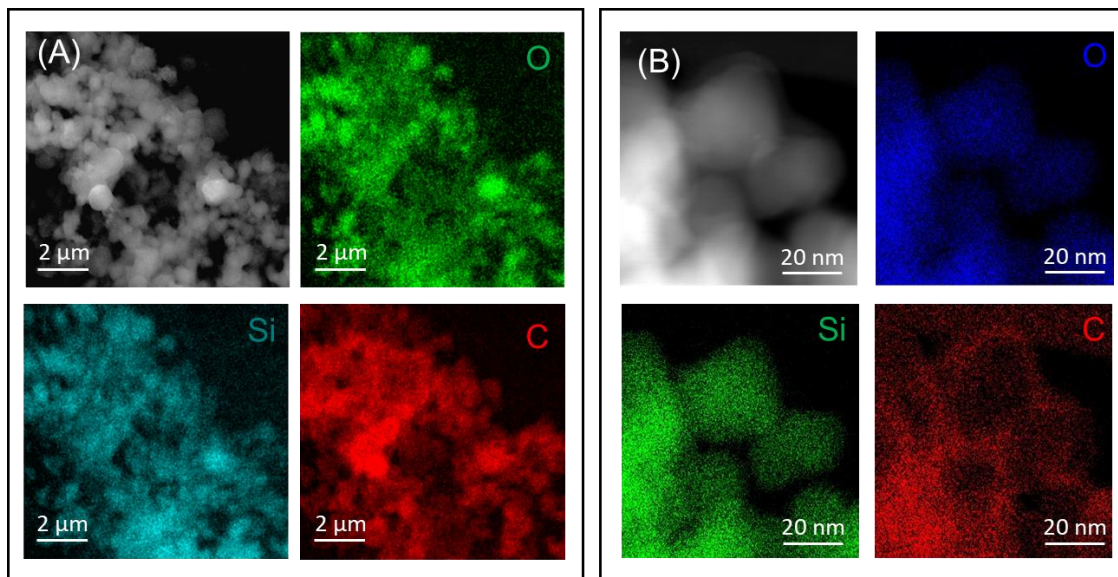


**Figure 6:**(A) SEM image with EDX (O: green, Si: blue, C: red; scale = 2 μm) and (B) TEM images with EDX (O: blue, Si: green, C: red; scale = 50 and 20 nm) of MFI@Polymer.

#### 3.3.4. Accessibility of the acid sites of MFI in MFI@Polymer

The accessibility of the acid sites of MFI zeolites (BAS (SiOHAl)), before (MFI) and after grafting (SPI-1-MFI) and polymerization (MFI@Polymer), is estimated upon adsorption of probe molecules: (i) pyridine that can be protonated by both internal and external acid sites and (ii) collidine, that specifically interacts with the external surface sites due to steric hindrance [42, 47]. The resulting IR spectra are displayed in **Figure 7** and correspond to the regions of the characteristic bands of each probe molecule. The band at  $1547\text{ cm}^{-1}$  in **Figure 7(A)** is attributed to the pyridinium ions interacting with the BAS [48]. For collidine, the bands situated at  $1637\text{-}1645\text{ cm}^{-1}$  are characteristic of collidinium ions [49] (**Figure 7(B)**). The amount of adsorbed pyridinium and collidinium formed on the acidic sites was determined by integrating the area of their characteristic bands and using the following molar absorption coefficients:  $\epsilon_{1547} = 1.13\text{ cm} \cdot \mu\text{mol}^{-1}$  [50], and  $\epsilon_{1637} = 10.1\text{ cm} \cdot \mu\text{mol}^{-1}$ [49], respectively.

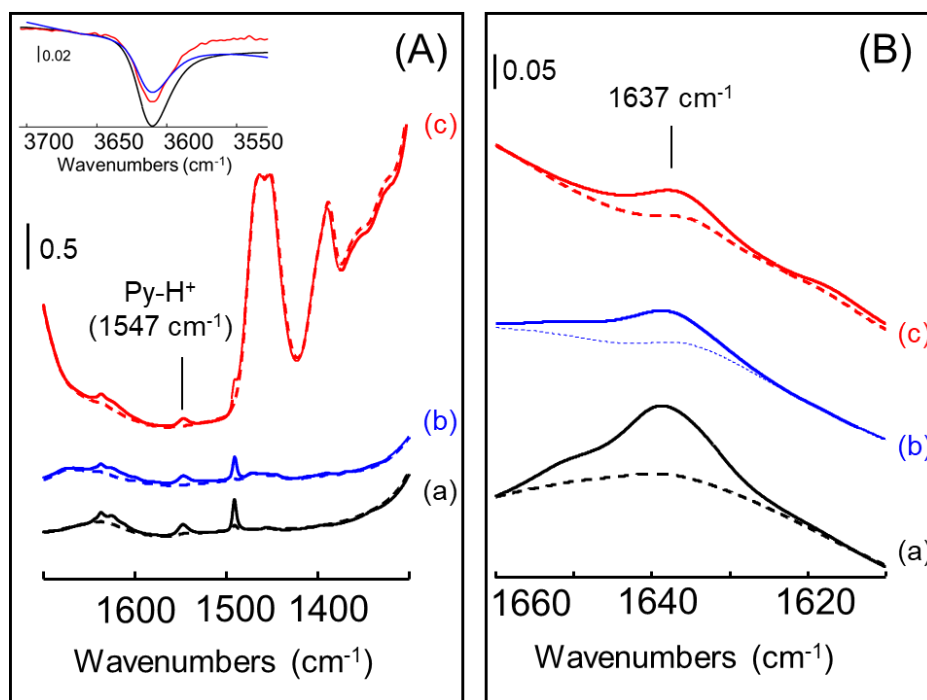


**Figure 7:** IR spectra of MFI ((a)- black), SPI-1-MFI ((b)- blue) and MFI@Polymer ((c)-red) before (dotted line) and after (solid line) (A) pyridine and (B) collidine adsorption. The inset of (A) corresponds to the subtraction spectra in the OH region. The spectra are collected after pyridine adsorption at 150 °C and after collidine adsorption at 100 °C and are normalized to the mass of the pellet (20 mg) and the mass of zeolite in each sample. The samples were previously degassed under vacuum at 150 °C.

The amount of BAS accessible to the two probe molecules in the three different samples are summarized in **Table 2**. The comparison of the amount of pyridinium (216  $\mu\text{mol. g}^{-1}$ ) and collidinium species (17  $\mu\text{mol. g}^{-1}$ ) detected on MFI shows that the proportion of Bronsted acid site located on the external surface is relatively low, about 9 % of the total number of BAS. The comparison of the amount of pyridinium detected on the three materials clearly shows that more than 90 % of the Bronsted acid site remains accessible to pyridine molecules after both SPI-1 grafting and polymerization. Interestingly, these results agree with the preservation of the microporous volume determined by the N<sub>2</sub> sorption experiment. This confirms that the encapsulation method used in the present study conserved the Bronsted acidity of the core material in addition to the high permeability of the polymer towards pyridine. The decrease of about 10 % of the total number of BAS in SPI-1-MFI and MFI@Polymer is mainly attributed to the significant decrease in the proportion of external Bronsted acid sites (more than 50 %). This is due to the poisoning or the disappearing of the outer BAS resulting from the grafting of the SPI-1 on the outer surface of the zeolite.

**Table 2:** Accessibility of MFI, SPI-1-MFI, and MFI@Polymer tested by adsorption of pyridine and collidine.

	MFI	SPI-1-MFI	MFI@Polymer
<b>n(μmol/g)</b> Pyridine	216 (100 %)	187 * (93 %)	197 ** (92 %)
<b>n(μmol/g)</b> Collidine	17 (100 %)	7 * (43 %)	9 ** (54 %)

The represented values with \* and that with \*\* are normalized to the mass of zeolite (94 %) and (60 %), calculated by TG, respectively. The values between parentheses correspond to the percentage of the accessible sites compared to the parent zeolite.

### 3.4. Affinities of MFI and MFI@Polymer hybrid materials toward ethanol, water and ethanol/water mixture:

#### 3.4.1. Water and ethanol adsorption capacities of MFI and MFI@Polymer:

After successfully synthesizing, characterizing the hybrid materials, and confirming the accessibility to the pores of the zeolites, the adsorption and separation capacities of the synthesized core-shell materials are tested for water, ethanol, and for ethanol/water mixture using the AGIR instrument [39, 40]. This technique allows determining the optical (by infrared) and the thermogravimetric isotherms by coupling the IR with a microbalance (gravimetry). It is therefore allows determining the molar extinction coefficient of a characteristic band, e.g. crucial for calculating the individual amount of adsorbed molecules during binary or multicomponent adsorption.

The evolution of the characteristic bands of ethanol at  $880\text{ cm}^{-1}$  attributed to the C-C-O vibrations ( $\nu_{C-C-O}$ ) and  $1450\text{ cm}^{-1}$  ( $\delta_{CH_3}$ ) and that of water at  $1630\text{ cm}^{-1}$  ( $\delta_{H_2O}$ ) and the combination band at  $5270\text{ cm}^{-1}$  ( $(\delta + \nu)_{H_2O}$ ) can be monitored during the adsorption process. However, in our case the characteristic band of ethanol at  $1450\text{ cm}^{-1}$  ( $\delta_{CH_3}$ ) and that of water at  $1630\text{ cm}^{-1}$  cannot be studied in the case of MFI@Polymer, due to their perturbation with a characteristic band of the polymer ( $\delta_{(C-H)}$  and  $\nu_{C=C}$ , respectively). Since the coupling of the TG with the IR allows quantifying the adsorbed amount and the corresponding vibrational band area, respectively, the molar absorption coefficient for the characteristic bands ( $\epsilon$  ( $\text{cm} \cdot \mu\text{mol}^{-1}$ )) of ethanol situated at  $\sim 880\text{ cm}^{-1}$  and that of water at  $\sim 5270\text{ cm}^{-1}$  for MFI and at  $\sim 5240\text{ cm}^{-1}$  for MFI@Polymer can be calculated (**Figure S9**). They allow later to determine the exact

quantity of the adsorbed species once they are simultaneously present. The shift of the combination band of the molecular water on MFI@Polymer in respect to pure MFI ( $\Delta\nu = 30 \text{ cm}^{-1}$ ) could reflect different configurations of adsorbed water and thus explains the difference between the values of the adsorption coefficients of the two materials. This shift might be explained by two hypotheses: the first one is that the external silanols on the zeolites of the MFI@Polymer sample are completely occupied by the polymer. Thus, the remaining active sites for water adsorption are the internal active sites in the pores of the zeolites. The second hypothesis is that the polymer is capable of adsorbing water by H-interactions between its carbonyl functions and water molecules. **Figure 8** shows the gravimetric adsorption isotherms of adsorbed ethanol and water on MFI and MFI@Polymer. The isotherms are determined after measuring the recorded change in mass using the microbalance of the AGIR setup as a function of the increasing partial pressures of each adsorbate. The evolution of the corresponding IR spectra and the rise of the intensities of the corresponding vibrational characteristic bands are represented in **Figure S10**. Upon ethanol adsorption and after normalization to the mass of the zeolite (inset of **Figure 8(A)**), the microporosity of the zeolite in the MFI@Polymer is filled with ethanol, slightly lower than that of MFI. Once the porosity of the zeolite is filled, the remaining ethanol is adsorbed on the mesoporous polymer. For example, at high ethanol partial pressures, the quantity of adsorbed ethanol on MFI@Polymer is  $\sim 1.5$  times higher than that adsorbed on pure MFI. Nevertheless, this trend is not observed for water (**Figure 8(B)**). The quantity of the adsorbed water in the zeolite micropores is low compared to the MFI zeolites and is not sufficient to fill its microporosity confirming the presence of a relatively hydrophobic barrier formed by the polymer around the MFI particles. For instance, at low water partial pressure ( $P/P_0 \leq 0.3$ ), water adsorption on MFI zeolites is more than two times higher than that on MFI@Polymer. However, the polymer demonstrates a capacity to interact weakly with water at relatively high partial pressure. The comparison between the water and the ethanol isotherms demonstrate that MFI have a good capacity to adsorb both water and ethanol, however MFI@Polymer's capacity to adsorb ethanol is much higher than that of water. The main adsorption of water at the outer surface (probably via a weak hydrogen bond with the polymer carbonyl function) may explain the observed shift of the water vibration band and the three times higher extinction coefficient in respect to MFI. This result suggests the highly

desirable behavior of the hybrid MFI@Polymer for ethanol dehydration at relatively low water partial pressure.

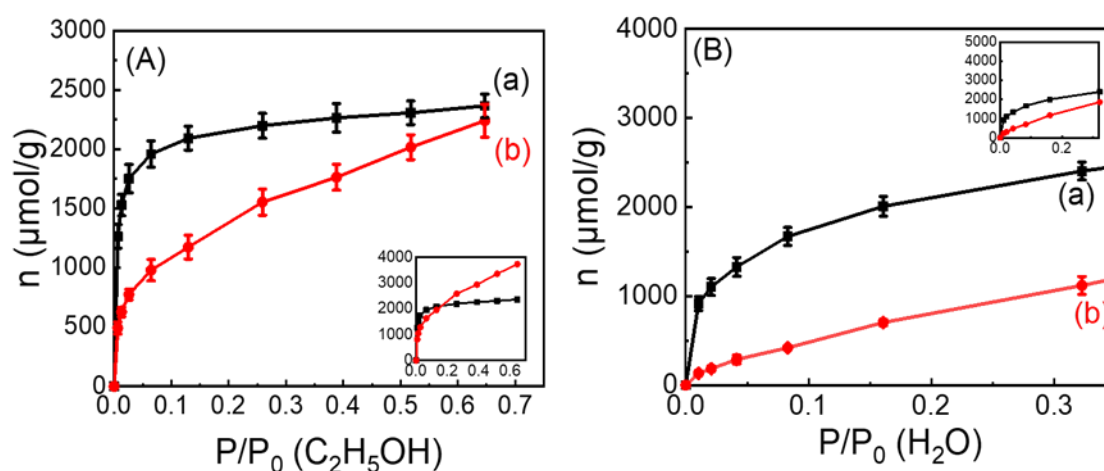


**Figure 8:** (A) Ethanol and (B) water gravimetric adsorption isotherms on MFI ((a)- black) and MFI@Polymer ((b)- red). The adsorptions were conducted at RT. The insets figures correspond to the adsorbed quantities of ethanol and water after normalization to the mass of zeolite, determined from the TG (60 % of zeolites in the sample MFI@Polymer).

### 3.4.2. Ethanol /water co-adsorption capacities of MFI and MFI@Polymer:

The coadsorption of ethanol/water mixture at RT is further studied on MFI and MFI@Polymer at a fixed water concentration and increasing ethanol partial pressure. First, a water partial pressure ( $P/P_0 = 0.3$ , 10000 ppm) is adsorbed on both samples and maintained constant. Once the equilibrium is reached, the gas flow is enriched with an increasing ethanol partial pressure. The evolution of the IR spectra of MFI and MFI@Polymer during the coadsorption of ethanol/water mixture is represented in **Figure 9(A)-(E)**. Using the previously determined values of the molar absorption coefficients, the quantities of adsorbed ethanol and water are calculated from the corresponding IR spectra (**Figure 9(F)**). The initial amount of adsorbed water on the MFI is greater than that adsorbed on MFI@Polymer, which is in accordance with the previous results of the pure adsorption of water. For MFI zeolites, at low ethanol partial pressure ( $P/P_0 < 0.1$ ), water is strongly desorbed. With the increase of the vapor pressure of the ethanol, the quantity of desorbed water is increasing, simultaneously with the increase of the quantity of adsorbed ethanol. At  $P/P_0 > 0.3$ , the adsorption capacity of the zeolite is reached where a steady state of the amount of ethanol and desorbed water is observed. This might be explained by the high basicity of ethanol

compared to H<sub>2</sub>O, that is being replaced on the acidic sites of the zeolite. A different trend is observed on MFI@Polymer. At P/P<sub>0</sub> of ethanol < 0.1, weakly adsorbed water molecules are replaced by ethanol. The remaining quantity not accessible for replacement on MFI@Polymer is greater than that on pure MFI (**Figure S11**).

Nevertheless, at higher pressures, the quantity of adsorbed H<sub>2</sub>O decreases slowly with the fast increase of the quantity of adsorbed ethanol. The residual adsorbed water is retained in the zeolite while ethanol is remained to be adsorbed on the polymer shell even at relatively high partial pressure, contrary to the MFI sample. This adsorption/desorption trend agrees with the previously discussed adsorption isotherms, where the modification of the surface engender higher ethanol adsorption capacity created in the mesoporosity of the polymer. Therefore, using the new synthesis approach it becomes possible to tune the hydrophobic/hydrophilic characters of the hybrid materials without modifying the core part, which can affect their adsorption capacity and their separation behavior.

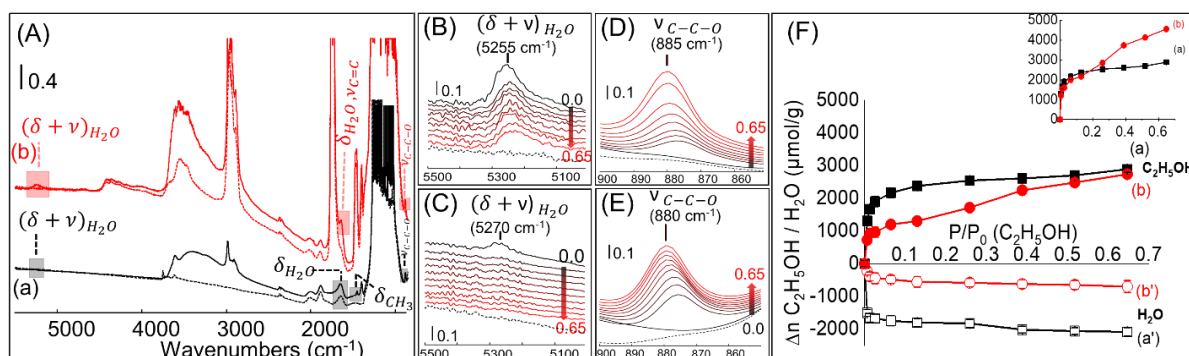


**Figure 9:** (A) IR spectra of MFI (a) and MFI@Polymer (b) upon adsorption of ethanol/water mixture ( $P/P_0$  C<sub>2</sub>H<sub>5</sub>OH = 0.013,  $P/P_0$  H<sub>2</sub>O = 0.3). Evolution of IR spectra for characteristic bands of water ((B) and (C)) and ethanol ((D) and (E)) upon the coadsorption of ethanol/water mixture with increasing  $P/P_0$  of ethanol from 0 to 0.65 on MFI@Polymer ((B) and (D)) and MFI ((C) and (E)). The dashed-line spectra correspond to the spectra of the activated sample. (F) Variation of the quantities of adsorbed water ((a') and (b')) and adsorbed ethanol ((a), (b)) on MFI (black) and MFI@Polymer (red) as a function of the partial pressure of ethanol (water concentration in the flow is fixed at 1%). The inset of (F) corresponds to the quantities on MFI@Polymer that are normalized to the mass of zeolite (60% of zeolite). The quantities of the adsorbates are determined from the areas of the characteristic bands of water at 5270 cm<sup>-1</sup> and ethanol at 880 cm<sup>-1</sup>.

## 4. Conclusion

In conclusion, a new synthesis approach of hybrid materials is validated by photopolymerization of TMPTA monomer under UV irradiation as an external shell on the surface of MFI zeolites in the presence of a silane-based photoinitiator (SPI-1). The quantities of the SPI-1 and polymer loading are determined using thermogravimetric analyses. The zeolite-polymer core-shell like structures with homogeneous polymer distribution around the zeolite particles are confirmed by SEM and TEM coupled with EDX. N<sub>2</sub> adsorption/desorption isotherms on the modified material compared to the parent zeolite show that around 90 % of the porosity of the MFI zeolites is still conserved with additional external mesoporosity offered by the polymer, creating thus a hierarchical material. These results are confirmed by adsorption of basic probe molecules. Due to these eminent properties, the hierarchical hybrid materials show a higher capacity to adsorb ethanol with lower capacity to adsorb water in respect to the parent MFI (taking into consideration the zeolite content in both materials). The new approach opens the way for new classes of hierarchical hybrid materials with tuned hydrophobic/hydrophilic behavior for applications in purification, separation and membranes.

## Associated content

**Supporting Information:** IR spectrum of liquid SPI-1 and compared to the subtraction spectrum between the grafted SPI and MFI, nitrogen adsorption/desorption isotherms at 77K for the three samples degassed at three different temperatures, NLDFT cumulative pore volumes, additional SEM and TEM micrographs with elemental mapping analyses are reported. Areas of the characteristic bands of ethanol and water plotted versus the adsorbed quantities to determine the adsorption coefficients are represented. The evolution of the IR spectra of water and ethanol adsorption, and the quantities of adsorbed water and ethanol during their coadsorption are also reported.

## Author Information

### Corresponding Authors

mohamad.elroz@ensicaen.fr

philippe.bazin@ensicaen.fr

### Author Contributions

The manuscript was written through the contributions of all authors. All authors have given approval to the final version of the manuscript.

### Funding Sources

This project is financed by European Union (3DZEOPOL project).

## Acknowledgment

Authors acknowledge the Normandy region and European Union for the financial support (3DZEOPOL project). Rita Z.D acknowledges the Normandy region for the doctoral funding.

## References

1. Ebadi, A., S. Mashhadikhan, and H. Sanaeepur, *Progress in Materials Science Substantial breakthroughs on function-Led design of advanced materials used in mixed matrix membranes (MMMs): A new horizon for efficient CO<sub>2</sub> separation*. Prog. Mater. Sci, 2019. **102**: p. 222-295.
2. Jusoh, N., et al., *Current development and challenges of mixed matrix membranes for CO<sub>2</sub>/CH<sub>4</sub> separation*. Separation & Purification Reviews, 2016. **45**(4): p. 321-344.
3. Dechnik, J., et al., *Mixed-matrix membranes*. Angewandte Chemie International Edition, 2017. **56**(32): p. 9292-9310.
4. Farnam, M., H. bin Mukhtar, and A. bin Mohd Shariff, *A Review on Glassy and Rubbery Polymeric Membranes for Natural Gas Purification*. ChemBioEng Reviews, 2021.
5. Castro-Muñoz, R. and V. Fila, *Progress on incorporating zeolites in matrimid® 5218 mixed matrix membranes towards gas separation*. Membranes, 2018. **8**(2): p. 30.
6. Gong, H., S.S. Lee, and T.-H. Bae, *Mixed-matrix membranes containing inorganically surface-modified 5A zeolite for enhanced CO<sub>2</sub>/CH<sub>4</sub> separation*. Microporous and Mesoporous Materials, 2017. **237**: p. 82-89.
7. Liu, X., et al., *Preparation and characterization of Silicalite-1/PDMS surface sieving pervaporation membrane for separation of ethanol/water mixture*. Journal of Applied Polymer Science, 2015. **132**(34).
8. Wu, D., et al., *Scale-up of zeolite-Y/polyethersulfone substrate for composite membrane fabrication in CO<sub>2</sub> separation*. Journal of Membrane Science, 2018. **562**: p. 56-66.
9. Hasebe, S., et al., *CO<sub>2</sub> separation of polymer membranes containing silica nanoparticles with gas permeable nano-space*. Journal of Membrane Science, 2017. **536**: p. 148-155.
10. Dechnik, J., C.J. Sumbly, and C. Janiak, *Enhancing mixed-matrix membrane performance with metal-organic framework additives*. Crystal Growth & Design, 2017. **17**(8): p. 4467-4488.
11. Cheng, Y., et al., *Ultrathin mixed matrix membranes containing two-dimensional metal-organic framework nanosheets for efficient CO<sub>2</sub>/CH<sub>4</sub> separation*. Journal of Membrane Science, 2017. **539**: p. 213-223.
12. Elrasheedy, A., et al., *Metal organic framework based polymer mixed matrix membranes: Review on applications in water purification*. Membranes, 2019. **9**(7): p. 88.
13. Kang, Z., et al., *Mixed matrix membranes (MMMs) comprising exfoliated 2D covalent organic frameworks (COFs) for efficient CO<sub>2</sub> separation*. Chemistry of Materials, 2016. **28**(5): p. 1277-1285.
14. Shan, M., et al., *Mixed-matrix membranes containing an azine-linked covalent organic framework: Influence of the polymeric matrix on post-combustion CO<sub>2</sub>-capture*. Journal of Membrane Science, 2018. **549**: p. 377-384.
15. Sun, H., et al., *Fabrication of polyimide and functionalized multi-walled carbon nanotubes mixed matrix membranes by in-situ polymerization for CO<sub>2</sub> separation*. Separation and Purification Technology, 2017. **177**: p. 327-336.
16. Molki, B., et al., *Mixed matrix membranes of polyurethane with nickel oxide nanoparticles for CO<sub>2</sub> gas separation*. Journal of Membrane Science, 2018. **549**: p. 588-601.
17. Kononova, S.V., et al., *Polymer nanocomposite membranes*. Applied Sciences, 2018. **8**(7): p. 1181.
18. Vinoba, M., et al., *Recent progress of fillers in mixed matrix membranes for CO<sub>2</sub> separation: A review*. Separation and Purification Technology, 2017. **188**: p. 431-450.
19. Hamid, M.R.A. and H.-K. Jeong, *Recent advances on mixed-matrix membranes for gas separation: Opportunities and engineering challenges*. Korean Journal of Chemical Engineering, 2018. **35**(8): p. 1577-1600.

20. Amooghin, A.E., et al., *Substantial breakthroughs on function-led design of advanced materials used in mixed matrix membranes (MMMs): a new horizon for efficient CO<sub>2</sub> separation*. Progress In Materials Science, 2019. **102**: p. 222-295.
21. Galizia, M., et al., *50th anniversary perspective: polymers and mixed matrix membranes for gas and vapor separation: a review and prospective opportunities*. Macromolecules, 2017. **50**(20): p. 7809-7843.
22. Maghami, M. and A. Abdelrasoul, *Zeolites-mixed-matrix nanofiltration membranes for the next generation of water purification*, in *Nanofiltration*. 2018, IntechOpen.
23. Castro-Muñoz, R., et al., *Mixed matrix membranes (MMMs) for ethanol purification through pervaporation: current state of the art*. Reviews in Chemical Engineering, 2019. **35**(5): p. 565-590.
24. Kamelian, F.S., T. Mohammadi, and F. Naeimpoor, *Fast, facile and scalable fabrication of novel microporous silicalite-1/PDMS mixed matrix membranes for efficient ethanol separation by pervaporation*. Separation and Purification Technology, 2019. **229**: p. 115820.
25. Wang, S., et al., *Advances in high permeability polymer-based membrane materials for CO<sub>2</sub> separations*. Energy & Environmental Science, 2016. **9**(6): p. 1863-1890.
26. Yang, H.-C., et al., *Surface and interface engineering for organic–inorganic composite membranes*. Journal of Materials Chemistry A, 2016. **4**(25): p. 9716-9729.
27. Golemme, G., et al., *Surface modification of molecular sieve fillers for mixed matrix membranes*. Colloids and Surfaces A: Physicochemical and Engineering Aspects, 2018. **538**: p. 333-342.
28. Maghami, M. and A. Abdelrasoul, *Zeolite mixed matrix membranes (Zeolite-Mmms) for sustainable engineering*. Zeolites and Their Applications; BoD–Books on Demand: Norderstedt, Germany, 2018: p. 115.
29. Aroon, M., et al., *Performance studies of mixed matrix membranes for gas separation: A review*. Separation and purification Technology, 2010. **75**(3): p. 229-242.
30. Bagheri, A. and J. Jin, *Photopolymerization in 3D printing*. ACS Applied Polymer Materials, 2019. **1**(4): p. 593-611.
31. Corrigan, N., et al., *Seeing the light: advancing materials chemistry through photopolymerization*. Angewandte Chemie, 2019. **131**(16): p. 5224-5243.
32. Douaihy, R.Z., et al., *Synthesis of silica-polymer core-shell hybrid materials with enhanced mechanical properties using a new bifunctional silane-based photoinitiator as coupling agent*. Materials Today Communications, 2021: p. 102248.
33. El Roz, M., S. Lakhdar, and I. Telegeiev, *Novel photoinitiators made from bifunctional silane*, in *U.S. Patent Application*. 2021. p. 16/764805.
34. El-Roz, M., et al., *Radical and cationic photopolymerization: New pyrylium and thiopyrylium salt-based photoinitiating systems*. Journal of Polymer Science Part A: Polymer Chemistry, 2008. **46**(22): p. 7369-7375.
35. Zhang, Y., et al., *Photopolymerization of Zeolite/Polymer-Based Composites: Toward 3D and 4D Printing Applications*. ACS Applied Polymer Materials, 2020. **3**(1): p. 400-409.
36. Xu, Y., et al., *Effect of zeolite fillers on the photopolymerization kinetics for photocomposites and lithography*. ACS Applied Polymer Materials, 2019. **1**(11): p. 2854-2861.
37. Rouquerol, J., P. Llewellyn, and F. Rouquerol, *Is the BET equation applicable to microporous adsorbents*. Stud. Surf. Sci. Catal, 2007. **160**(07): p. 49-56.
38. Zholobenko, V., et al., *Probing the acid sites of zeolites with pyridine: Quantitative AGIR measurements of the molar absorption coefficients*. Journal of Catalysis, 2020. **385**: p. 52-60.
39. Bazin, P., A. Alenda, and F. Thibault-Starzyk, *Interaction of water and ammonium in NaHY zeolite as detected by combined IR and gravimetric analysis (AGIR)*. Dalton Transactions, 2010. **39**(36): p. 8432-8436.

40. El-Roz, M., et al., *Pore Occupancy Changes Water/Ethanol Separation in a Metal-Organic Framework* Quantitative Map of Coadsorption by IR. The Journal of Physical Chemistry C, 2015. **119**(39): p. 22570-22576.
41. Forbes, W. and J. Myron, *Light absorption studies: part XX. The ultraviolet absorption spectra and Infrared carbonyl bands of benzoyl chlorides*. Canadian Journal of Chemistry, 1961. **39**(12): p. 2452-2465.
42. Thibault-Starzyk, F., A. Vimont, and J.-P. Gilson, *2D-COS IR study of coking in xylene isomerisation on H-MFI zeolite*. Catalysis today, 2001. **70**(1-3): p. 227-241.
43. El-Roz, M., et al., *Silica-silane reaction: Deciphering the silica-silane reaction mechanism for the development of a new generation of low rolling resistance tires*. Tire technology international, 2016. **2016**(43): p. 93-94.
44. El-Roz, M., F. Thibault-Starzyk, and A. Blume, *Infrared study of the silica/silane reaction. Part II*. KGK Kautschuk, Gummi, Kunststoffe, 2014. **67**(5): p. 53-57.
45. Thommes, M., et al., *Physisorption of gases, with special reference to the evaluation of surface area and pore size distribution (IUPAC Technical Report)*. Pure and applied chemistry, 2015. **87**(9-10): p. 1051-1069.
46. Cychosz, K.A., et al., *Recent advances in the textural characterization of hierarchically structured nanoporous materials*. Chemical Society Reviews, 2017. **46**(2): p. 389-414.
47. Vimont, A., F. Thibault-Starzyk, and M. Daturi, *Analysing and understanding the active site by IR spectroscopy*. Chemical Society Reviews, 2010. **39**(12): p. 4928-4950.
48. Vimont, A., F. Thibault-Starzyk, and J. Lavalley, *Infrared spectroscopic study of the acidobasic properties of beta zeolite*. The Journal of Physical Chemistry B, 2000. **104**(2): p. 286-291.
49. Nesterenko, N., et al., *The use of the consecutive adsorption of pyridine bases and carbon monoxide in the IR spectroscopic study of the accessibility of acid sites in microporous/mesoporous materials*. Kinetics and catalysis, 2006. **47**(1): p. 40-48.
50. Guisnet, M., P. Ayrault, and J. Datka, *Acid properties of dealuminated mordenites studied by IR spectroscopy. 2. Concentration, acid strength and heterogeneity of OH groups*. Polish journal of chemistry, 1997. **71**(10): p. 1455-1461.



# New approach for preparing zeolite-polymer hybrid materials with hierarchical porosity: promising materials for separation and membrane's applications

*Rita Zakhia Douaihy<sup>a</sup>, Houssein Nasrallah<sup>a</sup>, Oleg Lebedev<sup>b</sup>, Jaafar El Fallah<sup>a</sup>, Rémy Guillet-Nicolas<sup>a</sup>, Alexandre Vimont<sup>a</sup>, Philippe Bazin<sup>a,\*</sup>, Mohamad El-Roz<sup>a,\*</sup>*

<sup>a</sup> Normandie Université, ENSICAEN, UNICAEN, CNRS, Laboratoire Catalyse et Spectrochimie, 14050 Caen, France

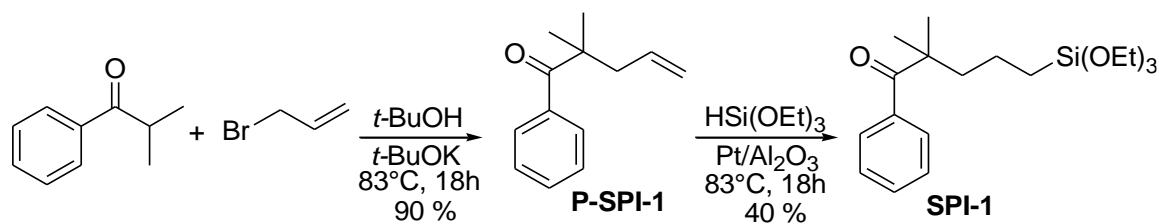
<sup>b</sup> Normandie Université, ENSICAEN, UNICAEN, CNRS, Laboratoire CRISMAT, 14050 Caen, France

\* Corresponding authors: mohamad.elroz@ensicaen.fr; philippe.bazin@ensicaen.fr

KEYWORDS: hybrid materials, zeolites, polymer, core-shell, dehydration

\* Corresponding author

## Supporting Information



**Scheme S1:** Schematic representation of the two-step reaction synthesis of SPI-1

2,2-Dimethyl-1-phenyl-pent-4-en-1-one (P-SPI-1):

Allyl bromide (11 mL, 128 mmol) was added dropwise to a mixture of isobutyrophenone (10 g, 67 mmol) and *t*-BuOK (15, 128 mmol) in 40 mL of *t*-BuOH. The overall mixture was stirred for overnight at 83 °C, poured into water, and then extracted with Et<sub>2</sub>O. Then, the obtained organic extracts were dried over anhydrous Na<sub>2</sub>SO<sub>4</sub>, filtered and evaporated affording 12.1 g of pure **P-SPI-1** (96%). <sup>1</sup>H NMR (400 MHz, CDCl<sub>3</sub>) δ (ppm) 7.64 (d, 2H, *J* = 7.9 Hz), 7.45 (t, 1H, *J* = 7.4 Hz), 7.39 (t, 2H, *J* = 7.4 Hz), 5.68-5.76 (m, 1H), 4.99-5.05 (m, 2H), 2.48 (d, 2H, *J* = 7.5), 1.32 (s, 6H).

2,2-dimethyl-1-phenyl-5-(triethoxysilyl) pentane-1-one (SPI-1):

**P-SPI-1** (1g, 5.3 mmol) was mixed with a solution of triethoxysilane (685 uL, 3.7 mmol) and Pt/Al<sub>2</sub>O<sub>3</sub> 5wt% (1.5g) without solvent in a Schlenk tube. The reaction was stirred overnight at 83 °C and washed with EtOH<sub>abs.</sub> through activated charcoal. After solvent evaporation using rotavapor, the excess of **P-SPI-1** and the byproduct were eliminated using Schenk line under reduced pressure at 100 °C to obtain 400 mg of **SPI** (40%). <sup>1</sup>H NMR (400 MHz, CDCl<sub>3</sub>) δ (ppm) 7.65 (d, 2H, *J* = 7.8 Hz), 7.44, (t, 1H, *J* = 7.2 Hz), 7.38 (t, 2H, *J* = 7.2 Hz), 3.75 (q, 6H, *J* = 7.0 Hz), 1.77-1.80 (m, 2H), 1.32-1.38 (m, 2H), 1.29 (s, 6H), 1.18 (t, 9H, *J* = 7.32 Hz), 0.56 (t, 2H, *J* = 8.1 Hz).

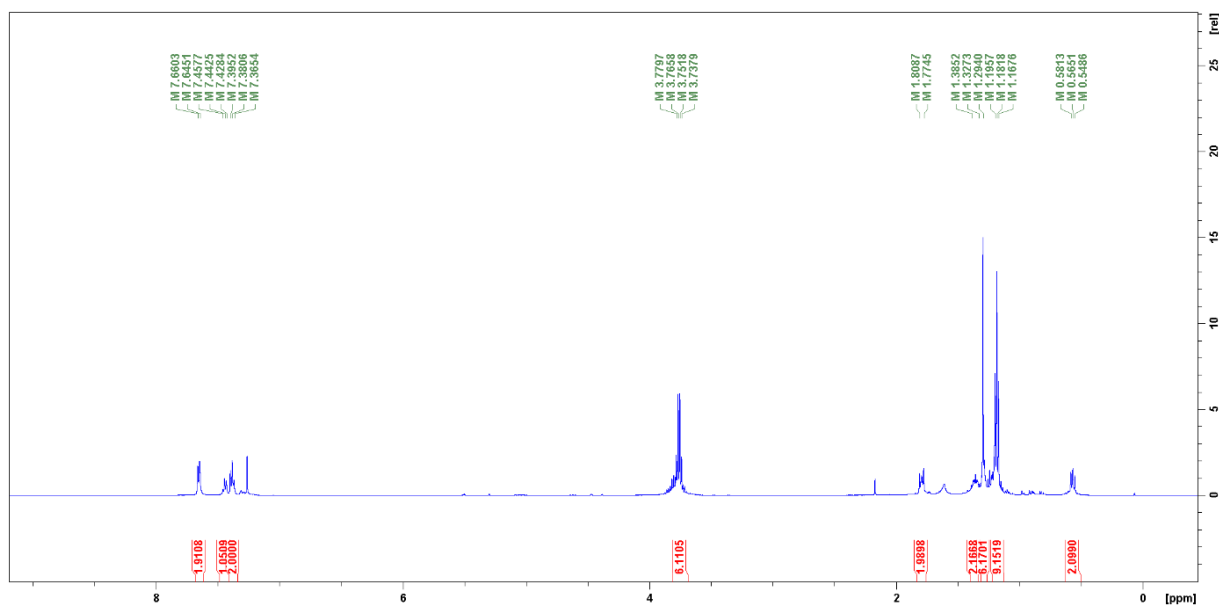


Figure S1: NMR spectrum of SPI-1

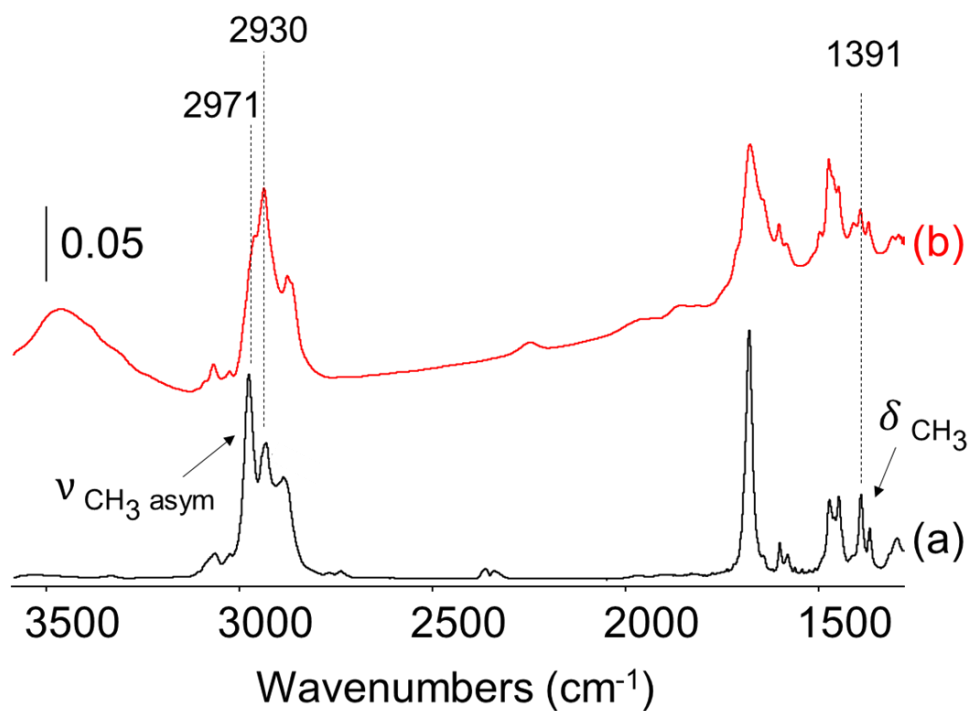
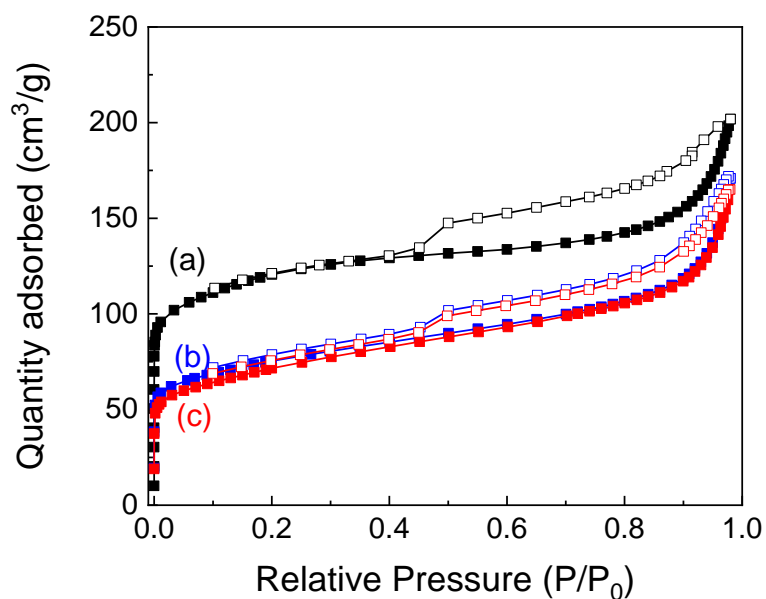


Figure S2: IR spectrum of SPI-1 in the liquid phase ((a)-black) and IR subtraction spectrum of SPI-1-MFI and MFI ((b)-red)



**Figure S3:** N<sub>2</sub> at 77K adsorption/desorption isotherms of MFI@Polymer at 3 different degassing temperatures: 150 °C ((a)-black), 180 °C ((b)- blue) and 200 °C ((c)-red).

**Table S1:** The porosity of MFI@Polymer tested by N<sub>2</sub> adsorption/desorption after degassing at three different temperatures.

	150 °C	180 °C	200 °C
S <sub>BET</sub> <sup>a</sup> (m <sup>2</sup> /g)	402	175	168
External surface area <sup>b</sup> (m <sup>2</sup> /g)	232	62	68
Total Volume (cm <sup>3</sup> /g)	0.312	0.177	0.167
Micropore volume <sup>c</sup> (cm <sup>3</sup> /g)	0.133	0.05	0.04

<sup>a</sup> BET surface area, <sup>b,c</sup> *t*-plot.

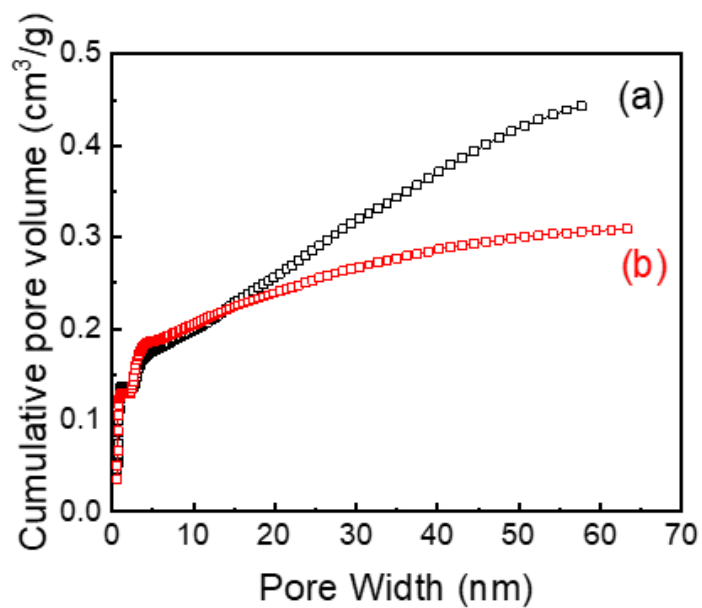


**Figure S4:** NLDFT Cumulative pore volumes (cm<sup>3</sup>/g) of MFI ((a)- black) and MFI@Polymer ((b)- red) calculated from the adsorption branch of nitrogen adsorption at 77 K. The curve (b) is normalized to the mass of zeolite (60 % zeolite and 40 % polymer).

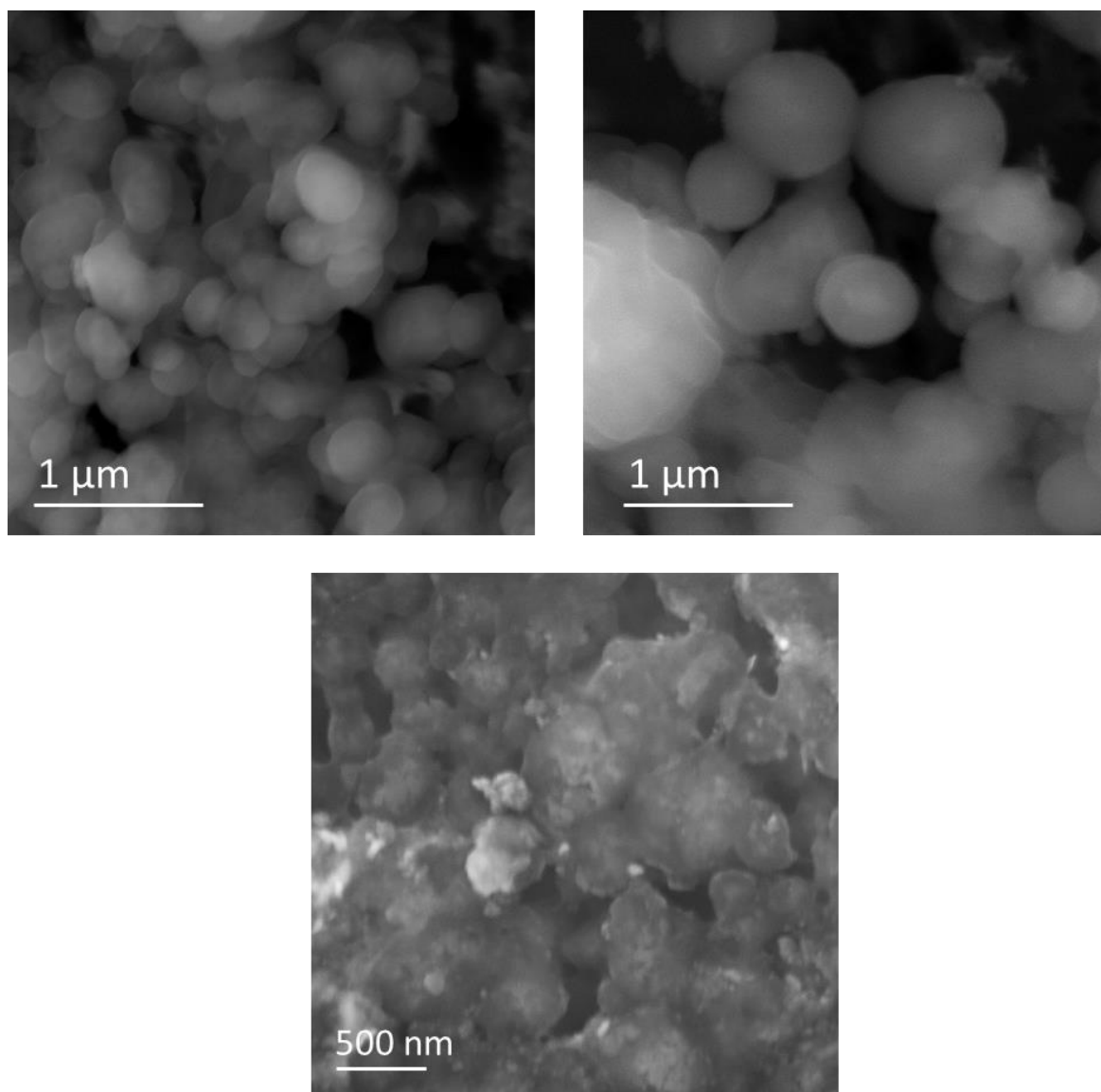


**Figure S5:** SEM images of MFI@Polymer at different scales.

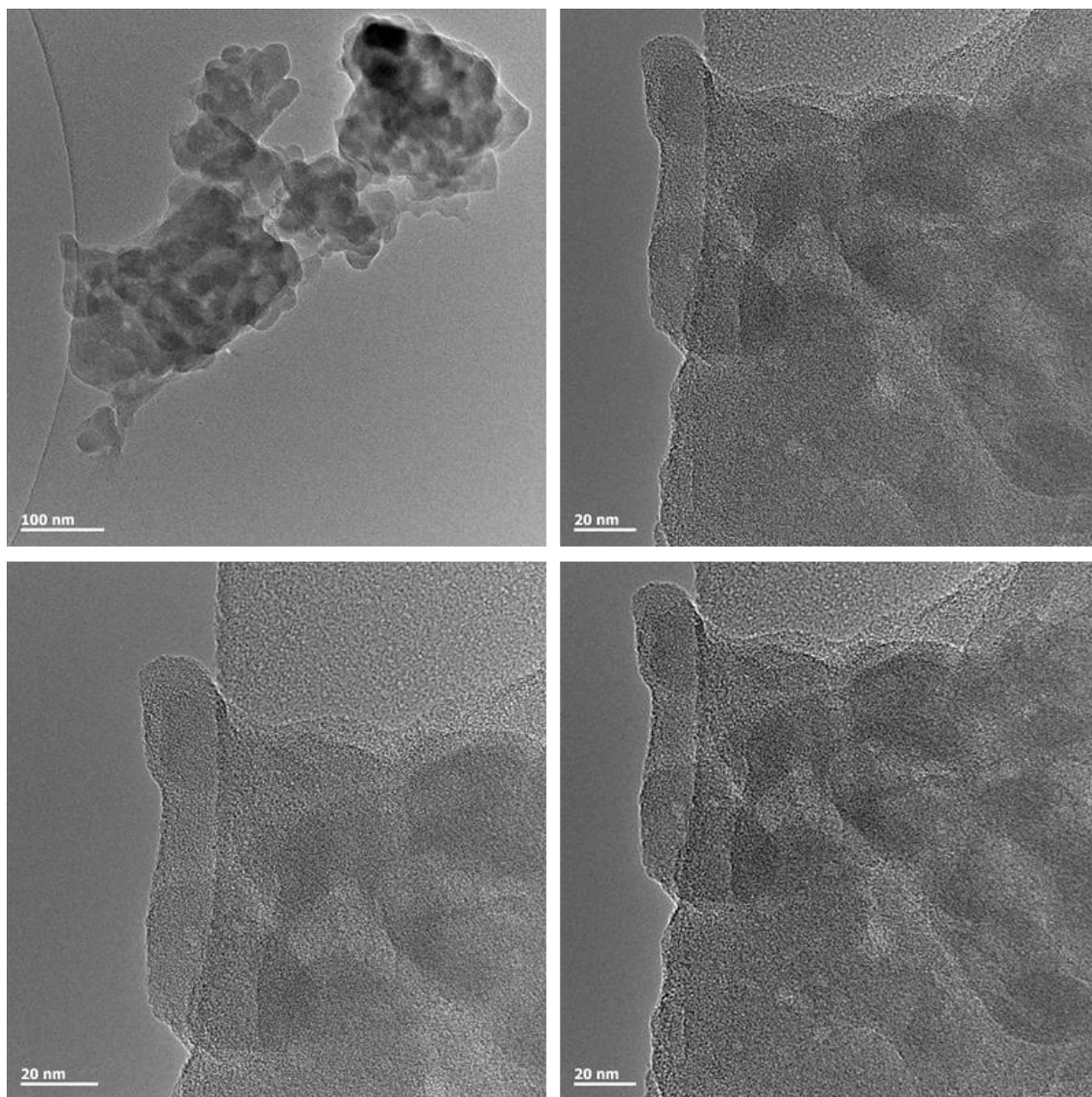


**Figure S6:** TEM images of MFI@Polymer.

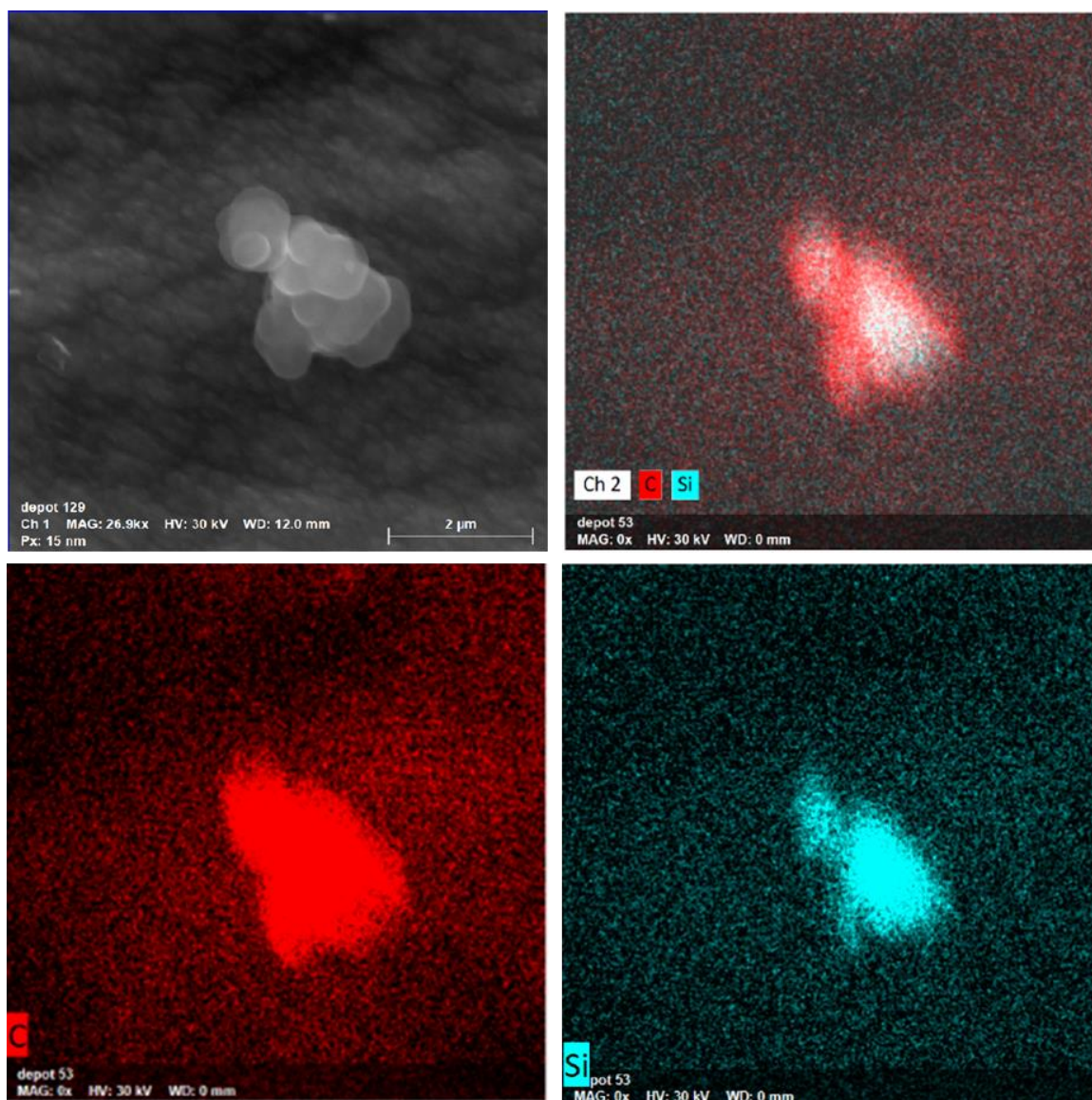


**Figure S7:** SEM image with EDX (Si: blue, C: red; scale = 2 μm) of MFI@Polymer.

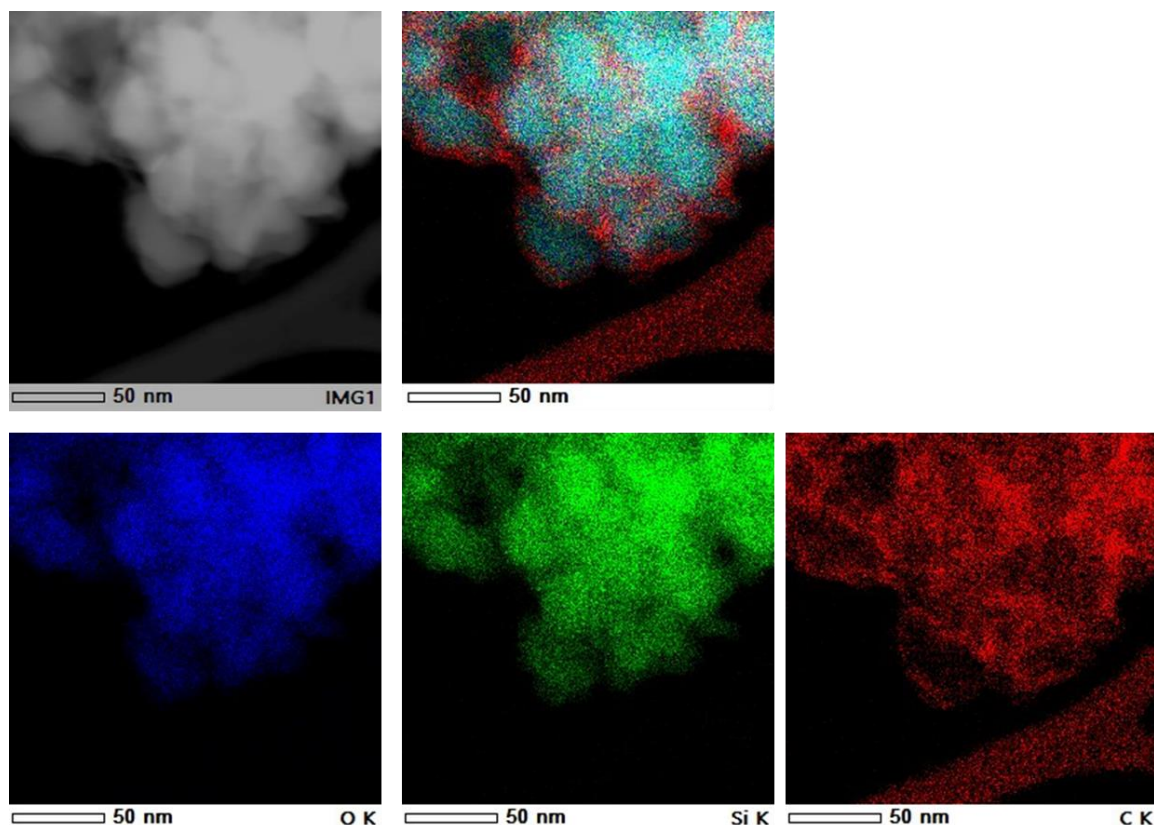


**Figure S8:** TEM image with EDX (O: blue, Si: green and C: red; scale = 50 nm) of MFI@Polymer.

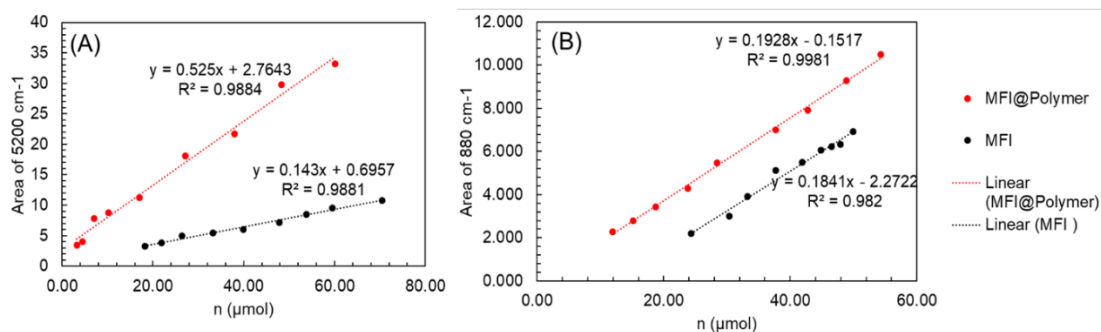


**Figure S9:** Evolution of the area of the characteristic bands of water ( $5200\text{ cm}^{-1}$ ) and ethanol ( $880\text{ cm}^{-1}$ ) as a function of the quantities adsorbed. The molar absorption coefficients are proportional to the slope of the area vs  $n$  (= slope multiplied by 2) for the characteristic bands and are determined from the AGIR experiments.

$$A = \varepsilon \cdot l \cdot c = \varepsilon \cdot l \cdot \frac{n}{V} = \varepsilon \cdot l \cdot \frac{n}{l \cdot S} = \varepsilon \cdot \frac{n}{S}$$

With  $A$  ( $\text{cm}^{-1}$ ) the area of the band,  $\varepsilon$  ( $\text{cm} \cdot \mu\text{mol}^{-1}$ ) the molar absorption coefficient,  $l$  (cm) the optical pathway,  $c$  ( $\mu\text{mol}$ ) the concentration of the adsorbate,  $V$  (mL) the volume of the pellet,  $S$  ( $\text{cm}^2$ ) the surface of the pellet and  $n$  ( $\mu\text{mol}$ ) the number of moles of the adsorbate.

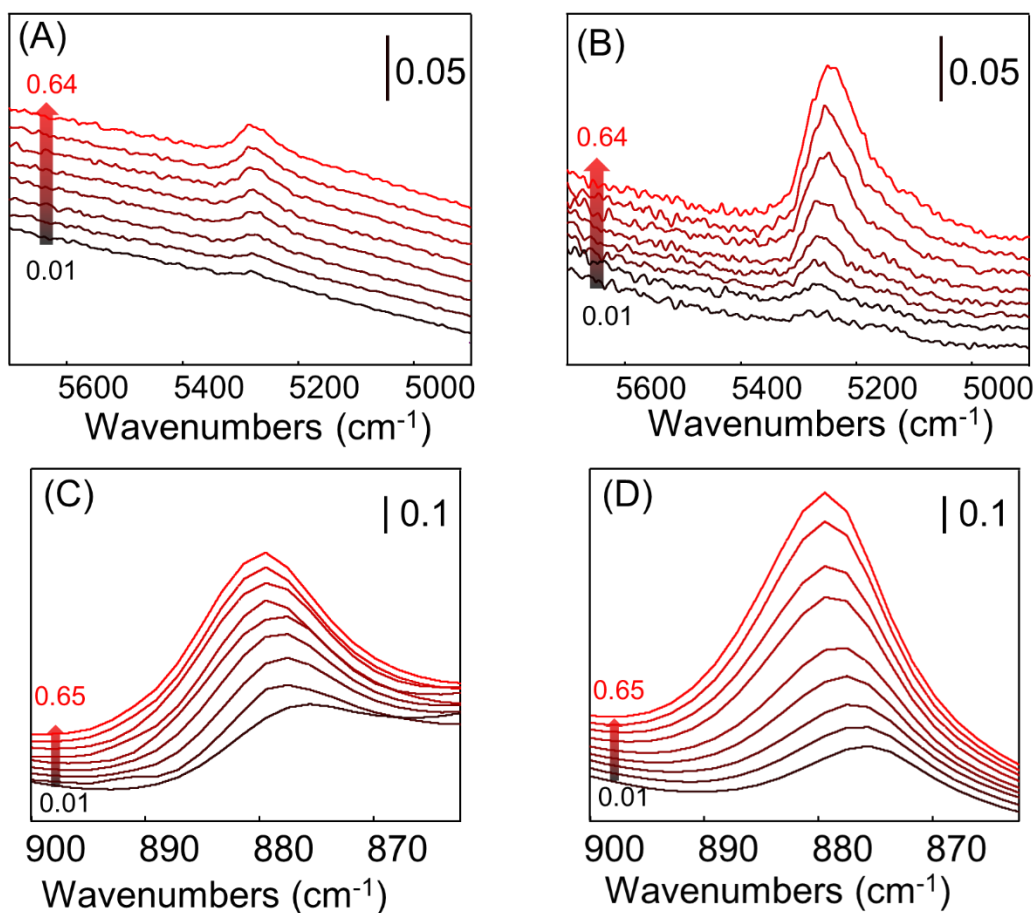


**Figure S10:** Evolution of the IR spectra of MFI ((A) and (C)) and MFI@Polymer ((B) and (D)) after water ((A) and (B)) and ethanol ((C) and (D)) adsorptions at different partial pressures.

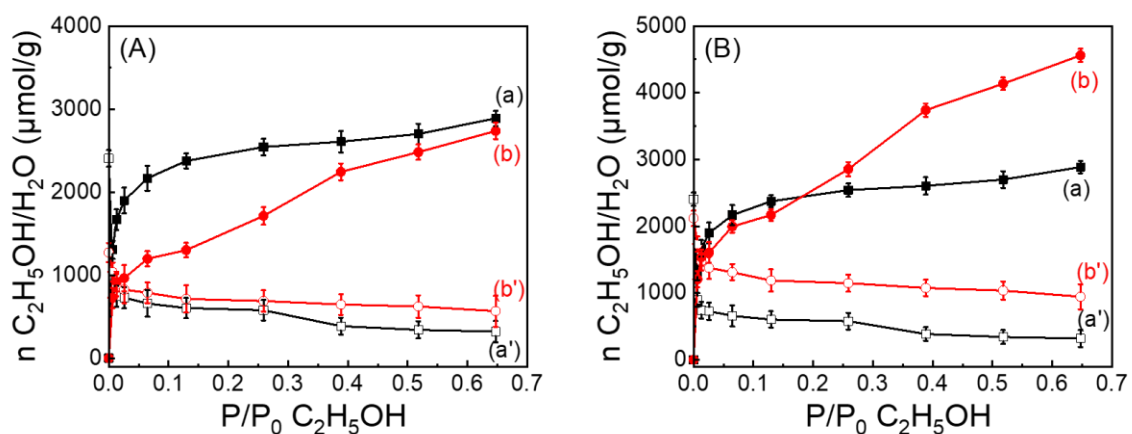


**Figure S11:** (A) and (B) Quantities of adsorbed water ((a') and (b')) and adsorbed ethanol ((a), (b)) on MFI (black) and MFI@Polymer (red) versus the partial pressure of ethanol (water concentration in the flow is fixed at 1%). (B) corresponds to the quantities normalized to the mass of zeolite (60 % of zeolite).





---

# GENERAL CONCLUSION AND PERSPECTIVES

---



## 1. General conclusions

Bioethanol purification is of great importance for its use as an additive or replacement for gasoline. Among the various purification processes, the literature mainly focuses on the purification of bioethanol from its aqueous mixture on porous materials, such as zeolites or hybrid zeolitic materials. Different experimental and computational approaches have been developed to study ethanol and water's adsorption and selective separation. IR spectroscopy is a powerful tool that has not yet been used to study the separation of binary system of ethanol/water.

Moreover, hybrid materials, such as core-shell and mixed matrix membranes, have attracted attention and have been widely used to separate binary mixtures. This is due to their eminent properties resulting from the combination of each constituent's properties and those resulting from their interactions. Their synthesis has been prone to several challenges due to difficulty to achieve homogeneous dispersion and strong interactions of the core particles in the shell layer, leading to reduced accessibility to the pores of the core particles. Hence, the synthesis of hybrid materials requires further improvement and optimization.

In the framework of this research, our work consists of studying first the adsorption and coadsorption of ethanol/water on zeolites using IR spectroscopy. The study is then extended to zeolite-polymer-based hybrid materials for their potential use as seeds for synthesizing mixed matrix membranes for bioethanol purification. Zeolite-polymer-based hybrid materials were synthesized after developing a new approach based on the photopolymerization of an acrylate monomer on the surface of zeolites previously grafted by a silane-based photoinitiator.

The most important findings in this work are highlighted as follows:

1- The adsorption isotherms of water and ethanol were studied on MFI zeolites as a function of the Si/Al ratio effect, using different IR spectroscopic techniques. The molar absorption coefficients of the characteristic bands of ethanol and water were determined by adsorption of ethanol or water separately and found to be independent of the Si/Al ratio. Their values remain unchanged during the adsorption of these

adsorbates in the binary system. Water adsorption capacity of MFI zeolites is highly affected by the Si/Al ratio and water molecules are adsorbed in tetrameric clusters on each Bronsted acid site of the zeolite. However, ethanol adsorbs in dimeric clusters on each Bronsted acid site and ethanol capacity is only affected by the Si/Al ratio at low ethanol partial pressure. Moreover, the effect of the Si/Al ratio and the role of coadsorbed water on the quantity of adsorbed ethanol have been investigated to determine the separation membrane's choice. The quantity of adsorbed ethanol decreases with the increase of the Si/Al ratio and the vapor water content.

2- The synthesis of hybrid materials has been successfully reported via a new approach: the photopolymerization of an acrylate monomer under UV-Visible irradiations in the presence of a silane-based photoinitiator previously grafted on the surface of the core particles. First, this approach has been validated on silica nanoparticles. The mechanical properties of the obtained films of Silica@polymer were studied using AFM and reveal a significant increase of the surface elastic modulus compared to that of the ungrafted silica mixed with polymer. The morphology of the synthesized hybrid materials examined using TEM is assimilated to a core-shell like structure, with homogeneous dispersion of silica nanoparticles and strong covalent interactions between them and the polymer matrix. The textural properties of the hybrid materials were further studied and revealed the creation of a mesoporosity on the surface of silica nanoparticles, attributed to the polymer. Based on these results, the hybrid materials were tested for the adsorption of ethanol and water using IR spectroscopy. The results revealed an increase in the ethanol adsorption capacity with the decrease of water adsorption capacity.

3- Due to the eminent properties of the hybrid materials obtained from the newly developed synthesis approach, zeolitic hybrid materials were also synthesized using the same approach. The synthesized MFI@Polymer hybrid materials were fully characterized: XRD patterns reveal their full their crystallinity after polymerization, UV-Visible and IR spectroscopies allow to detect the characteristic bands of the silane-based photoinitiator before grafting and that of the polymer after polymerization, thermogravimetric analyses were conducted to determine the hydrocarbon loading and SEM and TEM to examine their morphologies. The microscopy images show core-shell like structure of MFI@Polymer with homogenous dispersion of MFI particles in

the polymer. Moreover, the accessibility of the pores of the MFI zeolites was studied by nitrogen sorption and adsorption of basic probe molecules using IR spectroscopy. Interestingly, the pores of the zeolites remain accessible to more than 90 % after their coverage with the polymer. An additional mesoporosity was also detected on the hybrid material due to the presence of the polymer and created thus a hierarchical material. Finally, using IR spectroscopy, the hierarchical hybrid materials were tested for ethanol/water separation. The ethanol adsorption capacity of these materials increased while water capacity significantly decreased. The hydrophobic/hydrophilic characters were altered using this synthesis approach. Therefore, these materials are considered potential seeds for synthesizing mixed matrix membranes for ethanol/water separation.

The present work shows the importance of the advanced synthesis approach for developing outstanding hierarchical hybrid materials with prominent properties. It shows also the importance of coupling different analyzing techniques for advanced studies. Notably, the IR spectroscopy coupled with gravimetric analyses is very useful for understanding the adsorption process of water and ethanol on zeolites, in particular through the quantification of the adsorbed and coadsorbed species in relative with the nature of the adsorption sites.

## 2. Perspectives

This work provides an elaborative study of the separation of ethanol and water on zeolitic materials using developed IR spectroscopic techniques. IR spectroscopy proves to be powerful technique to investigate the mechanism of adsorption of the binary ethanol/water mixtures. For the future, testing different types of zeolites offers a good perspective for elucidating the effect of the zeolite structure on the adsorption mechanism.

Moreover, the developed IR methodology could be extended to investigate the adsorption mechanisms of other mixtures of industrial interest such as xylenes, biobutanol/water, etc...

In the scope of our work, zeolitic hybrid materials have been successfully synthesized via a new synthetic approach and tested in the selective separation of

ethanol and water. The synthesis of these materials was conducted in the presence of a silane based-photoinitiator active under UV-Visible irradiation. In the future, the development of new silane-based photoinitiators efficient under Visible light poses a promising perspective in light of novel 3D printing applications.

Despite overcoming the limitations in the synthesis of mixed matrix membranes (i.e. assuring a homogenous dispersion of zeolites, conserving their accessibility and enhancing the interactions with the polymer), the implementation of the hybrid materials for the synthesis of mixed matrix membranes was beyond the scope of our work. Therefore, the extension of this new approach in the synthesis of MMMs for ethanol/water separation could be proposed as a promising tactic to achieve ameliorated membranes.

Beyond the scope of our work, it would be worth exploring other zeolitic structures and different types of monomers for the synthesis of hybrid materials and mixed matrix membranes. This aspect will pave the way for future studies and extend the application of the novel synthesized hybrid materials.





---

# Résumé étendu en Français

---



Au cours de la dernière décennie, les préoccupations environnementales ont suscité l'intérêt des experts du monde en raison de leur grande importance et de leurs effets sur la survie de l'humanité. L'augmentation des niveaux de gaz à effet de serre, l'épuisement des réserves de pétrole et l'augmentation spectaculaire de la consommation d'énergie ont nécessité la recherche de ressources durables alternatives aux carburants à base d'hydrocarbures [1]. Les biocarburants, y compris les bio-alcools et les biogaz, ont été largement produits [2]. Le bioéthanol constitue l'un des principaux composants de ces biocarburants, vu qu'il peut être utilisé comme additive à l'essence [3].

En effet, le bioéthanol se caractérise par un indice d'octane élevé, un faible indice de cétane et une combustion émettant peu de  $\text{NO}_x$  [4]. Il est principalement obtenu à partir de la dégradation et de la décomposition de la biomasse [5]. Avant son utilisation comme additif ou alternative à l'essence, un processus de purification est nécessaire pour éliminer les traces d'eau indésirables. Pour cela, des procédés de distillation conventionnel ont été utilisés [6]. Cependant, la phase la plus critique consiste à surmonter la barrière azéotropique du mélange éthanol/eau [7]. Par conséquent, plusieurs techniques de séparation ont été mises en œuvre, telles que la séparation sur des matériaux poreux, des matériaux poreux hybrides et des membranes [8, 9]. Parmi ces matériaux, les zéolithes offrent des capacités de séparation à fort potentiel car elles sont caractérisées par une porosité importante et ajustable, un caractère hydrophile/hydrophobe variable et une activité importante grâce à leurs sites acides actifs [10]. Ces propriétés sont particulièrement améliorées lorsque les zéolithes sont couplées à d'autres composants pour former des matériaux hybrides de type core-shell ou lorsqu'elles sont utilisées pour des membranes à matrice mixte [11, 12]. Certes, ces dernières ont été abondamment synthétisées et utilisées dans la séparation des mélanges gazeux et liquides. Leur importance résulte de la combinaison des caractéristiques de séparation sélective et d'adsorption des particules poreuses inorganiques et des propriétés mécaniques et économiques des matrices polymères.

Cependant, la synthèse de membranes à matrice mixte a été enclin à plusieurs problématiques, notamment la dispersion homogène des particules inorganiques dans la matrice du polymère, la présence de fortes interactions entre les deux

constituants de la membrane, et surtout, l'accessibilité aux pores des composés inorganiques après leur couverture [11]. Ainsi, une étude approfondie de ces paramètres est nécessaire afin d'améliorer l'activité de la membrane, et notamment vis-à-vis de la purification de l'éthanol de son mélange aqueux, considéré comme un processus primordial pour la déshydratation du bioéthanol.

Différentes techniques ont permis d'étudier de manière approfondie la séparation ou l'adsorption sélective de l'éthanol d'un mélange hydraté sur des MMM. Pour cela, des méthodes volumétriques et gravimétriques couplées ont été appliquées pour étudier les isothermes d'adsorption/désorption de chaque composant du mélange [13, 14]. La résonance magnétique nucléaire (RMN) à gradient de champ pulsé (PFG) a également été utilisée pour étudier la diffusion de l'eau, de l'éthanol et de leur mélange dans des membranes en acide polyacrylique (PAA) PAA-polysulfone et chitosan [15, 16]. Cette technique a permis de déterminer les sites d'adsorption préférentiels de l'éthanol et l'eau présents dans ces membranes. Les résultats expérimentaux étaient en accord avec les études théoriques, y compris les simulations de Monte Carlo grand canonique et de dynamique moléculaire, menées dans le même but [17-19]. La spectroscopie infrarouge est une technique performante pour la caractérisation des sites d'adsorption à l'échelle moléculaire. Néanmoins, elle a été principalement utilisée que pour étudier l'adsorption de l'éthanol ou de l'eau séparément. L'étude de la coadsorption de l'éthanol et de l'eau par spectroscopie IR n'a pas été abordée dans la littérature, à l'exception d'une étude menée dans notre laboratoire sur des MOFs [20].

Par conséquent, ce projet a été initié pour synthétiser des matériaux zéolitiques hybrides de type core-shell via une procédure prometteuse pour améliorer la synthèse des membranes à matrice mixte. Dans un premier objectif, une étude a été menée sur différentes zéolithes de type MFI, avec des rapports Si/Al différents sur l'adsorption de l'éthanol et l'eau (adsorption des corps simples et coadsorption). Dans un second temps, des matériaux hybrides de type core-shell ont été synthétisés par photopolymérisation d'un monomère acrylate. Les performances de ces matériaux vis-à-vis de l'adsorption de l'éthanol et/ou de l'eau ont été testées par la suite.

Le manuscrit est rédigé sous la forme d'articles publiés/soumis et est divisé en deux parties. La première partie traite de l'adsorption de l'éthanol et/ou de l'eau sur les matériaux zéolitiques. La deuxième partie se concentre sur la synthèse des matériaux hybrides et leur application dans l'adsorption préférentielle de l'éthanol et/ou de l'eau.

Alors que le **deuxième chapitre** présente les méthodes et les matériaux utilisés dans ce travail, le **troisième chapitre** est consacré à l'étude spectroscopique de l'adsorption de l'éthanol et/ou de l'eau sur des zéolithes de type MFI et est en cours de soumission. Les zéolithes MFI ont été utilisées car leurs sites acides actifs présentent une double affinité pour l'éthanol et l'eau. Elles ont été caractérisées à l'aide des techniques de caractérisation de routine comme la DRX, la MEB et la sorption d'azote. Ensuite, la force de leurs sites acides et leur quantification par adsorption de molécule sonde basique (pyridine) a été réalisée par spectroscopie IR. De plus, les capacités d'adsorption simple et binaire de l'éthanol et de l'eau ont été étudiés à l'aide de techniques spectroscopiques développées au sein du laboratoire (les techniques AGIR et CARROUCELL). La spectroscopie IR couplée à des analyses gravimétriques a été utilisée pour déterminer les quantités des espèces adsorbées, leur nature et la nature des sites d'adsorption. Il est intéressant de noter qu'en corrélant la quantité des sites acides des zéolithes MFI avec celles des espèces adsorbées, le nombre de chaque adsorbant par site acide a été déterminé et comparé aux approches expérimentales et théoriques de la littérature. Enfin, l'effet du rapport Si/Al a été étudié lors de la coadsorption de l'éthanol et de l'eau. La sélectivité de l'éthanol sur les zéolithes MFI a été étudiée pour certaines zéolithes. En raison de limitations dans la mesure des aires des bandes Infrarouges caractéristiques des espèces adsorbées, un nouveau facteur dénomé 'rapport de l'éthanol adsorbé' a été introduit pour étudier l'effet du rapport Si/Al et de la pression d'eau sur l'adsorption de l'éthanol dans les systèmes binaires. Il a été démontré que l'adsorption de l'éthanol sur les zéolithes de type MFI est affectée à la fois par le rapport Si/Al et la teneur en eau en phase vapeur. En effet, l'éthanol est moins adsorbé lorsque la teneur en Al ou en eau est importante. Par conséquent, il a été conclu que le choix du matériau pour la synthèse des membranes pour la purification de l'éthanol est ainsi affecté.

Dans le **quatrième chapitre**, la synthèse de matériaux hybrides est élucidée via la polymérisation sous irradiation UV-visible d'un monomère acrylate à la surface

de nanoparticules de silice, préalablement greffées avec un nouveau photo-initiateur à base de silane (SPI-1). Le succès du greffage du photo-initiateur à base de silane sur les nanoparticules de silice a été prouvé par des spectroscopies UV-Visible et IR. Le mécanisme de greffage a été étudié par spectroscopie IR et se produit via de fortes interactions covalentes entre les groupes éthoxy du photo-initiateur et les groupes silanols des nanoparticules de silice. La quantité de matériau greffé et sa stabilité thermique ont été déterminées par des analyses thermogravimétriques. L'efficacité du SPI-1 greffé a ensuite été testée dans la polymérisation radicalaire d'un monomère acrylate sous irradiation UV-Visible. Une polymérisation homogène s'est produite à la surface des nanoparticules de silice, entraînant leur couverture totale. Les propriétés mécaniques des matériaux hybrides synthétisés ont été étudiées par microscopie à force atomique, et leur morphologie a été examinée par microscopie électronique. Les matériaux hybrides synthétisés ont été soumis à l'adsorption d'azote, et les résultats ont montré qu'une méso-porosité supplémentaire attribuée à la présence du polymère s'est formée. Les propriétés distinguées des matériaux hybrides sont attribuées à la structure de type core-shell à l'échelle microscopique, permettant leur application pour purifier l'éthanol de son mélange aqueux. Il a été démontré que la capacité d'adsorption du matériau augmente pour l'éthanol alors qu'elle diminue pour l'eau. Une partie de ces travaux a été publiée dans *Materials Today Communications*.

Puisque les zéolithes MFI présentent une forte affinité à la fois pour l'éthanol et l'eau, il est nécessaire de modifier leur surface pour ajuster leurs sélectivités d'adsorption. De plus, puisque la technique de synthèse discutée précédemment a révélé des résultats prometteurs dans la modification de la surface des nanoparticules de silice, dans le **cinquième chapitre**, nous l'appliquons à la synthèse de matériaux core-shell à base de zéolithes et de polymères.

C'est pour cela que l'efficacité du photo-initiateur à base de silane (SPI-1) dans des conditions UV-Visible est testée après greffage sur la surface des zéolithes MFI pour former des matériaux hybrides MFI@Polymer. Premièrement, les matériaux modifiés (SPI-1-MFI et MFI@Polymer) ont été caractérisés par DRX, UV-Visible et spectroscopie IR pour détecter les bandes caractéristiques vibrationnelles de la structure du SPI-1 et du polymère, ATG pour déterminer la charge en hydrocarbures, et microscopie électronique (SEM et TEM) pour examiner leurs morphologies.

Ensuite, la stabilité thermique des échantillons SPI-1-MFI a été étudiée par une désorption thermique programmée effectuée par spectroscopie IR. En outre, l'accessibilité des pores des particules zéolitiques est étudiée après adsorption de l'azote et des molécules sonde basiques par spectroscopie IR. Il a été observé que les pores des MFI restent toujours accessibles à ~ 90 % après le greffage et la polymérisation, avec une méso-porosité supplémentaire due au polymère. Les résultats indiquent que cette nouvelle technique peut être appliquée pour synthétiser de nouveaux matériaux hybrides hiérarchiques et peut être une voie de synthèse potentielle pour les membranes à matrice mixte puisque les particules inorganiques restent accessibles. En conséquence, on peut dire qu'un des problèmes majeurs de la synthèse des MMM a été surmonté. Enfin, les matériaux hybrides hiérarchiques synthétisés sont testés dans la séparation sélective et la purification de l'éthanol de son mélange aqueux. La modification de leur caractère hydrophobe/hydrophile a été détectée. Les matériaux hybrides ont révélé une forte capacité d'adsorption de l'éthanol avec une capacité en eau plus faible que la zéolithe parent. Ce travail est actuellement soumis pour la publication.

En conclusion, la combinaison d'une nouvelle voie de synthèse avec l'ensemble des caractérisations et performances associées donne lieu au développement de matériaux hybrides hiérarchiques, qui sont des candidats prometteurs pour la synthèse de membranes pour de nombreuses applications, notamment pour la séparation de l'éthanol et de l'eau. De plus, les résultats obtenus par les études spectroscopiques permettent d'élargir cette étude pour étudier d'autres mélanges.

## References

1. Karl, T.R. and K.E. Trenberth, *Modern global climate change*. science, 2003. **302**(5651): p. 1719-1723.
2. Abdeshahian, P., et al., *Production of biofuel using biomass as a sustainable biological resource*. Biotechnology, 2010. **9**(3): p. 274-282.
3. Kumar, S., N. Singh, and R. Prasad, *Anhydrous ethanol: A renewable source of energy*. Renewable and Sustainable Energy Reviews, 2010. **14**(7): p. 1830-1844.
4. Balat, M., *Global bio-fuel processing and production trends*. Energy Exploration & Exploitation, 2007. **25**(3): p. 195-218.
5. Socol, C.R., et al., *Lignocellulosic bioethanol: current status and future perspectives*, in *Biofuels: Alternative Feedstocks and Conversion Processes for the Production of Liquid and Gaseous Biofuels*. 2019, Elsevier. p. 331-354.
6. Vane, L.M., *Separation technologies for the recovery and dehydration of alcohols from fermentation broths*. Biofuels, Bioproducts and Biorefining, 2008. **2**(6): p. 553-588.
7. Siepmann, J.I., P. Bai, and M. Tsapatsis, *Zeolites for separation of ethanol and water*. 2018, Univ. of Minnesota, Minneapolis, MN (United States).
8. Davey, C.J., D. Leak, and D.A. Patterson, *Hybrid and mixed matrix membranes for separations from fermentations*. Membranes, 2016. **6**(1): p. 17.
9. Zhan, X., et al., *Pervaporation separation of ethanol/water mixtures with chlorosilane modified silicalite-1/PDMS hybrid membranes*. Chinese Journal of Polymer Science, 2010. **28**(4): p. 625-635.
10. Mintova, S., J.-P. Gilson, and V. Valtchev, *Advances in nanosized zeolites*. Nanoscale, 2013. **5**(15): p. 6693-6703.
11. Bastani, D., N. Esmaili, and M. Asadollahi, *Polymeric mixed matrix membranes containing zeolites as a filler for gas separation applications: A review*. Journal of Industrial and Engineering Chemistry, 2013. **19**(2): p. 375-393.
12. Ghosh Chaudhuri, R. and S. Paria, *Core/shell nanoparticles: classes, properties, synthesis mechanisms, characterization, and applications*. Chemical reviews, 2012. **112**(4): p. 2373-2433.
13. Dreisbach, F., H.W. Lösch, and K. Nakai, *Adsorption measurement of water/ethanol mixtures on activated carbon fiber*. Chemical engineering & technology, 2001. **24**(10): p. 1001-1005.
14. Naono, H., et al., *Separation of water and ethanol by the adsorption technique: selective desorption of water from micropores of active carbon*. Journal of Colloid and Interface science, 1996. **182**(1): p. 230-238.
15. Volkov, V.I., et al., *Self-diffusion of water-ethanol mixture in chitosan membranes obtained by pulsed-field gradient nuclear magnetic resonance technique*. Journal of Membrane Science, 1998. **138**(2): p. 221-225.
16. Volkov, V.I., et al., *Self-diffusion of water-ethanol mixtures in polyacrylic acid-polysulfone composite membranes obtained by pulsed-field gradient nuclear magnetic resonance spectroscopy*. Journal of membrane science, 1995. **100**(3): p. 273-286.
17. Furukawa, S.-i., et al., *Molecular simulation study on adsorption and diffusion behavior of ethanol/water molecules in NaA zeolite crystal*. Journal of chemical engineering of Japan, 2004. **37**(1): p. 67-74.
18. Shi, Q., et al., *Efficient ethanol/water separation via functionalized nanoporous graphene membranes: insights from molecular dynamics study*. Journal of Materials Science, 2017. **52**(1): p. 173-184.
19. Mulder, M. and C. Smolders, *On the mechanism of separation of ethanol/water mixtures by pervaporation I. Calculations of concentration profiles*. Journal of membrane science, 1984. **17**(3): p. 289-307.
20. El-Roz, M., et al., *Pore Occupancy Changes Water/Ethanol Separation in a Metal-Organic Framework: Quantitative Map of Coadsorption by IR*. The Journal of Physical Chemistry C, 2015. **119**(39): p. 22570-2257

## Abstract

Ethanol purification on porous materials such as zeolites and hybrid materials is a widely studied process for its use as an additive to gasoline. The synthesis of hybrid materials is prone to various problems affecting their adsorption capacities. Thus, this work aims to develop an enhanced approach for synthesizing hybrid materials and studying their ethanol and water adsorption capacities using IR spectroscopy. Herein, a mechanistic and quantitative study was carried out to investigate ethanol and/or water adsorption on MFI zeolites with different Si/Al ratios using developed vibrational spectroscopic techniques (IR spectroscopy). The nature and quantities of water and ethanol adsorption sites were determined to be tetrameric clusters for water and dimeric for ethanol on BAS at low partial pressures. The effect of the Si/Al ratio and the water content on the ethanol adsorption capacity of the MFI zeolites was also investigated to direct the choice of the separating membrane. In the second part of this work, we report a new approach for synthesizing hybrid materials (silica and zeolite-polymer based) via the polymerization of an acrylate monomer on the surface of the nanoparticles, in the presence of a silane-based photoinitiator and under UV-Visible conditions. A series of complementary characterizations was conducted to validate the synthesis of the hierarchical hybrid materials. Combined data confirmed the successful synthesis and the preservation of the accessibility to their pores by ~ 90%. The new materials were tested for the adsorption of unary and binary systems of ethanol and water. IR spectroscopy revealed the increase of the ethanol adsorption capacity on the hybrid materials and the decrease of water capacity, thus, making these materials highly promising for future applications in membrane synthesis and separation processes.

**Keywords:** *zeolites, hybrid materials, photopolymerization, IR spectroscopy, ethanol/water adsorption, ethanol purification*

---

## Résumé

La purification de l'éthanol sur des matériaux poreux tels que les zéolithes et les matériaux hybrides est un procédé largement étudié pour son utilisation comme additif à l'essence. La synthèse de matériaux hybrides est sujet à divers problèmes affectant leurs capacités d'adsorption. Ainsi, le but de ce travail est de développer une approche améliorée pour la synthèse des matériaux hybrides et d'étudier leurs capacités d'adsorption d'éthanol et d'eau en utilisant la spectroscopie IR. Dans ce travail, une étude mécanistique et quantitative a été menée pour étudier l'adsorption de l'éthanol et/ou de l'eau sur des zéolithes MFI avec différents ratios Si/Al en utilisant des techniques de spectroscopie vibrationnelle développées (spectroscopie IR). La nature et les quantités des sites d'adsorption de l'eau et de l'éthanol ont été déterminés comme étant des clusters tétramériques pour l'eau et dimériques pour l'éthanol sur les sites acides de Bronsted à faibles pressions partielles. L'effet du rapport Si/Al et de la teneur en eau sur la capacité d'adsorption de l'éthanol des zéolithes MFI a également été étudié afin d'orienter le choix de la membrane de séparation. Dans la seconde partie de ce travail, nous reportons une nouvelle approche de synthèse de matériaux hybrides (à base de silice et de zéolithe et de polymère) via la polymérisation d'un monomère acrylate à la surface des nanoparticules, en présence d'un photoinitiateur à base de silane et dans des conditions UV-Visible. Une série de caractérisations complémentaires a été menée pour valider la synthèse des matériaux hybrides hiérarchiques. Les données combinées ont confirmé la réussite de la synthèse et la préservation de l'accessibilité à leurs pores de ~ 90%. Les nouveaux matériaux ont été testés pour l'adsorption d'éthanol et/ou d'eau (adsorption de corps simple ou adsorption binaire). La spectroscopie IR a révélé l'augmentation de la capacité d'adsorption de l'éthanol sur les matériaux hybrides et la diminution de la capacité de l'eau ; ce qui rend ces matériaux très prometteurs pour de futures applications dans la synthèse de membranes et les processus de séparation.

**Mots clés :** *zéolithes, matériaux hybrides, photopolymérisation, spectroscopie IR, adsorption de l'eau et de l'éthanol, purification de l'éthanol.*